The Dynamic Behaviour and Stability of Streamlined Cables

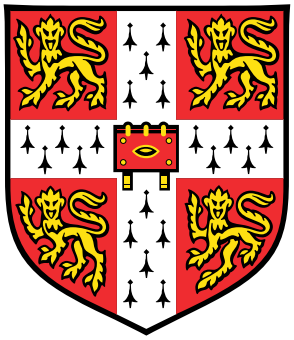

Hilary M. Costello

Department of Engineering

University of Cambridge

This dissertation is submitted for the degree of

Doctor of Philosophy

Churchill College

May 2014

To my parents, Hugh and Christine, to my sister Emily and to Rick.

Declaration

I hereby declare that except where specific reference is made to the work of others, the contents of this dissertation are original and have not been submitted in whole or in part for consideration for any other degree or qualification in this, or any other University. This dissertation is the result of my own work and includes nothing which is the outcome of work done in collaboration, except where specifically indicated in the text. This dissertation contains less than 65,000 words including appendices, bibliography, footnotes, tables and equations and has less than 150 figures.

Hilary M. Costello
May 2014

Acknowledgements

I would like to thank my supervisor Dr. Hugh Hunt for his support, enthusiasm and guidance throughout this research. My thanks also goes to Dr. Kirsty Kuo and Dr. James Talbot for their helpful discussions and advice throughout my PhD. I would also like to acknowledge Gareth Ryder, Mark Rainer, Andy Elson and Pete Smith without whom the experimental work and testing could not have been completed. I would like to thank my supervisor Dr. Hugh Hunt for his support, enthusiasm and guidance throughout this research. My thanks also goes to Dr. Kirsty Kuo and Dr. James Talbot for their helpful discussions and advice throughout my PhD. I would also like to acknowledge Gareth Ryder, Mark Rainer, Andy Elson and Pete Smith without whom the experimental work and testing could not have been completed.

I am grateful for all of those who have supported me in different ways over the past three and a half years. To the Rt. Hon. Sir Winston S. Churchill Society of Edmonton for their generous support, which has given me the opportunity to undertake this PhD. To Churchill College for providing a me with a sense of community, financial support and accommodation. To Rick Lupton for his willingness to discuss problems, offer advice and read over my work. To Alice Cicirello for being a constant source of positivity and encouragement in the office. To my parents and sister for always being willing to offer advice and encouragement. To my Grandpa, who will always be an inspiration to continue learning. Finally, to Rick Enns, for his unfaltering support and encouragement which helped motivate me to finish.

Abstract

The benefits of streamlining the cross-section of a cable are the reduction in drag and vortex induced vibrations (VIV). Streamlined, or faired, cables are used for underwater systems such as towed cable arrays and their use has been proposed for emerging technologies in air, such as high-altitude tethered balloons and kite-power generators. The main drawback of streamlining the cable is that instabilities such as flutter and divergence may be introduced. To take advantage of the streamlining benefits an understanding of the dynamic behaviour and stability of streamlined cables is essential. The current work contributes to the existing body of knowledge on streamlined cables through a combination of theoretical and experimental work.

To help predict the behaviour of streamlined cables three mathematical models are developed: a two-degree-of-freedom model, a continuous model and a finite-element model. The models include the effects of fully-unsteady fluid flow, geometric stiffening due to the applied tension and offset structural centres of mass, shear and tension. A programme to manufacture streamlined cable was undertaken; a machine was built which successfully produced lengths of streamlined cable up to approximately 150 m. In parallel with the development of the manufacturing process wind tunnel, kite and balloon tests were completed. An outdoor test of 50 m lengths of streamlined cable, supported horizontal, was used to study the stability of the cable given variations in the centre of mass. In this test, cables with centres of mass closer to the leading edge were observed to be more stable.

The developed mathematical models are validated against two benchmark cases (Goland wing and a beam under tension) and compared to the experimental observations. The models are then used to investigate how changes in the model parameters – such as position of the structural centres, magnitude of tension, varying wind profile and varying tension – influence the dynamic behaviour of the streamlined cable. This analysis sheds light on the mechanisms of streamlined cable instability and demonstrates how the model can be used as a tool in the future development of streamlined cables.

Contents

List of Figures

List of Tables

Nomenclature

Conventions

$\bar{a}$	Discrete element parameter
$\dot{a}$	Dot denotes a time derivative
a'	Prime denotes a spatial derivative
a^*	Parameter with respect to starred frame of reference
$\mathbf{A} = [\quad]$	Matrix denoted by bold upper-case and square brackets
$\mathbf{a} = \{\quad\}$	Vector denoted by bold lower-case and curly brackets

Roman Symbols

A	Area
b	Semi-chord
C	Coefficient (drag, lift)
c	Chord or viscous damping per unit length
D	Drag
d	Displacement at a node
E	Young's modulus
F	Force
f	Frequency in Hertz
G	Shear modulus

I_x, I_y, I_z Second moment of area

I_g, I_s Moment of inertia per unit length, about mass and shear centre respectively

J Torsion constant

K Shear constant

k Spring stiffness or reduced frequency

L Lift

l Characteristic length

M Moment

m Mass per unit length

N Number of finite-state equations

n Number of discrete elements

P Tension

p Dimensionless position of tension centre

PE Potential energy

r Dimensionless position of mass centre

S Shear

s Dimensionless position of shear centre

T Torque or period

U Fluid velocity

u, v, w Translational displacements in x, y and z respectively

W Power

x, y, z Spatial frame, x is parallel to cable length

Greek Symbols

α Growth rate or angle of attack

γ Wavenumber

λ Eigenvalue

μ Fluid parameter equal to $\rho_f \pi b^2$

ν Dynamic viscosity or poisson's ratio

ω Frequency in rad/s

ρ Density

σ Stress

τ Dimensionless tension

θ, ϕ, ψ Rotational displacements about x, y and z respectively

υ Induced flow velocity from shed vortex

Other Symbols

ℓ Element or cable length

$\mathcal{F}$ Dimensionless position of reference frame

Subscripts

a Cross-sectional area

b Bending

c Cable

e Element

f Fluid

g Geometric stiffness

i Finite-state induced flow

j Nodal index

p Tension

q Quarter chord

r Mass

s Shear

t Torsion

Superscripts

o Initial stress-state

Matrices and vectors

B Strain-displacement matrix

$\mathbf{b}, \mathbf{c}, \mathbf{A}_n, \mathbf{D}$ Finite-state approximation vectors and matrices

C Damping matrix

E Material stiffness matrix

f Vector of forces and moments

G Geometric initial stress-state matrix

K Stiffness matrix

M Mass matrix

N Shape-function matrix

q State-space vector

T Transformation matrix

u Displacement field vector

$\boldsymbol{\Upsilon}$ Finite-state induced flow matrix

$\boldsymbol{\upsilon}$ Induced flow vector

W Wave dispersion matrix

Chapter 1

Introduction

1.1 Motivation

Streamlining the cross-section of beams or cables under tension has two main benefits, to reduce drag and eliminate vortex-induced vibrations (VIV). These benefits are of interest in a number of applications such as tethered balloons, kite-power generators, towed cable arrays and off-shore risers. Taking advantage of these benefits presents an engineering challenge as streamlining a cable may introduce instabilities such as torsional divergence and flutter. There is therefore a need to understand when and why these instabilities occur and have models to predict their onset and the overall dynamic behaviour of the streamlined cable. These models must be able to account for effects such as variable fluid loading profiles and varying cable tension. The model must be general in nature so that appropriate boundary conditions – for example to represent a balloon or kite – may be included.

1.2 Research Objectives

The main objective of the current work is to develop modelling tools which can be used to predict and help understand the stability and dynamics of streamlined cables. The aim is to create modelling tools which are general in nature and provide a foundation for future streamlined cable development. Additional objectives include: developing a streamlined cable manufacturing process, modelling and assessing the physical properties of a streamlined cable and running experiments to gain insight into the behaviour of streamlined cables subject to environmental conditions.

1.3 Outline of the Report

The current work can be divided into four main sections: the literature review, the development of mathematical and computational models, manufacturing and experiments and, finally, model validation and results. A brief summary of each section is provided below.

The literature review introduces and discusses existing applications which are relevant to streamlined cables including: towed underwater arrays, off-shore risers, high-altitude aircraft, helicopters blades and wind turbine blades. A review of high-altitude tethered balloons and kite power generators (two potential streamlined cable applications in air) is completed. Reviewing the applications of streamlined cables and cable-like structures functions to highlight the relevant fields of study and theory required to model a streamlined cable. The review of the existing and potential applications identifies the need for, and solidifies the motivation of, the current research. The second part of the literature review focuses on the broad theory relevant to streamlined cables. Specifically, structural dynamics of beams and cables, steady and unsteady fluid dynamics and fluid-structure interaction.

The review of existing work relevant to streamlined cables provides a foundation for Chapter 3 to 5. These three chapters describe three mathematical streamlined cable models, each building on the next. The first model is an extension of the classic two-degree-of-freedom flutter model and includes the effect of an offset centre of tension. This simple model consists of a mass and spring structural model, coupled with fully-unsteady fluid-dynamic forcing. Chapter 4 presents a continuous streamlined cable model which assumes quasi-steady fluid dynamics. Wave propagation techniques including dispersion and power-flow analysis are explored as methods to investigate the stability of the continuous system. Chapter 5 presents the final most comprehensive model: a finite-element model of the streamlined cable which includes unsteady-fluid forcing. The finite-element model of the streamlined cable has the capability to analyse non-linear effects such as varying tension or wind distribution. Throughout the development of the three models, advantages and limitations of each are discussed.

Chapter 6 focuses on the practical side of streamlined cable development and details the manufacturing and testing of streamlined cable. This chapter documents the first streamlined cable prototypes and the streamlined cable manufacturing process developed by Elson Space Engineering (ESE Ltd.) and Davidson Technologies (DT Ltd.) for the Stratospheric Particle Injection for Climate Engineering (SPICE) project (which has an interest in the application of streamlined cables to high-altitude tethered balloons). The physical properties required as inputs for the models developed in Chapters 3 to 5 are determined for the man-

ufactured streamlined cable using experiments and cross-sectional modelling techniques. Finally, the preliminary experiments conducted with the manufactured streamlined cable – including wind tunnel, balloon, kite and fixed horizontal tests – are presented. Practicalities and lessons learned from the manufacturing and experimental testing are documented and discussed.

In Chapter 7, the models developed in Chapters 3 and 5 are validated against two benchmark cases. The results from the experimental measurements are detailed and, where possible, compared to the results from the discrete model developed in Chapter 5.

By using the manufactured samples as a realistic starting point, Chapter 8 investigates how variation in a streamlined cable's properties affect the overall dynamic behaviour. The aim of the chapter is to demonstrate how the model can be used to explore a streamlined cable's stability characteristics and to, at a high-level, understand the sensitivity of the streamlined cable's stability to various parameters. As the behaviour of the streamlined cable model is explored, the applicability to potential uses of a streamlined cable are discussed.

Finally, Chapter 9 summarises the work and draws some concluding remarks. The contributions of the thesis to the existing body of knowledge are highlighted. Recommendations for areas of future work are provided.

Chapter 2

Literature Review

To understand and model the behaviour of a streamlined cable, knowledge of the existing work on streamlined cables, and cable-like structures, is essential. The literature review presents a summary of the existing applications of streamlined cables in water. Parallels are then drawn between streamlined cables and flexible fixed-wing aircraft, helicopter blades and wind turbine blades. The chapter then reviews two proposed applications of streamlined cables for tethered balloons and kite-power generators. The focus then shifts from a review of the applications, to a review of the pertinent theory and modelling techniques needed to model a streamlined cable. The relevant fields of study include structural and fluid dynamics, and their union referred to as fluid-structure interaction, or aeroelasticity.

2.1 Streamlined Cable and Cable-Like Structures

At the time of writing, implementations of streamlined cables exist underwater and include the fairing of towed cable-arrays and offshore risers. In air, structures such as highly-flexible wings, helicopter rotors and wind turbine blades draw from similar structural and fluid dynamic theory but their main design purpose is not to withstand tension. Though few examples of streamlined cables in air exist, their use has been proposed and is being studied for applications such as high-altitude tethered balloons and kite-power generators.

2.1.1 Faired Off-Shore Structures

As water is about a thousand times more dense than air – and the drag forces therefore a thousand times greater – it is unsurprising that existing streamlined cable research is more focused on applications underwater than in air. Underwater cables are commonplace in the

off-shore industry be it for towing, mooring or as a pipeline. A brief review, focused on underwater streamlined cables, is provided below.

To the author's knowledge, interest in decreasing the drag and VIV on underwater cables dates back approximately 60 years. A large body of experimental work was completed at the David Taylor Model Basin, a large U.S. Navy tow-tank facility, beginning in the 1950's [43]. The work consisted of towing rigid models of faired cable at a range of speeds and inclination angle to measure the drag. In 1975, Folb [44] completed a report summarising drag properties of ten of the tested fairing designs.

Theoretical work on underwater streamlined cables includes the non-linear theory for heterogeneous, anisotropic elastic rods – developed by Hegemier and Nair [57] – which they applied to the stability of a faired underwater towing cables [93]. The model was ultimately used in 1984 by Hung and Nair [67] to study the stability of a towing cable, made of a moulded fiberglass core and a flexible hypalon rubber fairing, developed by Boeing.

At the time of writing, a number of commercial faired underwater cable companies, such as ODIM Brooke Ocean (part of the Rolls-Royce Group) and CWA Products Ltd. (acquired by Trelleborg PPL), provide faired cable products. Figures 2.1 and 2.2 show faired cable products from ODIM [108] and CWA Ltd. [32] respectively. Little published work on the study of the dynamics of these commercial faired cables exists.

Besides fairing towed-cables, faired off-shore risers are another relevant area of research. In a review paper by Every et al. [41], the merits of various VIV suppression systems are discussed for both towed cables and risers. He cites experimental testing as early as 1977 of tear-drop cross-section fairings on risers off the coast of Brazil by Albers and DaSilva [4] and Grant and Patterson [54]. Though the system encountered initial bearing problems between fairing elements, it operated successfully for over a year.

More recently, studies have been published which review available VIV suppression systems and characterise their dynamic behaviour. In 2008, Taggart and Tognarelli [122] reviewed a number of commercially available VIV suppression devices. These devices included helical wraps, fairings (both rigid and deformable) and fins/bumper bars. Although these devices are commercially available, research into characterising and understanding their dynamic behaviour is still on-going.

In 2002 Slocum et al. [117] used a classic two-degree-of-freedom aeroelastic model to try and characterise the dynamic behaviour of faired riser designs. They conducted experimental testing of rigid fairing designs at the David Taylor Model Basin and of flexible fairing designs using a rotating test rig at the Norwegian Marine Technology Research Institute. The rigid tests were completed successfully and the drag and VIV properties of the

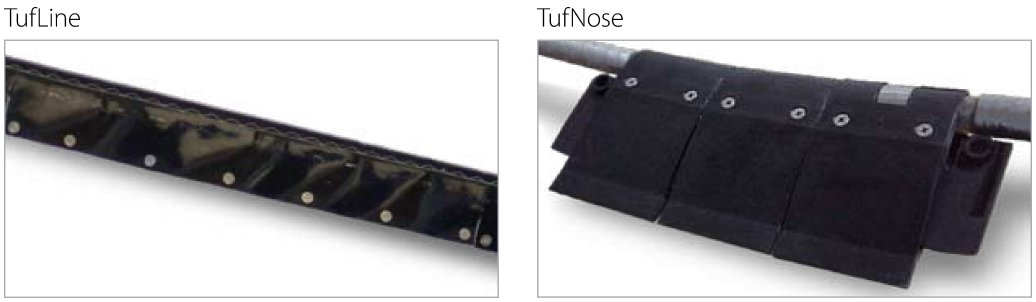

Fig. 2.1 ODIM Brooke Ocean streamlined towed-cable products [108].

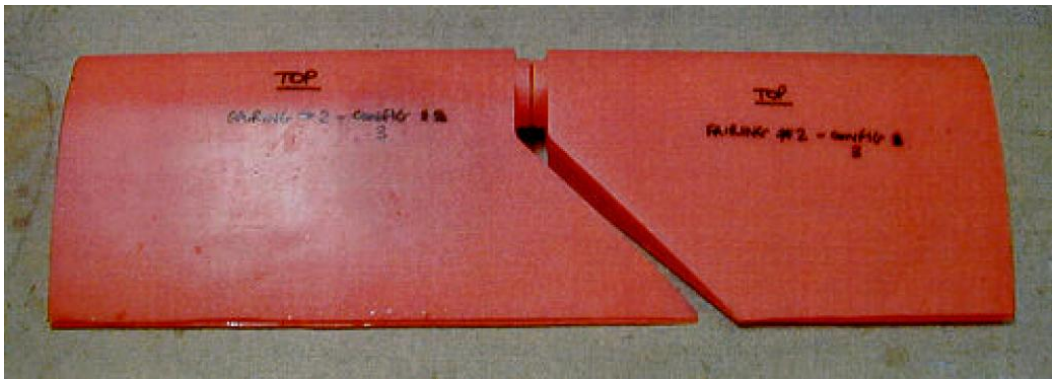

Fig. 2.2 CWA Products Ltd. moulded cable fairing [32].

fairings characterised. Conversely, the flexible faired riser designs were observed to oscillate at a critical speed and did not reach a steady-state amplitude. The flexible riser tests were stopped prematurely because the amplitudes were larger than expected and caused damage to some of the testing apparatus.

In 2009, Khorasanchi and Huang [75] extended the model developed by Slocum et al. The basis of their model is still the classic two-degree-of-freedom aeroelastic model. The extension to the model being that the fairing is treated as a rotating vane and the friction between the riser and fairing is included.

This brief review of faired off-shore structures demonstrates the on-going interest in the implementation of streamlined cables. In an underwater environment, the low drag and VIV suppression characteristics are highly desirable. However, as demonstrated in the tests by Slocum et al., streamlining the structure can introduce undesirable instabilities. The models currently used to understand these instabilities come from classic aeroelastic theory. The next section provides context to how and why these instability models – originally designed to model the behaviour of flexible wings – were developed and why they are applicable to streamlined cables.

2.1.2 Flexible Wings and Blades

Streamlined slender structures in air are generally confined to aerospace and wind turbine applications, where the main purpose of streamlining the structure is to create lift and decrease drag. Nevertheless, a streamlined cable can be thought of as a very high aspect ratio (the ratio of span to chord) version of an aircraft wing, helicopter blade or wind turbine blade. As it was through the development of aircraft wings that the first aeroelastic instabilities were observed and the theory to explain them formulated, a brief review of how the field has progressed is given below. Modern day research in two areas facing similar challenges to those associated with a streamlined cable – that of flexible high-altitude aircraft and that of rotating blades – is discussed.

Modern texts on aeroelasticity such as Wright and Cooper [136] and Hodges and Pierce [64] both introduce the subject by referring the reader to a diagram produced in 1978 by Collar [25]. Collar's diagram is a triangle which depicts how aeroelasticity is the study of the interactions between elasticity, inertia and fluid dynamics. Collar's figure is reproduced here as Figure 2.3. In the centre of the triangle is dynamic aeroelasticity, under which the phenomenon of flutter is classified. Fung [46] describes flutter as when "a small accidental disturbance of the the airfoil can serve as a trigger to initiate an oscillation of great violence". The first recorded flutter case to be successfully solved was the 1916 Handley Page O/400 bomber, which experienced violent oscillations of the tail. For a comprehensive review of aeroelastic theory, the reader is referred to two books, often referred to as classic aeroelastic texts, Bisplinghoff's *Aeroelasticity* [15] and Fung's *An Introduction to the Theory of Aeroelasticity* [46].

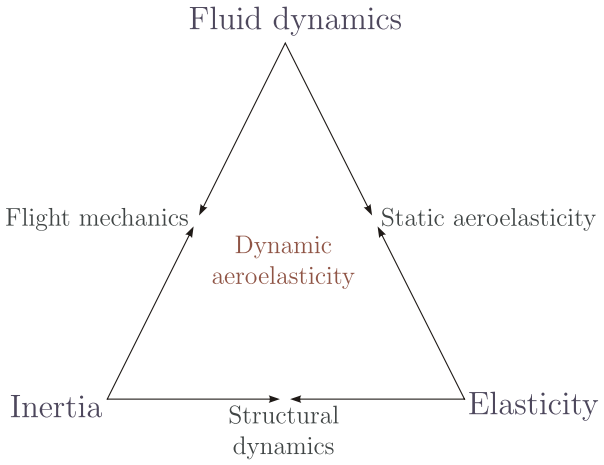

Fig. 2.3 Collar's [25] aeroelastic triangle depicting the interaction of topics within the field.

Fig. 2.4 NASA's Helios prototype flying wing [94].

In terms of modern day research, areas relevant to work on streamlined cables includes work on highly-flexible aircraft and work on flexible rotating blades. There is cross-over not only of the aeroelastic theory but also of the structural theory since streamlined cables, like helicopter blades and aircraft wings, are likely to be composite in construction.

The field of highly flexible aircraft is becoming more popular with the advent of unmanned high-altitude long endurance (HALE) aircraft. These aircraft are sometimes referred to as *flying wings* as they are high-aspect-ratio structures without a large conventional fuselage. Murua [90] provides an overview of some of the more recent projects which include AeroVironment and NASA's 80 m span solar plane Helios in 2003 (shown in Figure 2.4) and QinetiQ's 25.5 m span solar plane Zephyr in 2010.

As these aircraft are highly flexible compared to conventional aircraft, the computational models must include aeroelastic effects for large deformations. Extensive work on modelling these HALE aircraft has been completed by Patil, Hodges and Cesnik [101, 102]. Their approach uses a large-displacement geometrically-exact beam model – the theory of which was developed by Hodges [60–62] – and a fully unsteady, two-dimensional aerodynamic theory developed by Peters et al. [103]. Another group, lead by Palacios – including Murua, Graham and Hesse – at Imperial College London are also developing models for HALE aircraft [59, 90–92]. Their structural model uses a finite-element method and accounts for small deformation and large rigid-body motion. The aerodynamic loads are modelled using an unsteady vortex-lattice method, the details of which are given by Murua [90]. Though the work on HALE aircraft relates to the study of streamlined cables, it does not account for and investigate the effect of an applied external tension. An area of conventional aerospace research which includes the effect of tension is the study of rotating blades.

In applications with flexible spinning blades – for example helicopters and wind turbines – the centrifugal acceleration causes tension in the blades. The aerodynamic theories used for these applications are similar to conventional theories for fixed-wing aircraft. Leishman [82] provides a comprehensive review of helicopter aerodynamics, which provides a useful resource for unsteady flow theories. However, a focus of rotating blade dynamics – which is not a concern for fixed-wing aircraft or streamlined cables – are the wake-effects.

In rotating blade applications, the tension which arises due to the rotation is referred to as *centrifugal stiffening*. For a derivation in the context of helicopter blades see Johnson [132]. As described by Tong [129], in wind turbine blades, the axial forces are due not only to the rotation of the blade but also to the self-weight since the rotor is oriented parallel with gravity. In finite-element models of rotating blades, the stiffening effect due to the axial tension is generally accounted for by an additional stiffness matrix [11, 121]. As described by Cook [26], this stiffening matrix is referred to by a number of names including: initial stress stiffness matrix, differential stiffness matrix, geometric stiffness matrix and stability coefficient matrix . For a streamlined cable, a similar formulation can be used to account for the effect of varying tension.

Thus far a review of the work related to streamlined cables in underwater applications and the study of flexible fixed wing aircraft, helicopter blades and wind turbines has been presented. Culminating these fields of study leads to the idea of implementing streamlined cables in air. Streamlined cables have been proposed for high-altitude tethered balloons and kite-power generators but are not in regular use at the time of writing.

2.1.3 High-Altitude Tethered Balloons

One potential application of streamlined cables, which was the initial inspiration of the current work, is as the tether for high-altitude tethered balloons (HATB). High-altitude tethered balloons reaching altitudes of 20 km have been proposed for a number of applications, such as communications, surveillance, meteorological monitoring, solar power production, telescopes and climate engineering. The tether of these HATB may see relatively high wind speeds compared to equivalent structures at lower altitude. Though the air density at these altitudes is lower than at ground level, the drag is proportional to the square of the wind speed, so there is potential benefit to be gained by streamlining the balloon tether. As the balloon must lift the cable, there is a major trade-off between reduced drag and increased weight of the cable. The following section reviews the research to date on HATB and ends with a discussion of the Stratospheric Particle Injection for Climate Engineering project,

which provided the initial motivation for the current research.

Interest in HATB systems appears to date back to the 1960s. There is published work from this decade of testing completed by the U.S. Navy [38]. Other examples of early testing were conducted by the French government, who conducted a series of unsuccessful HATB tests between 1969 to 1976 [40].

HATB reaching altitudes of 20 km are an on-going area of research, but commercial tethered balloon companies offering lower altitude systems do exist. RosAeroSystems has the PUMA tethered aerostat [109] which can achieve altitudes of 4 km and TCOM L.P. has the 71M tethered aerostat [73, 74, 124] which can achieve altitudes of 4.6 km. It has been suggested by Bely et al. [12] that some of the commercial technology is capable of attaining heights of 8 km unmodified. TCOM and RosAeroSystems are two examples of specialist companies focused on lighter-than-air technology and manufacture tethered aerostats operating at a range of altitudes. Some major aerospace companies, such as Lockheed Martin, also produce tethered aerostats commercially and for the U.S. military [84]. All of these existing tethered-balloon systems are typically used in applications such as threat detection, radar, border control, communications and ecological monitoring.

One of the most thorough reviews of HATB technology is a collection of work between 1994 to 2002 by the John Hopkins University, Applied Physics Laboratory (JHU/APL). The work aimed to develop a 20 km HATB for the Ballistic Missile Defence Organization (BMDO). JHU/APL - and TCOM on their behalf - published a number of papers on the subject of what they call a Very High Altitude Tethered Balloon (VHATB). Work completed by Badesha, Euler and Schroeder between 1995 to 1996 includes: a feasibility study of VHATB during steady-state operation and during ascent [40]; a parametric sensitivity study on how various VHATB system parameters effect the balloon size [6]; and a study of the launch and recovery of the balloon using TCOM's dynamic motion simulation called TRAJECTORY [9]. In 2002, Badesha and Bunn [8], completed a feasibility analysis of a HATB's robustness when faced with a severe thunderstorm. The study concluded that the effect of a passing thunderstorm on the HATB system was benign since the balloon was located above the storm in relatively calm conditions. Other more recent publications show the military's continued interest in HATB technology. For example, Stanney and Rahn's 2006 paper [119] develop a model to investigate a tether's dynamic response to turbulence and acknowledges the U.S. Army Missile Defense Agency for supporting their research.

In 2010 a group at the University of Southampton published work on a HATB for photovoltaic power production. Using a HATB, photovoltaics could be kept above the clouds, allowing solar power to be more effectively used in typically cloud-covered countries. The

proposal is described in detail by S. Redi et al. [105] and by Aglietti et al. [3] who quantify the advantages of solar collectors at altitudes between 6 km to 12 km. Dynamic analysis of the HATB system was completed by Aglietti in 2009 [2] and the work expanded by Redi et al. in 2011 [106]. The results of both papers found the proposed balloon system to be feasible.

Two major research projects have been undertaken in the area of balloon-supported telescopes. The first project, named the POST concept [12], consists of a 12 km single tether system in the polar region where the tropopause dips to lower altitudes. The lower tropopause means that placing the balloon in the relatively non-turbulent stratosphere is more easily attainable compared to other locations. The second project was a multi-tether balloon for a large-scale radio telescope, referred to as the Large Adaptive Reflector (LAR) [79–81]. The aerostat for this telescope is much lower at 500 m. However, the work completed on the tether and balloon dynamics for the multi-tether arrangement was later expanded to single-tether balloons by Coulombe-Pontbriand [27, 28].

All the studies on HATB system discussed thus far have been using circular cross-section tethers. To the authors knowledge, the first mention of altering the tether to reduce drag is in a 2002 paper by Badesha, which presents a feasibility analysis of a 20 km balloon for communication purposes [7]. In addition to the feasibility analysis, Badesha notes a few ideas worth investigating to improve the HATB performance. One of these ideas is to attach a splitter plate on the cylindrical tether to decrease drag.

The most relevant HATB project to the current work is the Stratospheric Particle Injection for Climate Engineering (SPICE) project [118]. The author has worked closely with the project as it specifically investigates the use of a streamlined cable for a climate engineering HATB system. Climate engineering, or geoengineering, has been suggested as a means of actively counter-acting the effects of global warming. In 2006, Crutzen, a Nobel prize winner in Chemistry, sparked major interest in climate engineering with his editorial essay which called for research in the subject [31]. In 2009, a report by the Royal Society evaluated various geoengineering methods [125]. Stratospheric aerosols (which is the injection of particles at around 20 km to reflect a small amount of incoming solar radiation) were deemed a medium risk method which has the potential to be relatively effective and affordable compared to other geoengineering alternatives. The summary figure from the report, comparing the geoengineering methods, is included here as Figure 2.5.

Based on the findings of the Royal Society report, the SPICE project was created to research the use of stratospheric aerosols as a geoengineering method. The SPICE project is divided into three work packages (WP): the University of Bristol is leading WP 1 evaluating

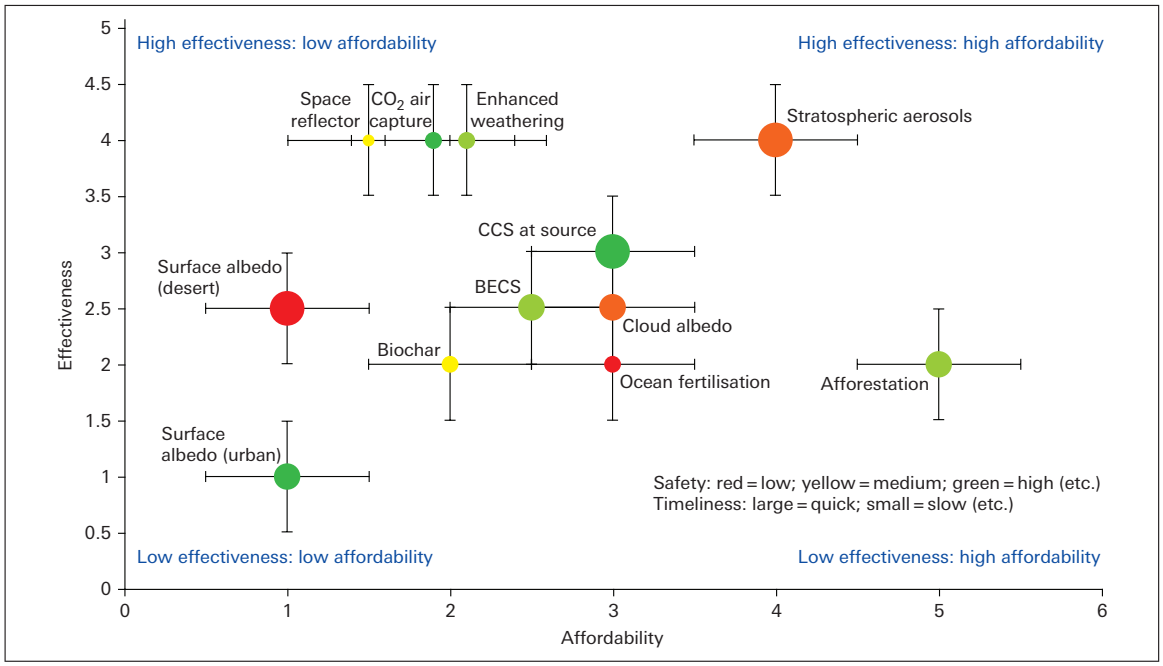

Fig. 2.5 Royal Society plot depicting the results from a preliminary evaluation of geoengineering methods [125].

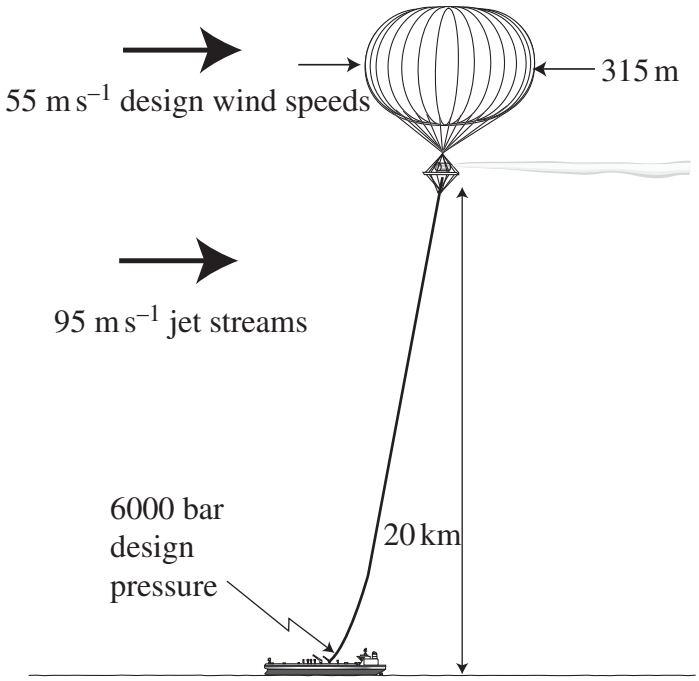

Fig. 2.6 SPICE particle delivery system using a 20 km tethered balloon [33].

candidate particles, the University of Cambridge is leading WP 2 analysing the feasibility of a delivery system and the University of Oxford is leading WP 3 researching and modelling the climate and environmental impacts of stratospheric aerosols. In addition to the Universities mentioned, the Met Office, the University of Edinburgh and Marshalls Aerospace also form part of the SPICE project team.

The proposed delivery system for SPICE is depicted in Figure 2.6. The system consists of a 20 km HATB with the tether serving as a pipe to deliver particles to the stratosphere. As the SPICE balloon tether is a fluid-carrying pipe, it would have a larger diameter tether than any of the other discussed HATB applications. A larger diameter tether means greater drag on the tether, which is why the SPICE project has a particular interest in the feasibility of streamlined cables.

A comparison between the discussed HATB applications is given in Table 2.1. The benefit of a streamlined cable for a particular HATB application is highly dependent on the specific operating conditions and must account for a number of factors such as wind profile, size of the tether and the acceptability of VIV.

Table 2.1 Applications of HATB and their estimated specifications.

Application	Altitude (km)	Balloon diameter (m)	Tether diameter (mm)
Communication [7]	20	52	11
Solar power [106]	6	65	-
POST Telescope [12]	12	90 (aerostat length)	15
SPICE [33]	20	315	200

2.1.4 Kite Energy

Another potential application of streamlined cables is to reduce the line drag for kite-power generating systems. One of the first documented proposals of tethered wind energy extraction dates back to 1980, where Loyd [85] proposes the use of a tethered aircraft for what he terms crosswind kite power. In his analysis, he calculates that a kite with a wing area of 576 m^2, on a 400 m tether, operating in a wind speed of 10 m/s could produce 6.7 MW of power. Loyd considers the tether to be shrouded with a drag coefficient of 0.04 (for comparison the drag coefficient of a cylinder is around 1) and remarks that the tether drag significantly limits the performance of the tethered system. Interest in kite-power generation was rekindled in the late 1990s when Ockels proposed and patented a kite-power generation concept and founded a kite-power research group at the Delft University of Technology (TU

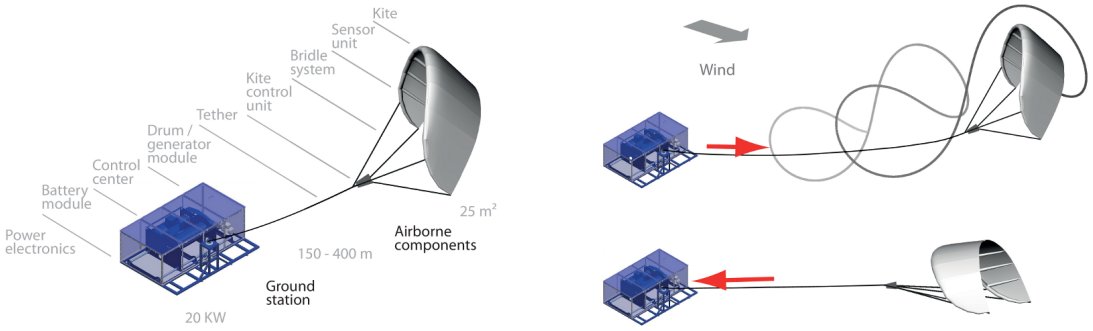

(a) Components of the generator.

(b) Launch and retrieval power cycle.

Fig. 2.7 Delft University of Technology Laddermill kite-power generator design [35].

Delft) [35, 98, 99]. From its inception to the time of writing, the TU Delft group has been researching and developing kite-power technology. Figure 2.7 shows the current TU Delft kite-power design, referred to as a Laddermill. The kite-power generator uses the wind to fly the kite in a figure-of-eight pattern, which unwinds the tether and generates power. Then, once the tether is fully unwound, the kite control unit reconfigures the kite so that it can be pulled back in a low drag configuration. Once the kite has been pulled back, the cycle is repeated. Simulation work by Ockels [99] sized three Laddermill systems operating at heights of 0.2 km, 3.2 km and 11 km and predicted the Laddermills to produce 0.01 MW, 1.2 MW and 48 MW respectively. Further simulation work by Williams et al. [134] explored the sensitivity of the kite-power generators to various system parameters. The work concluded that the power generated varies linearly with the tether drag, where a 15% reduction in tether drag gives roughly a 10% increase in power generation. The potential benefit in decreasing the drag on the tether further motivates the need for streamlined cable research.

Some preliminary research on reduced drag cables has been conducted at TU Delft. In 2008, Zandbergen [141] prototyped and tested a number of concept designs which included splitters and hard fairings. Experimental results showed some of designs achieved up to a 30% reduction in drag compared to the bare cable. Over the course of the tests, unstable behaviour was observed for a number of the samples. In addition to TU Delft, there are a number of other institutions researching kite-power generation including: the University of Sydney [107], Katholieke Universiteit Leuven [142], Politecnico di Torino [42] and the Tampere University of Technology [5].

A number of start-up kite-power companies, also exist [39, 76, 77, 86]. Limited published research exists from the start-up kite-power generation companies except in the form

of patents. Most relevant to the current research, is a faired tether patent from the California based company Makani Power Inc. which was acquired by Google in 2013 [55]. The patent relates to aerodynamic or faired tethers which are either passively or actively aligned with the wind.

Thus far, the literature review has presented the very broad range of existing work which relates to a streamlined cable. Work in the areas of underwater towed cables, faired offshore risers, high-altitude long-endurance aircraft, helicopters, wind turbines, high-altitude tethered balloons and kites all contribute to the body of knowledge on the subject of streamlined cables. From the work in both academia and industry, it is clear that to benefit from the advantages of a streamlined cable, further research into the dynamics and stability of streamlined cables is required. The focus of the review has been on the applications and not on the details of the underlining science. The next section reviews the relevant theory and modelling techniques necessary to model the dynamic behaviour of a streamlined cable.

2.2 Structural Dynamics of Beams and Cables

A common feature from the research areas reviewed in the previous section is that the length of structures is large relative to their cross-sectional dimensions (an attribute inherent to beams and cables). Generally, cables have greater ratios of length to cross-sectional dimensions than beams, making them more flexible. Beam and cable theory is well established and for a review of the subject the reader is referred to texts such as Timoshenko [127], Irvine [70], Przemieniecki [104], Graff [53] and Newland [95]. This review focuses strictly on laying the foundation needed for the current work on streamlined cables.

2.2.1 Classic Beam and Cable Theory

Beam and cable analysis typically reduces a three-dimensional structure to a one-dimensional one. Beams are generally modelled using an Euler-Bernoulli or a Timoshenko model. The Euler-Bernoulli model neglects shear deformation and rotary inertia and is suitable for relatively long beams. During deformation, the cross-sectional planes are assumed to remain perpendicular to the longitudinal axis of the beam. Conversely, Timoshenko theory accounts for shear deformation and rotary inertia effects.

In classic beam theory it is helpful to define three structural cross-sectional centres: the mass centre, the shear centre and the tension centre (also referred to as the normal centre). Figure 2.8 depicts the shear and tension centre definitions. The shear centre is where torsion

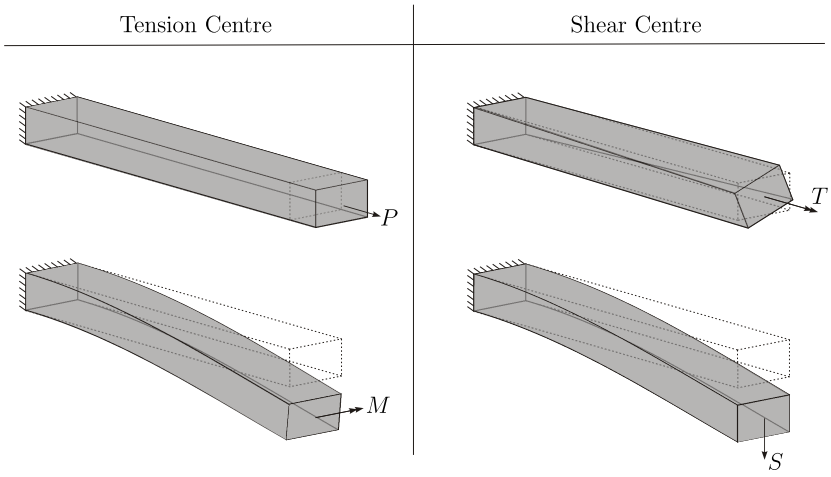

Fig. 2.8 Depiction of the definition of the tension and shear centres.

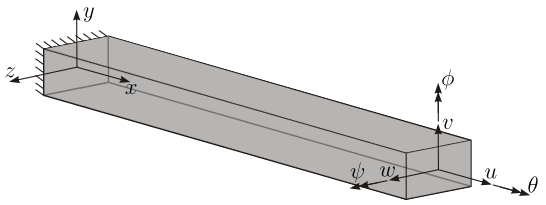

Fig. 2.9 Displacements conventions of a deformed beam.

and shear uncouple. If a torque is applied at the shear centre, the beam will deform in pure twist; if a transverse force is applied at the shear centre, the beam will deform in pure translation. The tension centre is where axial extension and bending uncouple. If an axial force is applied at the tension centre, the beam will deform in pure extension; if a moment is applied at the tension centre, the beam will bend and the reference axis will not elongate.

In classic beam analysis, the beam is typically of symmetric cross-section, prismatic (i.e. of constant cross-section) and made from isotropic, linear-elastic material. In this case, the three structural centres are concentric. Figure 2.9 shows the spatial reference frame and the displacement conventions which will be used throughout the current work.

If the beam is of constant cross-section, the elastic and inertial properties of the beam can be written as a cross-sectional matrix. The constitutive equation relates the beam deformation to applied forces as $\mathbf{f} = \mathbf{K}_\mathrm{a}\mathbf{u}$, where $\mathbf{f} = \{F_x, F_y, F_z, M_x, M_y, M_z\}^\mathrm{T}$ is the force vector, $\mathbf{u} = \{u, v, w, \theta, \phi, \psi\}^\mathrm{T}$ the displacement vector and $\mathbf{K}_\mathrm{a}$ the cross-sectional stiffness matrix. Taking a reference frame fixed at the location of the concentric centres with the $y-z$ axis aligned with the principal bending axis, for a generalised Timoshenko beam, the cross-

sectional stiffness matrix $\mathbf{K}_\mathrm{a}$ can be written as the diagonal matrix

$$\mathbf{K}_\mathrm{a} = \begin{bmatrix} EA & 0 & 0 & 0 & 0 & 0 \\ 0 & GK_y & 0 & 0 & 0 & 0 \\ 0 & 0 & GK_z & 0 & 0 & 0 \\ 0 & 0 & 0 & GJ & 0 & 0 \\ 0 & 0 & 0 & 0 & EI_y & 0 \\ 0 & 0 & 0 & 0 & 0 & EI_z \end{bmatrix} \tag{2.1}$$

where E is the young's modulus, A the cross-sectional area, G the shear modulus, K_y and K_z the shear coefficients in y and z, J the torsion constant, and I_y and I_z the second moment of area about the y and z axes respectively. The terms running down the diagonal are the axial (EA), shear (GK), torsion (GJ) and bending (EI) stiffnesses. Similarly, the inertial forces related to acceleration through Newton's laws of motion can be written in the matrix form $\mathbf{f} = \mathbf{M}_\mathrm{a}\ddot{\mathbf{u}}$. The matrix $\mathbf{M}_\mathrm{a}$ is the cross-sectional mass matrix given by

$$\mathbf{M}_\mathrm{a} = \begin{bmatrix} m & 0 & 0 & 0 & 0 & 0 \\ 0 & m & 0 & 0 & 0 & 0 \\ 0 & 0 & m & 0 & 0 & 0 \\ 0 & 0 & 0 & I_{gx} & 0 & 0 \\ 0 & 0 & 0 & 0 & I_{gy} & 0 \\ 0 & 0 & 0 & 0 & 0 & I_{gz} \end{bmatrix} \tag{2.2}$$

where m is the beam mass per unit length and I_{gx}, I_{gy} and I_{gz} are the mass moment of inertia per unit length about the x, y and z axes respectively.

The brief summary of beam theory presented here is by no means exhaustive, the aim being strictly to lay-down the foundations, notation and conventions used in the current work. The formulations presented are for classic beams which are prismatic and homogenous made of isotropic, linear-elastic materials. Composite beams, which are generally used to construct aircraft wings, turbine blades and existing underwater streamlined cables, typically exhibit more complicated behaviour.

2.2.2 Composite Beams

For cross-sections which are asymmetric, inhomogenous and made of anisotropic materials the cross-sectional mass and stiffness matrices are generally coupled. The mass matrix is relatively straightforward to determine for an inhomogenous beam, as the derivation follows

from the parallel axis theorem. The derivation of the stiffness matrix, however, is not as straightforward and various methods exist to determine it.

The more simplified approaches assume the beam is prismatic and made of isotropic material. Using this assumption, Hartsuijker and Welleman [56] extend the classic beam analysis to a cross-section made up of a number of homogeneous regions. They use this method to determine the position of the tension centre and derive the axial and bending portions of the constitutive relationship. A limitation of this method is that it cannot be easily extended to calculate the torsional stiffness, shear stiffness or shear centre. Other authors, such as Hodges [62] and Svendsen [121], derive the stiffness matrix for a prismatic and isotropic cross-section where the position of the shear and tension centre are assumed to be known. If the shear and tension centre are non-concentric, stiffness coupling terms are introduced into the cross-sectional stiffness matrix.

For a more comprehensive analysis of a composite cross-section, which can account for effects such as anisotropic materials, numerical models are required. In 2008, Chen et al. [24] completed an assessment of five computer tools available to determine the cross-sectional matrices and the location of the shear, tension and mass centres. The methods can be roughly separated into three types: thin-walled, variational asymptotic and finite-element models. As the name suggests, thin-walled models use thin-wall theory, where analytical solutions for the torsion constant and shear centre can be determined. Variational asymptotic methods use theory largely developed by Hodges, Cesnik and Wu over the past 20 years [21, 22, 63, 65, 140]. The theory is implemented into the commercially available software VABS (Variational Asymptotic Beam Section). Hodges 2006 book on the subject [62] provides a comprehensive review on the theory. Finite-element methods extract the stiffness matrix from three-dimensional finite-element models of the structure [47, 87]. Chen found that of the tools assessed, the variational aymptotic model, implemented in the commercial software package VABS (Variational Asymptotic Beam Section) consistently calculated the correct cross-sectional properties. In 2010, Blasques et al. [16] used the same variational aymptotic theory as VABS in a software they created called BECAS (BEam Cross section Analysis Software). The work by Blasques takes VABS as the state of the art and uses it to benchmark the BECAS results.

Obtaining the cross-sectional properties of the beam is still only one piece of the beam model. To model the overall dynamics, or analyse the stability of the beam, the cross-sectional properties must be incorporated into the equations of motion, and the equations of motion solved.

2.2.3 Finite Element Beam and Cable Models

Typically the streamlined structures discussed in the previous sections (towed-cables, offshore risers, fixed-wing aircraft, helicopters, wind turbines) use finite-element methods to model the structure. Finite-element methods cover a broad range of study and the models can be classified in a number of ways. Here the common assumptions used to model the inertia and elasticity of beam are briefly discussed.

The inertia of beam and cable models is generally considered as either lumped or consistent. Lumped-mass models assume the mass is concentrated at the nodes of the discretisation and either neglects the rotary inertia or assigns it an approximate value [26]. Consistent elements describe the displacement of the element using shape functions and considers the mass to be distributed along the length of the element. Merits of a lumped-mass method include simplicity and computational efficiency, as the mass matrix reduces to a diagonal matrix. The main limitation of lumped-mass models are that they may yield inaccurate results. Though for some problems, such as wave propagation, lumped-mass models may offer greater accuracy [13, 26]. Generally however, consistent mass matrices are more accurate but more computationally demanding than their lumped-mass counterparts.

The elasticity of the beam or cable may also be modelled in a number of ways and may account for longitudinal, transverse and/or torsional elasticity. Some finite-element cable models, often referred to as finite-segment models, may not include the elasticity of the structure. Instead the finite segment approach models the cable as a series of rigid elements connected together with rotational joints [58]. If elasticity is included, the constitutive equations discussed in section 2.2.1 provide the relationship between the elasticity, deformation and internal forces of the structure. In lumped-mass models the elasticity is often modelled as a series of axial and rotational spring connecting the lumped masses [27, 28, 37, 78, 81]. Torsional stiffness effects have been included in lumped parameter models of symmetric cross-section cables [20, 23]. For composite, asymmetric cross-section, models generally use consistent stiffness matrices obtained from the cross-sectional stiffness, shape functions and strain displacement relations.

In terms of finite-element models of streamlined cables, little work has been completed. Existing models of underwater streamlined risers use a two-degree-of-freedom model which neglects longitudinal effects and tension [75, 117]. Many circular cross-section cables models exist and many streamlined beam models exist. The cable models focus on incorporating large deformations and the effect of tension but neglect the characteristic fluid effects of a streamlined profile. The streamlined beam models focus on including unsteady fluid-dynamic effects as opposed to cable-like dynamics and the influence of tension.

2.3 Fluid Dynamics

The field of fluid dynamics is vast, encompassing a huge number of industries, types of structures and levels of complexity. The motivation of the current work is to decrease the drag force and instability of a cable through streamlining its shape. Therefore, the fluid forces acting on both circular cross-sections and streamlined shapes are reviewed. These forces are first introduced in terms of steady flow, which considers the flow to be constant in time. The effects of unsteadiness in the flow and how it influences the fluid forces is subsequently reviewed.

2.3.1 Steady Fluid Forces

The force that fluid exerts on a body due to the relative motion between the fluid and the body is highly dependent on the shape of the body. In the current work, the focus is on two particular shapes, a typical cable of circular cross-section and a cable with a streamlined cross-section. Assuming the flow is steady, the drag force per unit length D, which is parallel to the flow velocity, can be expressed in terms of the drag coefficient C_D, the air density ρ_f, the free-stream velocity U, the characteristic length l and the angle of attack α as

$$D = \frac{1}{2} C_D \rho_\mathrm{f} U^2 l \alpha \tag{2.3}$$

which can be found in many fluid dynamics textbooks such as Hoerner [66], White [133] and Munson et al. [89]. The drag coefficient is a function of the body's shape, material and the Reynolds number (Re=Ul/ν where ν is the dynamic viscosity of the fluid).

For a circular cross-section, the characteristic length is the diameter and the drag coefficient is independent of angle of attack but varies with Reynolds number. Figure 2.10, reproduced from Munson et al. [89] (originally created by Blevins [18]), shows the characteristic length and drag coefficient for five common shapes, including a circular and streamlined cross-section. For the particular streamlined section shown, when aligned with the flow, the drag coefficient can be between 10 to 100 times less than its circular counter-part.

For a streamlined cable application, a comparison of conventional drag coefficients may not provide a like-for-like comparison and may be misleading. For example, if the streamlining consists of fairing a circular cable, the frontal area of the faired and bare cable remains approximately the same. To make a fair comparison, the drag coefficients of the bare and faired cable should both be scaled by the frontal area. Thus, the drag coefficient of the streamlined body in Figure 2.10 should be divided by a factor of 0.18. This alters the drag

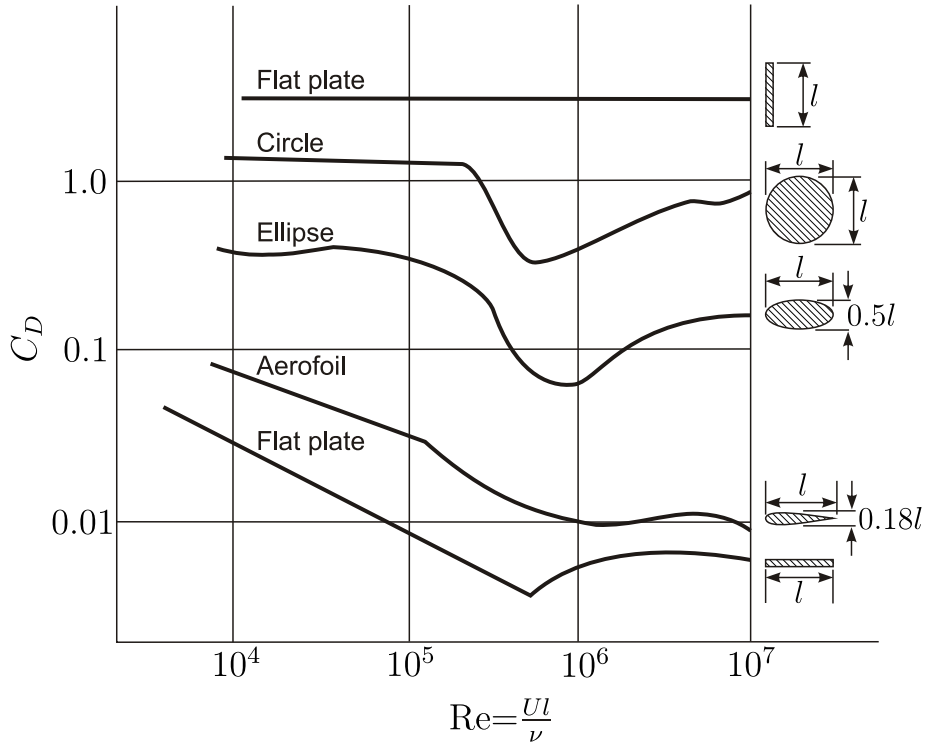

Fig. 2.10 Drag coefficient with Reynolds number for five cross-sections [89] .

coefficient comparison between the streamlined and circular cross-section from a 10 to 100 time reduction to a 1.8 to 18 time reduction. Streamlined cable designs with equal strength to a circular cable and smaller frontal area could be conceived and would give a greater drag reduction. The 1.8 to 18 times reduction in drag for the geometry given could therefore be considered a conservative estimate.

A more visual depiction of the advantage of streamlining a body is given by Hoerner [66]. Hoerner's depiction, reproduced here as Figure 2.11, shows a scale drawing of a circular and streamlined body of equal drag. For the particular streamlined geometry and Reynolds number shown, this represents a 7.5 time reduction of frontal area. The visual presentation makes it immediately clear that a significant advantage can be gained by streamlining.

The profile shown in Figure 2.11 is a four-digit NACA series aerofoil. There exist numerous streamlined shapes of varying geometry, the NACA series being one of the most widely studied. Due to the wealth of existing data on the NACA profiles, they were chosen as the baseline shape for the current work. The four-digits specify the shape of the aerofoil: the first two digits the camber and the final two digits the thickness as a ratio of the chord. For example, the NACA 0025 aerofoil shown in Figure 2.11 is not cambered (i.e. it

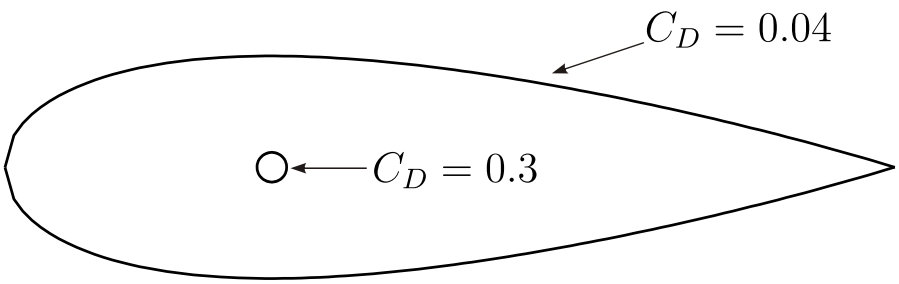

Fig. 2.11 Hoerner's [66] scale representation of a cylinder and NACA 0025 aerofoil of equal drag (Re=10^6 to 10^7).

is symmetric) and has a thickness which is 25% of the chord. Jacobs et al.[72] specify the geometry of the NACA section by the equation

$$y = \frac{t_c c}{0.2}\left(0.2969\sqrt{\frac{x}{c}} - 0.1260\frac{x}{c} - 0.3516\left(\frac{x}{c}\right)^2 + 0.2843\left(\frac{x}{c}\right)^3 - 0.1015\left(\frac{x}{c}\right)^4\right) \tag{2.4}$$

where c and t_c are the aerofoil's chord and thickness respectively. The equation is useful in specifying the profile for numerical purposes such as meshing.

The steady lift per unit length of an aerofoil follows a similar formulation to the drag and is

$$L_{\mathrm{S}} = \frac{1}{2} C_L \rho_{\mathrm{f}} U^2 l \alpha \tag{2.5}$$

where C_L is the lift coefficient. The lift coefficient is generally determined experimentally and, in the context of fixed-wing aircraft, the exact lift curve slope is of interest. As optimising the performance of the aerofoil is not the main focus of the current work, thin aerofoil theory is used. According to thin aerofoil theory – which can be found in sources such as Abbott [1] – the lift of an aerofoil for small angles of attack (up to approximately 8 degrees) increases linearly. The slope of the lift curve as a function of the angle of attack is 2π, i.e. $C_L = 2\pi$. Another important result from thin aerofoil theory is the location of the aerodynamic centre. The aerodynamic centre is defined as the location at which the pitching moment becomes independent of angle of attack. According to thin aerofoil theory, this point is one quarter of the chord length, as measured from the leading edge.

Experiments have been conducted to determine the steady lift and drag coefficient for high angles of attack [30, 115]. Figures 2.12 and 2.13 show the lift and drag curves for a NACA 0012 aerofoil from Leishman [82] and Critzos et al. [30]. Though the relation is not used in the current work, it shows the importance of having the streamlined body aligned with the flow. Should the tether "flip" and become perpendicular to the flow, depending on the Reynolds number, the drag increases by approximately 20 to 200 times.

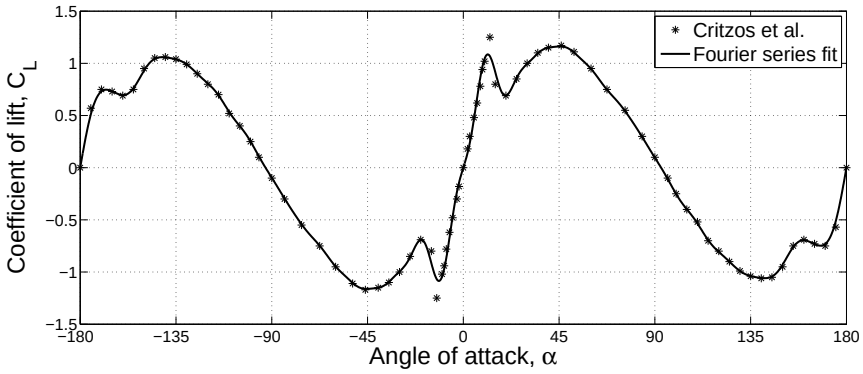

Fig. 2.12 Experimental lift results for a NACA 0012 over a 360 degree range of angle of attack [30, 82]. C_L is scaled with respect to the chord.

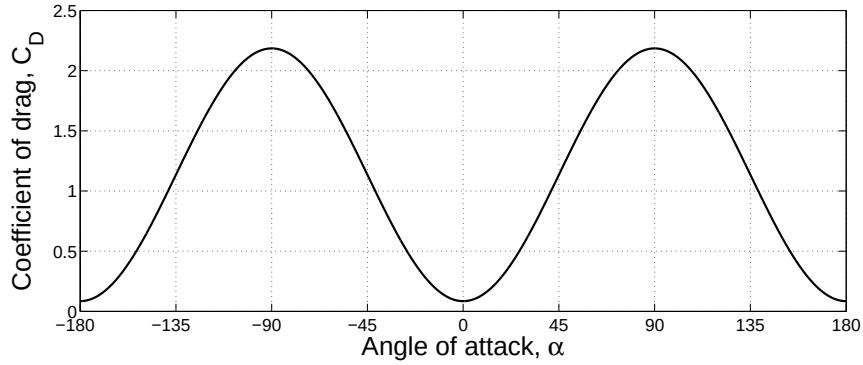

Fig. 2.13 Fit of experimental drag results for a NACA 0012 over a 360 degree range of angle of attack [30, 82]. C_D is scaled with respect to the chord.

The steady results are important for understanding the advantages that may be gained from streamlining a cable. However, in terms of understanding the stability of the system, steady flow theory is insufficient. Authors such as Fung [46] and Hodges [64], give the example of moving a cylindrical shaped stick through water at a constant velocity. According to steady theory, the stick would move through the water smoothly. The person holding the stick would only feel resistance opposite the direction of motion due to the drag force. In reality, the result is not so simple and when moving the stick through the water, the person experiences an oscillatory response and the stick moves in a sinusoidal motion. This phenomenon is explained by unsteady flow theory.

2.3.2 Unsteady Fluid Flow

The simple experiment of moving a cylindrical stick through water is an example of unsteady flow. As the stick moves through the water, alternating vortices are shed, causing the stick to move sinusoidally. The study of unsteady flow spans a number of topics; those most relevant to circular and streamlined cables include vortex-induced vibration (VIV) and unsteady flow around a two-dimensional aerofoil.

Vortex-Induced Vibration

Vortex shedding is a phenomenon that occurs due to instability of the wake behind a bluff body in fluid flow. The theory of vortex shedding and flow instability is detailed in numerous books. The following review draws extensively from Simiu and Scanlan [116], Blevins [17] and Fung [46].

Vortex shedding is a phenomenon highly dependent on the Reynolds number. At low Reynolds numbers, vortex shedding does not generally exist. As the Reynolds number increases various vortex shedding patterns may occur depending on the geometry of the structure. Figure 2.14 shows Simiu and Scanlan's [116] depiction of one of the most common examples of vortex shedding: the flow around a cylinder in uniform flow. The figure shows typical vortex shedding behaviour, which occurs between a Reynolds number of 30 to 5000. Vortices are shed from alternate sides of the cylinder to form the distinctive Von-Karman vortex trail.

In the context of elastic structures, vortex shedding is particularly concerning because the shedding frequency may *lock-in* or *synchronise* to a natural frequency of the structure. This can lead to large deformations and, ultimately, failure of the structure. The vortex shedding frequency is described by the non-dimensional Strouhal number

$$\mathrm{St} = \frac{fl}{U} \tag{2.6}$$

where f is the vortex shedding frequency in Hertz, l is the characteristic dimension (diameter for a cylinder) and U is the free-stream velocity. The Strouhal number has been empirically determined for a number of bluff-body shapes at varying Reynolds number. As shown in Figure 2.16 – taken from Blevins [17] – a value of 0.2 is a good approximation for a circular cross-section over a range of Reynolds number.

Vortex shedding itself is not a focus of the current research, but the theory is reviewed because streamlining a bluff-body – or introducing a splitter behind a bluff-body – is a form

of vortex suppression [100, 116]. Figure 2.15 shows the flow pattern behind a cylinder with a splitter. Simiu and Scanlan [116] describe how introducing a splitter inhibits crossover flow in the wake, thus stabilising it. Moreover, they compare the flow behaviour around a splitter to that of flow around a symmetric aerofoil.

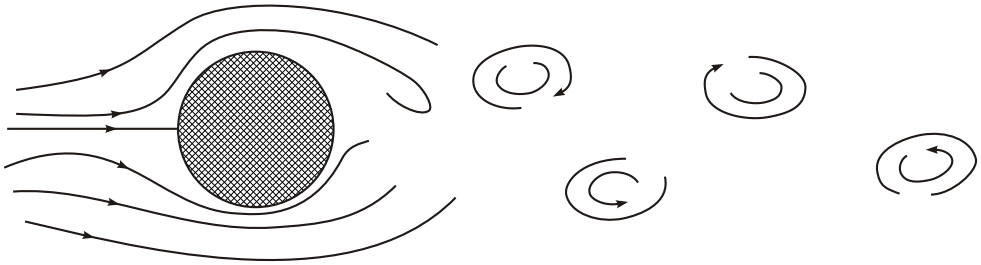

Fig. 2.14 Schematic of vortices generated by the sinous instability of the wake behind a bluff cylindrical body in uniform flow [116].

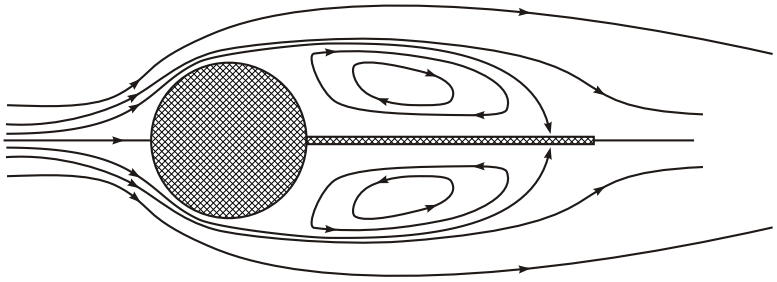

Fig. 2.15 Schematic of the flow pattern around a cylindrical body with a splitter [116].

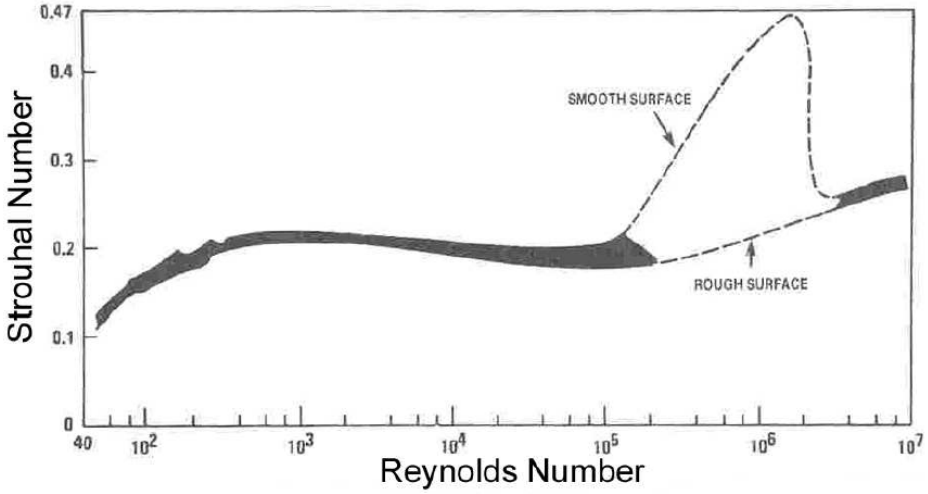

Fig. 2.16 Strouhal number for a circular cylinder from Blevins [17].

Unsteady Flow of an Aerofoil

The unsteady flow around an aerofoil is due to: the apparent fluid velocity from the motion of the aerofoil, the inertia effects of the fluid which is entrained with the aerofoil and the induced flow from any shed vortices. These three effects are briefly reviewed and then combined to obtain the equations describing the unsteady forces on an aerofoil. Figure 2.17 shows the aerofoil properties, where b is the semi-chord, θ the rotational displacement, $\mathcal{F}$ is the dimensionless position of the reference frame (from which the translation displacement v is measured), L is the lift per unit span and M_{q} is the aerodynamic pitching moment per unit span.

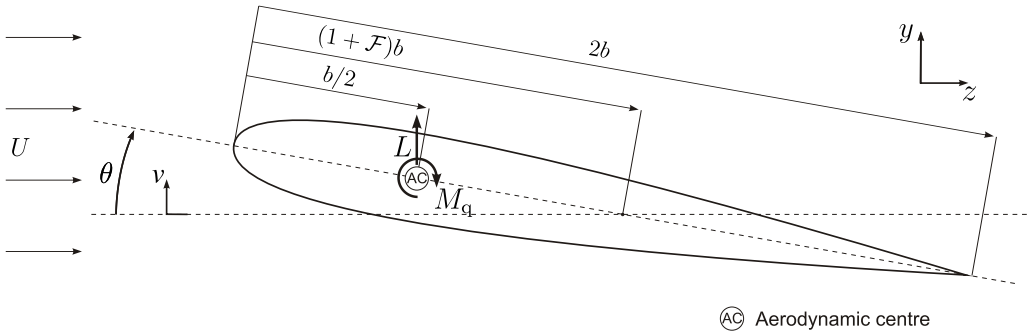

Fig. 2.17 Convention for the position of the reference frame $\mathcal{F}$, translation v and rotation θ. The lift and aerodynamic moment at the aerodynamic centre.

The effect of the apparent fluid velocity due to the motion of the aerofoil alters the angle of attack α in equation (2.5) and a full derivation is given by Fung [46]. Fung finds that the expression is equivalent to calculating the induced velocities with respect to the 3/4 chord point. Figure 2.18 shows how the translational and rotational motion of the aerofoil induces apparent flow terms and equation (2.7) gives the expression for the induced angle of attack.

$$\alpha = \theta - \frac{1}{U}\dot{v} + \frac{(0.5-\mathcal{F})b}{U}\dot{\theta}. \tag{2.7}$$

A second unsteady effect is due to the inertia of the fluid entrained during aerofoil motion, known as *non-circulatory*, *added mass* or *virtual mass* effects. Theodorsen [126] was the first to publish a complete solution for thin aerofoils in incompressible flow. The reader is referred to Bisplinghoff et al. [15] for an extensive description of the derivation. The non-circulatory lift and moment are

$$L_{\mathrm{NC}} = \pi\rho_{\mathrm{f}}b^2\left(U\dot{\theta} - \ddot{v} - b\mathcal{F}\ddot{\theta}\right) \tag{2.8}$$

$$M_{\mathrm{NC}} = -\pi\rho_{\mathrm{f}}b^3\left(U\dot{\theta} - 0.5\ddot{v} + b(0.125 - 0.5\mathcal{F})\ddot{\theta}\right) \tag{2.9}$$

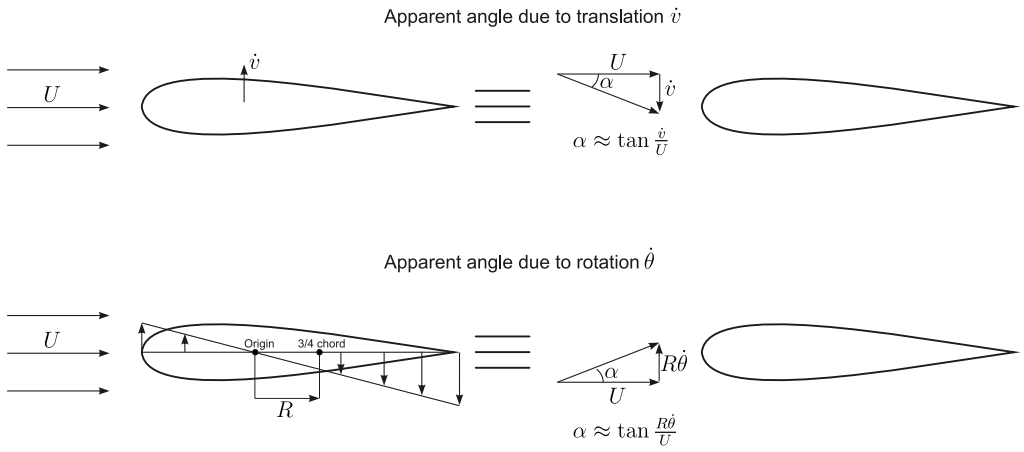

Fig. 2.18 Apparent angle of attack due to the translational and rotational motion of the aerofoil.

respectively. Bisplinghoff et al. give a brief physical description of each component. The first two terms in (2.8) are added mass terms which oppose the translational acceleration (the fluid velocity in y is giving by $U\theta$ and the corresponding acceleration by $U\dot{\theta}$). The first two terms in (2.9) are the corresponding moment terms. Note that when the reference axis is aligned with the midchord ($\mathcal{F} = 0$), the lift term in (2.8) associated with the angular acceleration $\ddot{\theta}$ is zero and the term $0.125\pi\rho_f b^4$ in (2.9) can be thought of as an added moment of inertia opposing the direction of rotation. Offsetting the reference from midchord gives the lift term $-\pi\rho_f b^3\mathcal{F}$ and, by the parallel axis theorem, the moment of inertia becomes $-\pi\rho_f b^4(0.125-0.5\mathcal{F})\ddot{\theta}$.

Substituting the induced angle of attack (2.7) into the steady lift equation (2.5) and including the non-circulatory effects gives the a quasi-steady form of the lift and moment per unit span as

$$L_{\mathrm{QS}} = \underbrace{\pi\rho_f b^2\left(U\dot{\theta} - \ddot{v} - b\mathcal{F}\ddot{\theta}\right)}_{\text{non-circulatory}} + \underbrace{2\pi\rho_f U b\left(U\theta - \dot{v} + b(0.5-\mathcal{F})\dot{\theta}\right)}_{\text{circulatory}} \tag{2.10}$$

and

$$M_{\mathrm{QS}} = \underbrace{-\pi\rho_f b^3\left(U\dot{\theta} - 0.5\ddot{v} + b(0.125-0.5\mathcal{F})\ddot{\theta}\right)}_{\text{non-circulatory}} \tag{2.11}$$

respectively. This quasi-steady form of the lift and moment is used as an approximation in some problems, especially where the fluid velocity is large relative to the velocity of the aerofoil. The lift can be separated into non-circulatory and circulatory terms, the moment is strictly non-circulatory.

The final unsteady term is due to the flow induced from any shed vortices, which alters the flow field in the vicinity of the aerofoil. The induced flow affects the lift but not the moment. Theodorsen [126] accounted for this effect for the case of simple harmonic motion, and gives the unsteady lift as

$$L = \pi\rho_{\mathrm{f}} b^2 \left(U\dot{\theta} - \ddot{v} - b\mathcal{F}\ddot{\theta}\right) + C(k)2\pi\rho_{\mathrm{f}} U b \left(U\theta - \dot{v} + b(0.5 - \mathcal{F})\dot{\theta}\right) \tag{2.12}$$

which is equivalent to the quasi-steady form except now the circulatory terms are multiplied by Theordorsen's function $C(k)$. Theodorsen's function is a complex function dependent on the reduced frequency $k = \omega b/U$ and is given in terms of Hankel functions. As described by Hodges [64], the effect of $C(k)$ reduces the magnitude of the unsteady terms relative to the steady term and introduces a phase shift between the rotational and translational oscillations. A limitation of Theodorsen's formulation is that it is only valid for simple harmonic motion and the frequency of the aerofoil motion must be specified in order to determine the lift. This limits the applicability of the Theodorsen's model in the time domain.

Hodges [64] derives the unsteady lift as a function of the average induced flow υ_o as (2.13). The brackets highlight the contribution of the steady, apparent velocity and induced-flow components.

$$L = \pi\rho_{\mathrm{f}} b^2 \left(U\dot{\theta} - \ddot{v} - b\mathcal{F}\ddot{\theta}\right) + 2\pi\rho_{\mathrm{f}} U b \left(\underbrace{U\theta}_{\text{steady}} \overbrace{-\dot{v} + b(0.5 - \mathcal{F})\dot{\theta}}^{\text{apparent velocity}} \underbrace{-\upsilon_o}_{\text{induced-flow}} \right) \tag{2.13}$$

The issue with this formulation is representing the induced-flow term υ_o. Methods of accounting for the influence of the shed vortices often employ Wagner's function [130] for a transient step change in angle of attack [15, 46, 82]. Analytical solutions using these methods are limited and numerical methods are typically employed. Another method of representing the induced flow is via a finite-state representation, which allows for the lift to be written in a form similar to structural dynamics formulation. For example, Peters et al. [103] derives a finite-state representation from the potential flow equations and shows that the result compares well with both Theodorsen's frequency domain and Wagner's time domain representations.

In this section the steady and unsteady fluid dynamic effects on a circular and streamlined cross-section have been reviewed. Combining these effects with the structural dynamics, reviewed in section 2.2, leads to the field of *fluid-structure interaction* or *dynamic aeroelasticity*.

2.4 Fluid-Structure Interaction

Two fluid-structure interaction phenomena, *torsional divergence* and *flutter*, are relevant to the streamlined cable work. Classic texts on the subject include Blevins [17], Simiu and Scanlan [116], Fung [46] and Bisplinghoff [15]. More recent texts with a focus on aeroelasticity include Hodges and Pierce [64] and Wright and Cooper [136].

A classic model relevant to both torsional divergence and flutter, discussed in all of the above mentioned texts, is the two-degree-of-freedom model shown in Figure 2.19. Typically the classic flutter model includes a linear spring k_b to model the bending elasticity and a torsional spring k_t to model the torsional elasticity, both acting at the shear centre. The centre of mass is taken as eccentric and is offset from the shear centre.

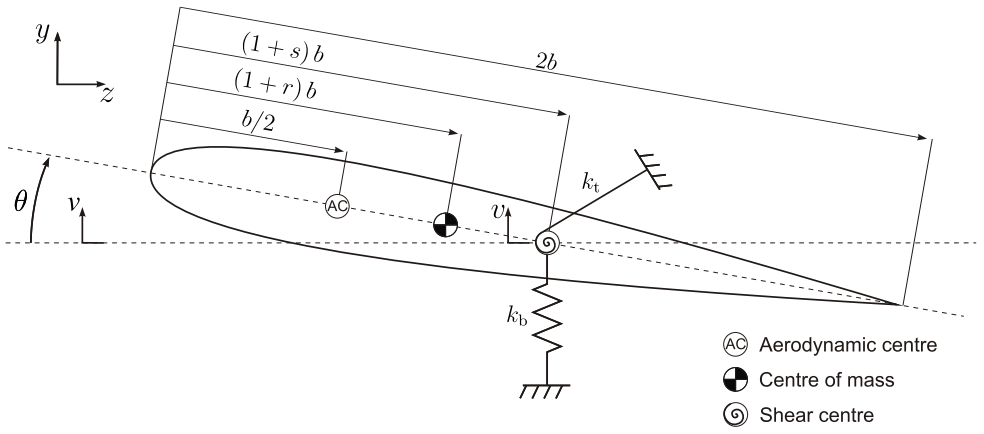

Fig. 2.19 Classic two-degree-of-freedom aeroelastic model.

2.4.1 Torsional Divergence

Torsional divergence is a phenomenon associated with a non-oscillatory, exponentially growing response. From a physical perspective, this corresponds to the moment from the fluid forces exceeding the moment from the elastic restoring force. In the context of a streamlined cable, this behaviour leads to the cable flipping so that the chord of the streamlined profile becomes perpendicular to the wind direction.

As a simple example, take the classic flutter model but assume the initial equilibrium position is offset by a small angle θ_o. Assuming small angles and a uniform flow velocity U, the moment about the shear centre due to the steady lift force is

$$M = 2\mu U^2(0.5+s)(\theta+\theta_o) \tag{2.14}$$

where $\mu = \rho_f \pi b^2$. The corresponding restoring force of the torsional spring is $k_t\theta$. Taking the static equilibrium and solving for the angle θ gives

$$\theta = \frac{2\mu U^2(0.5+s)\theta_o}{k_t - 2\mu U^2(0.5+s)}. \tag{2.15}$$

Equation 2.15 shows that the response θ goes to infinity when the denominator is equal to zero, which occurs at a critical wind speed of

$$U_{\text{divergence}} = \sqrt{\frac{k_t}{2\mu(0.5+s)}}. \tag{2.16}$$

There is no real solution to equation (2.16) when the shear centre is forward of the aerodynamic centre (i.e. $s < -0.5$). This case corresponds to the aerodynamic moment acting in the same direction as the torsional spring to restore the aerofoil to its un-deflected state.

For a streamlined cable, where the goal is to decrease drag, torsional divergence is highly problematic. As described in Figure 2.20, when the streamlined profile flips, the coefficient of drag may increase by approximately 200 times. A compounding effect is that once flipping occurs, the cable will be subject to bending in its lower second moment of area axis, making it more difficult to recover back to the aligned orientation. This situation, with approximate physical drag and bending properties, is shown in Figure 2.20.

Torsional divergence is a static instability and the destabilising fluid dynamic term could be considered as a negative stiffness. Including the dynamic effects introduces flutter instability, which is associated with negative damping.

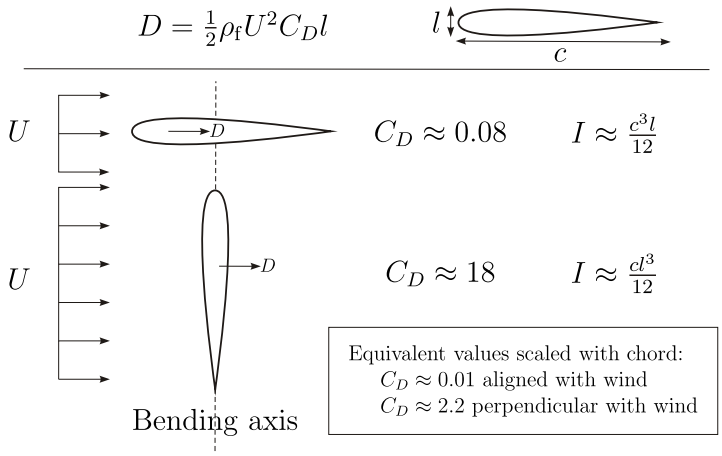

Fig. 2.20 Approximate values of the drag coefficient (scaled with frontal area) and second moment of area for a NACA 0012 aerofoil aligned or perpendicular to the flow [30].

2.4.2 Flutter

Flutter analysis is commonly grouped into four types of analysis [64, 103, 136]: k-type, p-type, indicial and finite-state. In k-type methods, simple harmonic motion is assumed *a-priori*, which limits the solution of the flutter boundary. In p-type analysis, an eigenvalue analysis is employed. Indicial methods typically use numerical time-stepping techniques to solve for the motion given Wagner's function. Finally, finite-state methods approximate the unsteady aerodynamics (which is an infinite state process) using a finite number of states. For a full treatment of the various flutter analysis methods, the reader is referred to the works by Wright and Cooper [136], Hodges [64] and Peters et al. [103].

Blevins provides a helpful table which summarizes stability results from the classic flutter model with quasi-steady forcing (reproduced here as Table 2.2). According to classic flutter theory, the location of the centre of mass and the aerodynamic centre relative to the shear centre strongly influences the model's stability to torsional divergence and flutter. The most stable condition is with the centre of mass forward of the shear centre and the shear centre forward of the aerodynamic centre.

Table 2.2 Flutter and divergence stability criteria of classic two-degree-of-freedom model assuming quasi-steady flow [17].

	Centre of mass AFT of shear centre	Centre of mass FORWARD of shear centre
Aerodynamic centre FORWARD of shear centre	Flutter Divergence	No flutter Divergence
Aerodynamic centre AFT of shear centre	Flutter No divergence	No flutter No divergence

The literature review reveals that a very broad range of background knowledge is required to understand and model the dynamics and stability of a streamlined cable. The review gives a summary of the significant body of research which has been completed in the context of faired off-shore structures, fixed-wing aircraft, helicopters and wind turbines. The review also identifies the need for streamlined cable research, especially as it relates to emerging technologies such as high-altitude tethered balloons and kite-power generators.

2.5 Contributions of Current Research

The objective of the current research is to contribute to the understanding of the dynamics and stability of streamlined cables. In terms of existing streamlined cables, the work to date has focused on underwater applications and existing models draw from simple two-degree-of-freedom models from aeroelastic theory for fixed-wing aircraft. Interest in taking advantage of the reduced drag and VIV suppression characteristics of streamlined cables is growing in new areas of research such as high-altitude tethered balloons and kite-power generators. To assess the potential implementation of streamlined cables for these applications, more comprehensive models are required. There is a need for tools which can predict the dynamic behaviour and help guide the design of streamlined cables. There is also a need to develop the streamlined cable itself, as no specific manufacture process for the applications of streamlined cable in air currently exists. To address some of these challenges and contribute to the existing knowledge on streamlined cables, specific research objectives of the current work include:

1. Reviewing the existing work on streamlined cables and identifying the areas in which research is required.

2. Developing mathematical and theoretical models of a streamlined cable to predict its dynamic behaviour and guide future streamlined cable development. The models should be able to account for affects such as unsteady flow, composite cross-sections, wave-propagation along the length, variations in tension over the length and non-uniform fluid loading profiles.

3. Identify practical challenges in the development and implementation of streamlined cable through manufacture and experimental testing.

4. Validate the theoretical models against benchmark cases and, where available, experimental results.

5. Establish how the effect of tension, non-uniform wind and variations in cable tension may affect the dynamic behaviour of a streamlined cable.

Having established the objectives of the research, the first streamlined cable model is introduced. The model stems from the classic two-degree-of-freedom aeroelastic model which, as discussed in the literature review, has more recently been used to model faired off-shore structures.

Chapter 3

Classic Flutter Model with Tension

The two-degree-of-freedom aeroelastic model introduced in the literature review is useful in understanding, at a high level, the stability of a classic wing. The main difference between a classic wing and a streamlined cable is the addition of tension. In the current chapter, the classic two-degree-of-freedom model is extended to include the effect of tension. Fully unsteady fluid dynamic loading is included using a finite-state representation.

3.1 Structural Two-Degree-of-Freedom Model

The simplified two-degree-of-freedom model of the streamlined cable is a symmetric cross-section with non-coincident centres of mass, shear, tension and aerodynamic forcing. Figure 3.1 shows an example cross-section with the aerodynamic and three structural centres.

The shear centre is the location on the cross-section where an applied torque results in pure twist and an applied transverse force results in pure bending. The tension centre is the location where an applied axial force results in pure extension and an applied moment results in pure bending. A depiction and more detailed description of the cross-sectional centres is given in section 2.2.1.

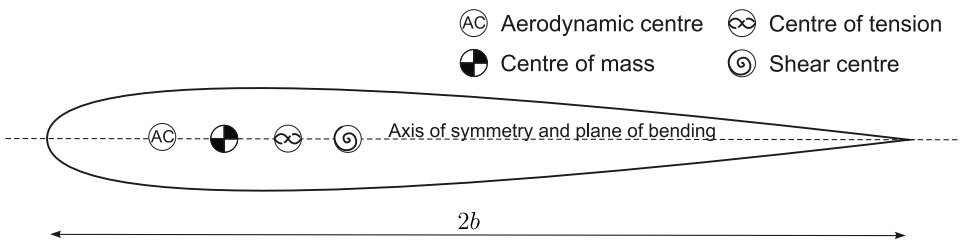

Fig. 3.1 Cross-section model with three offset structural centres.

The classic flutter model reduces the bending and torsional elasticity to an axial and torsional spring of stiffness k_b and k_t respectively. Similarly, the transverse restoring force of tension can be reduced to a spring of stiffness k_p acting at the centre of tension. The classic flutter model extended to include the effect of tension is shown in figure 3.2. Positions of the centres are taken with respect to the leading edge and are scaled by the semi-chord b. The position of the centres of tension, mass and shear are given by p, r and s respectively. These dimensionless positions vary from -1 for a centre located at the leading edge to 1 for a centre located at the trailing edge. The origin of the coordinate system for the overall motion of the streamlined cable is located at the shear centre.

Assuming small displacements and employing d'Alembert's principle, the dynamics problem can be reduced to a statics problem. Figure 3.3 shows the elastic and inertial forces acting on the streamlined cable cross-section, depicted by solid and dashed arrows respectively.

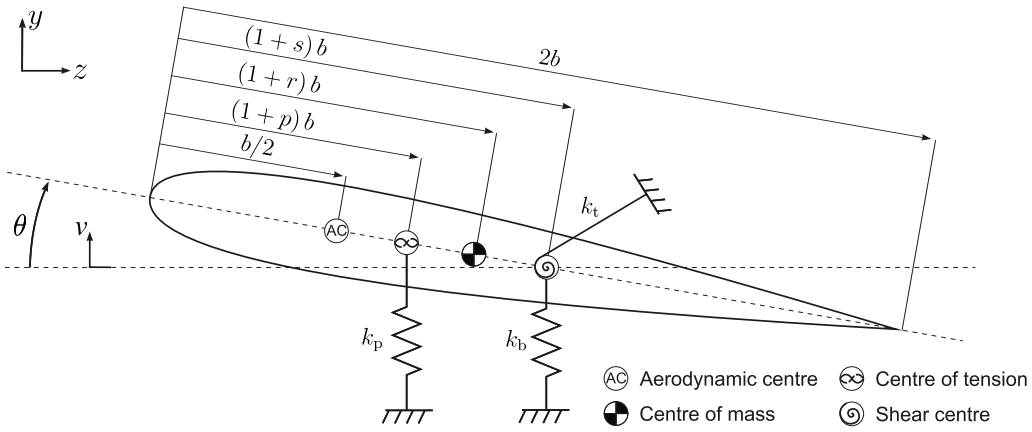

Fig. 3.2 Classic two-degree-of-freedom model extended to include the effect of tension.

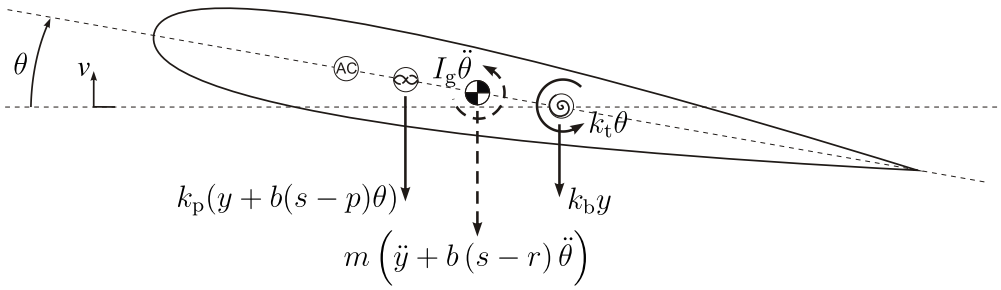

Fig. 3.3 Free-body diagram of the extended two-degree-of-freedom model (d'Alembert inertia shown using dashed arrows).

Taking the force and moment equilibrium about the shear centre gives the equations of motion as

$$\begin{bmatrix} m & mbz_{\mathrm{r}} \\ mbz_{\mathrm{r}} & I_{\mathrm{s}} \end{bmatrix} \begin{Bmatrix} \ddot{v} \\ \ddot{\theta} \end{Bmatrix} + \begin{bmatrix} k_{\mathrm{b}} + k_{\mathrm{p}} & k_{\mathrm{p}} bz_{\mathrm{p}} \\ k_{\mathrm{p}} bz_{\mathrm{p}} & k_{\mathrm{t}} + k_{\mathrm{p}} (bz_{\mathrm{p}})^2 \end{bmatrix} \begin{Bmatrix} v \\ \theta \end{Bmatrix} = \begin{Bmatrix} 0 \\ 0 \end{Bmatrix}, \tag{3.1}$$

where I_{s} is the mass moment of inertia about the shear centre, z_{r} is the dimensionless distance from the shear centre to the centre of mass $s-r$ and z_{p} is the dimensionless distance from the shear centre to the tension centre $s-p$. The equations of motion (3.1) reduce to the matrix form

$$\mathbf{M}_{\mathrm{c}} \ddot{\mathbf{u}} + \mathbf{K}_{\mathrm{c}} \mathbf{u} = \mathbf{0}, \tag{3.2}$$

where

$$\mathbf{u} = \begin{Bmatrix} v \\ \theta \end{Bmatrix}. \tag{3.3}$$

Examining equation (3.1), it can be seen that the addition of tension introduces symmetric, off-diagonal coupling terms in the stiffness matrix. Effectively, the addition of tension increases the bending and torsional stiffness, irrespective of whether the centre of tension is forward or aft of the shear centre. Also, as expected, when the tension is zero the equations of motion reduce to the classic flutter form.

3.2 Fluid-Dynamic Model

According to thin aerofoil theory, the fluid-dynamic loading on an aerofoil section can be separated into a lift force, drag force and moment acting at the quarter chord point (aerodynamic centre). In the current analysis, the drag force is considered negligible since, for small angles of attack, the drag will be small in comparison to the lift. For example, in an analysis completed by Patil et al. [102] on a high-aspect ratio wing (chord of 1 m and half-span of 16 m), neglecting the effect of drag caused errors of 0.16% in the flutter speed and 0.22% in the flutter frequency.

As described in section 2.3.2, the unsteady lift and moment per unit length acting at the aerodynamic centre are

$$L = \pi \rho_{\mathrm{f}} b^2 \left(U\dot{\theta} - \ddot{v} - bs\ddot{\theta} \right) + 2\pi \rho_{\mathrm{f}} U b \left(U\theta - \dot{v} + b(0.5 - s)\dot{\theta} - \upsilon_o \right) \tag{3.4}$$

and

$$M_{\mathrm{q}} = -\pi \rho_{\mathrm{f}} b^3 \left(U\dot{\theta} - 0.5\ddot{v} + b(0.125 - 0.5s)\ddot{\theta} \right). \tag{3.5}$$

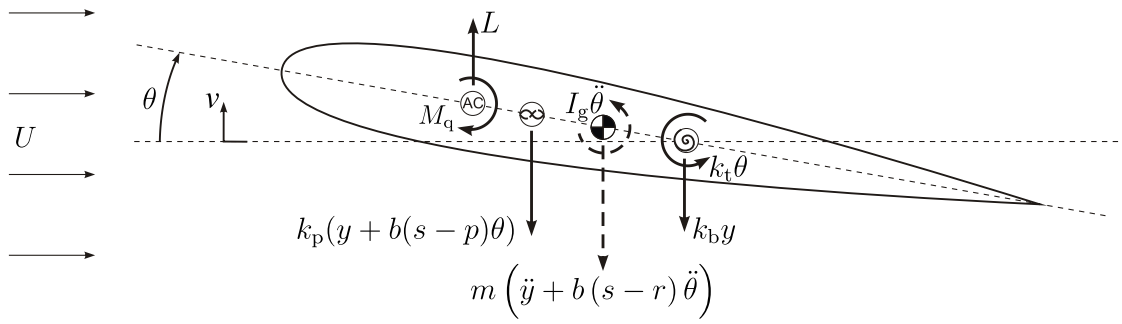

Fig. 3.4 Free-body diagram of the extended two-degree-of-freedom model with fluid-dynamic loading (d'Alembert inertia shown using dashed arrows).

Figure 3.4 shows the free-body diagram of the streamlined section including the fluid-dynamic loads due to the free-stream fluid velocity U.

Including the fluid-dynamic loading in the equations of motion, the force and moment about the shear centre can simply be included in equation (3.1) as

$$\begin{Bmatrix} L \\ M_q + Lb(0.5+s) \end{Bmatrix}. \tag{3.6}$$

The equations of motion with the fluid-dynamic loading can be rewritten in the matrix form of equation (3.2) as

$$(\mathbf{M}_c - \mathbf{M}_f)\,\ddot{\mathbf{u}} - \mathbf{C}_f\dot{\mathbf{u}} + (\mathbf{K}_c - \mathbf{K}_f)\,\mathbf{u} = \boldsymbol{\Upsilon}\boldsymbol{\upsilon}, \tag{3.7}$$

where $\mathbf{M}_f$, $\mathbf{C}_f$ and $\mathbf{K}_f$ are the fluid-dynamic mass, damping and stiffness matrices given by equations (3.8), (3.9) and (3.10) respectively. The damping matrix is split to show the non-circulatory (left matrix) and circulatory (right matrix) terms. To simplify the notation $\mu = \rho_f \pi b^2$.

$$\mathbf{M}_f = -\mu \begin{bmatrix} 1 & bs \\ bs & b^2(s^2+0.125) \end{bmatrix} \tag{3.8}$$

$$\mathbf{C}_f = \mu U \begin{bmatrix} 0 & 1 \\ 0 & b(s-0.5) \end{bmatrix} - 2\mu U \begin{bmatrix} 1/b & s-0.5 \\ s+0.5 & b(s^2-0.25) \end{bmatrix} \tag{3.9}$$

$$\mathbf{K}_f = 2\mu U^2 \begin{bmatrix} 0 & 1/b \\ 0 & s+0.5 \end{bmatrix} \tag{3.10}$$

The $\boldsymbol{\Upsilon}\boldsymbol{\upsilon}$ term in equation 3.7 is related to the finite-state approximation of the unsteady component of the fluid-dynamic loading (υ_o term in the lift equation 3.4).

To account for this unsteady fluid-dynamic term, a finite-state approximation derived by Peters et al. [103] for a two-dimensional thin aerofoil is employed. Unlike theories which assume simple harmonic motion *a priori*, an advantage of the finite-state theory is that it holds for arbitrary motion (i.e. it is valid outside of the flutter boundary). Hodges [64] gives a succinct summary of the finite-state theory, from which much of the implementation to the extended two-degree of freedom model below is drawn.

Equations for the induced flow from the shed wake vorticity are derived based on the assumption that the shed vortices travel at the same speed as the free-stream velocity and remain in the plane of the aerofoil. The derivation leads to an induced flow parameter υ_o approximated by the power series

$$\upsilon_o = \frac{1}{2}\sum_{n=1}^{N} b_n \upsilon_n = \frac{1}{2}\begin{Bmatrix} b_1 \\ b_2 \\ \vdots \\ b_N \end{Bmatrix}^T \begin{Bmatrix} \upsilon_1 \\ \upsilon_2 \\ \vdots \\ \upsilon_N \end{Bmatrix} = \frac{1}{2}\mathbf{b}^T \boldsymbol{\upsilon} \tag{3.11}$$

and N finite-state equations relating the induced flow to the aerofoil motion, written in matrix form as

$$\mathbf{A}_{\mathrm{n}}\dot{\boldsymbol{\upsilon}} + \frac{U}{b}\boldsymbol{\upsilon} = \mathbf{c}\left(-\ddot{v} + U\dot{\theta} + b(0.5-s)\ddot{\theta}\right). \tag{3.12}$$

Equation (3.12) can be rewritten in terms of the displacement vector $\mathbf{u}$ as

$$\mathbf{A}_{\mathrm{n}}\dot{\boldsymbol{\upsilon}} + \frac{U}{b}\boldsymbol{\upsilon} = \mathbf{M}_{\mathrm{i}}\ddot{\mathbf{u}} + \mathbf{C}_{\mathrm{i}}\dot{\mathbf{u}}, \tag{3.13}$$

where

$$\mathbf{M}_{\mathrm{i}} = \mathbf{c}\begin{Bmatrix} -1 \\ b(0.5-s) \end{Bmatrix}^T \quad \text{and} \quad \mathbf{C}_{\mathrm{i}} = \mathbf{c}\begin{Bmatrix} 0 \\ U \end{Bmatrix}^T. \tag{3.14}$$

The terms $\mathbf{b}$, $\mathbf{A}$ and $\mathbf{c}$ are given by

$$\mathbf{A}_{\mathrm{n}} = \mathbf{D} + \mathbf{d}\mathbf{b}^T + \mathbf{c}\mathbf{d}^T + \frac{1}{2}\mathbf{c}\mathbf{b}^T, \tag{3.15}$$

where

$$D_{nm} = \begin{cases} \frac{1}{2n}, & \text{for } n = m+1 \\ \frac{-1}{2n}, & \text{for } n = m-1 \\ 0, & \text{for } n \neq m \pm 1 \end{cases} \tag{3.16}$$

$$b_n = \begin{cases} (-1)^{n-1} \frac{(N+n-1)!}{(N-n-1)!} \frac{1}{(n!)^2}, & \text{for } n \neq N \\ (-1)^{n-1}, & \text{for } n = N \end{cases} \tag{3.17}$$

$$d_n = \begin{cases} \frac{1}{2}, & \text{for } n = 1 \\ 0, & \text{for } n \neq 1 \end{cases} \tag{3.18}$$

and

$$c_n = \frac{2}{n}. \tag{3.19}$$

Equations (3.11) to (3.15) define the N finite-state equations and induced flow term υ_o. The unsteady forcing term in the equation of motion 3.7 can therefore be written as

$$\boldsymbol{\Upsilon}\boldsymbol{\upsilon} = \frac{-\mu U}{b} \begin{bmatrix} \mathbf{b}^T \\ b(s+0.5)\mathbf{b}^T \end{bmatrix} \boldsymbol{\upsilon}. \tag{3.20}$$

The definition of this unsteady term completes the derivation of the equations of motion of the two-degree-of-freedom streamlined-cable model, which is given as the matrix equation (3.7). Though the system has only two degrees-of-freedom, the finite-state approximation of the induced flow term introduces an additional N equations. Therefore, the two-degree-of-freedom model is described by $N+2$ coupled second-order equations. In the next section, this system of equations is reduced to first-order by using a state-space representation. Then, section 3.4 converts this first-order system of equations into an eigenvalue problem, which can be used to analyse the model's stability.

3.3 Two-Degree-of-Freedom Model State-Space Problem

Converting the system of $N+2$ second order equations into a first-order system of equations follows a standard order reduction method used in mechanical vibrations and control theory, for example by Newland [95] or Friedland [45]. First, the displacements and velocities (both structural and induced flow) are combined into the single vector

$$\mathbf{q} = \begin{Bmatrix} \mathbf{u} \\ \dot{\mathbf{u}} \\ \boldsymbol{\upsilon} \end{Bmatrix}. \tag{3.21}$$

Then, the time derivative of $\mathbf{q}$ is

$$\dot{\mathbf{q}} = \begin{Bmatrix} \dot{\mathbf{u}} \\ \ddot{\mathbf{u}} \\ \dot{\boldsymbol{\upsilon}} \end{Bmatrix}. \tag{3.22}$$

Having defined the vector $\mathbf{q}$ and its derivative $\dot{\mathbf{q}}$, the $N+2$ second-order equations given by the matrix equations (3.7) and (3.13) can be converted to $N+4$ first order equations, written in matrix form as

$$\left[\begin{array}{c|c|c} \mathbf{C} & \mathbf{M} & \mathbf{0} \\ \hline \mathbf{I} & \mathbf{0} & \mathbf{0} \\ \hline \mathbf{0} & -\mathbf{M}_\mathrm{i} & \mathbf{A}_\mathrm{n} \end{array}\right] \dot{\mathbf{q}} + \left[\begin{array}{c|c|c} \mathbf{K} & \mathbf{0} & -\boldsymbol{\Upsilon} \\ \hline \mathbf{0} & -\mathbf{I} & \mathbf{0} \\ \hline \mathbf{0} & -\mathbf{C}_\mathrm{i} & \frac{U}{b}\mathbf{I} \end{array}\right] \mathbf{q} = \mathbf{0}, \tag{3.23}$$

where

$$\begin{aligned} \mathbf{M} &= \mathbf{M}_\mathrm{c} - \mathbf{M}_\mathrm{f} \\ \mathbf{C} &= -\mathbf{C}_\mathrm{f} \\ \mathbf{K} &= \mathbf{K}_\mathrm{c} - \mathbf{K}_\mathrm{f}. \end{aligned} \tag{3.24}$$

The first order system of equations (3.23) can also be written in the compact matrix form

$$\mathbf{A}\dot{\mathbf{q}} + \mathbf{J}\mathbf{q} = \mathbf{0}. \tag{3.25}$$

Equation (3.25) gives the fully unsteady two-degree-of-freedom model in a form suitable to be solved numerically in the time domain using an ordinary differential equation solver. Alternatively, the state-space representation can be converted to an eigenvalue problem to analyse the overall stability of the system, as described in the following section.

3.4 Two-Degree-of-Freedom Model Eigenvalue Problem

Reformulating the equations of motion of the two-degree-of-freedom system into an eigenvalue problem provides a means with which to investigate the stability of the streamlined cable. The time domain, state-space equation (3.25) can easily be converted to an eigenvalue problem. To reformulate the problem, assume a general response of the form

$$\mathbf{q} = \mathbf{Q}\mathrm{e}^{\lambda t}. \tag{3.26}$$

Substituting the general response into equation (3.25), the equation can be rewritten as the eigenvalue problem

$$\lambda \mathbf{Q} = -\mathbf{A}^{-1}\mathbf{J}\mathbf{Q}. \tag{3.27}$$

The eigenvalues and eigenvectors of this problem give information about the stability of the system. The j^{th} eigenvalue of the system of equations can be written in the general form

$$\lambda_j = \alpha_j + i\omega_j \tag{3.28}$$

and can be real, imaginary or complex. The imaginary component of the eigenvalue ω_j gives the modal frequency and the real component α_j the modal growth. The value α_j is important for stability analysis as it gives the growth of the response in time. Specifically, a positive value indicates an unstable response growing in time, a negative value indicates a damped response decaying in time and a value equal to zero indicates a stability boundary where the response remains constant in time. The magnitude of ω_j is of interest as it indicates the frequency of vibration or, if the value of ω_j is zero, that the response is non-oscillatory and will either converge or diverge depending on the sign of α_j. Hodges [64] helpfully summarises the meaning of the eigenvalues in a table, reproduced here as Table 3.1.

Table 3.1 Response and stability characteristics of an eigenvalue.

α	ω	Response in time	Stability
>0	$\neq 0$	Growing oscillation	Unstable
<0	$\neq 0$	Decaying oscillation	Stable
=0	$\neq 0$	Constant oscillation	Stability boundary
>0	=0	Divergence	Unstable
<0	=0	Convergence	Stable
=0	=0	Independent of time	Stability boundary

3.5 Conclusions

In the current chapter, a two-degree-of-freedom streamlined-cable model was developed by extending the classic flutter model – typically used to analyse the stability of structures such as aircraft wings – to include the transverse effect of tension. The two-degree-of-freedom model includes fully unsteady flow effects using a finite-state method which approximates the induced flow velocity using N additional equations. Therefore, the motion of the streamlined cable is given by $N+2$ coupled, second order equations. A state-space method is used

to reduce the system of equations to a first order form, which could be analysed in the time domain using numerical methods. Finally, the reduced set of equations is presented as an eigenvalue problem. The meaning of the eigenvalues in terms of investigating stability is discussed. The two-degree-of-freedom model provides a simple representation for the stability of a streamlined cable, and is useful in introducing some of the issues – such as offset structural centres and fully unsteady flow – associated with modelling the dynamic behaviour of a streamlined cable. However, an evident limitation of the two-degree-of-freedom model is that effects due to the cable length, such as wave propagation, are neglected. The next chapter presents a continuous streamlined cable model which aims to address this issue.

Chapter 4

Continuous Streamlined Cable Model

A natural extension of the two-degree-of-freedom streamlined cable model is to a continuous case where waves can travel in the spanwise direction. In this chapter, the equations of motion of a continuous streamlined cable with quasi-steady fluid loading are derived. A travelling wave solution is assumed which transforms the equations into a form where the wave dispersion characteristics can be assessed. Spatial, temporal and power flow methods are proposed as a means to study the overall stability of the continuous streamlined cable model. Finally, the limitations of the continuous streamlined cable model are discussed.

4.1 Equations of Motion

Similar to the two-degree-of-freedom model, the continuous model includes translation in y and rotation about x. Figure 4.1 depicts a view of the trailing edge of the continuous streamlined cable with the fluid flow being out of the page. Consider a small element dx of the streamlined cable. Figure 4.2 shows the tension P, shear S, bending M, torque T, lift L and moment (due to non-circulatory fluid effects) M_{q} acting on the element dx in the x-y plane. Figure 4.3 shows an end-on view, in the y-z plane, of the same streamlined cable element.

The unsteady lift and moment per unit length, acting at the aerodynamic centre, are given by equations (3.4) and (3.5). To simplify the equations in the continuous model, the induced flow term v_o is neglected and the fluid effects are assumed to be quasi-steady. As described by Leishman [82], the quasi-steady assumption is a good approximation when the reduced frequency $\omega b/U$ is below 0.05 but yields inaccurate results for greater values where the unsteady effects become significant. The quasi-steady lift and moment per unit

length on the element dx, taking $\mu = \rho_{\mathrm{f}} \pi b^2$, are given as

$$\begin{aligned} L &= \mu \left(U\dot{\theta} - \ddot{v} - bs\ddot{\theta} \right) + \frac{2U\mu}{b} \left(U\theta - \dot{v} + b(0.5 - s)\dot{\theta} \right) \\ M_{\mathrm{q}} &= -\mu b \left(U\dot{\theta} - 0.5\ddot{v} + b(0.125 - 0.5s)\ddot{\theta} \right) \end{aligned} \tag{4.1}$$

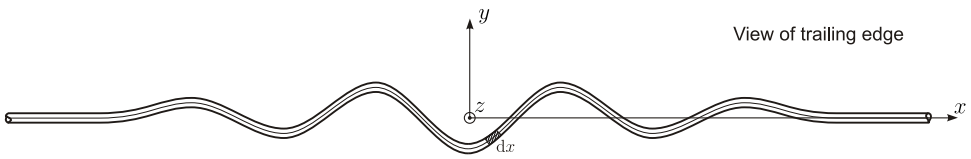

Fig. 4.1 Trailing edge view of the continuous streamlined cable model, the fluid velocity is out of the page.

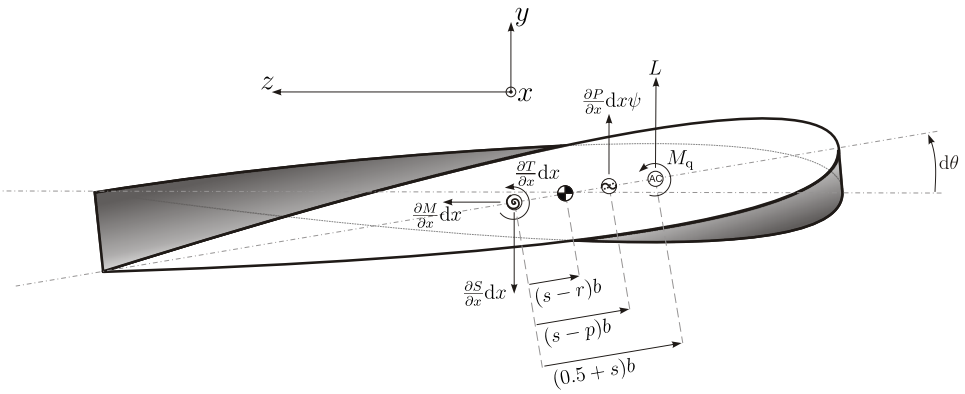

Fig. 4.2 Free-body diagram of streamlined cable element dx with tension P, shear S, bending M, torque T, lift L and non-circulatory fluid moment M_{q}.

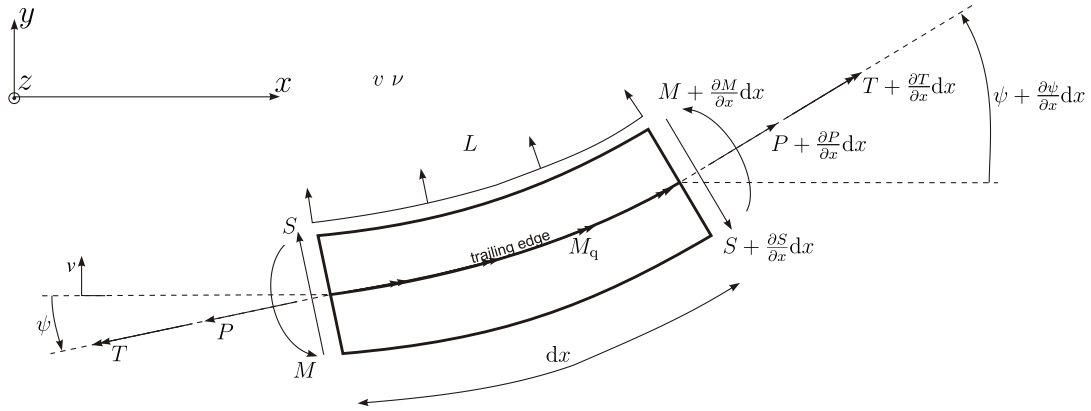

Fig. 4.3 Free-body diagram of an end-on view of the streamlined cable element dx.

Following a procedure similar to Graff [53] (for a beam on an elastic foundation) and Blevin [17] (for two-degree-of-freedom torsion-plunge coupled flutter) the transverse and torsional equations of motion are derived. Assuming small angles and representing time derivatives using dot notation, the force equilibrium in the y direction is

$$m\ddot{v} + m(s-r)b\ddot{\theta} = \frac{\partial P}{\partial x}\psi - \frac{\partial S}{\partial x} + L. \tag{4.2}$$

Taking moments about the z-axis and neglecting rotary inertia and second-order terms, gives the familiar shear and moment relation $S = \frac{\partial M}{\partial x}$. Then, from classic bending beam theory, the rate of change of shear is

$$\frac{\partial S}{\partial x} = EI\frac{\partial^4 v}{\partial x^4}. \tag{4.3}$$

Substituting the shear expression (4.3) into equation (4.2), assuming constant tension and taking the small angle approximation $\psi = \frac{\partial v}{\partial x}$, the equilibrium equation becomes

$$m(\ddot{v} + (s-r)b\ddot{\theta}) = P\frac{\partial^2 v}{\partial x^2} - EI\frac{\partial^4 v}{\partial x^4} + L. \tag{4.4}$$

Similarly, from Figure 4.3, the moment equilibrium about the shear centre (assuming constant tension, small angles and taking the torque as $T = GJ\frac{\partial \theta}{\partial x}$) may be written as

$$I_s\ddot{\theta} + m(s-r)b\ddot{v} = GJ\frac{\partial^2 \theta}{\partial x^2} + P\frac{\partial^2 v}{\partial x^2}(s-p)b + M_q + Lb(0.5+s). \tag{4.5}$$

Equations (4.4) and (4.5) give two coupled equations of motion for the continuous streamlined cable with quasi-steady fluid loading. The fluid load L in equation (4.4) and $M_q + Lb(0.5+s)$ in equation (4.5) are equivalent to equation (3.6) in the two-degree-of-freedom model. Consequently, forming a displacement vector $\mathbf{u} = \{y, \theta\}^T$, the fluid effects can be written in terms of the same $\mathbf{M}_f$, $\mathbf{C}_f$ and $\mathbf{K}_f$ matrices given by equations (3.8) to (3.10). A proposed method for studying the dynamic behaviour and stability of this continuous streamlined cable is using wave-propagation techniques such as dispersion or using power flow analysis.

4.2 Dispersion Analysis

Dispersion analysis provides a means to study the wave propagation along the continuous streamlined cable. By assuming a travelling wave solution of the form $v(x,t) = Ye^{i(\gamma x - \omega t)}$,

the dispersion equation relating the angular frequency ω and the wavenumber γ can be determined from the coupled equations of motion. The analysis of dispersion relations range from classic examples, such as the work presented by Graff on the propagation of flexural waves in thin rods [53] to more complicated coupled-beams. For example, Bhaskar [14] presents the general case of a triple-coupled beam in which flexural vibrations in two directions are coupled with torsional vibrations.

The continuous streamlined cable model is structurally double-coupled, as the flexural vibration in y is coupled to the torsional vibration θ. The continuous streamlined cable model is further coupled due to its interaction with the surrounding fluid. To determine the dispersion relation, travelling wave solutions

$$\begin{aligned} v(x,t) &= Y\mathrm{e}^{i(\gamma x-\omega t)} \\ \theta(x,t) &= \Theta\mathrm{e}^{i(\gamma x-\omega t)} \end{aligned} \tag{4.6}$$

are substituted into the equations of motion (4.2) and (4.5). The resulting matrix equation is

$$(\mathbf{W}_\mathrm{c}-\mathbf{W}_\mathrm{f})\begin{Bmatrix} Y \\ \Theta \end{Bmatrix} = \begin{Bmatrix} 0 \\ 0 \end{Bmatrix} \tag{4.7}$$

where

$$\mathbf{W}_\mathrm{c} = \begin{bmatrix} -m\omega^2+EI\gamma^4+P\gamma^2 & -m(s-r)b\omega^2 \\ -m(s-r)b\omega^2+P(s-p)b\gamma^2 & -I_\mathrm{s}\omega^2+GJ\gamma^2 \end{bmatrix} \tag{4.8}$$

and

$$\mathbf{W}_\mathrm{f} = -\omega^2\mathbf{M}_\mathrm{f}-i\omega\mathbf{C}_\mathrm{f}+\mathbf{K}_\mathrm{f}. \tag{4.9}$$

Equation (4.7) is given in terms of the matrices $\mathbf{W}_\mathrm{c}$ and $\mathbf{W}_\mathrm{f}$ to separate the structural streamlined cable terms from the fluid loading terms. Writing the relation in this way, it is easy to observe that the terms in the continuous model align with the structural matrices (3.1) and circulatory fluid loading matrices (3.9) and (3.10) of the two-degree-of-freedom model derived in the previous chapter. For non-trivial solutions of equation (4.7), the determinant of the 2 by 2 matrix $\mathbf{W}_\mathrm{c}-\mathbf{W}_\mathrm{f}$ must be zero. Thus, the $\det(\mathbf{W}_\mathrm{c}-\mathbf{W}_\mathrm{f})=0$ gives the characteristic – or dispersion – function. The full dispersion function for the continuous streamlined cable model is 6^{th} order in γ and 4^{th} order in ω, therefore no general solution formula exists.

In order to explore the wave propagation characteristics of the dispersion function, the analysis can be broken into temporal and spatial analyses. For a spatial analysis, the wavenumber γ is calculated for real values of the frequency ω. This equates to determining how harmonic waves will propagate along the length of the cable. Based on the sign and

magnitude of the real and imaginary parts of the wavenumber, a wave solution can be classified as one of three types listed below. Figure 4.4 provides a visual summary of the three waves types.

1. A free-propagating wave, where γ is real. If the sign of γ is positive, the wave propagates to the right, while if the sign is negative, the wave propagates to the left.

2. An evanescent wave, where γ is purely imaginary. If the sign of γ is positive, the wave amplitude decays with distance x, while if the sign is negative, the wave amplitude increases with distance x.

3. A leaky wave, where γ is complex. This wave can be thought of as a combination of the free-propagating and evanescent waves. The leaky wave propagates and either grows or decays with distance. The sign of the real part of γ determines wave direction, while the sign of the imaginary part of γ determines the growth rate.

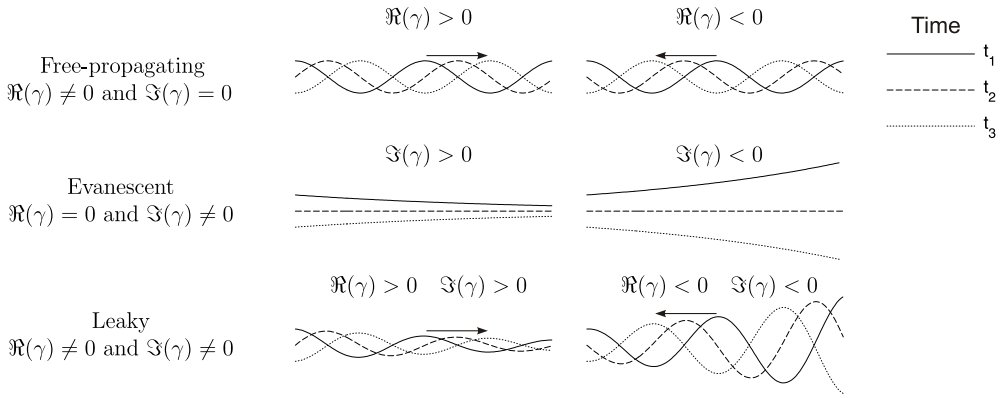

Fig. 4.4 Wave types in spatial analysis where ω is real.

Alternatively, a temporal approach investigates how waves which are periodic in space, develop in time. Here, the frequency ω is calculated as a function of a real wavenumber γ. Similar to the spatial analysis, the waves can be classified into three categories, listed below, based on whether ω is real, purely imaginary or complex. Figure 4.5 provides a visual summary of the three waves types.

1. If ω is real, the wave is free-propagating. Note that this solution is exactly the same as the first wave described in the spatial analysis as both γ and ω are real. The sign of the real part of ω must always be positive, as negative frequencies have no physical meaning. i.e. the sign of the real part of ω indicates the direction in time, which must

always be forward. As in the spatial analysis, the sign of the real part of γ indicates the propagation direction.

2. If ω is purely imaginary, the amplitude of the wave, which is periodic with distance, will grow or decay in time. A positive imaginary ω indicates growth whereas a negative imaginary ω indicates decay.

3. If ω is complex, the wave is a combination of the above two cases. The wave propagates and either grows or decays in time based on the sign of the imaginary part of ω.

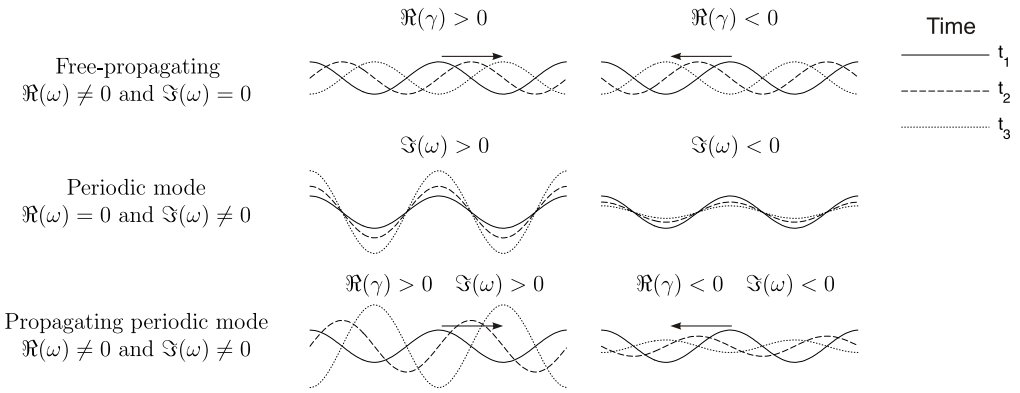

Fig. 4.5 Wave types in temporal analysis where γ is real.

Thus, the stability of the streamlined cable system could be analysed using a spatial and/or temporal method, where growth of a wave in space or time signals instability. Another proposed method to study the stability of the streamlined cable is using power flow analysis. The next section describes how power flow could be used to study the stability of the streamlined cable and gives example results for a general case.

4.3 Power-Flow Analysis

The use of power flow is proposed as a tool to assess the general stability characteristics of the streamlined cable. Consider the streamlined cable is harmonically forced at a point, the average power required to maintain a steady-state motion is a measure of the power dissipated by damping. Reactive power, which balances the kinetic and potential energy exchange, is also present but over the course of one cycle averages to zero. For a succinct derivation of this result see Talbot [123]. Thus, the average driving-point power is directly

related to the damping; if the damping becomes negative, the average power must also be negative. For classic flutter, which is associated with negative damping, the average power required to sustain a harmonic excitation should therefore be an indicator of stability. If power is positive, the system is stable as energy must be provided to the system to sustain the steady-state motion. Conversely, if power is negative, the system is unstable as energy is being withdrawn from the system. Figure 4.6 summarises the power flow analysis method.

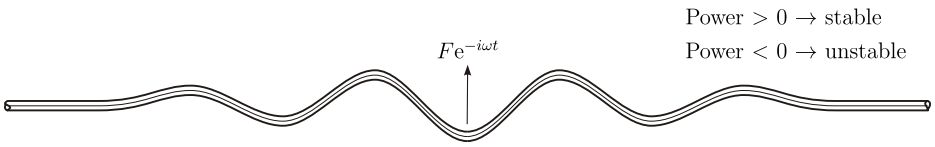

Fig. 4.6 Power flow analysis method, a harmonic force is applied and the sign of the power required to sustain the steady-state motion indicates stability.

In the example provided here, the streamlined cable is considered infinite. Though no cable will ever be infinite, it is a useful mathematical assumption as it eliminates the need to treat boundary reflections. The infinite case will be equivalent to the results for a bounded cable if the response from the point forcing decays to zero prior to reaching the boundaries. An equivalent analogy holds if the cable tension varies with length. The result from the infinite, constant tension case will approach the result for a cable of varying tension if the length scale of the response occurs over a region which has a relatively small change in tension. Figure 4.7 depicts when the infinite case can be a useful tool for analysing real, bounded cables.

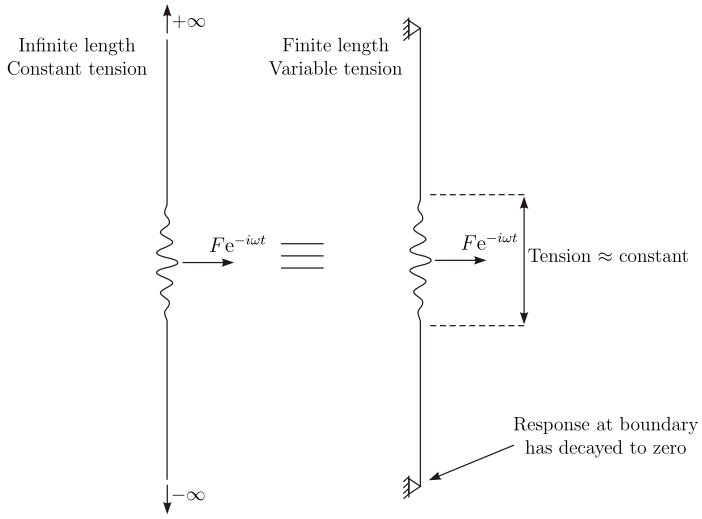

Fig. 4.7 Conditions for an infinite cable of constant tension to be valid for a finite cable of varying tension.

To apply power-flow analysis, a harmonic force $F\mathrm{e}^{-i\omega t}$ is applied at $x = 0$ and the driving-point power is calculated. Cremer and Heckl [29] derive the general expression for the driving-point power as

$$W = \frac{1}{2}F^2\Re\left(\frac{1}{Z}\right) \tag{4.10}$$

where $Z = F/(-i\omega Y(0,\omega))$ is the impedance. A harmonic torque $T\mathrm{e}^{-i\omega t}$ could also be applied, in which case Y would be replaced by Θ and F by T in the power equation (4.10). Given the addition of an applied force, the equation of motion from equation (4.7) becomes

$$(\mathbf{W}_\mathrm{c} - \mathbf{W}_\mathrm{f})\begin{Bmatrix} Y \\ \Theta \end{Bmatrix} = \begin{Bmatrix} F \\ 0 \end{Bmatrix}. \tag{4.11}$$

Prior to an example of the continuous streamlined beam, it is useful to examine the power-flow relations for the more straightforward cases of a beam or string on an elastic and viscous foundation, depicted in Figure 4.8. The variables m, c and k are the mass, damping and stiffness per unit length respectively. These classic cases provide a useful comparison to the streamlined beam. The fluid effects applied to the streamlined beam are analogous to the stiffness, damping and mass terms of a beam/string on a foundation. In both cases, the mass, damping and stiffness terms are constant over the length and depend only on time.

The wavenumber γ and impedance Z for point-excited infinite beams and strings can be found in texts such as Cremer and Heckl [29] and Graff [53]. Table 4.1 summarises the closed-form solutions for an infinite beam in bending, transverse motion of a string and bar in torsion on elastic and viscous foundations. The results for a beam, string or bar

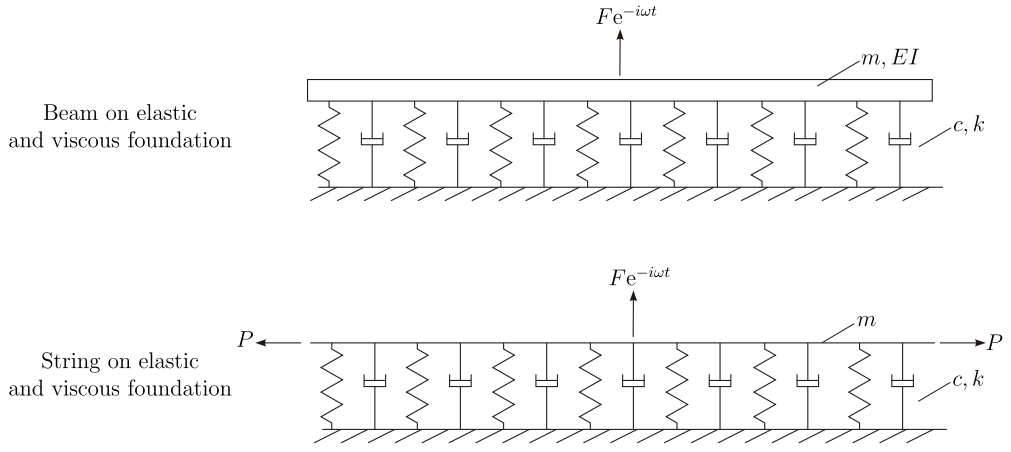

Fig. 4.8 Beam and string on an elastic and viscous foundation.

unsupported by the foundation are given by taking the stiffness k and damping c as zero. Also worth noting, is that the string and bar follow the same differential equation and thus give the same result where m is replaced by I_g and P by GJ.

Table 4.1 Wavenumber and impedance of structures on an elastic and viscous foundation.

	Wave number γ	Impedance Z
Bending beam	$\gamma^4 = \frac{m\omega^2+ci\omega-k}{EI}$	$\frac{4EI\gamma^3}{(1+i)\omega}$
Transverse string	$\gamma^2 = \frac{m\omega^2+ci\omega-k}{P}$	$\frac{2P\gamma}{\omega}$
Torsion bar	$\gamma^2 = \frac{I_g\omega^2+ci\omega-k}{GJ}$	$\frac{2GJ\gamma}{\omega}$

Figure 4.9 shows a comparison of the driving-point power for a string and beam with no foundation ($k = c = 0$). As the driving-point power for the string is independent of frequency, it provides a convenient value with which to normalise the power. Thus, the power normalised with respect to the tension result is given as $W/W_p = \frac{4W\sqrt{Pm}}{F^2}$. Note that a bar, excited by a harmonic torque, will follow the same relation as the string and be independent of frequency. Thus the power for a torque input can be normalised as $W/W_t = \frac{4W\sqrt{GJI_g}}{T^2}$. The driving-point power of the beam varies as the inverse of the square of frequency.

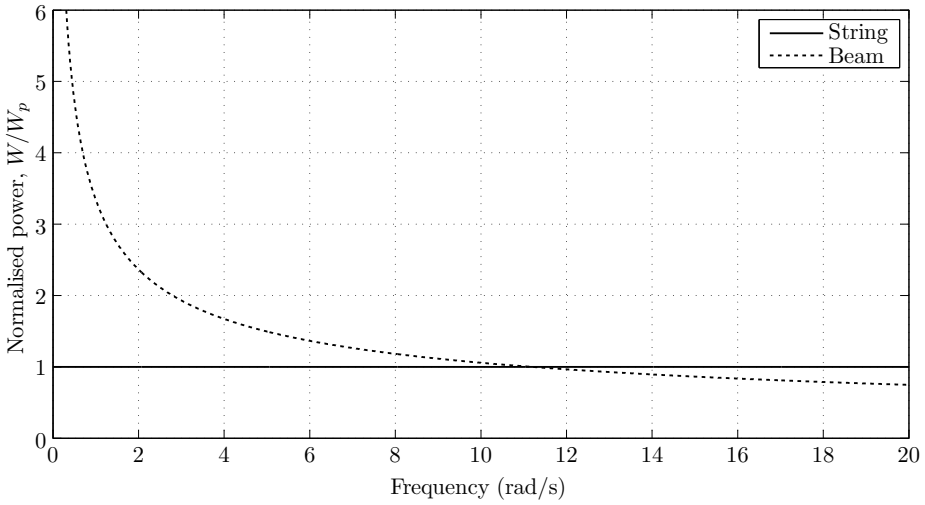

Fig. 4.9 String and beam normalised driving-point power as a function of input frequency.

The addition of an elastic and viscous foundation alters the driving-point power. Figure 4.10 (a) shows the normalised power of the string with the individual effects of the addition of an elastic or viscous foundation and Figure 4.10 (b) the result if both the stiffness and damping are included. Figure 4.11 (a) and (b) give the equivalent plots for the beam. Note that though the tension in the beam case is zero, the result is still normalised with respect to the tension result to give consistent comparisons. The results are not unexpected, the elastic foundation causes a cut-off frequency, which is analogous to the excitation point causing the system to vibrate as a rigid body (infinite wavelength) and is equal to $\omega_{\text{cut-off}} = \sqrt{k/m}$. The cut-off frequency thus provides a convenient value to normalise frequency as $\frac{\omega}{\omega_{\text{cut-off}}}$. The viscous foundation causes a decrease in the power at lower frequencies and tends towards the undamped case as the excitation frequency increases.

It is interesting in these classic examples to look at the effect of negative stiffness or damping, which compares to the case of divergence or flutter. Taking the string case shown in Figure 4.10 (b) the result if the stiffness or damping is negative is shown in Figure 4.12 (a) and (b) respectively. The negative damping result is as expected and causes the power to switch from positive to negative indicating instability. Conversely, the negative stiffness case gives positive power, even though negative stiffness is inherently unstable. Thus, caution must be exercised when using the power flow method as it will not give an indication of instabilities related to negative stiffness. To use the power-flow method the system should first be checked for negative stiffness. If negative stiffness is present the system is statically unstable; if the stiffness is positive a power-flow method may be used.

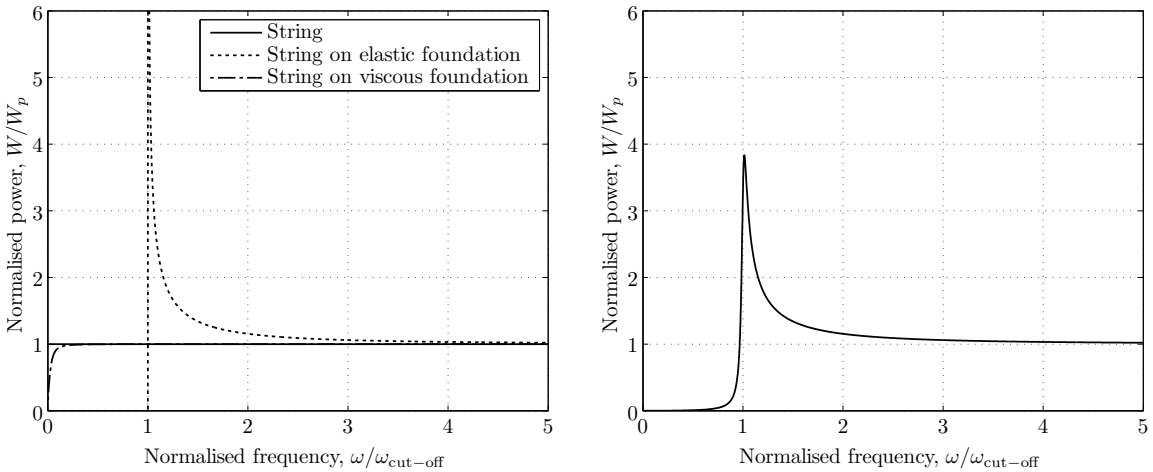

(a) Elastic or viscous foundation

(b) Overall response

Fig. 4.10 Normalised driving-point power of a string on an elastic and viscous foundation.

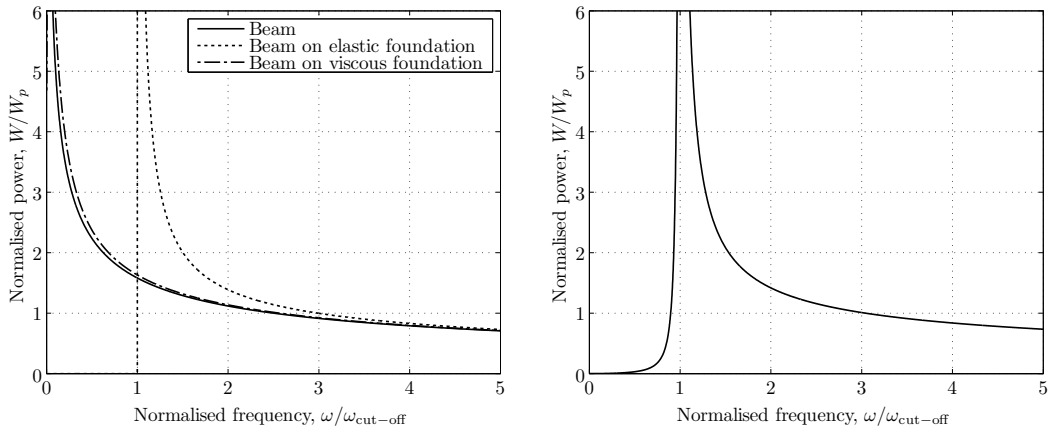

(a) Elastic or viscous foundation (b) Overall response

Fig. 4.11 Normalised driving-point power of a beam on an elastic and viscous foundation.

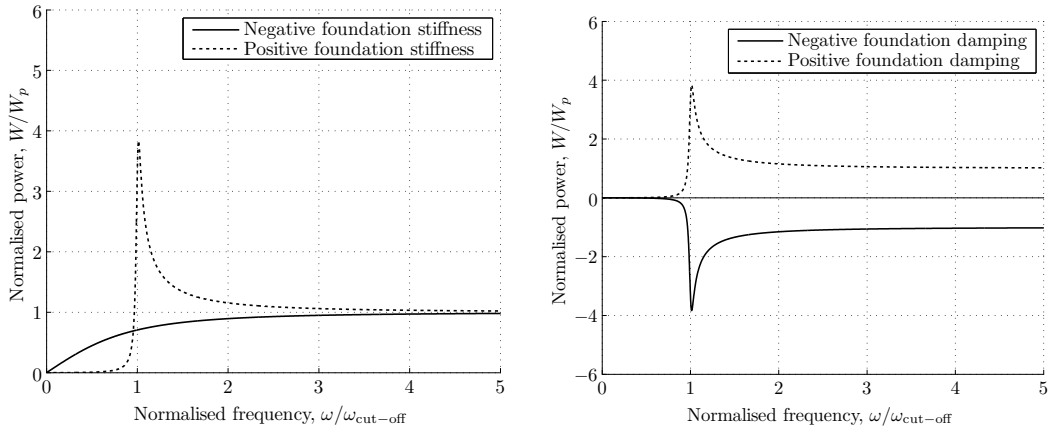

(a) Effect of negative foundation stiffness (b) Effect of negative foundation damping

Fig. 4.12 Effect of negative foundation values on normalised driving-point power of a string.

The string and beam solution are now combined to model a beam under tension on an elastic and viscous foundation. The system is solved using a numerical Fast Fourier Transform (FFT) method adapted from Hunt [68]. The FFT method is used to solve for the power of a beam subject to increasing tension. Figure 4.13 shows the normalised results, where the power and tension are normalised with respect to the $P = P_o$ case. The combination of tension and bending is not linear as the wavenumber γ is related to tension as a 2^{nd} power and to the bending as a 4^{th} power. Comparing the numerical results to the closed-form solutions shows that the FFT method gives reasonable results. Without tension, the relation is equivalent to that of a beam on a viscous foundation shown in Figure 4.11. As the tension increases, the power relation tends towards the string solution given by Figure 4.10.

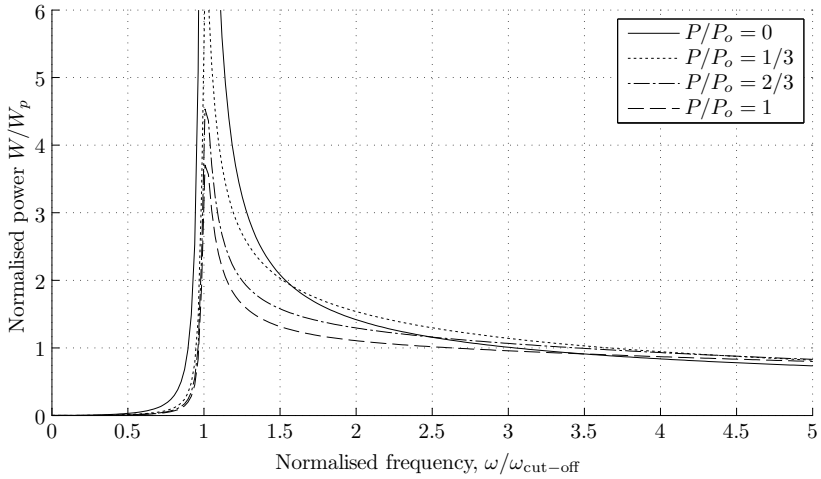

Fig. 4.13 Power of a beam under tension P on a viscous foundation. Results are normalised with respect to the $P = P_o$ solution.

Having explored the driving-point power relation for more classic cases, an example of the power flow for the continuous streamlined cable model is given. Structurally, the streamlined cable is a beam under tension but includes offset centres of mass, tension, shear and aerodynamic forcing. Therefore, without wind, assuming a small amount of structural damping (c=0.01), the driving-point response will follow a similar relation to that given in Figure 4.13. The fluid loading gives stiffness and damping terms which are roughly comparable to the effect of the elastic and viscous foundation in the previous cases.

As described by Blevins [17], a general result from classical flutter analysis is that positioning the centre of mass (COM) forward of the shear centre (SC) inhibits flutter (see section 2.4.2 for more detail). Using this classic result as a starting point, the power flow of an infinite streamlined cable under tension is compared for a position of the COM forward and aft of the SC. To ensure there are no negative stiffness effects, the shear and tension centre are taken as concentric and forward of the aerodynamic centre with a dimensionless position of $s = p = -0.6$ (the discrete model presented in the next chapter is also used to verify the no negative stiffness assumption). The wind is taken as 10 m/s, the fluid density as 1.2 kg/m^3 and the semi-chord of the cross-section as 25 mm. The driving-point power over an input frequency range from 0 to 20 rad/s is calculated, which is within the bounds of the quasi-steady assumption, as it gives a reduced frequency between 0 to 0.05. The dimensionless position of the COM for the forward and aft case are taken as $r = -0.65$ and $r = -0.45$ respectively. Figure 4.14 shows the normalised driving-point power for a harmonic force input for the two COM cases with and without wind. Figure 4.15 shows the equivalent result for an applied harmonic torque.

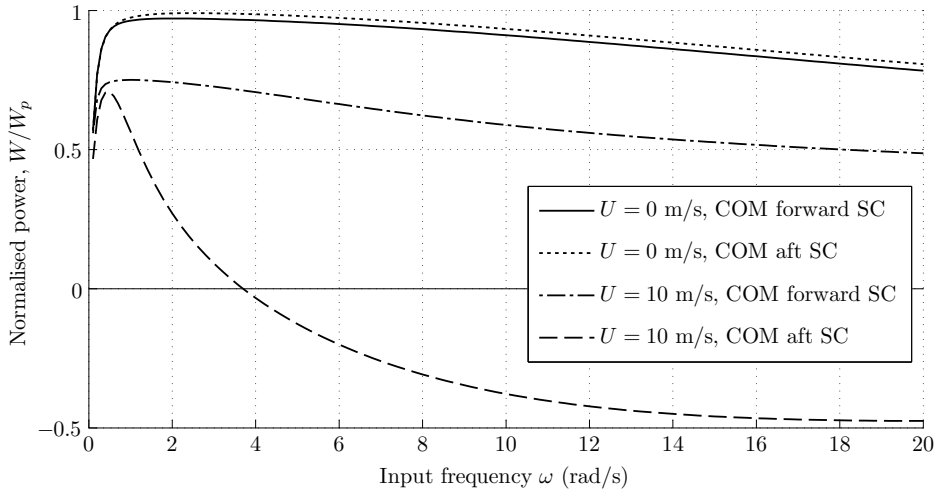

Fig. 4.14 Driving-point power of a streamlined beam, with and without wind, subject to an applied harmonic force at x=0. The case with the COM aft of the SC gives negative power.

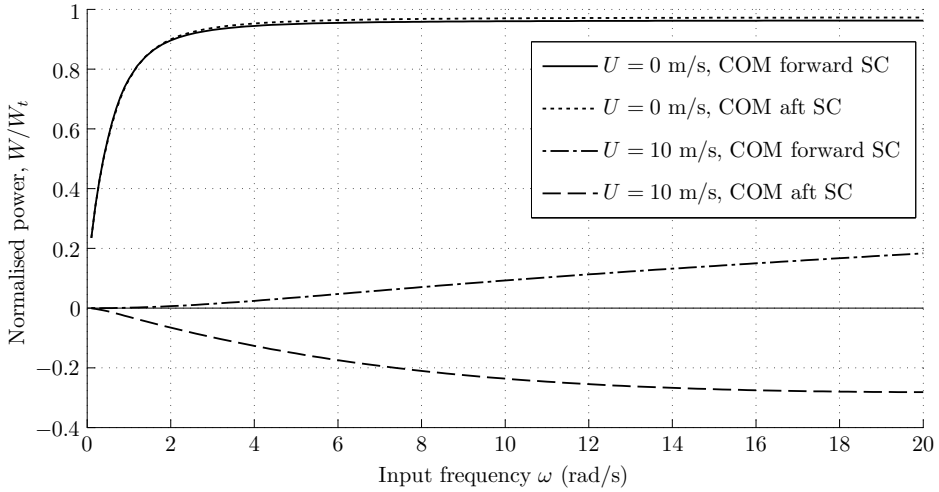

Fig. 4.15 Driving-point power of a streamlined beam, with and without wind, subject to an applied harmonic torque at x=0. The case with the COM aft of the SC gives negative power.

The results with no wind serve to verify that the model is giving sensible results as the power relation agrees with the tensioned beam case (Figure 4.13 for $P = P_o$). At low frequencies, for a force input, the normalised power is about 1, indicating it is approximately equal to the driving-point power for a tensioned string. As the frequency increases there is a decrease in power due to the effect of the beam bending, which gives power as inversely proportional to the input frequency. For the case of an input torque without wind, the normalised power is approximately equal to 1, indicating the solution converges to the torsion bar case.

The results with wind generally agree with Blevin's classic flutter result as shifting the COM aft of the SC causes instability, as seen by the negative power result in both the input force and input torque cases. The stable case with the COM forward of the SC gives positive power over the range of investigated input frequencies. For the harmonic torque case, the unstable case with the COM aft of the SC gives negative power over the range of investigated input frequencies. For the harmonic forcing case, the power changes from positive to negative power between 3.5 rad/s to 4.0 rad/s. In classic flutter analysis, it is the torsional mode that becomes unstable to flutter as the wind speed increases. This could explain why the power is negative over the entire range of investigated frequencies for the torsion input case but not the forcing input case. As the forced case exhibits a stability boundary (power changes from positive to negative) at a specific input frequency, it is explored in more detail.

Figure 4.16 compares the deflected position of the streamlined cable for a harmonic force input of 3.5 rad/s and 4.0 rad/s. The figure shows that when the response becomes unstable, there is a decrease in the amplitude of the y displacement and an increase in the rotation angle θ, but the overall shape stays approximately the same. The deflection bowl (the length scale over which the beam is deflected due to the point loading) is between 200 m to 300 m. Figure 4.16 depicts how the displacement response at x=0 changes for input frequencies of 3.0 rad/s, 3.5 rad/s, 4.0 rad/s and 4.5 rad/s over one forcing cycle of period T. From this depiction, a phase shift in position of y as the streamlined cable moves from positive (3.0 rad/s and 3.5 rad/s) to negative power (4.0 rad/s and 4.5 rad/s) is seen. In the positive power cases, at $t = T/4$ (when the force is zero), the streamlined cable has positive y displacement. Conversely, in the negative power case, at $t = T/4$ the streamlined cable has negative y displacement.

Figure 4.17 shows how the phase shift varies over the range of input frequencies. The figure shows that the onset of negative power, between an input frequency of 3.5 rad/s to 4.0 rad/s, corresponds to the phase shift switching from negative to positive. In a classic mass and spring system which is harmonically forced, the phase is always negative and the displacement lags the force. Here, in the unstable streamlined cable case, the displacement leads the force and the power is negative. Figure 4.17 also shows the phase shift relation given changes of the viscous damping c (included to model a small structural damping). It can be seen that the stability boundary (where the phase becomes positive) is related to the magnitude of c. This result suggests that it is the torsional mode, here analogous to the power given a harmonic input torque, that drives stability. For small changes in the chosen value of c, the driving-point power given an input torque does not exhibit the same sensitivity to the chosen value of c.

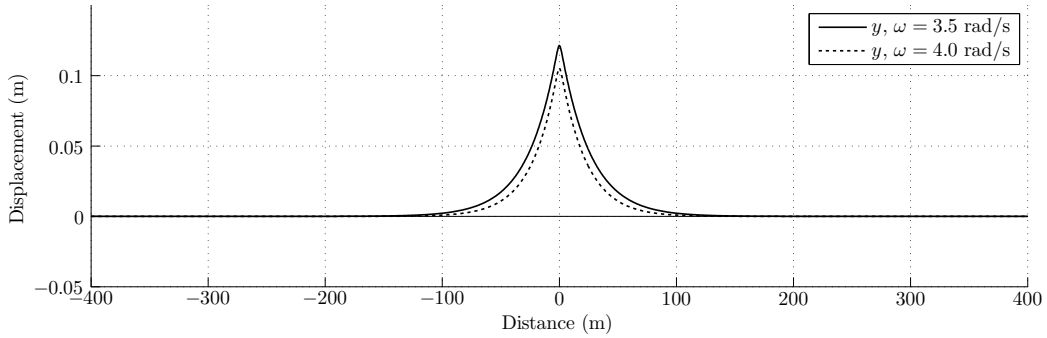

(a) Displacement y

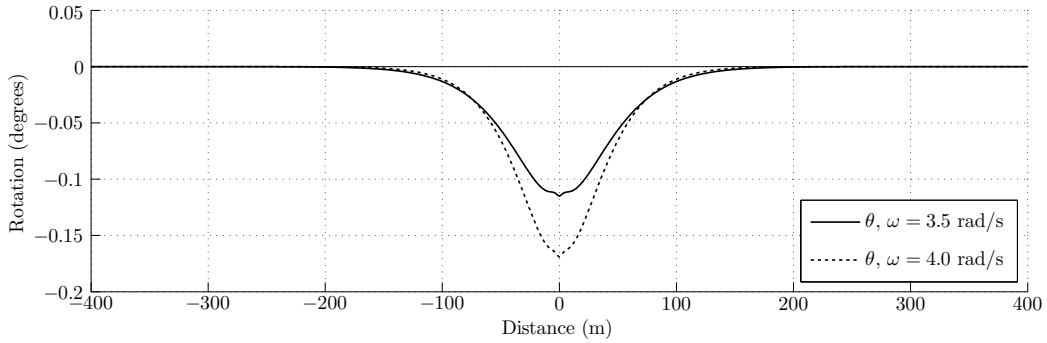

(b) Displacement θ

Fig. 4.16 Mode shape of the displacement for the continuous streamlined cable for a positive power ($\omega = 3.5$ rad/s) and negative power ($\omega = 4.0$ rad/s) case.

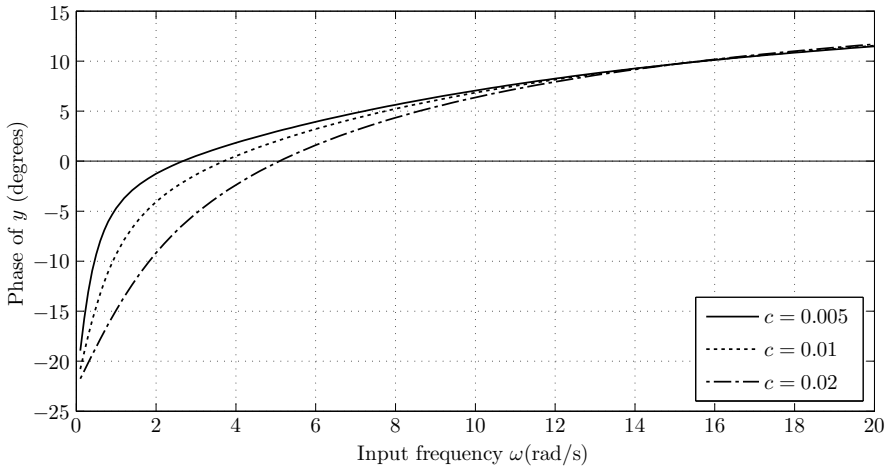

Fig. 4.17 Phase shift of y displacement for increasing input frequency, the power becomes negative when the phase becomes positive.

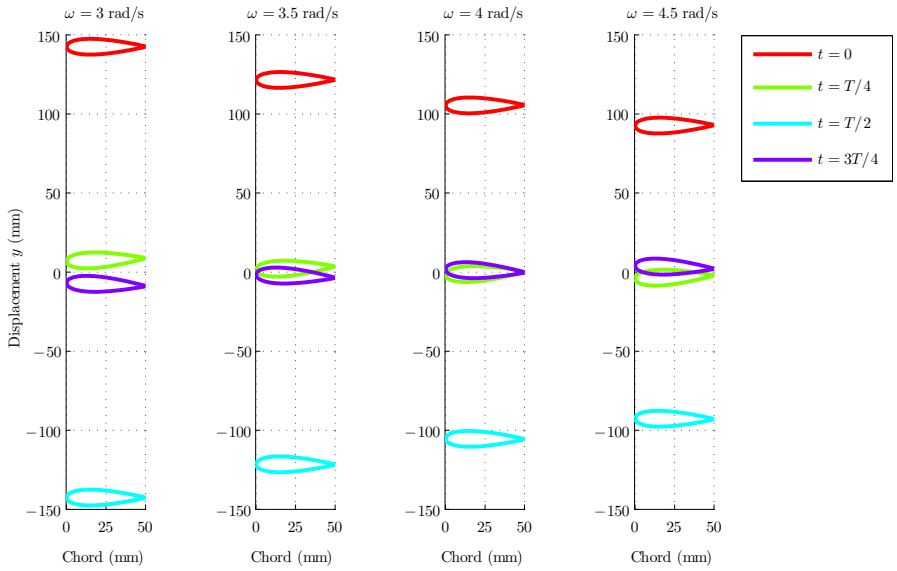

Fig. 4.18 Normalised displacement over one cycle for stable (ω=3.0 and 3.5 rad/s) and unstable input frequency (ω=4.0 and 4.5 rad/s).

This simple example illustrates how the power flow method could be used to investigate the stability of a streamlined cable. Here only one wind speed is explored but the model has potential to investigate the stability behaviour over a range of wind speeds and structural input conditions to gain a better understanding of the streamlined cable's dynamic behaviour and stability. The continuous model is highly theoretical and some of the simplifying assumptions do restrict its scope as an analysis tool.

One limitation of the continuous model it that both the tension and fluid velocity have been assumed constant over the entire length of the streamlined cable. Though these assumptions simplify the equations of motion, they limit the scope of the model in analysing real streamlined cable applications. For example, many potential applications – such as a tethered balloons and kites – orient the streamlined cable parallel to gravity in an environment with a non-constant velocity profile. In these applications, assuming constant tension and constant fluid velocity may not be appropriate.

A second limitation of the continuous model is that the flow is assumed to be quasi-steady. This assumption is valid when the reduced frequency $\omega b/U$ is below 0.05. To include fully unsteady effects the induced flow from the shed vortex must be included, for example, as it was in the two-degree-of-freedom model using the finite-state representation. As the continuous model is limited not only in the fluid dynamic assumption, but is also constrained by the constant tension and constant fluid velocity profile, the inclusion of fully unsteady flow was not pursued in the current work. Though the continuous model

is subject to a number of limitations its appealing features are the relative simplicity and computationally efficiency compared to large finite-element models.

4.4 Conclusions

This chapter has presented the derivation of the equations of motion for a continuous streamlined cable. Using the derived equations of motion a wave-technique was used to derive the dispersion equation, which provides a means of studying the wave propagation in the streamlined cable. As the dispersion equation is 6^{th} order in wavenumber γ and 4^{th} order in frequency ω, spatial, temporal and power methods were proposed as possible methods to study stability. Finally, the limitations of the continuous model were discussed.

The discussion concluded that the model is a computationally efficient method to obtain information on the dynamics and stability of a simplified streamlined cable case. The limitations of the continuous model in analysing a wider range of issues associated with streamlined cable applications, such as varying tension and wind speed, suggests a less restrictive model is required. A discrete streamlined cable model, which overcomes some of the discussed limitations, is presented in the next chapter.

Chapter 5

Discrete Streamlined Cable Model

To overcome the limitations of the continuous model, a discrete, small-displacement, numerical model is developed. This discrete model can be used to investigate how non-linear effects, such as varying tension and wind profile, affect the stability of a streamlined cable. The discrete model takes into account the eccentricity of the aerodynamic, mass, tension and shear centres. The effect of the applied external tension is included by means of a geometric stiffness matrix. Fully unsteady fluid loading is included using the finite-state representation described in chapter 3 for the two-degree-of-freedom model. The equations of motion for the discrete model are given in a state-space form, which may be used for time domain analysis, and are also reduced to an eigenvalue problem, which can be used to study stability. Finally, as an initial verification of the discrete model, it is used to obtain the same results as those from the continuous model.

5.1 Streamlined Cable Discretisation

The streamlined cable is discretised using a finite-element method. Figure 5.1 shows an n element discretisation of a length ℓ_c of streamlined cable, with (a) showing the element numbering and (b) the corresponding node numbering. In a general form, the m^{th} element is bounded by nodes $j = m$ and $k = m+1$ where $m = 1, 2, \ldots n$. The general displacement field of the discrete model comprises three translations (u, v, w) and three rotations (θ, ϕ, ψ) taken with respect to the x, y and z axes. In vector form, the displacement field is written as $\mathbf{u} = \{u, v, w, \theta, \phi, \psi\}^{\mathrm{T}}$.

A two node, twelve degree-of-freedom beam element is chosen to model the cable. Figure 5.2 shows the m^{th} element with six degrees-of-freedom at the bounding nodes j and k.

It is worth noting that, throughout this chapter, quantities representing a node are denoted by the subscript index j and those representing an element by an over-bar. The equivalent properties for the entire streamlined cable have no index or over-bar. Following this convention, the vector of displacements at the j^{th} node is

$$\mathbf{d}_j = \{u_j, v_j, w_j, \theta_j, \phi_j, \psi_j\}^{\mathrm{T}}, \tag{5.1}$$

the vector of the m^{th} element displacements is

$$\bar{\mathbf{d}} = \begin{Bmatrix} \mathbf{d}_j \\ \mathbf{d}j+1 \end{Bmatrix} \tag{5.2}$$

and the displacement vector for the discretised streamlined cable is

$$\mathbf{d} = (\mathbf{d}_1, \mathbf{d}_2, ..., \mathbf{d}_n, \mathbf{d}_{n+1})^{\mathrm{T}}. \tag{5.3}$$

The displacement field within an element is interpolated from the nodal displacements and the shape function matrix $\mathbf{N}$ by

$$\bar{\mathbf{u}} = \mathbf{N}\bar{\mathbf{d}}. \tag{5.4}$$

The displacements are taken with respect to the spatial reference frame x-y-z. Aligning the reference frame with one of the structural or aerodynamic centres can simplify the resulting equations of motion.

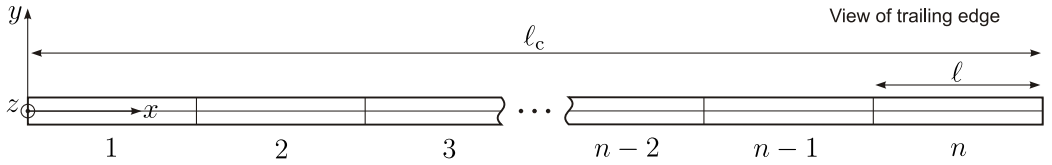

(a) n element discretisation of a length ℓ_c of streamlined cable.

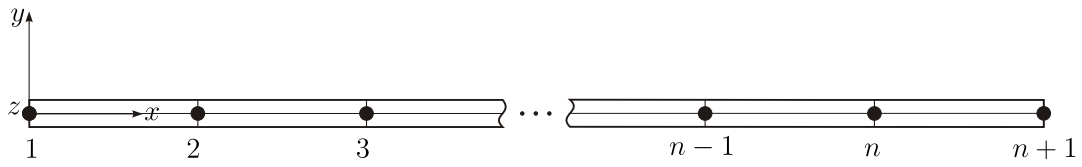

(b) Numbering of $n+1$ nodes of the n element streamlined cable discretisation.

Fig. 5.1 Streamlined cable discretisation showing element and node numbering. View is of the trailing edge.

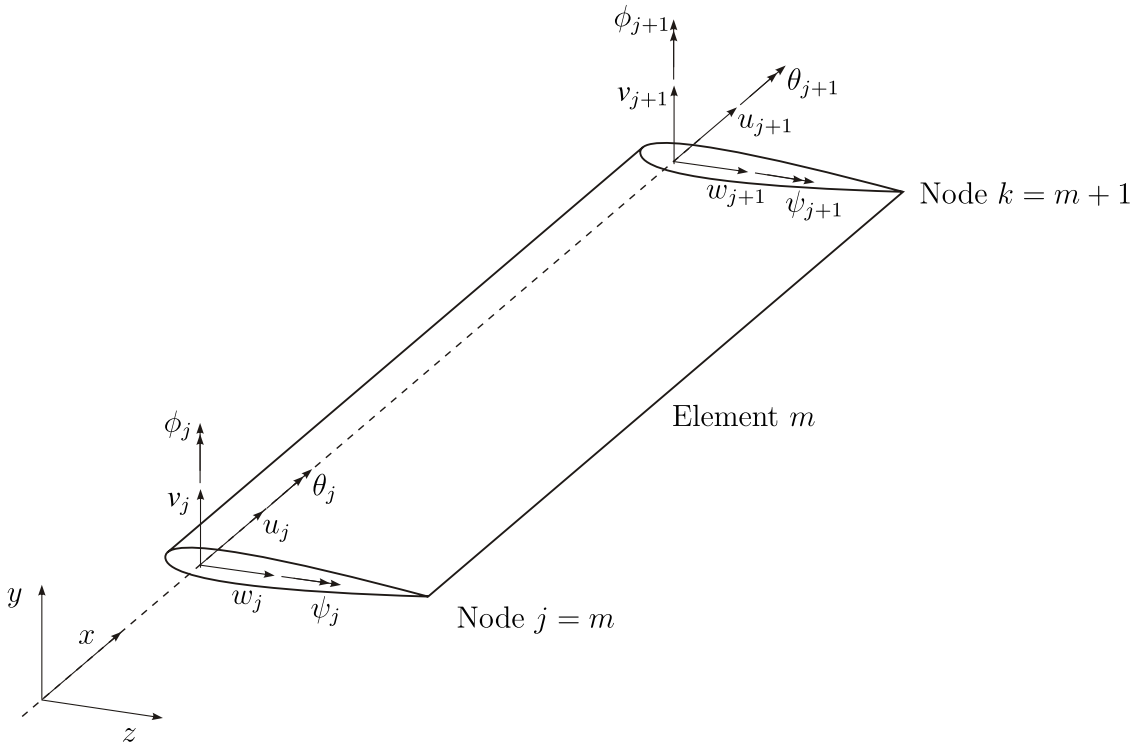

Fig. 5.2 Two node, twelve degree-of-freedom streamlined beam element.

5.2 Reference Frame Transformation

The streamlined cable is assumed to have four centres: an aerodynamic centre, mass centre, tension centre and shear centre. Each centre decouples the streamlined beam equations in a different way. Aligning the spatial reference frame with any one of these centres provides some simplification in the model derivation. By defining a general method to transform the reference frame between centres, the simplifications offered by each centre can be exploited.

Following a similar convention to the two-degree-of-freedom and continuous model, Figure 5.3 shows two reference frames *x*-*y*-*z* and x^*-y^*-z^*. The location of the reference frames are taken with respect to the leading edge of the cross-section. The starred reference frame is offset by $z = (\mathcal{F}^* - \mathcal{F})\,b$ from the *x*-*y*-*z* frame. The displacements taken with respect to frame *x*-*y*-*z* and x^*-y^*-z^* are defined as $\mathbf{u}$ and $\mathbf{u}^*$ respectively. Since the two

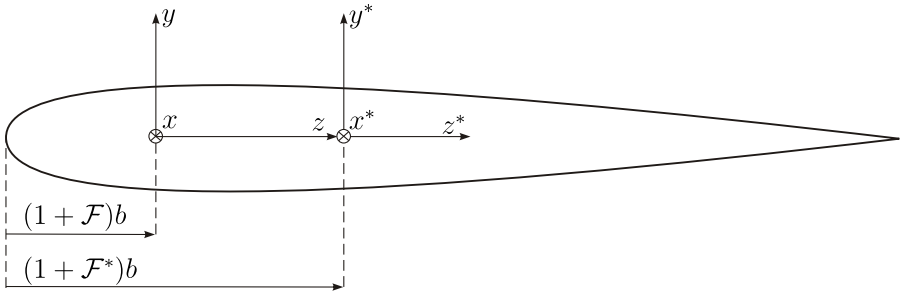

Fig. 5.3 Position of two reference frames x-y-z and x^*-y^*-z^*.

frames remain parallel (they are only translated and not rotated), the rotations θ, ϕ and ψ are equivalent to θ^*, ϕ^* and ψ^* respectively. Assuming no warping (i.e. that the cross-section remains plane) and small displacements, the translation displacements in frame x^*-y^*-z^* can be written as a function of the displacements in frame x-y-z as

$$\begin{aligned} u^* &= u + z\phi \\ v^* &= v - z\theta \\ w^* &= w. \end{aligned} \tag{5.5}$$

Taking the time derivative of (5.5) to obtain the velocities and accelerations gives

$$\begin{aligned} \dot{u}^* &= \dot{u} - z\dot{\psi} \\ \dot{v}^* &= \dot{v} \\ \dot{w}^* &= \dot{w} + z\dot{\theta} \\ \ddot{u}^* &= \ddot{u} - z\ddot{\psi} \\ \ddot{v}^* &= \ddot{v} - z\dot{\psi}^2 \\ \ddot{w}^* &= \ddot{w} + z\ddot{\theta} - z\dot{\theta}^2. \end{aligned} \tag{5.6}$$

Assuming small displacements, the second order centripetal terms are neglected and equations (5.5) to (5.6) relating the displacements, velocities and accelerations in the two frames can be written as

$$\begin{aligned} \mathbf{u}^* &= \mathbf{T}\mathbf{u} \\ \dot{\mathbf{u}}^* &= \mathbf{T}\dot{\mathbf{u}} \\ \ddot{\mathbf{u}}^* &= \mathbf{T}\ddot{\mathbf{u}} \end{aligned} \tag{5.7}$$

where $\mathbf{T}$ is the transformation matrix

$$\mathbf{T} = \begin{bmatrix} 1 & 0 & 0 & 0 & z & 0 \\ 0 & 1 & 0 & -z & 0 & 0 \\ 0 & 0 & 1 & 0 & 0 & 0 \\ 0 & 0 & 0 & 1 & 0 & 0 \\ 0 & 0 & 0 & 0 & 1 & 0 \\ 0 & 0 & 0 & 0 & 0 & 1 \end{bmatrix}. \tag{5.8}$$

Similar to shifting displacements and rotations, equivalent forces and moments can be determined between reference frames. Consider the loads $\mathbf{f} = \{F_x, F_y, F_z, M_x, M_y, M_z\}^{\mathrm{T}}$ centered at the origin of frame x-y-z and loads $\mathbf{f}^* = \{F_x^*, F_y^*, F_z^*, M_x^*, M_y^*, M_z^*\}^{\mathrm{T}}$ centred at the origin of frame x^*-y^*-z^*, as depicted in Figure 5.4. Moments are independent of the location of the coordinate frame since x^*-y^*-z^* consists of only a translation of x-y-z. Forces acting in one reference frame can be converted to equivalent forces and moments in the translated reference frame if

$$\begin{aligned} F_x &= F_x^* \\ F_y &= F_y^* \\ F_z &= F_z^* \\ M_x &= M_x^* - F_y^* z \\ M_y &= M_y^* + F_x^* z \\ M_z^* &= M_z. \end{aligned} \tag{5.9}$$

Rearranging equations (5.9) in a matrix form gives

$$\mathbf{f} = \mathbf{T}^{\mathrm{T}} \mathbf{f}^*. \tag{5.10}$$

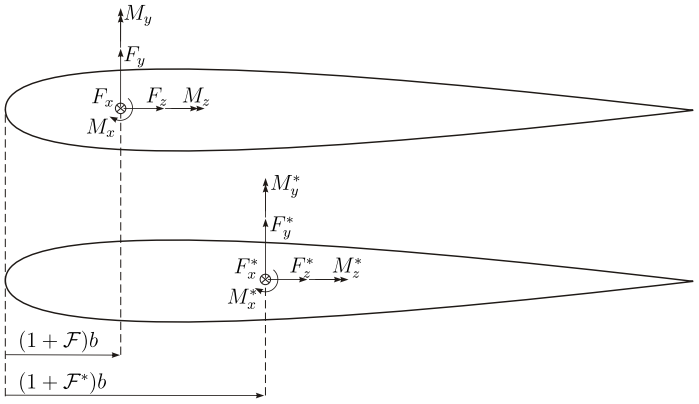

Fig. 5.4 Equivalent forces and moments with a coordinate system shift.

The transformation matrix $\mathbf{T}$ can be used to shift a mass, damping or stiffness matrix between reference frames. For example, assuming that the cross-sectional constitutive law is known in terms of the starred reference frame as $\mathbf{f}^* = \mathbf{K}^*\mathbf{u}^*$, the transformation to the shifted coordinate system follows from

$$\begin{aligned}\mathbf{f} &= \mathbf{T}^{\mathrm{T}}\mathbf{f}^* \\ &= \mathbf{T}^{\mathrm{T}}\mathbf{K}^*\mathbf{u}^* \\ &= \mathbf{T}^{\mathrm{T}}\mathbf{K}^*\mathbf{T}\mathbf{u}.\end{aligned} \tag{5.11}$$

Therefore, an equivalent stiffness matrix (or mass, or damping matrix, as the above equations still hold) for a shift in the coordinate system can be written as

$$\mathbf{K} = \mathbf{T}^{\mathrm{T}}\mathbf{K}^*\mathbf{T}. \tag{5.12}$$

Note that the same overall result can be obtained using a kinetic and potential energy method, as demonstrated by Chen et al. [24].

5.3 Structural Streamlined Cable Model

The inertia and elasticity of the streamlined cable is modelled using classic mass and stiffness finite-element matrices altered to account for the eccentricity of the structural centres. The applied tension contributes geometric stiffening to the structure, included as an additional stiffness matrix.

To derive the elemental mass and stiffness matrices, the classic volume element mass and stiffness matrices are converted to a cross-sectional form. The classic volume element mass and stiffness matrices, as described by Cook [26], are given by the volume integrals

$$\begin{aligned}\overline{\mathbf{M}}_{\mathrm{e}} &= \int_{V_{\mathrm{e}}} \rho(y,z)\mathbf{N}^{\mathrm{T}}\mathbf{N}\mathrm{d}V \\ \overline{\mathbf{K}}_{\mathrm{e}} &= \int_{V_{\mathrm{e}}} \mathbf{B}^{\mathrm{T}}\mathbf{E}\mathbf{B}\mathrm{d}V\end{aligned} \tag{5.13}$$

where $\mathbf{N}$, $\mathbf{B}$ and $\mathbf{E}$ are the shape function, strain-displacement and material stiffness matrices respectively. The density ρ is a function of the cross-section position since the streamlined cable may be composite in construction. Assuming that the streamlined cable has a constant cross-section over its length, the volume integral can be simplified to a length integral. The length integral is a function of a cross-sectional mass or stiffness matrix denoted as $\mathbf{M}_{\mathrm{a}}$ and

$\mathbf{K}_\mathrm{a}$ respectively. Following formulations similar to Blasques et al. [16] and Svendsen [121], the integral equations (5.13) become

$$\begin{aligned}\overline{\mathbf{M}}_\mathrm{e} &= \int_\ell \mathbf{N}^\mathrm{T}\mathbf{M}_\mathrm{a}\mathbf{N}\mathrm{d}x \\ \overline{\mathbf{K}}_\mathrm{e} &= \int_\ell \mathbf{B}^\mathrm{T}\mathbf{K}_\mathrm{a}\mathbf{B}\mathrm{d}x.\end{aligned} \tag{5.14}$$

For cross-sections with complicated geometry and anisotropic material properties, the cross-sectional matrices must be determined numerically. Examples of existing computational cross-sectional analysis software includes VABS (Variational Asymptotic Beam Sectional Analysis) by Yu et al. [139] or BECAS (Beam Cross-section Analysis Software) by Blasques et al. [16]. If the cross-section is highly coupled its cross-sectional matrices may be fully populated.

In the current model, a simplified approach is used to obtain the cross-sectional matrices. Though the simplified approach does not account for all the possible coupling, it offers a direct means to explore how certain cross-sectional properties affect the dynamic and stability behaviour of the streamlined cable model. In future work, if the model is used to analyse a specific streamlined cable design, the simplified cross-sectional matrices can be directly replaced by ones computed numerically using software such as VABS or BECAS.

The simplified cross-sectional approach uses the same assumption as the two-degree-of-freedom and continuous models. The streamlined cross-section is assumed to have non-concentric aerodynamic, mass, tension and shear centres. Figure 5.5 (a) shows the position of the centres, taken with respect to the leading edge of the streamlined cable. Figure 5.5 (b) defines the position of the centres with respect to an element reference frame *x*-*y*-*z* with dimensionless position $\mathcal{F}$. The values of z_q, z_r, z_p and z_s are related to the leading edge reference by equations (5.15). This definition is consistent with the transformation matrix derivation, where $\mathcal{F}^*$ is now replaced by the dimensionless position of one of the four centres (e.g. r, p, s). With this simplified cross-sectional model and the general expression (5.14) for the mass and stiffness matrix of a constant cross-section element, the streamlined beam mass and stiffness element matrices can be determined.

$$\begin{aligned}z_\mathrm{q} &= (1/2+\mathcal{F})\,b \\ z_\mathrm{r} &= (r-\mathcal{F})\,b \\ z_\mathrm{p} &= (p-\mathcal{F})\,b \\ z_\mathrm{s} &= (s-\mathcal{F})\,b\end{aligned} \tag{5.15}$$

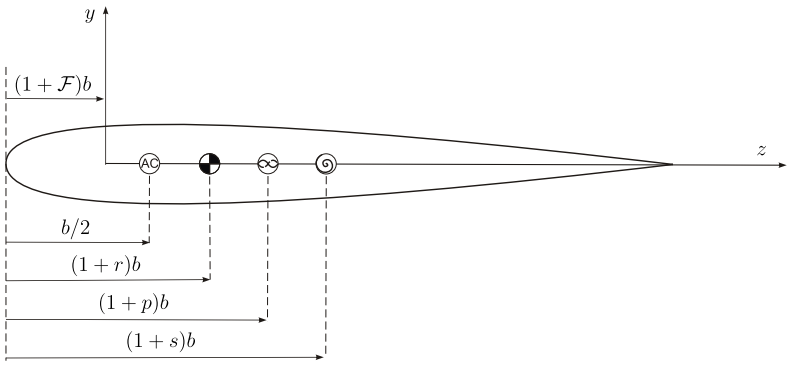

(a) Position with respect to leading edge.

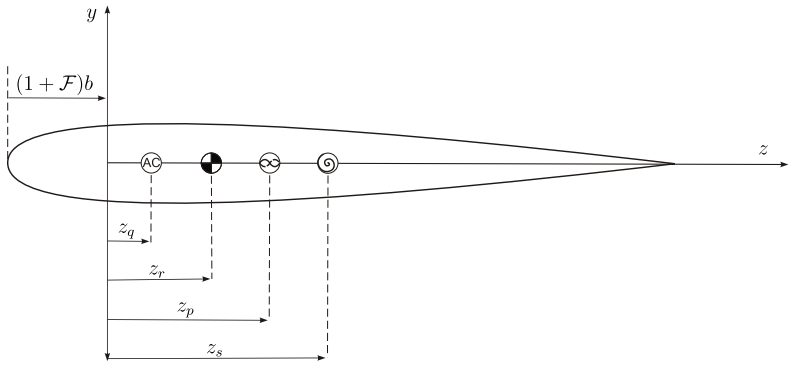

(b) Position with respect to reference frame.

Fig. 5.5 Cross-sectional reference frame.

5.3.1 Element Mass Matrix

To obtain the element mass matrix, the cross-sectional mass matrix $\mathbf{M}_\mathrm{a}$ and the shape function matrix $\mathbf{N}$ must be defined. The matrix $\mathbf{M}_\mathrm{a}$ is easily obtained using a transformation matrix. Consider a reference frame x^*-y^*-z^* with its origin at the centre of mass. The cross-sectional mass matrix $\mathbf{M}_\mathrm{a}^*$ is then a diagonal matrix with the vector $\{m,m,m,I_{xx},I_{yy},I_{zz}\}$ forming the main diagonal, where m is the mass per unit length and I_{xx}, I_{yy} and I_{zz} the mass moments of inertia per unit length. The cross-sectional mass matrix $\mathbf{M}_\mathrm{a}^*$ is transformed to the frame x-y-z by

$$\mathbf{M}_\mathrm{a} = \mathbf{T}^\mathrm{T}\mathbf{M}_\mathrm{a}^*\mathbf{T} \tag{5.16}$$

where $\mathbf{T}$ is given by (5.8) with $z = z_\mathrm{r}$ from (5.15). Note that the shifted cross-sectional mass matrix gives the same result as applying the parallel axis theorem to the individual mass moment of inertia terms.

The shape function matrix **N** follows from Cook's derivation for a plane frame element [26]. The shape function matrix is taken as a combination of C^0 (continuity in the displacement field but not its derivatives) and C^1 (continuity in the displacement field and its first derivative) functions. The C^0 function is defined as

$$\begin{aligned} N_0 &= \left\{ N_{01}, \quad N_{02} \right\} \\ &= \left\{ \tfrac{\ell - x}{\ell}, \quad \tfrac{x}{\ell} \right\} \end{aligned} \tag{5.17}$$

and the C^1 function as

$$\begin{aligned} N_1 &= \left\{ N_{11}, \quad N_{12}, \quad N_{13}, \quad N_{14} \right\} \\ &= \left\{ \tfrac{2x^3}{\ell^3} - \tfrac{3x^2}{\ell^2} + 1, \quad x - \tfrac{2x^2}{\ell} + \tfrac{x^3}{\ell^2}, \quad \tfrac{3x^2}{\ell^2} - \tfrac{2x^3}{\ell^3}, \quad \tfrac{x^3}{\ell^2} - \tfrac{x^2}{\ell} \right\}. \end{aligned} \tag{5.18}$$

The u and θ displacement fields – associated with the longitudinal and torsional deformation respectively – are taken as C^0. The v and w displacement fields – associated with shear deflection – are taken as C^1. As the cable is relatively long (i.e. the cross-sectional dimensions are small compared to the overall length), it is modelled as an Euler-Bernoulli beam. The rotations ϕ and ψ are taken as w' and $-v'$ respectively, where the prime denotes a derivative with respect to x, and the rotary inertia I_{yy} and I_{zz} are neglected. Following from the Euler-Bernoulli assumption, the shape function describing the ϕ and ψ rotations is

$$\begin{aligned} N_1' &= \left\{ N_{11}', \quad N_{12}', \quad N_{13}', \quad N_{14}' \right\} \\ &= \left\{ \tfrac{6x^2}{\ell^3} - \tfrac{6x}{\ell^2}, \quad 1 - \tfrac{4x}{\ell} + \tfrac{3x^2}{\ell^2}, \quad \tfrac{6x}{\ell^2} - \tfrac{6x^2}{\ell^3}, \quad \tfrac{3x^2}{\ell^2} - \tfrac{2x}{\ell} \right\}. \end{aligned} \tag{5.19}$$

Combining the shape functions for the displacement fields u, v, w, θ, ϕ and ψ forms the shape function matrix

$$\mathbf{N} = \begin{bmatrix} N_{01} & 0 & 0 & 0 & 0 & 0 & N_{02} & 0 & 0 & 0 & 0 & 0 \\ 0 & N_{11} & 0 & 0 & 0 & N_{12} & 0 & N_{13} & 0 & 0 & 0 & N_{14} \\ 0 & 0 & N_{11} & 0 & N_{12} & 0 & 0 & 0 & N_{13} & 0 & N_{14} & 0 \\ N_{01} & 0 & 0 & 0 & 0 & 0 & N_{02} & 0 & 0 & 0 & 0 & 0 \\ 0 & N_{11}' & 0 & 0 & 0 & N_{12}' & 0 & N_{13}' & 0 & 0 & 0 & N_{14}' \\ 0 & 0 & -N_{11}' & 0 & -N_{12}' & 0 & 0 & 0 & -N_{13}' & 0 & -N_{14}' & 0 \end{bmatrix}. \tag{5.20}$$

Although the Euler-Bernoulli beam assumption has simplified the derivation, as discussed by Hodges and Yu [65], it limits the location of the reference frame to the shear centre. Taking the reference frame to be located at the shear centre, $\mathcal{F} = s$ and $z_{\mathrm{r}} = (r - s)b$.

Then, substituting $\mathbf{M}_\mathrm{a}$ and $\mathbf{N}$ – (5.16) and (5.20) respectively – into (5.14) and integrating gives the streamlined-beam element mass-stiffness matrix

$$\overline{\mathbf{M}}_\mathrm{e} = \overline{\mathbf{M}}_\mathrm{classic} + \overline{\mathbf{M}}_\mathrm{shifted} \tag{5.21}$$

where

$$\overline{\mathbf{M}}_\mathrm{classic} = m\ell \begin{bmatrix} \frac{1}{3} & 0 & 0 & 0 & 0 & 0 & \frac{1}{6} & 0 & 0 & 0 & 0 & 0 \\ & \frac{13}{35} & 0 & 0 & 0 & \frac{11\ell}{210} & 0 & \frac{9}{70} & 0 & 0 & 0 & \frac{-13\ell}{420} \\ & & \frac{13}{35} & 0 & \frac{-11\ell}{210} & 0 & 0 & 0 & \frac{9}{70} & 0 & \frac{13\ell}{420} & 0 \\ & & & \frac{I_g}{3m} & 0 & 0 & 0 & 0 & 0 & \frac{I_g}{6m} & 0 & 0 \\ & & & & \frac{\ell^2}{105} & 0 & 0 & 0 & \frac{-13\ell}{420} & 0 & \frac{-\ell^2}{140} & 0 \\ & & & & & \frac{\ell^2}{105} & 0 & \frac{13\ell}{420} & 0 & 0 & 0 & \frac{-\ell^2}{140} \\ & & & & & & \frac{1}{3} & 0 & 0 & 0 & 0 & 0 \\ & & & & & & & \frac{13}{35} & 0 & 0 & 0 & \frac{-11\ell}{210} \\ & & & & \text{Sym.} & & & & \frac{13}{35} & 0 & \frac{11\ell}{210} & 0 \\ & & & & & & & & & \frac{I_g}{3m} & 0 & 0 \\ & & & & & & & & & & \frac{\ell^2}{105} & 0 \\ & & & & & & & & & & & \frac{\ell^2}{105} \end{bmatrix} \tag{5.22}$$

and

$$\overline{\mathbf{M}}_\mathrm{shifted} = mz_\mathrm{r} \begin{bmatrix} 0 & 0 & \frac{-1}{2} & 0 & \frac{-\ell}{12} & 0 & 0 & 0 & \frac{1}{2} & 0 & \frac{\ell}{12} & 0 \\ & 0 & 0 & \frac{-7\ell}{20} & 0 & 0 & 0 & 0 & 0 & \frac{-3\ell}{20} & 0 & 0 \\ & & \frac{6z_\mathrm{r}}{5\ell} & 0 & \frac{-z_\mathrm{r}}{10} & 0 & \frac{-1}{2} & 0 & \frac{-6z_\mathrm{r}}{5\ell} & 0 & \frac{-z_\mathrm{r}}{10} & 0 \\ & & & \frac{z_\mathrm{r}\ell}{3} & 0 & \frac{-\ell^2}{20} & 0 & \frac{-3\ell}{20} & 0 & \frac{z_\mathrm{r}\ell}{6} & 0 & \frac{\ell^2}{30} \\ & & & & \frac{2z_\mathrm{r}\ell}{15} & 0 & \frac{\ell}{12} & 0 & \frac{z_\mathrm{r}}{10} & 0 & \frac{-z_\mathrm{r}\ell}{30} & 0 \\ & & & & & 0 & 0 & 0 & 0 & \frac{-\ell^2}{30} & 0 & 0 \\ & & & & & & 0 & 0 & \frac{1}{2} & 0 & \frac{-\ell}{12} & 0 \\ & & & & & & & 0 & 0 & \frac{-7\ell}{20} & 0 & 0 \\ & & & & \text{Sym.} & & & & \frac{6z_\mathrm{r}}{5\ell} & 0 & \frac{z_\mathrm{r}}{10} & 0 \\ & & & & & & & & & \frac{z_\mathrm{r}\ell}{3} & 0 & \frac{\ell^2}{20} \\ & & & & & & & & & & \frac{2z_\mathrm{r}\ell}{15} & 0 \\ & & & & & & & & & & & 0 \end{bmatrix}. \tag{5.23}$$

The mass matrix is separated into a "classic" and "shifted" component. This separation shows that if the centre of mass is not offset and $z_\mathrm{r} = 0$, the mass matrix reduces to the "classic" form found in finite element texts such as Przemieniecki [104] or Cook [26]. Showing the "shifted" components as a separate matrix makes it easier to see how terms are affected by an offset centre of mass.

5.3.2 Element Elastic Stiffness Matrix

The derivation of the elastic stiffness matrix follows a similar formulation to the mass matrix. To obtain the element stiffness matrix, the cross-sectional stiffness matrix $\mathbf{K}_\mathrm{a}$ and the strain-displacement matrix $\mathbf{B}$ must be defined. Hodges [62] and Svendsen [121] derive $\mathbf{K}_\mathrm{a}$ for a prismatic beam made of isotropic materials with known tension and shear centre posi-

tions. Following the work by Svendsen [121], $\mathbf{K}_\mathrm{a}$ is derived for the simplified streamlined beam cross-section.

Consider a streamlined cross-section with two reference frames which take advantage of the decoupled definitions of the centres. One is located at the centre of tension and one at the shear centre. The reference frames are assumed to be parallel with both the bending and shear principle axes. Assume a tension force and two uncoupled moments act at the tension centre and two shear forces and a torque act at the shear centre. The corresponding displacements for the given forces and moments are: longitudinal extension and bending rotations taken at the tension centre and, shear translations and a torsional rotation taken at the shear centre.

This somewhat unconventional definition, with displacement and forces taken with respect to two reference frames, reduces the cross-sectional stiffness matrix to a diagonal matrix defined here as $\mathbf{K}_\mathrm{a}^*$. The main diagonal of $\mathbf{K}_\mathrm{a}^*$ is the vector $\{EA, GK_y, GK_z, GJ, EI_x, EI_y\}^\mathrm{T}$, which is comprised of the classic beam theory axial, shear, torsion and bending stiffnesses. Relating this definition to the streamlined cable cross-section of Figure 5.5, the position of the reference frames at the tension and shear centres are defined by z_p and z_s respectively. Following the same derivation as the general transformation matrix, the defined coordinates give the cross-sectional stiffness matrix at the reference frame *x*-*y*-*z* as

$$\mathbf{K}_\mathrm{a} = \mathbf{T}^\mathrm{T}\mathbf{K}_\mathrm{a}^*\mathbf{T} \tag{5.24}$$

where the transformation matrix is given by (5.8) with $z = z_\mathrm{p}$ in the first row and $z = z_\mathrm{s}$ in the second row of the matrix. This results in the same cross-sectional stiffness matrix given by Svendsen [121] and Hodges [62].

The strain-displacement matrix **B** must also be defined. Taking the result from Blasques [16], the strain-displacement matrix for a constant cross-section beam element can be written as

$$\mathbf{B} = (\mathbf{R} + \frac{\partial}{\partial x})\mathbf{N} \tag{5.25}$$

where **R** is

$$\mathbf{R} = \begin{bmatrix} 0 & 0 & 0 & 0 & 0 & 0 \\ 0 & 0 & 0 & 0 & 0 & -1 \\ 0 & 0 & 0 & 0 & 1 & 0 \\ 0 & 0 & 0 & 0 & 0 & 0 \\ 0 & 0 & 0 & 0 & 0 & 0 \\ 0 & 0 & 0 & 0 & 0 & 0 \end{bmatrix}. \tag{5.26}$$

Substituting $\mathbf{K}_\mathrm{a}$ and **B** into (5.14) gives a general form for the element stiffness matrix $\overline{\mathbf{K}}_\mathrm{e}$. In the current model, the beam is modelled according to Euler-Bernoulli theory and

the shear stiffness terms GK_y and GK_z are neglected. Following the mass matrix derivation, the reference frame is taken at the shear centre making $\mathcal{F} = s$ and, therefore, $z_\mathrm{s} = 0$ and $z_\mathrm{p} = (p-s)b$. Integrating (5.14) gives $\overline{\mathbf{K}}_\mathrm{e}$ as equations (5.27) to (5.29). Separating $\overline{\mathbf{K}}_\mathrm{e}$ into a "classic" and "shifted" matrix shows that the "classic" matrix is equal to the results given in texts such as Shabana [112], Cook [26] and Przemieniecki [104]. The "shifted" matrix is a zero matrix when $z_\mathrm{p} = 0$, meaning the centre of tension is aligned with the shear centre.

$$\overline{\mathbf{K}}_\mathrm{e} = \overline{\mathbf{K}}_\mathrm{classic} + \overline{\mathbf{K}}_\mathrm{shifted} \tag{5.27}$$

where

$$\overline{\mathbf{K}}_\mathrm{classic} = \frac{1}{\ell}\begin{bmatrix}
EA & 0 & 0 & 0 & 0 & 0 & -EA & 0 & 0 & 0 & 0 & 0 \\
 & \frac{12EI_z}{\ell^2} & 0 & 0 & 0 & \frac{6EI_z}{\ell} & 0 & \frac{-12EI_z}{\ell^2} & 0 & 0 & 0 & \frac{6EI_z}{\ell} \\
 & & \frac{12EI_y}{\ell^2} & 0 & \frac{-6EI_y}{\ell} & 0 & 0 & 0 & \frac{-12EI_y}{\ell^2} & 0 & \frac{-6EI_y}{\ell} & 0 \\
 & & & GJ & 0 & 0 & 0 & 0 & 0 & -GJ & 0 & 0 \\
 & & & & 4EI_y & 0 & 0 & 0 & \frac{6EI_y}{\ell} & 0 & 2EI_y & 0 \\
 & & & & & 4EI_z & 0 & \frac{-6EI_z}{\ell} & 0 & 0 & 0 & 2EI_z \\
 & & & & & & EA & 0 & 0 & 0 & 0 & 0 \\
 & & & & & & & \frac{12EI_z}{\ell^2} & 0 & 0 & 0 & \frac{-6EI_z}{\ell} \\
 & & & \text{Sym.} & & & & & \frac{12EI_y}{\ell^2} & 0 & \frac{6EI_y}{\ell} & 0 \\
 & & & & & & & & & GJ & 0 & 0 \\
 & & & & & & & & & & 4EI_y & 0 \\
 & & & & & & & & & & & 4EI_z
\end{bmatrix} \tag{5.28}$$

and

$$\overline{\mathbf{K}}_\mathrm{shifted} = \frac{EAz_\mathrm{p}}{\ell}\begin{bmatrix}
0 & 0 & 0 & 0 & -1 & 0 & 0 & 0 & 0 & 0 & 1 & 0 \\
 & 0 & 0 & 0 & 0 & 0 & 0 & 0 & 0 & 0 & 0 & 0 \\
 & & \frac{12z_\mathrm{p}}{\ell^2} & 0 & \frac{-6z_\mathrm{p}}{\ell} & 0 & 0 & 0 & \frac{-12z_\mathrm{p}}{\ell^2} & 0 & \frac{-6z_\mathrm{p}}{\ell} & 0 \\
 & & & 0 & 0 & 0 & 0 & 0 & 0 & 0 & 0 & 0 \\
 & & & & 4z_\mathrm{p} & 0 & 1 & 0 & \frac{6z_\mathrm{p}}{\ell} & 0 & 2z_\mathrm{p} & 0 \\
 & & & & & 0 & 0 & 0 & 0 & 0 & 0 & 0 \\
 & & & & & & 0 & 0 & 0 & 0 & -1 & 0 \\
 & & & & & & & 0 & 0 & 0 & 0 & 0 \\
 & & & \text{Sym.} & & & & & \frac{12z_\mathrm{p}}{\ell^2} & 0 & \frac{6z_\mathrm{p}}{\ell} & 0 \\
 & & & & & & & & & 0 & 0 & 0 \\
 & & & & & & & & & & 4z_\mathrm{p} & 0 \\
 & & & & & & & & & & & 0
\end{bmatrix}. \tag{5.29}$$

The matrix $\overline{\mathbf{K}}_\mathrm{e}$ gives the element stiffness due to the material elasticity. The stiffness due to the applied external tension is included in the discrete model through a geometric stiffness matrix.

5.3.3 Element Geometric Stiffness Matrix

This stiffness which arises due to external loading is referred to as stress-stiffening or geometric stiffening. As the name implies, the additional stiffness is dependent on the geometry, initial stress and deformation of the structure.

The geometric stiffness matrix for the streamlined cable model follows Svendsen's [121] derivation for the geometric stiffening of a wind turbine blade. Svendsen derives the geometric stiffness matrix by substituting the beam displacement field into Washizu's [131] linearised equation for the potential energy of a volume element with an initial stress state. Svendsen's derivation is repeated here for the streamlined cable element subject to a tension force P. In the streamlined cable model, only a longitudinal initial stress σ_{xx} due to tension is considered. The potential energy, PE, of the volume element is

$$PE = \frac{1}{2}\int_{V_e} \sigma_{xx}\left[\left(\frac{\partial \Delta z}{\partial x}\right)^2 + \left(\frac{\partial \Delta y}{\partial x}\right)^2\right] \mathrm{d}V \tag{5.30}$$

where Δy and Δz are the transverse displacement field components. Following the relations described in section 5.2, the general transverse displacement of the cross-section can be written as

$$\begin{aligned} \Delta y &= v - z\theta \\ \Delta z &= w + y\theta. \end{aligned} \tag{5.31}$$

The initial force and moments acting on the cross-section are related to the initial stress by

$$\begin{aligned} F_x^o &= \int_A \sigma_{xx}\mathrm{d}A \\ M_y^o &= \int_A \sigma_{xx} z \mathrm{d}A \\ -M_z^o &= \int_A \sigma_{xx} y \mathrm{d}A. \end{aligned} \tag{5.32}$$

Substituting in the displacement field equations (5.31) into the potential energy expression (5.30) and integrating over the area of the cross-section gives

$$PE = \frac{1}{2}\int_\ell \left(F_x^o w'w' - 2w'\theta' M_z^o + F_x^o v'v' - 2v'\theta' M_y^o + T^o \theta'\theta'\right) \mathrm{d}x \tag{5.33}$$

where the prime indicates a derivative taken with respect to x and

$$T^o = \int_A \sigma_{xx}(y^2 + z^2)\mathrm{d}A. \tag{5.34}$$

The stress integral T^o is analogous to the material torsional stiffness. Equation (5.33) can be written in the matrix form

$$PE = \frac{1}{2}\int_\ell (\mathbf{u}^{\mathrm{T}}, \mathbf{u}'^{\mathrm{T}}) \left[\begin{array}{c:c} \mathbf{0_6} & \mathbf{0_6} \\ \hdashline \mathbf{0_6} & \mathbf{G} \end{array}\right] \left\{\begin{array}{c} \mathbf{u} \\ \mathbf{u}' \end{array}\right\}, \tag{5.35}$$

where

$$\mathbf{G} = \begin{bmatrix} 0 & 0 & 0 & 0 & 0 & 0 \\ & F_x^o & 0 & -M_y^o & 0 & 0 \\ & & F_x^o & -M_z^o & 0 & 0 \\ & & & T^o & 0 & 0 \\ & \text{Sym.} & & & 0 & 0 \\ & & & & & 0 \end{bmatrix}. \tag{5.36}$$

Equation (5.4) gives the displacement field $\mathbf{u}$ in terms of the shape function matrix and the nodal displacements. Thus, the vector of displacements in equation (5.35) is

$$\left\{\begin{array}{c} \mathbf{u} \\ \mathbf{u}' \end{array}\right\} = \left\{\begin{array}{c} \mathbf{N} \\ \mathbf{N}' \end{array}\right\} \bar{\mathbf{d}}. \tag{5.37}$$

Substituting (5.37) into the the potential energy expression (5.35), the expression is reduced to

$$PE = \frac{1}{2}\bar{\mathbf{d}}^{\mathrm{T}} \overline{\mathbf{K}}_{\mathrm{g}} \bar{\mathbf{d}}, \tag{5.38}$$

where $\overline{\mathbf{K}}_{\mathrm{g}}$ is geometric stiffness matrix

$$\overline{\mathbf{K}}_{\mathrm{g}} = \int_\ell \left[\mathbf{N}^{\mathrm{T}}, \mathbf{N}'^{\mathrm{T}}\right] \left[\begin{array}{c:c} \mathbf{0_6} & \mathbf{0_6} \\ \hdashline \mathbf{0_6} & \mathbf{G} \end{array}\right] \left[\begin{array}{c} \mathbf{N} \\ \mathbf{N}' \end{array}\right] \mathrm{d}x. \tag{5.39}$$

In order to integrate the expression and obtain the geometric stiffness matrix, the initial axial force F_x^o, initial moments M_y^o and M_z^o and the stress integral T^o must be defined. For the simplified streamlined cable cross-section, these terms are given as functions of the applied tension P and the position of the centre of tension z_{p}.

Taking the shear centre as the origin of the reference frame and assuming the tension force P acts through the tension centre, the initial forces and moments can be taken as $F_x^o = P$, $M_y^o = Pz_{\mathrm{p}}$ and $M_z^o = 0$. For an inhomogeneous cross-section with complicated geometry the stress-integral T^o typically needs to be evaluated numerically. However, the term can be approximated if the stresses are assumed to be constant over the cross-section

and given by $\sigma_{xx} = P/A$, where A is the cross-sectional area. The stress integral is then

$$\begin{aligned} T^o &= \sigma_{xx}(I_{yy} + I_{zz}) \\ &= \frac{P}{A} I_{xx}. \end{aligned} \tag{5.40}$$

Though an approximation, the term captures the general behaviour of increasing the torsional stiffness as tension increases. The approximation also provides a simple means to compare the stress-stiffening torsion term T^o to the analogous material torsional stiffness. The term I_{xx} compares to the torsion constant J (for a homogeneous circular cross-section they are equal). The stress due to tension σ_{xx} compares to the material shear stiffness G. This comparison provides an indication of the significance of the torsional stress stiffening term T^o relative to the material torsional stiffness GJ.

Integrating equation (5.39) gives the element geometric stiffness matrix as

$$\overline{\mathbf{K}}_{\mathrm{g}} = \frac{P}{30\ell} \begin{bmatrix} 0 & 0 & 0 & 0 & 0 & 0 & 0 & 0 & 0 & 0 & 0 & 0 \\ & 36 & 0 & -30z_{\mathrm{p}} & 0 & 3\ell & 0 & -36 & 0 & 30z_{\mathrm{p}} & 0 & 3\ell \\ & & 36 & 0 & -3\ell & 0 & 0 & 0 & -36 & 0 & -3\ell & 0 \\ & & & \frac{30I_x}{A} & 0 & 0 & 0 & 30z_{\mathrm{p}} & 0 & -\frac{30I_x}{A} & 0 & 0 \\ & & & & 4\ell^2 & 0 & 0 & 0 & 3\ell & 0 & -\ell^2 & 0 \\ & & & & & 4\ell^2 & 0 & -3\ell & 0 & 0 & 0 & -\ell^2 \\ & & & & & & 0 & 0 & 0 & 0 & 0 & 0 \\ & & & & & & & 36 & 0 & -30z_{\mathrm{p}} & 0 & -3\ell \\ & & & \text{Sym.} & & & & & 36 & 0 & 3\ell & 0 \\ & & & & & & & & & \frac{30I_x}{A} & 0 & 0 \\ & & & & & & & & & & 4\ell^2 & 0 \\ & & & & & & & & & & & 4\ell^2 \end{bmatrix}. \tag{5.41}$$

The resulting matrix $\overline{\mathbf{K}}_{\mathrm{g}}$ is consistent with classic geometric stiffening results. If there is no offset between the elastic axis and shear centre ($z_{\mathrm{p}} = 0$), the geometric stiffness matrix reduces to the case for a symmetric, homogeneous beam, as given in finite-element texts such as Cook [26]. Having derived the element mass and stiffness matrices, they are assembled into global mass and stiffness matrices to model the overall streamlined cable system.

5.3.4 Structural Model Assembly

The global element mass and stiffness matrices are obtained following conventional finite-element methods. The element mass matrix $\overline{\mathbf{M}}$ is equal to the mass matrix $\overline{\mathbf{M}}_{\mathrm{e}}$ from equation (5.21). The overall stiffness matrix $\overline{\mathbf{K}}$ is the sum of the elastic and geometric stiffness

matrices given by equations (5.27) and (5.41) respectively.

$$\begin{aligned} \overline{\mathbf{M}} &= \overline{\mathbf{M}}_{\mathrm{e}} \\ \overline{\mathbf{K}} &= \overline{\mathbf{K}}_{\mathrm{e}} + \overline{\mathbf{K}}_{\mathrm{g}} \end{aligned} \tag{5.42}$$

The global mass and stiffness matrices are straightforward to assemble as the elements of the streamlined cable sequentially attached, one after another. The assembly is easily written in matrix form by dividing the element matrix in to four sub-matrices. The superscript of the sub-matrix indicates the element and the subscripts indicate the bounding nodes. For example, the stiffness matrix of the m^{th} element, bounded by nodes j and k is

$$\overline{\mathbf{K}}^m = \begin{bmatrix} \mathbf{K}^m_{jj} & \mathbf{K}^m_{jk} \\ \mathbf{K}^m_{kj} & \mathbf{K}^m_{kk} \end{bmatrix}. \tag{5.43}$$

The global assembly of an n element streamlined cable is then

$$\mathbf{K}_{\mathrm{c}} = \begin{bmatrix} \mathbf{K}^1_{11} & \mathbf{K}^1_{21} & \mathbf{0} & \cdots & \mathbf{0} \\ \mathbf{K}^1_{21} & \mathbf{K}^1_{22}+\mathbf{K}^2_{22} & \mathbf{K}^2_{23} & \ddots & \vdots \\ \mathbf{0} & \mathbf{K}^2_{32} & \mathbf{K}^2_{33}+\mathbf{K}^3_{33} & \ddots & \\ & \ddots & \ddots & \ddots & \mathbf{0} \\ \vdots & & \ddots & \ddots & \mathbf{K}^{n-1}_{nn}+\mathbf{K}^n_{nn} \quad \mathbf{K}^n_{nk} \\ \mathbf{0} & \cdots & \mathbf{0} & \mathbf{K}^n_{kn} & \mathbf{K}^n_{kk} \end{bmatrix}. \tag{5.44}$$

The global mass matrix follows the same convention to give $\mathbf{M}_{\mathrm{c}}$. The $\mathbf{M}_{\mathrm{c}}$ and $\mathbf{K}_{\mathrm{c}}$ matrices form the structural model of the streamlined cable. Having defined a structural streamlined cable model, an equivalent discrete model of the fluid dynamic effects is required.

5.4 Discrete Fluid Dynamic Model

The fluid-dynamic loading on the streamlined cable follows a similar formulation as the two-dimensional case described in section 3.2. To simplify the derivation of the fluid-dynamic loading, which accounts for fully-unsteady flow, the fluid effects are assumed to be lumped at the nodes. The position, velocity and acceleration of the node is used to calculate the corresponding lift and moment per unit span given by equations (3.4) and (3.5). The force and moment at the node are obtained by multiplying the result by an appropriate length scale $\ell_{\mathrm{f}j}$ (here taken as an element length at interior nodes and half an element length at the

end nodes). Figure 5.6 depicts how the fluid-dynamic forces are reduced to point forces and moments at the nodes. Using a finite-state theory to include fully unsteady effects, the lift and moment forces at a general node j are derived.

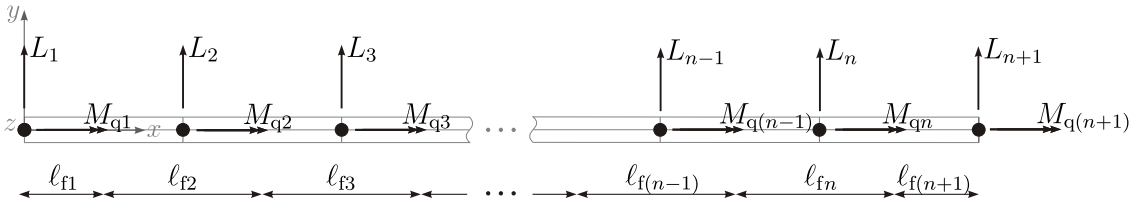

Fig. 5.6 Distributed lift and moment reduced to point force and moment at the nodes.

5.4.1 Unsteady Fluid-Dynamic Model

To be consistent with the structural streamlined cable model, the expressions for the fluid loading at node j are derived with respect to a reference frame located at the shear centre. The lift and moment per unit length are given by equations (3.4) and (3.5). These equations are written in terms of a coordinate system located at the shear centre with the force and moment acting at the aerodynamic centre (quarter chord). Writing this force and moment as the vector $\mathbf{f}_{qj} = \{0, L_j, 0, M_{qj}, 0, 0\}^T$, the force and moment can be transformed to an equivalent force and moment at the shear centre using the transformation matrix $\mathbf{T}$, given by equation (5.8), with $z = z_q = (1/2+s)b$. The vector of fluid-dynamic forces and moments, acting at node j, is given by (5.45), where $\mu = \rho\pi b^2$ and the $\mathbf{M}_{fj}$, $\mathbf{C}_{fj}$ and $\mathbf{K}_{fj}$ matrices for node j are defined by (5.46), (5.47) and (5.48) respectively.

$$\begin{aligned}\mathbf{f}_j &= \mu\ell_{fj}\mathbf{T}^T\mathbf{f}_{qj} \\ &= \mu\ell_{fj}\mathbf{T}^T\left(\mathbf{M}_{fj}\ddot{\mathbf{d}}_j + \mathbf{C}_{fj}\dot{\mathbf{d}}_j + \mathbf{K}_{fj}\mathbf{d}_j + \boldsymbol{\Upsilon}_j\upsilon_j\right)\end{aligned} \tag{5.45}$$

$$\mathbf{M}_{fj} = \begin{bmatrix} 0 & 0 & 0 & 0 & 0 & 0 \\ 0 & -1 & 0 & -bs & 0 & 0 \\ 0 & 0 & 0 & 0 & 0 & 0 \\ 0 & \frac{1}{2}b & 0 & -b^2\left(\frac{1}{8}-\frac{1}{2}s\right) & 0 & 0 \\ 0 & 0 & 0 & 0 & 0 & 0 \\ 0 & 0 & 0 & 0 & 0 & 0 \end{bmatrix} \tag{5.46}$$

$$\mathbf{C}_{fj} = \begin{bmatrix} 0 & 0 & 0 & 0 & 0 & 0 \\ 0 & -2\frac{U_j}{b} & 0 & 2U_j(1-s) & 0 & 0 \\ 0 & 0 & 0 & 0 & 0 & 0 \\ 0 & 0 & 0 & -bU_j & 0 & 0 \\ 0 & 0 & 0 & 0 & 0 & 0 \\ 0 & 0 & 0 & 0 & 0 & 0 \end{bmatrix} \tag{5.47}$$

$$\mathbf{K}_{\mathrm{f}j} = \begin{bmatrix} 0 & 0 & 0 & 0 & 0 & 0 \\ 0 & 0 & 0 & 2\frac{U_j}{b} & 0 & 0 \\ 0 & 0 & 0 & 0 & 0 & 0 \\ 0 & 0 & 0 & 0 & 0 & 0 \\ 0 & 0 & 0 & 0 & 0 & 0 \\ 0 & 0 & 0 & 0 & 0 & 0 \end{bmatrix} \tag{5.48}$$

The term $\boldsymbol{\Upsilon}_j \upsilon_j$ accounts for the induced flow velocity and is given by

$$\boldsymbol{\Upsilon}_j \upsilon_j = -2\frac{U_j}{b} \begin{Bmatrix} 0 & 1 & 0 & 0 & 0 & 0 \end{Bmatrix}^{\mathrm{T}} \upsilon_j. \tag{5.49}$$

The induced flow term υ_j is approximated using the finite-state method described in chapter 3. The method uses an N term power series approximation for υ_j, given by equation 3.11 in Chapter 3. In the discrete model, the finite-state power series approximation for the induced flow at node j is

$$\upsilon_j = \frac{1}{2}\sum_{n=1}^{N} b_n \upsilon_{nj} = \frac{1}{2} \begin{Bmatrix} b_1 \\ b_2 \\ \vdots \\ b_N \end{Bmatrix}^T \begin{Bmatrix} \upsilon_{1j} \\ \upsilon_{2j} \\ \vdots \\ \upsilon_{Nj} \end{Bmatrix} = \frac{1}{2}\mathbf{b}^T \boldsymbol{\upsilon}_j. \tag{5.50}$$

Substituting the power series approximation (5.50) into the induced flow velocity expression (5.49) gives

$$\boldsymbol{\Upsilon}_j \upsilon_j = -\frac{U_j}{b} \begin{Bmatrix} 0 & 1 & 0 & 0 & 0 & 0 \end{Bmatrix}^{\mathrm{T}} \mathbf{b}^{\mathrm{T}} \boldsymbol{\upsilon}_j. \tag{5.51}$$

The additional N equations necessary to define the induced-flow term $\boldsymbol{\upsilon}_j$ are given by Peters [103] finite-state equation, defined in Chapter 3 as equation (3.13). In the discrete model, the matrix equation is written with respect to the nodal velocities and accelerations as

$$\mathbf{A}_{\mathrm{n}j}\dot{\boldsymbol{\upsilon}}_j + \frac{U_j}{b}\boldsymbol{\upsilon}_j = \mathbf{M}_{\mathrm{i}j}\ddot{\mathbf{d}}_j + \mathbf{C}_{\mathrm{i}j}\dot{\mathbf{d}}_j \tag{5.52}$$

where

$$\mathbf{M}_{\mathrm{i}j} = \mathbf{c} \begin{Bmatrix} 0 & -1 & 0 & b(0.5-s) & 0 & 0 \end{Bmatrix} \tag{5.53}$$

and

$$\mathbf{C}_{\mathrm{i}j} = \mathbf{c} \begin{Bmatrix} 0 & 0 & 0 & U_j & 0 & 0 \end{Bmatrix}. \tag{5.54}$$

The matrix $\mathbf{A}_{\mathrm{n}j}$ and vectors $\mathbf{b}$ and $\mathbf{c}$ as defined by equations (3.16) to (3.19) in Chapter 3. This completes the definition of the fluid-dynamic forcing at the j^{th} node. The matrices

derived in this section can be assembled into global fluid loading matrices which model the fluid-dynamic forcing over the entire streamlined cable.

5.4.2 Fluid Dynamic Model Assembly

As the fluid-dynamic forces are assumed to act at the nodes, the global fluid-dynamic matrices for the streamlined cable are given by block diagonal matrices. For example, for an n element streamlined cable with $k = n+1$ nodes, the global fluid-dynamic mass matrix is

$$\mathbf{M}_{\mathrm{f}} = \begin{bmatrix} \mathbf{M}_{\mathrm{f}1} & 0 & \dots & 0 \\ 0 & \mathbf{M}_{\mathrm{f}2} & \dots & 0 \\ \vdots & \vdots & \ddots & \vdots \\ 0 & 0 & \dots & \mathbf{M}_{\mathrm{f}k} \end{bmatrix} \tag{5.55}$$

where the diagonal terms $\mathbf{M}_{\mathrm{f}j}$ are given by (5.46). Table 5.1 summarises the global matrices used to model the fluid loading. The first column gives the global matrices, the second the nodal matrix used as the block diagonal and the third the dimensions of the matrix blocks. The dimension of the global matrices will be $n+1$ times the size of the block matrix as there is one block for each node.

Table 5.1 The block matrices used to form the global fluid-dynamic matrices. N is the chosen number of finite states and 6 is the degrees-of-freedom at a node.

Global matrix	Blocks	Block size
$\mathbf{M}_{\mathrm{f}}$	$\mathbf{M}_{\mathrm{f}j}$	6×6
$\mathbf{C}_{\mathrm{f}}$	$\mathbf{C}_{\mathrm{f}j}$	6×6
$\mathbf{K}_{\mathrm{f}}$	$\mathbf{K}_{\mathrm{f}j}$	6×6
$\boldsymbol{\Upsilon}$	$\boldsymbol{\Upsilon}_j$	$6 \times N$
$\mathbf{M}_{\mathrm{i}}$	$\mathbf{M}_{\mathrm{i}j}$	$N \times 6$
$\mathbf{C}_{\mathrm{i}}$	$\mathbf{C}_{\mathrm{i}j}$	$N \times 6$
$\mathbf{A}_{\mathrm{n}}$	$\mathbf{A}_{\mathrm{n}j}$	$N \times N$
$\mathbf{U}$	$\frac{U_j}{b}\mathbf{I}$	$N \times N$

Similar to the vector of nodal displacements given as (5.3), a single induced-flow vector is formed as $\boldsymbol{\upsilon} = \{\boldsymbol{\upsilon}_1, \boldsymbol{\upsilon}_2, \dots, \boldsymbol{\upsilon}_{n+1}\}^{\mathrm{T}}$. Having the global structural and fluid-dynamic matrices, the equations of motion for the streamlined cable can be formed.

5.5 Equations of Motion

The global mass and stiffness matrices $\mathbf{M}_c$ and $\mathbf{K}_c$ – which model the inertia, elasticity and geometric stiffness of the streamlined cable – and the fluid-dynamic matrices defined in Table 5.1 are combined to form the streamlined cable equations of motion. The equations of motion can be written in a simple matrix form as

$$\mathbf{M}\ddot{\mathbf{d}} + \mathbf{C}\dot{\mathbf{d}} + \mathbf{K}\mathbf{d} - \boldsymbol{\Upsilon}\boldsymbol{\upsilon} = \mathbf{0} \tag{5.56}$$

where

$$\begin{aligned} \mathbf{M} &= \mathbf{M}_c - \mathbf{M}_f \\ \mathbf{C} &= -\mathbf{C}_f \\ \mathbf{K} &= \mathbf{K}_c - \mathbf{K}_f. \end{aligned} \tag{5.57}$$

The finite-state equation, given as (5.52) for a single node, becomes

$$\mathbf{A}_n\dot{\boldsymbol{\upsilon}} + \mathbf{U}\boldsymbol{\upsilon} = \mathbf{M}_i\ddot{\mathbf{d}} + \mathbf{C}_i\dot{\mathbf{d}}. \tag{5.58}$$

In exactly the same way as presented in Chapter 3, the second-order equation of motion can be reduced to first order using a state-space representation. Following the same procedure, the displacements and velocities (both structural and induced flow) are combined into the single vector

$$\mathbf{q} = \begin{Bmatrix} \mathbf{d} \\ \dot{\mathbf{d}} \\ \boldsymbol{\upsilon} \end{Bmatrix} \tag{5.59}$$

and its time derivative

$$\dot{\mathbf{q}} = \begin{Bmatrix} \dot{\mathbf{d}} \\ \ddot{\mathbf{d}} \\ \dot{\boldsymbol{\upsilon}} \end{Bmatrix}. \tag{5.60}$$

The equation of motion (5.56) and the finite-state representation (5.58) can be written in terms of the vector $\mathbf{q}$ as

$$\left[\begin{array}{c|c|c} \mathbf{C} & \mathbf{M} & \mathbf{0} \\ \hline \mathbf{I} & \mathbf{0} & \mathbf{0} \\ \hline \mathbf{0} & -\mathbf{M_i} & \mathbf{A_n} \end{array}\right]\dot{\mathbf{q}} + \left[\begin{array}{c|c|c} \mathbf{K} & \mathbf{0} & -\boldsymbol{\Upsilon} \\ \hline \mathbf{0} & -\mathbf{I} & \mathbf{0} \\ \hline \mathbf{0} & -\mathbf{C_i} & \mathbf{U} \end{array}\right]\mathbf{q} = \mathbf{0}. \tag{5.61}$$

The eigenvalue problem for the discrete system follows the same representation as the two-degree-of-freedom eigenvalue problem in Chapter 3. Writing equation (5.61) as

$$\mathbf{A}\dot{\mathbf{q}} + \mathbf{J}\mathbf{q} = \mathbf{0} \tag{5.62}$$

and assuming general solutions of the form

$$\mathbf{q} = \mathbf{Q}\mathrm{e}^{\lambda t} \tag{5.63}$$

gives the eigenvalue problem

$$\lambda\mathbf{Q} = -\mathbf{A}^{-1}\mathbf{J}\mathbf{Q}. \tag{5.64}$$

As discussed in Chapter 3, the state-space representation may be used in numerical time-domain simulations and the eigenvalue form is useful in studying the stability of streamlined cable.

5.6 Comparison of Continuous and Discrete Models

As an initial verification of the discrete model, it is compared to the continuous model developed in Chapter 4. The power flow and mode shape results obtained with the continuous model are obtained using the discrete model. To make an equivalent comparison to the continuous model which assumes quasi-steady flow, the induced-flow term in the discrete model is neglected. The boundaries of the discrete model are taken as pinned. The pinned condition at the boundary is taken as no translational displacement u, v and w, no rotational displacement θ and free rotational displacements ϕ and ψ.

Figure 5.7 compares the y and θ displacement of the continuous and discrete model, which shows excellent agreement. The discrete model converges to the continuous model result as the number of elements is increased. The difference in boundary conditions (pinned versus infinite) in the two models does not impact the overall result as the response has decayed to zero before reaching the boundaries.

Figure 5.8 shows the normalised power given a harmonic force input for cases with the centre of mass forward and aft of the shear centre in a constant wind of U=0 m/s (see Figure 4.16). The driving-point power results from the continuous and discrete models show excellent agreement. The discrete model was also used to verify that the system does not exhibit negative stiffness. To verify for negative stiffness, the eigenvalues of the stiffness matrix $\mathbf{K}$ were calculated. For a statically unstable case there will be zero and/or

negative eigenvalues; for a statically stable case the eigenvalues will all be positive. For the streamlined beam properties used in the current example, the eigenvalues of discrete model's stiffness matrix are all non-zero and positive.

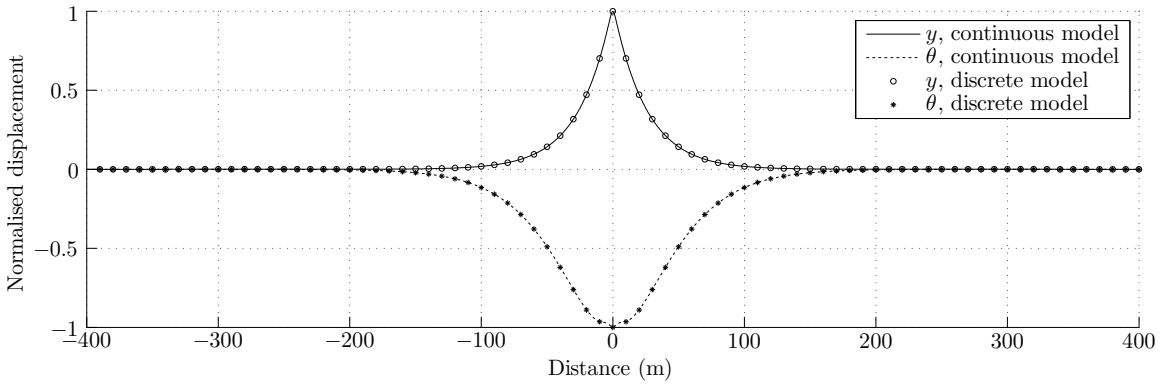

Fig. 5.7 Comparison of continuous and discrete model displacement response to a harmonic force input at x=0.

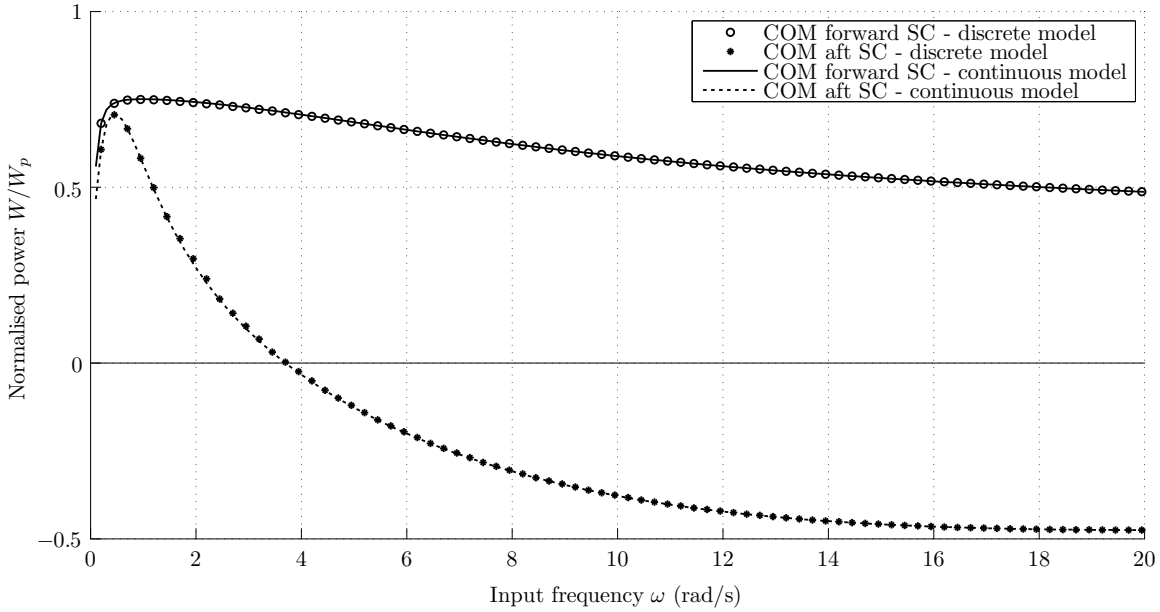

Fig. 5.8 Normalised driving-point power for a harmonic force input. Calculated using the continuous and discrete models.

5.7 Conclusions

The two-degree-of-freedom and continuous models developed in Chapters 3 and 4 provided a foundation for the discrete streamlined cable model developed in this chapter. The discrete model accounts for unsteady fluid loading using the same finite-state representation used in the two-degree-of-freedom model and includes wave-propagation effects such as those explored in the continuous model. The results from the continuous model are used as an initial validation of the discrete model. Comparisons of the displacement and driving-point power calculated independently with each model show excellent agreement. The main advantage of the discrete model is its ability to account for non-linear effects such as varying fluid velocity, fluid density and tension along its length. The discrete model also provides a platform for future work, which could investigate the effects of initial curvature and large deformations.

The work presented thus far has focused on the development of theoretical models to understand the dynamics and stability of a streamlined cable. The work presented in the next chapter focuses on the more practical side of streamlined cable development, including manufacturing and testing.

Chapter 6

Streamlined Cable Manufacture, Properties and Experiments

The work presented in the previous chapters introduced mathematical and computer models to analyse the dynamics and stability of a streamlined cable. Manufacturing a streamlined cable and testing it outdoors raises a completely new set of challenges. To address the practical aspects of streamlined cable dynamics, a programme to manufacture and test streamlined cables was completed. The main goals were to prove manufacturing feasibility, assess and model the structural properties of the manufactured cable and gain some insight on the general behaviour of a streamlined cable subject to environmental conditions.

This chapter begins by describing the development of the manufacturing process. Four manufactured samples are described and their cross-sectional properties determined using two modelling methods. The results of the two models are compared to each other and measured values. The second half of the chapter details the streamlined cable experiments completed in parallel with the development of the manufacturing process. These include wind tunnel, kite, balloon and horizontal field tests. The practicalities of the manufacturing and testing are discussed throughout the chapter.

6.1 Streamlined Cable Manufacture

The streamlined cable design concept is a composite construction, the main components being cable, polyurethane foam and polyethylene film. The foam and film provide the streamlined shape and the fibre cable is the tension carrying element. The foam concept allows for materials, such as steel wire, to be incorporated into the streamlined cable. The reason for including additional materials is as a means to alter the cross-sectional properties (e.g. the

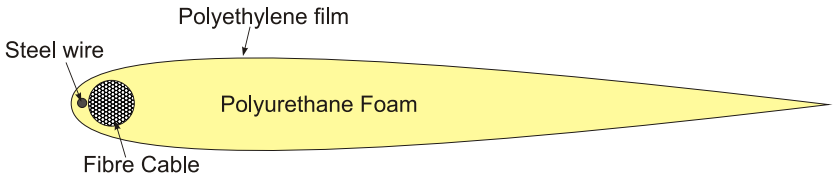

Fig. 6.1 Schematic cross-section of the streamlined cable design concept.

position of the centre of mass). Figure 6.1 shows a schematic of a general streamlined cable cross-section, which includes a wire to shift the centre of mass towards the leading edge.

The first prototype streamlined sections manufactured were relatively short 3.8 and 6.9 aspect ratio (length to chord) samples and provided a preliminary test of the design concept. Davidson Technology Ltd. (DT Ltd.) manufactured the first samples, with an aspect ratio of 6.9. The 3.8 aspect ratio samples, with a chord length of 100 mm, were later produced at the University of Cambridge by the current author. The streamlined sections were fabricated by lining a NACA 0020 mould with a thin plastic film, mixing and injecting a two part foam into the mould, sealing the mould and letting it set. The centre of mass was varied by the addition of a brass rod or the removal of foam material. See Appendix A for more detail on the manufacturing of the prototype sections. Due to their low aspect ratios, these sections were not representative of streamlined cables. However, the work helped to assess the feasibility of manufacturing streamlined cables with varying centre of mass using a foam injection process. Figure 6.3 shows cross-sectional schematics of five manufactured samples. Figure 6.2 shows a photo of samples (d) and (e) from Figure 6.3 while Figure 6.4 shows a side-view of the five manufactured sections.

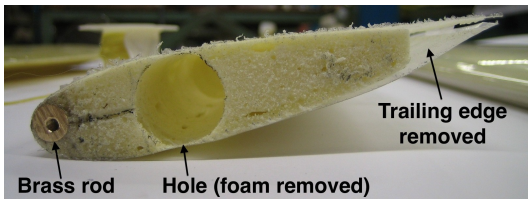

(a) See Figure 6.3 (d).

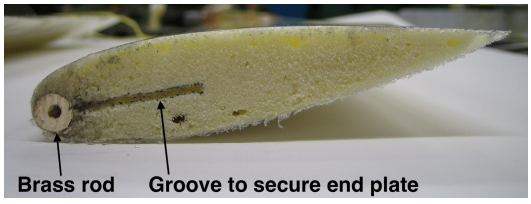

(b) See Figure 6.3 (e).

Fig. 6.2 Cross-sectional view of two NACA 0020 streamlined samples with 100 mm chord.

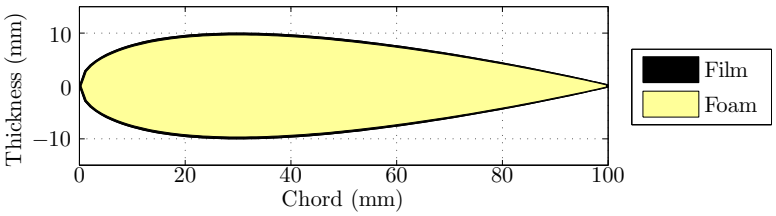

(a) Aerofoil 1: Foam filled (ρ=210 kg/m^3).

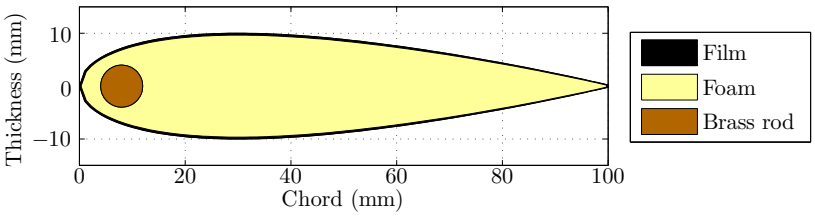

(b) Aerofoil 2: Foam filled (ρ=210 kg/m^3), 8 mm diameter brass rod.

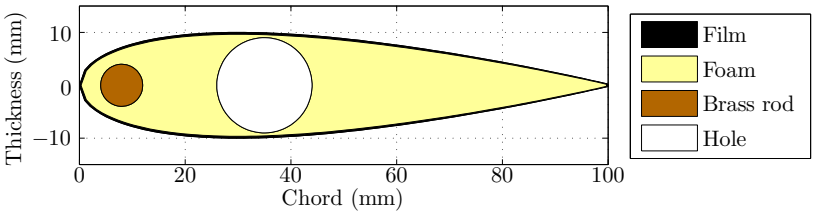

(c) Aerofoil 3: Foam filled (ρ=210 kg/m^3), 8 mm diameter brass rod, 18 mm diameter hole.

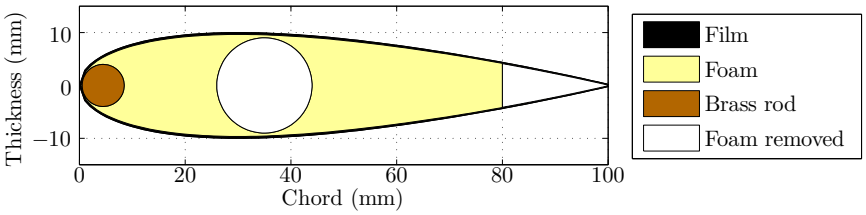

(d) Aerofoil 4: Foam filled (ρ=120 kg/m^3), 8 mm diameter brass rod, 18 mm diameter hole, tail removed.

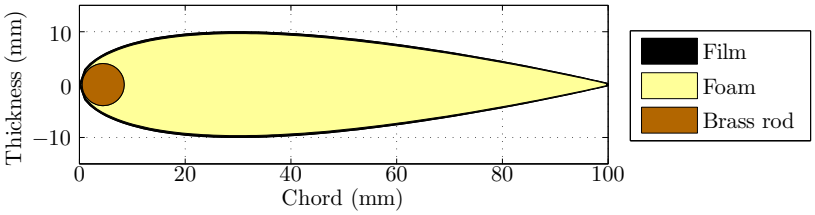

(e) Aerofoil 5: Foam fill (ρ=120 kg/m^3), 8 mm diameter brass rod.

Fig. 6.3 CUED manufactured prototype sections tested in the wind tunnel with centre of mass properties given in Table 6.1.

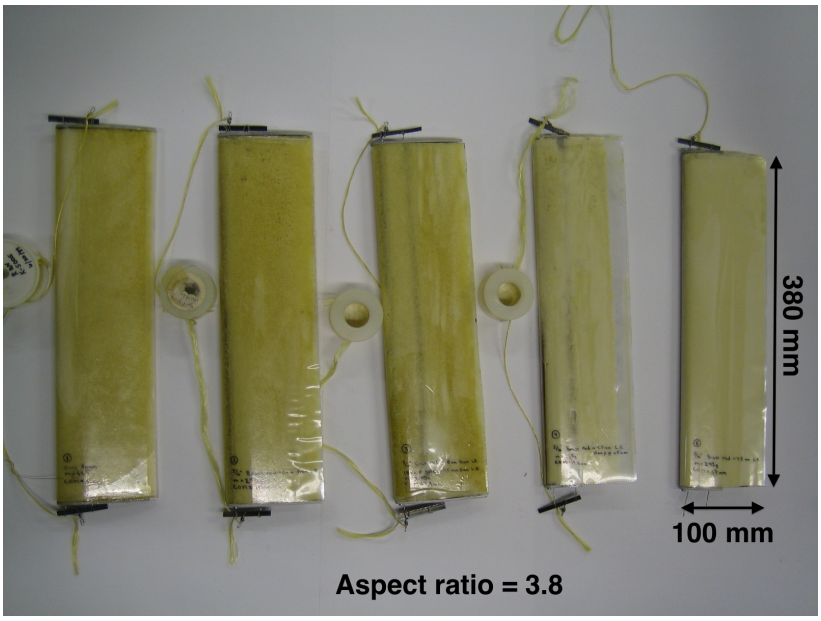

Fig. 6.4 Five of the manufactured NACA 0020 streamlined samples.

Following the work at Cambridge, the design and implementation of manufacturing streamlined cables greater than 50 m in length was contracted to Elson Space Engineering Ltd. (ESE Ltd.) and DT Ltd. The work was based in Somerset England. The contract was funded by the SPICE project, as part of its investigation into the application of streamlined cables to high-altitude tethered balloons.

In August 2012, the first 10 m long sample was produced by a prototype machine. Over the course of the following year, the process and consequently the quality and length of the manufactured streamlined cable improved. By August 2013, the machine could run continuously and produce streamlined cables with varying centres of mass in the range of 50 m to 150 m. The manufacturing machine was built on site at ESE Ltd. The manufacturing process can be broken into six overall steps shown in Figure 6.6 and detailed in the list below.

1. The polyethylene film, cable and wire are unwound under tension from their drums. A series of pulleys guide the cable, wire and film into position for foam injection. The film is folded in half with the cable and wire inside. The fold-end will form the leading edge and the open-end the trailing edge of the streamlined profile.

2. The two foam precursors, Daltofoam and Suprasec, supplied by Huntsman [69] are mixed by a rotary shaft mixer designed by ESE Ltd. The mixture is then injected near the leading edge of the profile.

3. Once the foam is injected, the film is welded together at the trailing edge of the profile and any excess film is cut-off.

4. The welded film – containing expanding foam, the fibre cable and the wire – enters the NACA 0020 mould. The mould is a powered continuous track which drives the entire process (i.e. it pulls the film and cables through the process by friction). Within the mould, the foam expands and sets into its streamlined shape.

5. Upon leaving the mould, the streamlined cable is kept in a straight configuration for a few meters to ensure the foam has cooled and set completely.

6. The streamlined cable is wound onto a drum of approximately 1 m in diameter for storage and later use. The drum is powered by a small motor to wind the streamlined cable onto the drum at the same rate it is produced.

Figure 6.5 shows an annotated photo of the final machine set-up and Figures 6.7 to 6.10 show details of the first four manufacturing steps. Note that there is no foam in the photos as the machine is not in the process of producing streamlined cable.

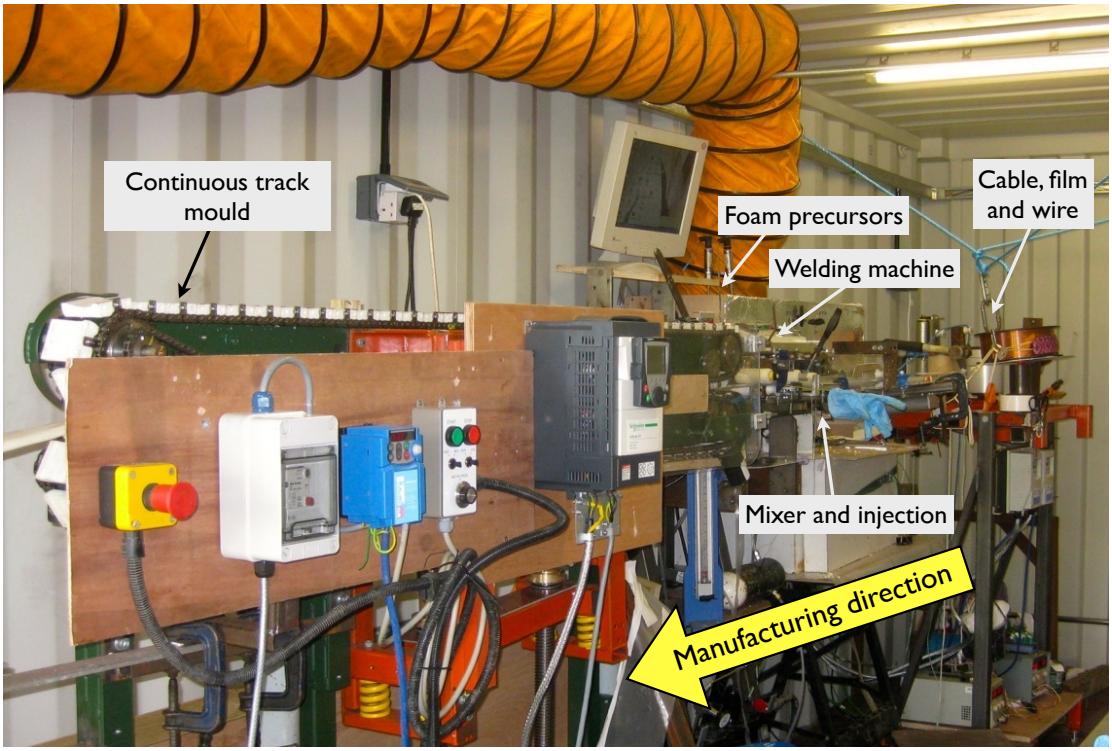

Fig. 6.5 Streamlined cable manufacturing machine.

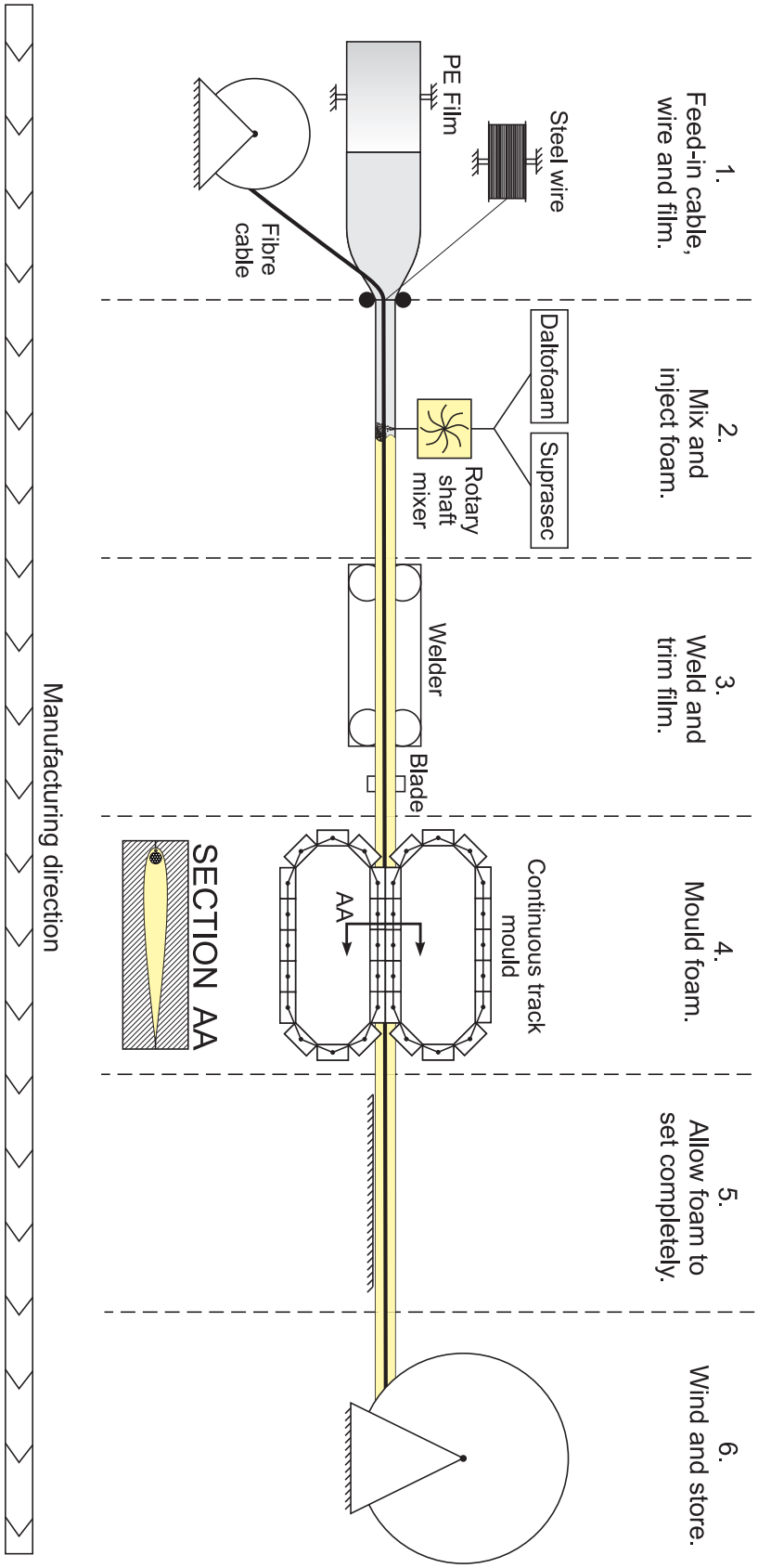

Fig. 6.6 Schematic of streamlined cable manufacturing process and machine.

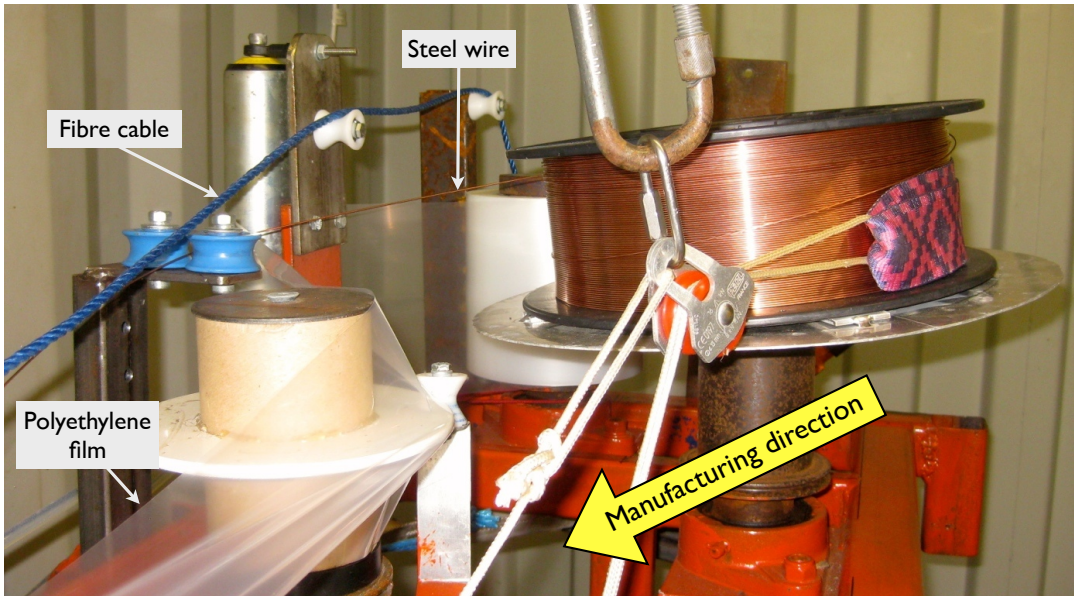

Fig. 6.7 Step 1, the polyethylene film, fibre cable and steel wire ready to feed into the manufacturing process.

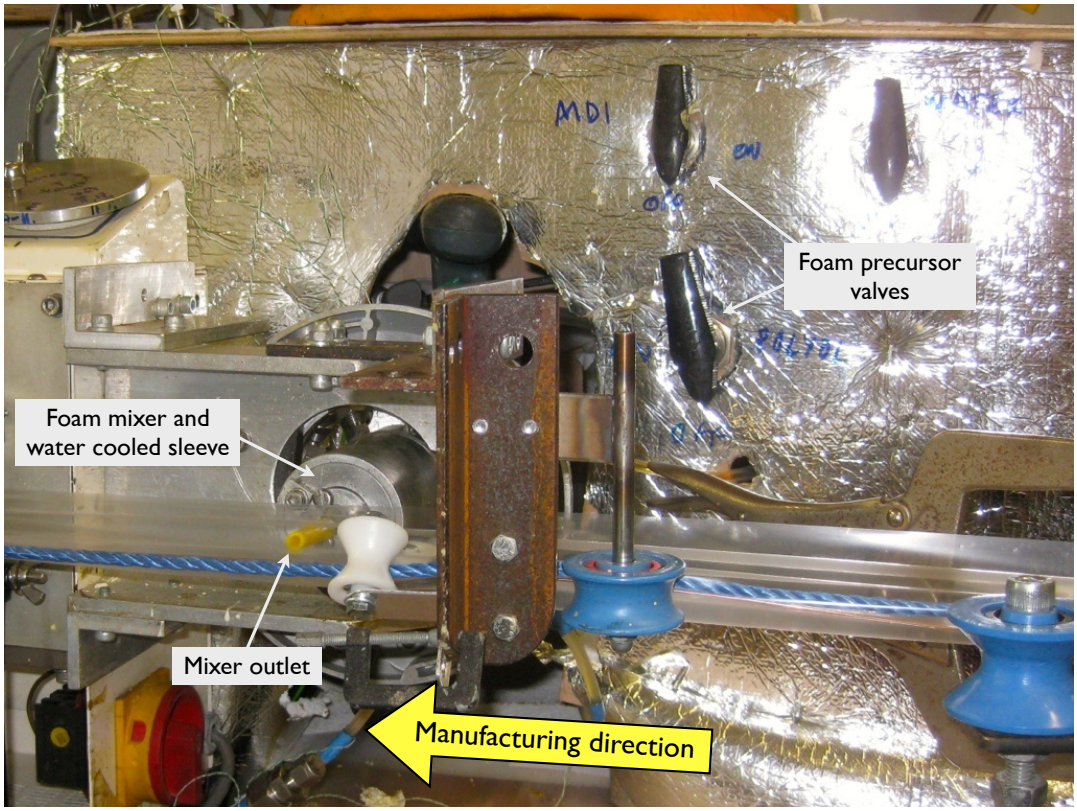

Fig. 6.8 Step 2, foam mixer and injector.

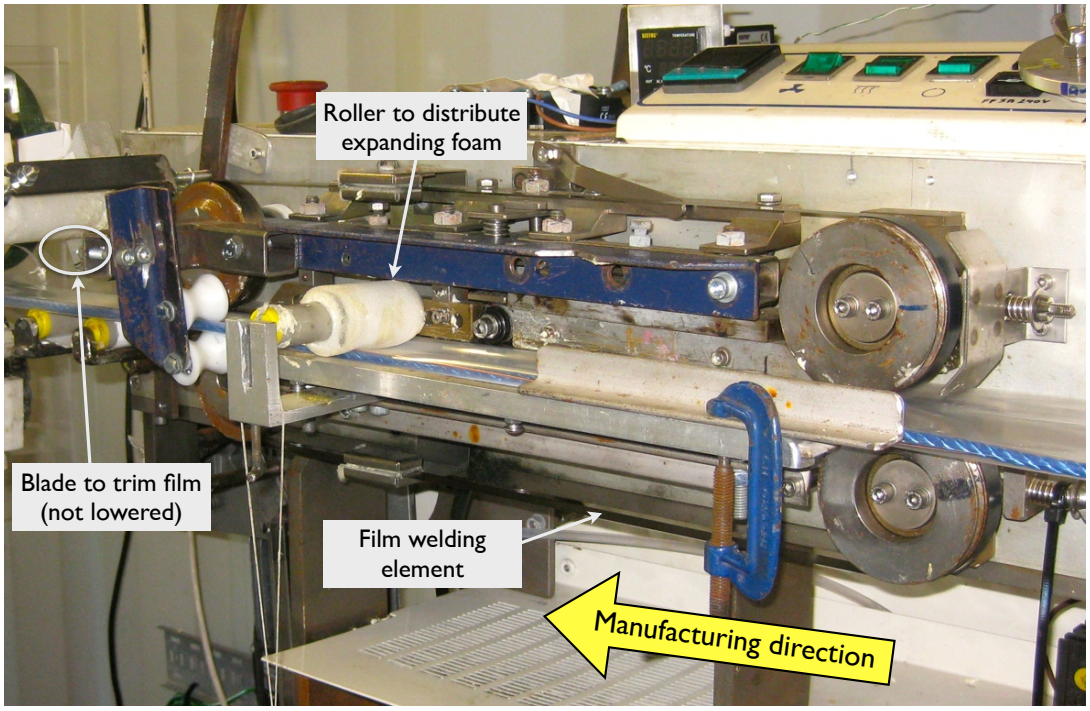

Fig. 6.9 Step 3, the film welding machine.

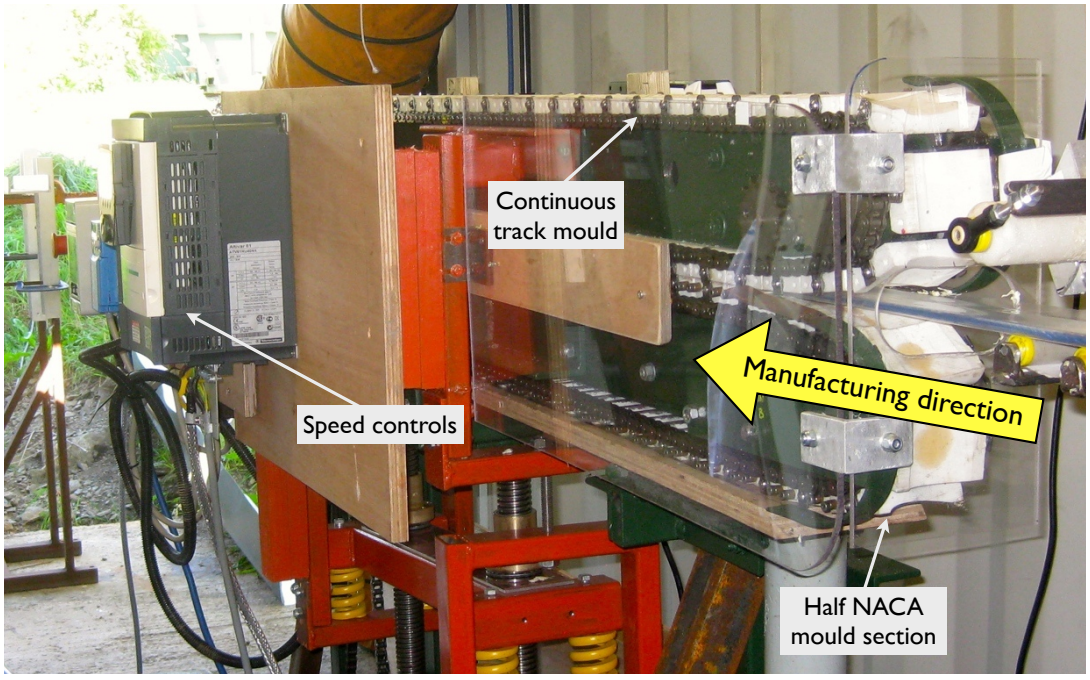

Fig. 6.10 Step 4, continuous track NACA 0020 streamlined cable mould.

The design and implementation of a manufacturing process highlighted the challenges associated with producing a streamlined cable. Throughout the project, improvements to the overall process were identified. As this is the first known attempt to manufacture streamlined cable of this type, it is worth noting some of the challenges encountered and lessons learnt.

The manufacturing process is very sensitive to temperature changes as they cause the foam expansion and setting times to vary. The manufacturing process requires that: the film is welded shut before the foam expands, the foam expands while in the mould and the foam sets prior to leaving the mould. Consequently, changes in the timing of the foam reaction can throw the entire manufacturing process off. A water-cooled sleeve was added to the mixer and helped control the temperature of the produced foam. However, the location where the machine was housed was not climate controlled and changes in the outdoor temperature affected the foam reaction time.

The polyurethane foam was initially selected for its low density (specified as 65 kg/m^3) so that the streamlined cable was kept relatively light. When the foam is injected into the streamlined cable, there is a trade-off between achieving the desired density and completely filling the mould. A slight super-pressure in the mould gives a good shape but causes an increase in the foam density.

In addition to injecting the correct amount of foam, the foam needs to be injected so that it fills the profile without altering the position of the cable. If too much foam is injected at the leading edge, it can cause the fibre cable to be pushed towards the trailing edge as the foam expands. Too little foam at the leading edge gives a poor shape to the nose of the aerofoil. Injecting the foam so that it sprays slightly was found to work well, as it distributed the foam on the film and fibre cable.

6.2 Manufactured Samples and Their Properties

Over the course of developing the manufacturing process, various configurations of streamlined cable were constructed and tested. Figure 6.11 shows four manufactured samples and Table 6.1 lists their properties.

The properties necessary for modelling the streamlined cable are the inertial and elastic cross-sectional properties, as described in Chapter 5. In the following sections, these properties are determined from an inhomogeneous cross-section model (implemented in Matlab), from BEam Cross-sectional Analysis Software (BECAS) developed at the Technical University of Denmark and from experimental measurements.

Both the inhomogeneous and BECAS cross-section models require the properties of the

(a) Blue polyester.

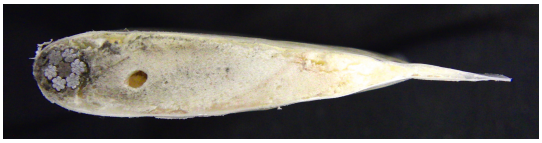

(b) Wound steel.

(c) Red polyester.

(d) Polyester and steel.

Fig. 6.11 Manufactured 50 mm chord streamlined cable cross-sections with properties listed in Table 6.1. (See Figure 6.12 for a schematic of each sample).

Table 6.1 Geometry and materials of four streamlined cables shown in Figure 6.11.

Sample	Cable or wire diameter	Cable or wire mass	Foam density	Film thickness
	(mm)	(kg/m)	(kg/m^3)	(μm)
a) Blue polyester	6	2.9×10^{-2}	108	150
b) Wound steel	5	10×10^{-2}	104	150
c) Red polyester	6	2.9×10^{-2}	98	50
d) Polyester and	6	2.9×10^{-2}	86	50
steel wire	1.2	0.85×10^{-2}		

individual component materials as input. Some of these properties are not readily available or easily measured. Table 6.2 gives the material properties used in the cross-sectional models. Values without a footnote specifying the source of information are measured values from the streamlined cable samples. The work here aims to introduce methods to calculate the cross-sectional properties and obtain approximate values to use in the streamlined cable model. Therefore, as an approximation, all the materials are considered isotropic. Future work could include a more thorough analysis to determine the cross-sectional properties of the composite streamlined-cable cross-section.

6.2.1 Inhomogeneous Cross-Section Model

The inhomogeneous cross-section model assumes the cross-section is composed of multiple, homogeneous, isotropic regions. To calculate the inertial and stiffness properties of a cross-section with n homogeneous regions, the geometric area, centroid and second moments of

Table 6.2 Material properties of streamlined cable components.

Symbol	Units	PE	PU Foam	Polyester Cable	Steel Cable	Steel Wire
ρ	kg/m^3	955 - 976	86 - 108	-	-	-
$m^{'}$	kg/m	-	-	0.03	0.10	0.01
E	GPa	0.6 - 1.4 [1]	0.012 - 0.027 [2]	4 - 6.5 [3]	126 [4]	210 [5]
G	GPa	0.85 [1]	0.0063 [2]	≈ 0	≈ 0	81 [5]
ν	-	0.45 [6]	0.32 [2]	0.5 [7]	0.3 [5]	0.3 [5]

[1]Springer Handbook of Condensed Matter and Materials Data [88].
[2]Experimental measurement by Witkiewicz et al. [135].
[3]Estimate based on break load of 1390 kg and polyester cable stiffness from DeAndrade [34].
[4]Estimate based on break load of 17 kN and metallic area of 7x7 wound cable.
[5]Cambridge Engineering Databook [36].
[6]Experimental measurement by Nitta et al. [96].
[7]From synthetic cable estimate by Tjavaras et al. [128].

area – denoted by A_n, $\hat{y}_n$, $\hat{z}_n$, I_{yn} and I_{zn} respectively – for each region must be determined. Calculating these properties is straightforward for simple shapes such as circles. For more complex shapes, such as the streamlined profile, the region is defined by a closed polygon. The method presented by Steger [120] on the calculation of moments of polygons is used to determine the geometric properties. As the number of sides of the polygon increases, the better the polygon approximates the true geometry.

Knowing the geometric and material properties of each region, the inertial cross-sectional properties are straightforward to calculate. If there are n components making up the cross-section, the familiar Equations (6.1) to (6.6) – found in many mechanics texts such as Goldstein [51] and Likins [83] – give the mass per unit length, centre of mass and three mass moments of inertia per unit length, respectively.

$$m^{'} = \sum_{i=1}^{n} \rho_i A_i \tag{6.1}$$

$$\hat{y} = \frac{1}{m^{'}} \sum_{i=1}^{n} \rho_i A_i \hat{y}_i \tag{6.2}$$

$$\hat{z} = \frac{1}{m^{'}} \sum_{i=1}^{n} \rho_i A_i \hat{z}_i \tag{6.3}$$

$$I_{Gy}^{'} = \sum_{i=1}^{n} \rho_i \left(I_{yi} + A_i (\hat{y}_i - \hat{y})^2 \right) \tag{6.4}$$

$$I'_{Gz} = \sum_{i=1}^{n} \rho_i \left(I_{zi} + A_i (\hat{z}_i - \hat{z})^2 \right) \tag{6.5}$$

$$I'_{Gx} = I'_{Gy} + I'_{Gz} \tag{6.6}$$

The elastic cross-sectional properties are calculated using the method described by Hartsuijker and Welleman [56], which extends the classic fibre model to one suitable for inhomogeneous cross-sections. The method can be used to calculate the elastic extension and bending stiffnesses EA, EI_x and EI_y. However, the torsional stiffness GJ and shear centre cannot be calculated using this method since, for non-circular geometry, the torsion constant J is not equal to the second moment of area.

The elastic properties EA, EI_x and EI_y are determined with respect to the elastic centre. Hartsuijker and Welleman [56] define them as “double letter symbols" since the value of E varies over the cross-section. The axial stiffness and elastic centre of the inhomogeneous section are given by

$$EA = \sum_{i=1}^{n} E_i A_i \tag{6.7}$$

$$y_p = \frac{1}{EA} \sum_{i=1}^{n} E_i A_i \hat{y}_i \tag{6.8}$$

$$z_p = \frac{1}{EA} \sum_{i=1}^{n} E_i A_i \hat{z}_i. \tag{6.9}$$

Knowing the location of the elastic centre, the bending stiffnesses are calculated using the parallel axis theorem as

$$EI_y = \sum_{i=1}^{n} E_i I_{yi} + E_i A_i (\hat{y}_i - y_p)^2 \tag{6.10}$$

$$EI_z = \sum_{i=1}^{n} E_i I_{zi} + E_i A_i (\hat{z}_i - z_p)^2. \tag{6.11}$$

The inertial and elastic properties of the four samples given in Figure 6.11 were calculated using the described inhomogeneous method. The origin of the cross-sectional coordinate system is positioned at the leading edge. Each region is considered to be isotropic and the value of E is taken from Table 6.2. Figure 6.12 shows the inhomogeneous model of the four sections with the homogeneous regions of each section listed in the legend. The calculated values of the inertial and elastic properties are compared to the BECAS and measured results in section 6.2.3.

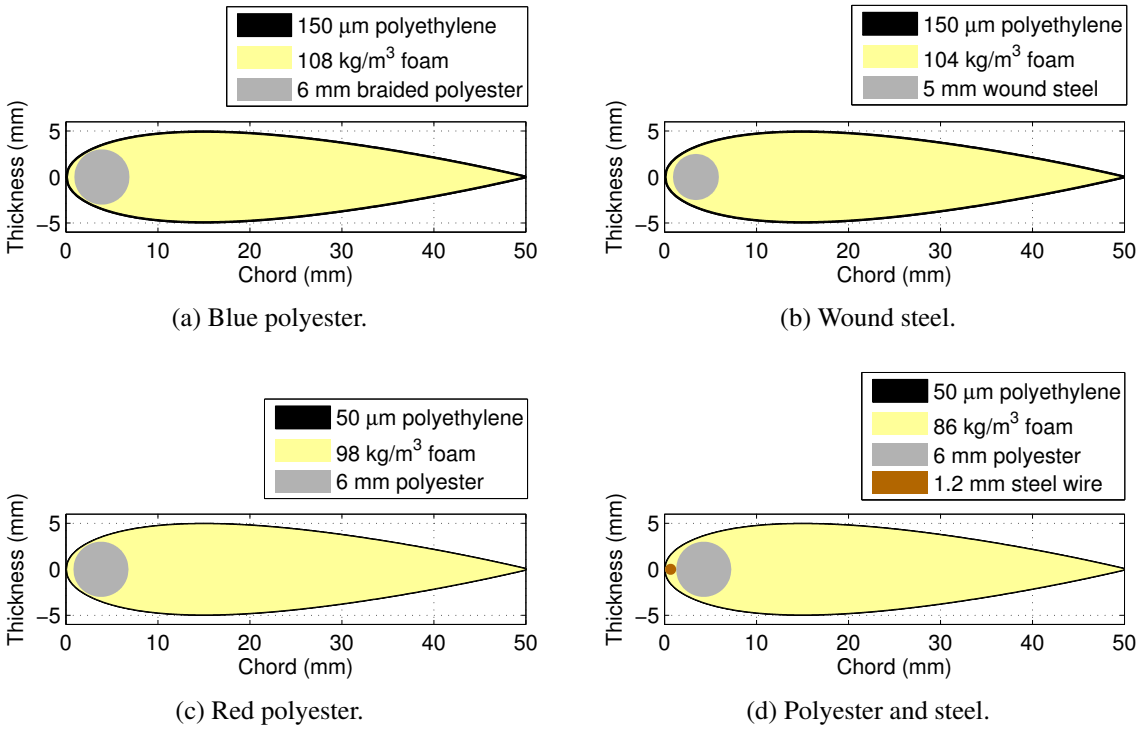

(a) Blue polyester.

(b) Wound steel.

(c) Red polyester.

(d) Polyester and steel.

Fig. 6.12 Inhomogenous model of 4 streamlined cable samples given in Figure 6.11 with properties listed in Table 6.1.

6.2.2 BECAS Model

The main limitation of the inhomogeneous model is its inability to calculate the torsional stiffness and shear centre. Additionally, each region is considered isotropic, when in fact, elements such as the braided fibre rope are anisotropic. Blasques et el. [16] developed BECAS to calculate the cross-sectional inertial and elastic properties of sections with complicated geometry and anisotropic materials. The software uses a finite element method to calculate all inertial and elastic properties, including the torsional stiffness and shear centre.

To obtain the cross-sectional properties of the four samples in Figure 6.11 from BECAS, a four-node quadrilateral element mesh is required. An open source mesh generator developed by Geuzaine and Remacle [48] called Gmsh was used to mesh the cross-sections. Figure 6.13 shows a mesh of the blue polyester streamlined cable depicted in Figure 6.12 (a) using 1390 quadrilateral elements.

The cross-sectional properties of the four manufactured samples were calculated using the BECAS model. Though the model has the scope to include anisotropic materials, as a preliminary estimate, all the materials were considered isotropic. The convergence results

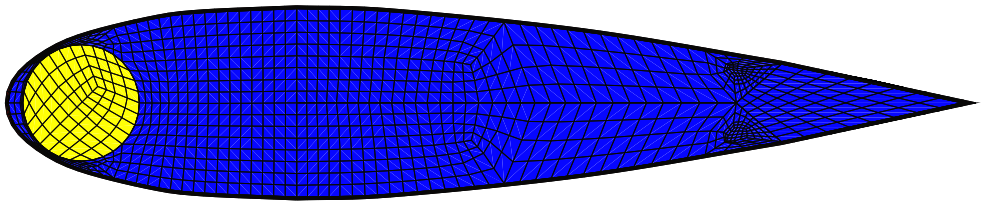

Fig. 6.13 Gmsh quadrilateral mesh of a streamlined cable cross-section with 1390 elements.

given mesh refinement – for the inertial and elastic properties of the blue polyester sample – are given in Table 6.3. The results show that the model is converging with an increasing number of elements. The cross-sectional models of the remaining three samples show the same overall convergence. The maximum and minimum percent difference of the six calculated values m, I, EA, EI_y, EI_z and GJ are given with respect to a 5630 element run. The calculated values of the inertial and elastic properties are compared to the inhomogeneous model and measured results in the following section.

Table 6.3 BECAS model convergence. Maximum and minimum percent difference of m, I, EA, EI_y, EI_z and GJ values relative to a 5630 element run.

Number of elements	Minimum difference	Maximum difference
850	2.0 %	7.4 %
1270	0.6 %	4.4 %
1630	0.2 %	2.4 %
3620	0.1 %	1.3 %

6.2.3 Measured Properties and Model Results

Measurements of the inertial and elastic properties of the manufactured streamline cable were taken to compare the results with the inhomogeneous and BECAS models. The mass per unit length and centre of gravity were measured for all samples. The bending stiffness in one direction (EI_z), shear centre and torsional stiffness were measured for the blue polyester and wound steel samples. The measurement methodology is described in Appendix B. Tables 6.4 to 6.7 compare the calculated and measured cross-sectional properties of the four samples. A range is given for some values due to the range in material values in Table 6.2.

Comparing the results, the nine properties for each sample generally agree between the models and measurements except for the bending stiffness EI_z of the wound steel sample and

the torsional stiffness GJ of both measured samples. More specifically, taking the measured value (or where it is unavailable the BECAS value) as the baseline, the percent difference varies between 1% to 29% for all values except the bending and torsional stiffnesses.

The calculated torsional stiffness compared to the measured value is 3.7 times greater for the blue polyester sample and 4.5 times greater for the wound steel sample. In both cases, the measured value is lower than the calculated one. A possible explanation for the difference is that the skin is modelled as a closed thin-walled section. In reality, the film is welded at the trailing edge and sometimes splits open or is not fully welded. As a rough comparison to the streamlined cable skin, consider a 10 mm diameter tube made of 150 µm polyethylene film. Using Roark's formulas [138], if the tube is closed, the torsional stiffness is about 3,000 time greater than if the tube is open. Therefore, small defects in the streamlined cable welding, causing the section to be "open" could explain why the modelled torsional stiffness is greater than the measured value. The discrepancy in the calculated and measured bending stiffness values for the wound steel sample is likely because the cross-sectional models do not account for slipping between the strands of the wound steel cable.

The first six cross-sectional properties (with dimensions) given in Tables 6.4 to 6.7 are calculated with respect to a reference frame located at the shear centre with the z-axis parallel to, and the y-axis perpendicular to, the chord length. The properties are the mass per unit length m, the mass moment of inertia about the centre of mass I_G, the axial stiffness EA, the bending stiffness EI_y, the bending stiffness EI_z and the torsional stiffness GJ. The remaining three properties r, p and s are the dimensionless position of the mass, tension and shear centre respectively. The dimensionless form is consistent with the values used in the models derived in Chapters 3 to 5. The dimensionless position is such that -1 is the leading edge, 0 is the mid-chord point and 1 is the trailing edge.

Table 6.4 Properties of blue polyester sample given in Figure 6.11 (a)

Symbol	Inhomogenous model	BECAS	Measured	Units
m	0.077	0.076	0.085	kg/m
I_G	1.3E-05	1.4E-05	-	kgm^2
EA	0.13-0.22	0.13-0.21	-	MN
EI_y	6.5 to 14	7.0 to 16	-	Nm^2
EI_z	0.33 to 0.58	0.39 to 0.74	0.25	Nm^2
GJ	-	0.63	0.17	Nm^2
r	-0.37	-0.38	-0.33	-
p	-0.79 to -0.70	-0.76 to -0.74	-	-
s	-	-0.44 to -0.41	-0.56	-

Table 6.5 Properties of wound steel sample given in Figure 6.11 (b)

Symbol	Inhomogenous model	BECAS	Measured	Units
m	0.15	0.15	0.16	kg/m
I_G	1.9E-05	1.9E-05	-	kgm^2
EA	2.5	2.5	-	MN
EI_y	11 to 20	11 to 21	-	Nm^2
EI_z	3.9 to 4.0	4.0 to 4.1	0.30	Nm^2
GJ	-	0.63	0.14	Nm^2
r	-0.63	-0.62	-0.55	-
p	-0.88 to -0.86	-0.86 to -0.85	-	-
s	-	-0.53 to -0.52	-0.59	-

Table 6.6 Properties of red polyester sample given in Figure 6.11 (c)

Symbol	Inhomogenous model	BECAS	Measured	Units
m	0.066	0.065	0.070	kg/m
I_G	1.1E-05	1.1E-05	-	kgm^2
EA	0.12-0.20	0.12-0.20	-	MN
EI_y	3.7 to 8.0	3.7 to 8.2	-	Nm^2
EI_z	0.29 to 0.51	0.32 to 0.56	-	Nm^2
GJ	-	0.25	-	Nm^2
r	-0.44	-0.45	-0.44	-
p	-0.82 to -0.80	-0.80 to -0.79	-	-
s	-	-0.49 to -0.47	-	-

Table 6.7 Properties of polyester and wire sample given in Figure 6.11 (d)

Symbol	Inhomogeneous model	BECAS	Measured	Units
m	0.069	0.069	0.070	kg/m
I_G	1.1E-05	1.1E-05	-	kgm^2
EA	0.36-0.44	0.35-0.43	-	MN
EI_y	5.3 to 10	5.4 to 11	-	Nm^2
EI_z	0.32 to 0.53	0.34 to 0.58	-	Nm^2
GJ	-	0.26 to 0.27	-	Nm^2
r	-0.51	-0.51	-0.52	-
p	-0.91 to -0.88	-0.91 to -0.88	-	-
s	-	-0.52 to -0.49	-	-

6.3 Streamlined Cable Dynamics Experiments

Testing streamlined cable was an objective throughout the project and over the course of the work has included wind tunnel testing, flying sections of streamlined cable as kite line, using the streamlined cable as balloon tether and horizontal field tests. The streamlined cable itself being in the preliminary phase of development, the objective of the experiments was not purely to gather data to validate the streamlined cable models. The objective of the testing was also to assess the benefits and limitations of the potential streamlined cable applications, testing methods and measurement techniques. Consequently, as samples became available through the development of the manufacturing process, they were incorporated into experimental tests. Figure 6.15 gives a timeline of the manufacturing, experimental testing and development of measurement techniques associated with the current work. The experimental work was funded by the SPICE project, the manufacturing developed by ESE Ltd. and DT Ltd. , the experimental set-up and testing undertaken by the current author and an optical cable dynamics measurement system developed by Shaw [113, 114]. A brief discussion on the wind tunnel, kite, balloon and horizontal tests is provided in the next sections.

6.3.1 Wind Tunnel Tests

The initial, prototyped sections, with varying centres of mass manufactured at CUED were tested. The sections were supported in the Markham wind tunnel (working section of 1.1 m height and width of 1.7 m) using string as shown in Figure 6.14. The objective of the testing was to see how changes in the centre of mass and point of attachment of the tensioned string affected the stability of the aerofoil section. Table 6.8 gives the calculated and measured position of the centre of mass of the cross-sections shown in Figure 6.3.

Aerofoils 1, 2, 3 and 5 showed unstable behaviour in the wind tunnel. They exhibited strong growing oscillatory behaviour almost immediately once wind was introduced. Other interesting phenomena, such as 360^{o} flipping, was also observed. Aerofoil 4, which has the forward most centre of mass, exhibited more stable behaviour than the other four aerofoils. The aerofoil was taken up to a speed of 22 ms^{-1} and exhibited fairly stable behaviour. Interestingly, on ramp down of the wind speed, the aerofoil went into a highly unstable mode and oscillated to failure. This indicates that the effects of rapidly changing wind speed could be an important focus of future work.

Although the controlled environment of a wind tunnel is appealing, the size of the wind tunnel limits the length of streamlined cable which can be tested. The samples tested were

relatively short and rigid and the aerodynamics at the ends likely influenced the overall behaviour. For a given length of streamlined cable to exhibit cable-like behaviour, the cross-sectional dimensions must be small relative to the overall length. However, as the cross-section becomes smaller, the streamlined cable becomes more difficult to manufacture.

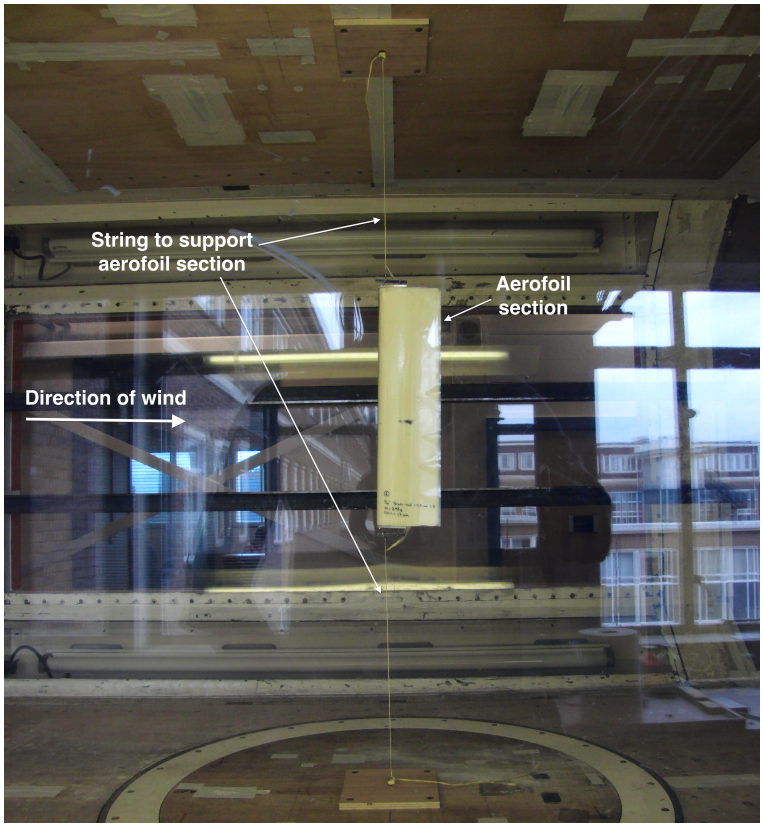

Fig. 6.14 Preliminary tests in the wind tunnel using the CUED manufactured sections supported under tension by two strings.

Table 6.8 Measured and calculated centre of mass of CUED manufactured streamlined sections. Position taken with respect to the leading edge.

	Center of mass (% of chord)	
Sample	Measured	Calculated
1	43	42
2	23	25
3	23	24
4	15	15
5	17	17

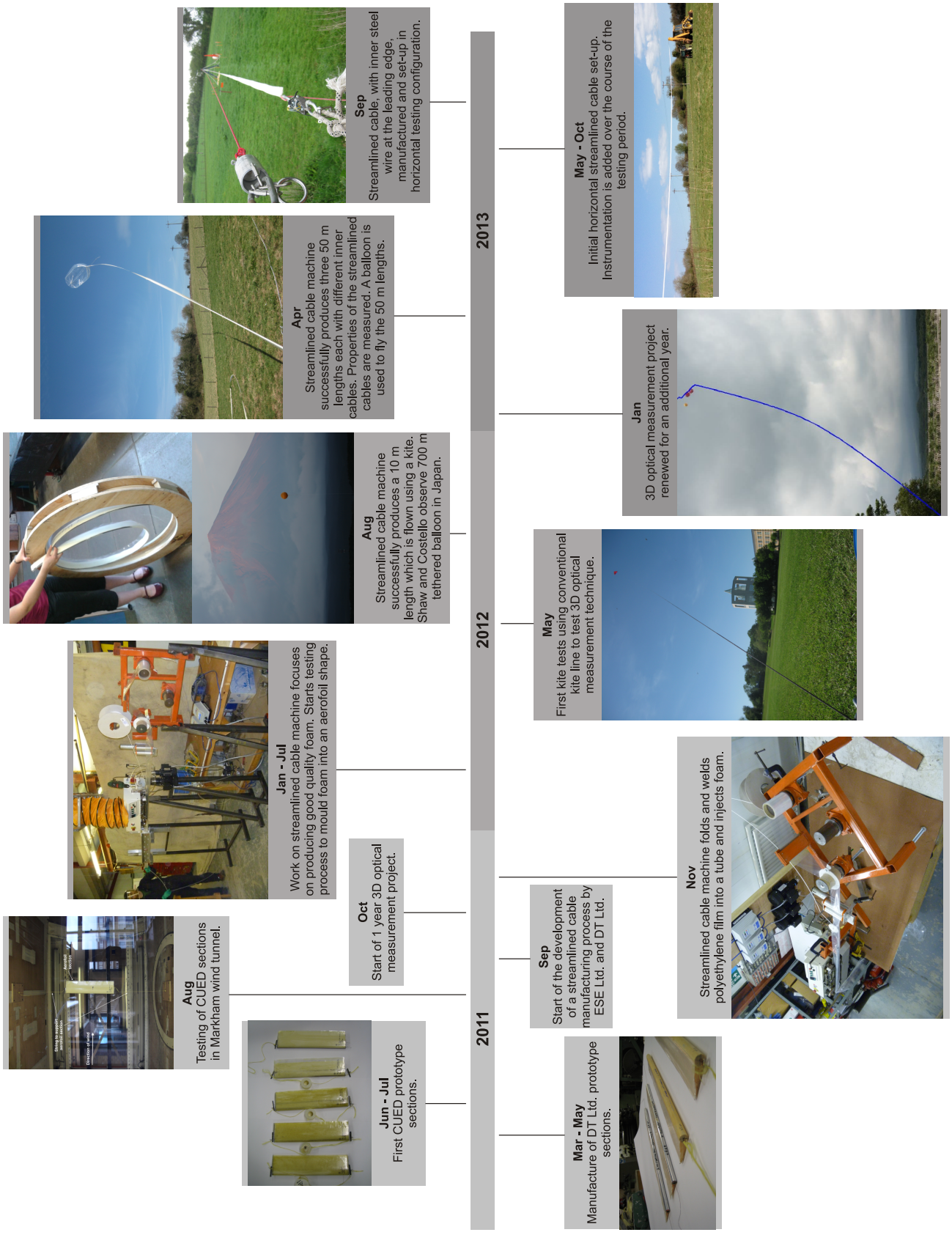

Fig. 6.15 Streamlined cable manufacturing and experimental testing timeline.

6.3.2 Tethered Balloon and Kite Tests

As kites and balloons are proposed applications for the use of streamlined cable, they were a natural choice of testing method. Kite and balloon flights were completed in conjunction with Shaw, who used the flights as a test of his 3D optical measurement system. Kite and balloon tests were carried out in Cambridge, Japan and Somerset and each group of tests is briefly summarised below. Figures 6.16 to 6.18 at the end of this section show some of the test configurations and results from Shaw's optical measurement system.

The first tests were carried out with a kite, in Cambridge, in the fields of Churchill College. The tests were part of work by Shaw to develop an optical cable dynamic measurement technique. The technique uses two cameras to record the motion of the cable, then image-processing techniques are used to identify the location of the tether in each frame. The position of the cable in three-dimensions is determined from the stereo vision set-up of the cameras and calibration techniques. The first tests were conducted with a simple kite-line and, when the first 10 m streamlined section was available, it was attached in series with the kite line and flown. The 10 m sample exhibited unstable behaviour and also showed that the winding effected the streamlined cable shape. In an unloaded state, the 10 m sample was curved, and even when under the tension of the kite line, did not straighten completely. Observation of this behaviour fed back into the manufacturing process and measures were taken to ensure that the foam cured fully in a straight position before being wound onto the storage drum. Parts of the kite testing program was documented by the Royal Institution in collaboration with the Royal Academy of Engineering [110, 111].

As part of the cable dynamics optical measurement work, members of the SPICE project were invited to observe the launch of a tethered balloon in Japan. The tethered balloon launch was for the Japan Space Elevator Competition (JSEA) and was flown up to altitudes of 700 m. The current author and Shaw attended the competition and used the opportunity to test the cable dynamic measurement technique and generally gain knowledge on the practical issues of launching and operating tethered balloons.

When 50 m lengths of streamlined cable were successfully manufactured, they were flown beneath a helium balloon with the assistance of ESE Ltd. The attempt highlighted the difficulties of using balloons as a means for preliminary streamlined tether tests. The additional dynamics of the balloon made it difficult to gain fundamental insight into the stability of the streamlined cable itself. The drag on the balloon dictated the overall motion of the balloon and, due to the weight of the streamlined cable and size of balloon available, the configuration did not fly higher than approximately 20 m. Future work could consider using a streamlined aerostat which would be more stable in the wind.

Another challenge of the balloon and kite testing are the weather conditions. For kite testing there must be sufficient wind to fly the kite and lift the cable; for balloon testing, if the winds are too high the system will blow-over. Thus, the testing using both methods is limited by having to wait and mobilise when appropriate weather conditions arise.

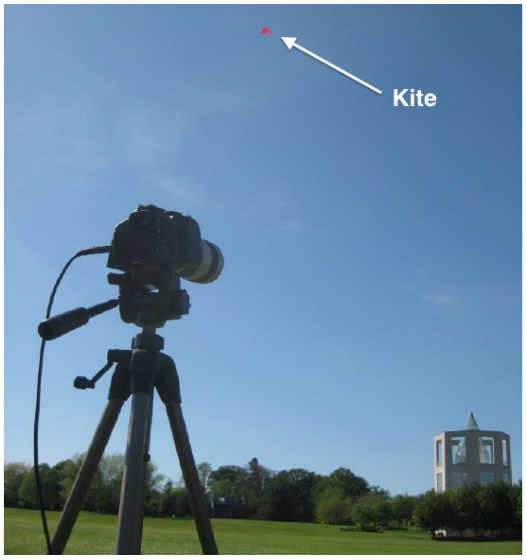

Fig. 6.16 Kite flying showing one of the cameras for the optical measurement technique [113]. The red kite is seen at the top of the photo, the kite-line is not visible.

(a) Image of a tethered balloon.

(b) Cable detected by Shaw's algorithm.

Fig. 6.17 Demonstration of Shaw's cable detection algorithm of the JSEA balloon [114].

Fig. 6.18 Length of 50 m streamlined cable flown using a helium balloon in Somerset.

6.3.3 Horizontal Streamlined Cable Test

The final and simplest test was to permanently set-up a length of horizontal streamlined cable in an open field, a few meters above the ground. Although this means that gravity affects the alignment of the streamlined cable relative to the wind, the test was appealing due to its simplicity and "hands-off" nature. The set-up could easily be left for days, collecting data at various wind conditions.

Figure 6.19 shows a schematic of the experimental set-up consisting of a 50 m length of both streamlined and bare cable, supported horizontally. A chain block and load cell were attached in series on each cable to adjust and measure the tension. Swivels, with rotational Hall effect sensors incorporated into them, were fixed at both ends of the streamlined cable to measure the orientation. Finally, bi-axial accelerometers were attached to both cables. The wind speed and direction were measured by an anemometer and wind-vane affixed to a nearby building. The sensor output wires were run to this building, which served to house the data logging equipment.

An aerial view of the set-up location is shown in Figure 6.20. The red path shown indicates the location of the cable set-up as measured by GPS. Figure 6.21 shows a photo of the horizontal set-up, with the bare red polyester cable just visible above the light yellow streamlined cable.

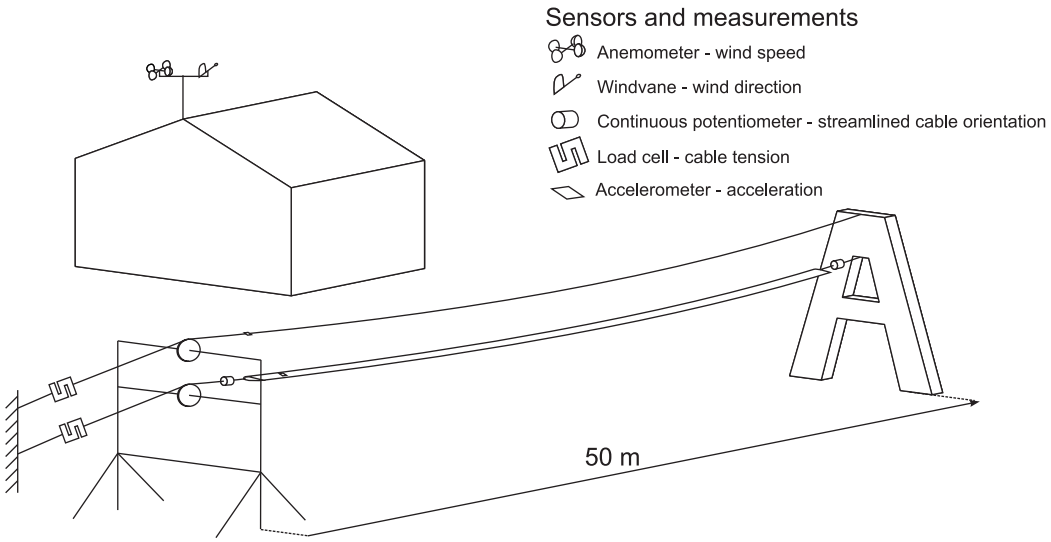

Fig. 6.19 Schematic of horizontal experimental set-up.

Fig. 6.20 Aerial view of the experimental location with GPS measurements [52].

Fig. 6.21 Side-view of the horizontal experiment.

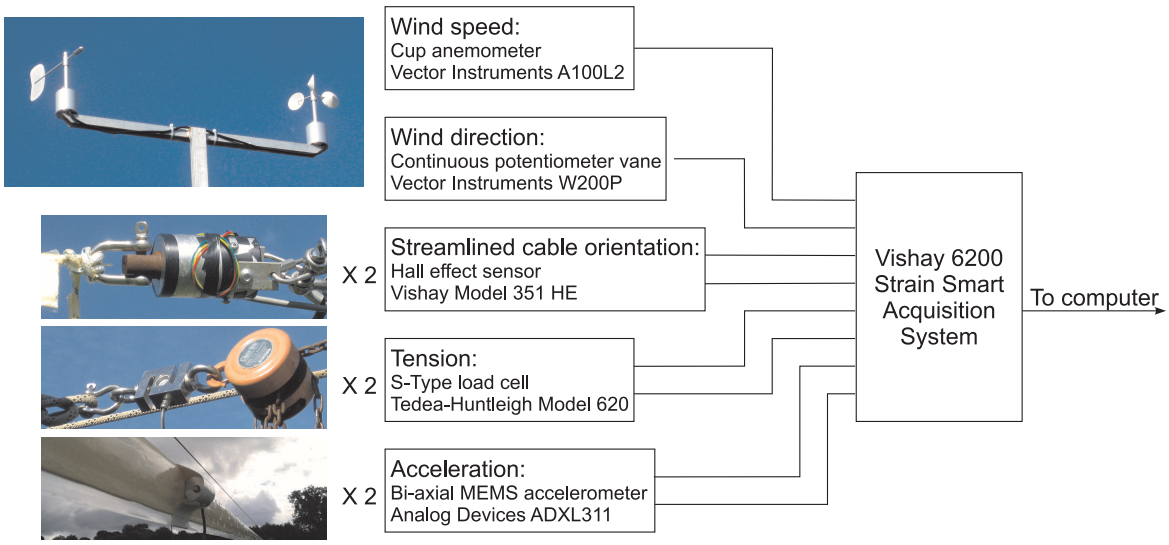

Fig. 6.22 Overview of sensors and data-logging set-up.

Eight channels were collected with a Vishay 6200 Strain Smart data acquisition system: two load cells, two Hall effect sensors, two accelerometers, the anemometer and the wind-vane. Figure 6.22 gives a general overview of the data-logging system including sensor information and photos of the sensors in place.

Over the course of the horizontal field experiment, problems related to the construction and degradation of the streamlined cable were identified. These issues are presented and briefly discussed in this section.

One of the first issues initially became apparent during tests under a balloon with the wound steel cable: the streamlined cable would twist under tension. When the wound steel streamlined cable was tested horizontally the same twisting behaviour was observed. Initial hypotheses of why the cable twisted were that it was a side-effect of the manufacturing process or due to the wound steel cable not being torque balanced. It was concluded that the twisting was due to the rotational imbalance of the wound steel cable as the twist became worse with increased tension and the braided polyester streamlined cables did not show the same behaviour. Figure 6.23 shows the twisted configuration of the wound steel cable supported horizontally under tension.

At this stage of the project, feeding more than one lengthwise element had not been incorporated into the manufacturing process. The wound steel cable was chosen in the streamlined cable construction as a straightforward method to move the centre of mass of the cable towards the leading edge (relative to a polyester streamlined cable). A search for alternative inner cables, with similar mass per unit length and diameter, which were torque balanced

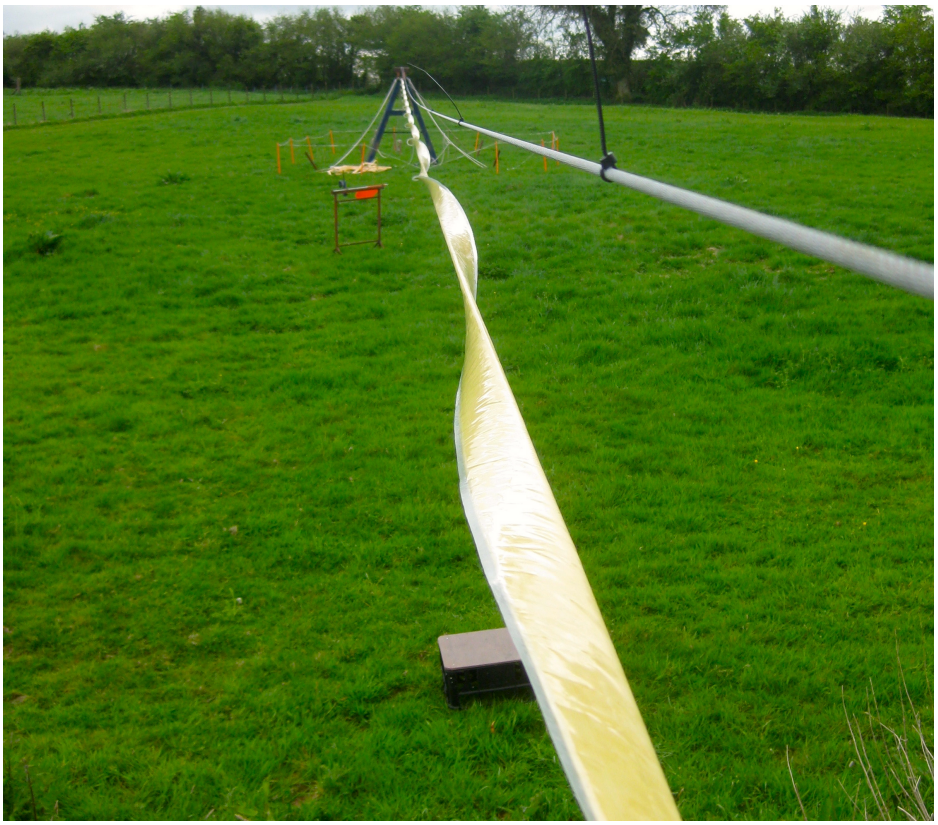

Fig. 6.23 Twisting behaviour of the wound steel streamlined cable under tension.

yielded only a few options. Of the options, a 5 mm diameter "rotationally resistant" cable consisting of wound elements in opposing directions was selected. The rotationally resistant cable was incorporated into a streamlined cable. However, when tensioned, the streamlined cable exhibited the same twisting behaviour but to a lower extent. The unavailability of a cable with large enough mass per unit length to significantly alter the centre of mass and small enough diameter to fit at the nose of the aerofoil motivated the development of including both a braided fibre cable and steel wire into the streamlined cable manufacturing process.

Further issues which became apparent through testing were related to the streamlined cable's wear and degradation. One of the appealing features of the horizontal set-up was that it could be left to collect data over the course of a few days. However, when left exposed to the sun and rain, the polyurethane foam degraded relatively quickly. For example, as seen in the Figure 6.11 and 6.23, the polyurethane foam used to manufacture the streamlined cable is initially firm and pale yellow to white in colour. Figure 6.24 shows a streamlined cable after being exposed to the sun for two days, the foam has begun to degrade, the signs of which are a loss of firmness and discolouration to a darker brownish-yellow. A potential

solution to this problem would be using an opaque film so that the foam is not exposed to the sun. However, the transparent film was helpful in developing the manufacturing process to see defects, foam quality and cable position.

In addition to the environmental factors contributing to the degradation of the streamlined cable, the loading also caused the foam to crack and the wire in the polyester and steel sample to move within the cross-section. Figure 6.25 shows a backlit view of the streamlined cable where cracks have developed due to the applied tension. As the streamlined cable is tensioned, the polyester cable and film extend axially. Therefore, the foam, which is fused to the film and cable, must also extend. If the foam cannot elastically deform with the film and cable, cracks develops.

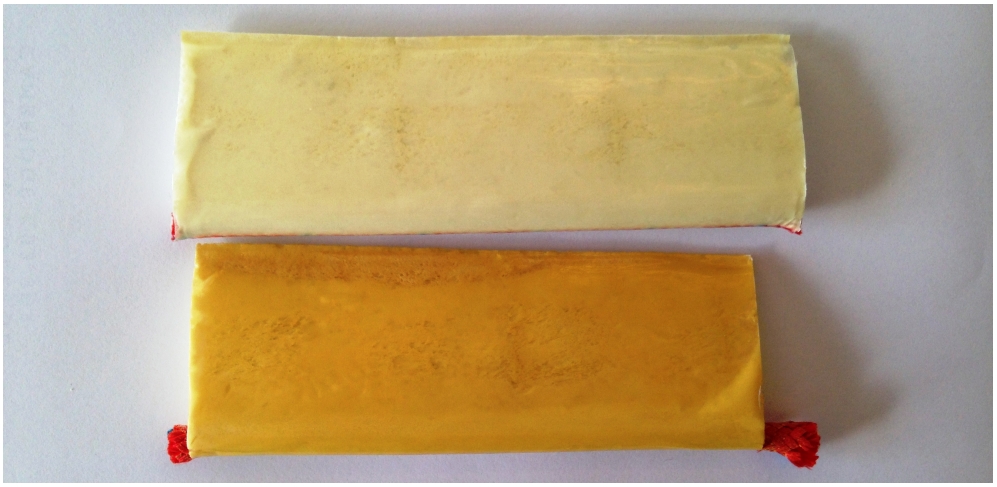

Fig. 6.24 Streamlined cable foam degradation to a brownish-yellow colour.

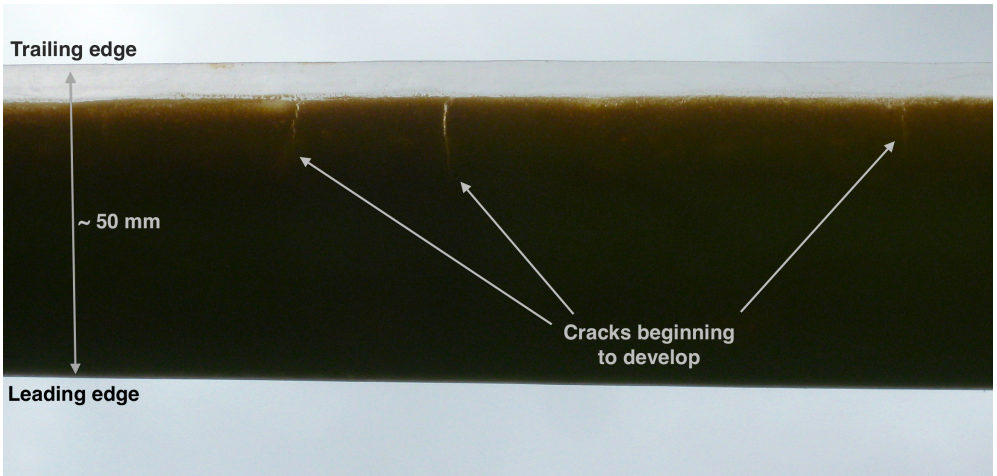

Fig. 6.25 Streamline cable crack.

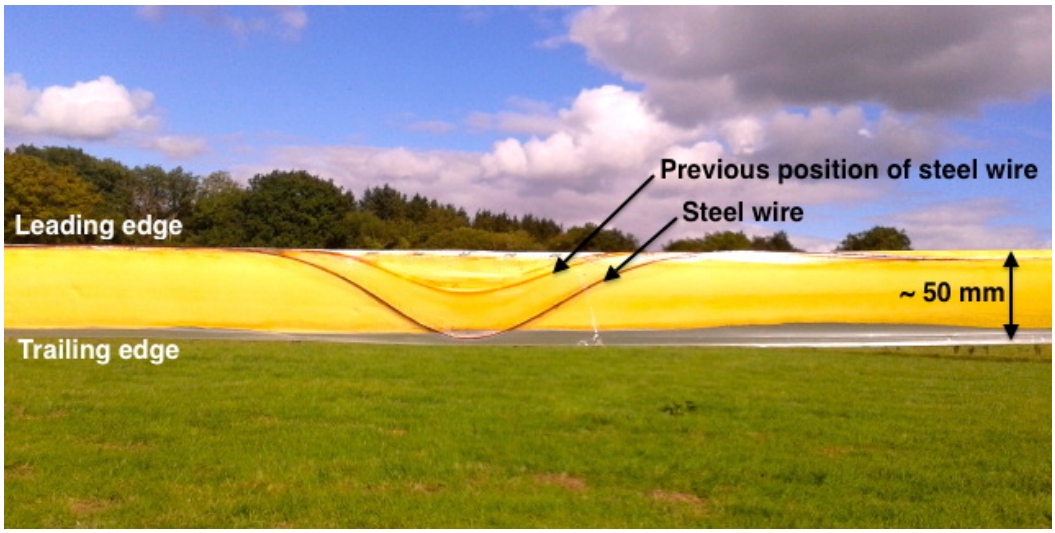

Fig. 6.26 Steel wire movement after cyclic loading of the polyester and steel wire streamlined cable.

Figure 6.26 shows the polyester and steel sample after it has been loaded at various tensions. Two dark brown curved lines are visible, the top one is a residual stain from a previous location of the steel wire and the bottom curve is the steel wire itself. Loading and unloading the streamlined cable seems to have forced the steel wire to shift along the length and, even when the streamlined cable itself is under tension, the steel wire is in a compressed state causing this curved shape. How the streamlined cable is terminated likely plays an influential role in this behaviour. In the horizontal experiment, the tension was applied to the fibre rope and the two ends of the steel wire are free. This behaviour highlights how composite cross-sections can complicate the cable termination.

As demonstrated by the horizontal streamlined cable experiment, the issues associated with a streamlined cable are not only related to stability. Running the horizontal experiment helped highlight and identify some of the practical issues associated with implementation of a streamlined cable.

6.4 Conclusions

This chapter has described how a manufacturing process for streamlined cable was developed and the produced cable incorporated into a horizontal field experiment. The manufacturing process initially began on a small scale by prototyping short streamlined sections using foam injected into a mould. This process was scaled-up by ESE Ltd. and DT Ltd. who developed a streamlined cable manufacturing machine. The machine successfully produced

lengths of streamlined cable between 50 m to 150 m. Two cross-sectional models were used to obtain the cross-sectional properties of the samples, which are necessary for the dynamic modelling presented in the previous chapters. The results of these two cross-sectional models compared well with each other. Where possible, the calculated cross-sectional properties were also compared to experimental measurements. All the calculated values matched the measured results to within 29% apart from the torsional stiffness. The large discrepancy in the torsional stiffness result was attributed to whether the polyethylene film, forming an exterior skin of the streamlined cable act as a closed or open thin-walled section. Finally, various experiments using the manufactured streamlined cable were described including wind tunnel, kite, balloon and a horizontal field test. The horizontal field test was an experiment monitoring the behaviour of a 50 m length of streamlined cable subjected to wind loading. The results from the cross-sectional modelling and the experimental measurements from the horizontal test are used in the next chapter to help validate the dynamic models presented in the previous three chapters.

Chapter 7

Model Validation and Experimental Results

In order to build confidence that the two-degree-of-freedom and discrete models give correct results, they are used to model two benchmark cases: the Goland wing and a beam under tension. The wing case is also used to examine the effect of assuming steady, quasi-steady or fully unsteady aerodynamic loading. The properties of the manufactured cable calculated in Chapter 6 and the discrete model are used to model the horizontal set-up. The experimental results are used to determine the natural frequencies of the system and verify whether the system suppresses VIV. The behaviour predicted by the discrete model and the observed behaviour are compared.

7.1 Benchmark Case: Goland Wing

The Goland wing is a relatively short, uniform, cantilevered wing often used to validate the behaviour of aeroelastic models, for example by Patil et al. [101] and Murua et al. [92]. Goland's original paper [49] defines the properties of the cantilevered wing and solves for the flutter speed and frequency. However, it should be noted that although the methodology is correct, due to numerically incorrect aerodynamic parameters, the calculated result is incorrect. The correct flutter speed and frequency are given in a short appendix of a later paper by Goland and Luke [50]. Table 7.1 gives the physical properties, flutter speed and flutter frequency of the Goland wing.

Disregarding fluid effects, the Goland wing is an inertially eccentric (centre of mass is offset from the shear centre) beam. This eccentricity causes the torsion and bending of the beam to be coupled. Banerjee [10] derives explicit expressions for the natural frequency and

mode shapes of a bending-torsion coupled beam and uses the Goland wing as an illustrative application of the derived expressions. Table 7.2 gives the first four natural frequencies of the cantilevered wing neglecting fluid effects.

The eigenvalue problems (3.27) and (5.64) define the stability, at a prescribed wind speed, of the two-degree-of-freedom and discrete models respectively. As described in section 3.4, solving the eigenvalue problem gives eigenvalue solutions of the form $\lambda_j = \alpha_j + i\omega_j$. To determine the stability boundary, eigenvalues are calculated at increasing wind speed. When the increase in wind speed causes the real part of one of the eigenvalues (α_j) to transition from negative to positive, the system becomes unstable. The wind speed at which $\alpha_j = 0$ is the stability boundary.

Table 7.1 Properties of the Goland wing.

Symbol	Property	Value	Units
L	Span	6.096	m
b	Semi-chord	0.9144	m
m	Mass per unit length	35.72	kg/m
I_s	Moment of inertia per unit length	8.643	kgm
EI_z	Bending stiffness	9.773×10^6	Nm^2
GJ	Torsional stiffness	9.876×10^5	Nm^2
r	Centre of mass	-0.14 (43% chord)	
s	Shear centre	-0.34 (33% chord)	
ρ_a	Air density	1.226	kg/m^3
U_f	Flutter speed	137.2	m/s
ω_f	Flutter frequency	70.69	rad/s

Table 7.2 Natural frequencies of Goland wing without fluid effects.

Mode	Natural frequency (rad/s)
1	48.2
2	95.7
3	244
4	348

7.1.1 Two-Degree-of-Freedom Goland Wing Model

To model the Goland wing as a two-degree-of-freedom system, the elasticity and inertia of the uniform cantilever beam are reduced to equivalent forms. Using the closed-form solution for the tip deflection of a cantilever beam subject to a distributed load [36], the bending and torsional elasticity can be reduced to equivalent springs of stiffness

$$k_{\mathrm{b}} = \frac{8EI}{\ell^4} \tag{7.1}$$

and

$$k_{\mathrm{t}} = \frac{2GJ}{\ell^2} \tag{7.2}$$

respectively. As the natural frequencies and equivalent stiffness of the beam is known, the equivalent inertia is calculated from the eigenproblem form of the structural equations of motion (3.1). The calculated equivalent mass per unit length is m=22.9 kg/m and rotary inertia about the centre of mass is I_{g}=6.26 kgm. Having reduced the cantilever beam to an equivalent two-degree-of-freedom form, the eigenvalues are calculated with increasing wind speed to analyse stability.

Figures 7.1a to 7.1c show how the eigenvalues, separated into the frequency and growth components, vary with increasing wind speed for the steady, quasi-steady and unsteady aerodynamic load assumptions. Any location where the growth rate becomes positive indicates a flutter or divergence condition.

Comparing Figures 7.1 (a), (b) and (c), it is apparent that the dependence of the eigenvalues on wind speed differs dramatically between aerodynamic assumptions. Table 7.3 summarises the calculated flutter speed and frequency and compares the result to the closed-form solution. The quasi-steady assumption yields the worst result, this is because the flutter occurs at a relatively high reduced frequency of 0.47. Typically, values above 0.2 are considered highly unsteady [82]. Unsurprisingly, the unsteady aerodynamic loading assumption, which is the most comprehensive of the assumptions, best models the Goland wing with about a 7% error in both the calculated flutter speed and frequency.

7.1.2 Discrete Goland Wing Model

The Goland wing case is also used to validate the aeroelastic behaviour of the discrete model. Neglecting fluid effects, Banerjee's explicit expressions [10] for the natural frequencies and mode shapes of a bending-torsion coupled beam are used to ensure that the discrete model captures the correct structural coupling. Figure 7.2 shows the convergence of the

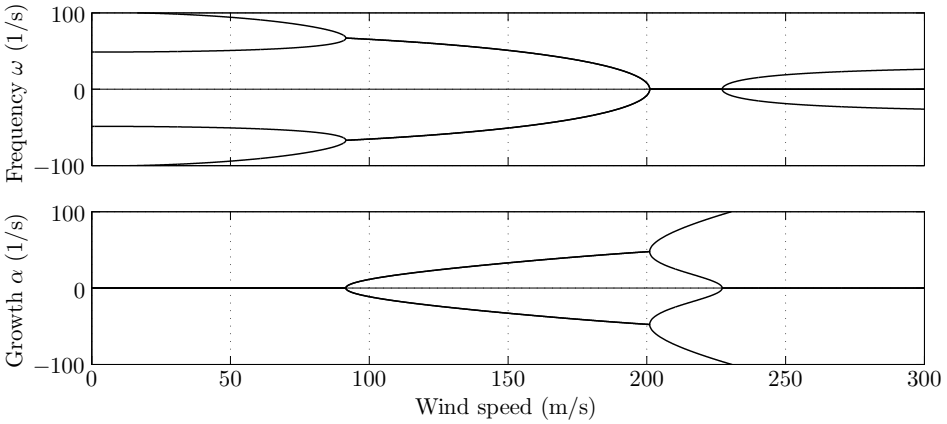

(a) Steady aerodynamic loading, flutter occurs at 91.6 m/s and 66.9 rad/s.

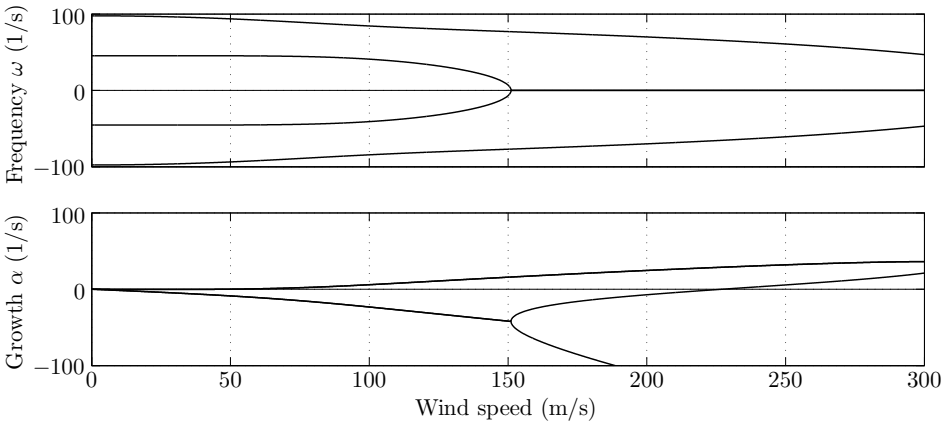

(b) Quasi-steady aerodynamic loading, flutter occurs at 48.1 m/s and 94.0 rad/s.

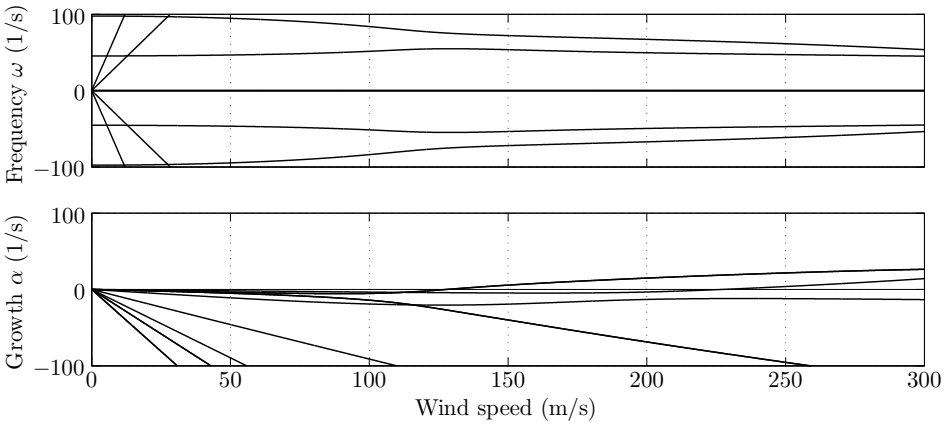

(c) Unsteady aerodynamic loading, flutter occurs at 127 m/s and 75.4 rad/s.

Fig. 7.1 Growth rate and frequency of eigenvalues of the two-degree-of-freedom Goland model assuming steady, quasi-steady and unsteady aerodynamic loading.

Table 7.3 Flutter boundary of two-degree-of-freedom Goland wing model.

Aerodynamic assumption	Flutter speed		Flutter frequency	
	(m/s)	(% error)	(rad/s)	(% error)
Steady	91.6	33	66.9	5.3
Quasi-steady	47.8	65	94.0	33
Unsteady	128	6.8	75.3	6.5

first four bending-torsion natural frequencies of the beam, normalised with respect to the analytical solution. As expected, the higher modal frequencies require a greater number of elements to converge to the correct solution. With nine elements, the model captures the first four frequencies to within 0.8% of the closed-form solution. Figures 7.3 and 7.4 compare the closed-form mode shape solution to the result from a 10 element discrete model for the first two bending-torsion coupled modes. The bending and torsion modes are normalised so that the largest mode shape displacement is unity. The closed-form solution is shown as a continuous line and the discrete model by a marker at each node. The discrete model correctly models the eccentric beam as the markers representing the nodal displacements lie directly along the closed-form solution.

As the discrete model correctly reproduces the structural behaviour of the wing, the aeroelastic behaviour is verified. The stability of the discrete Goland wing model is analysed by calculating the eigenvalues of the discrete system, given by equation (5.64), for increasing wind speed. Similar to the two-degree-of-freedom case, eigenvalue results for the steady, quasi-steady and unsteady aerodynamic loading assumptions are compared in Figures 7.5 (a), (b) and (c).

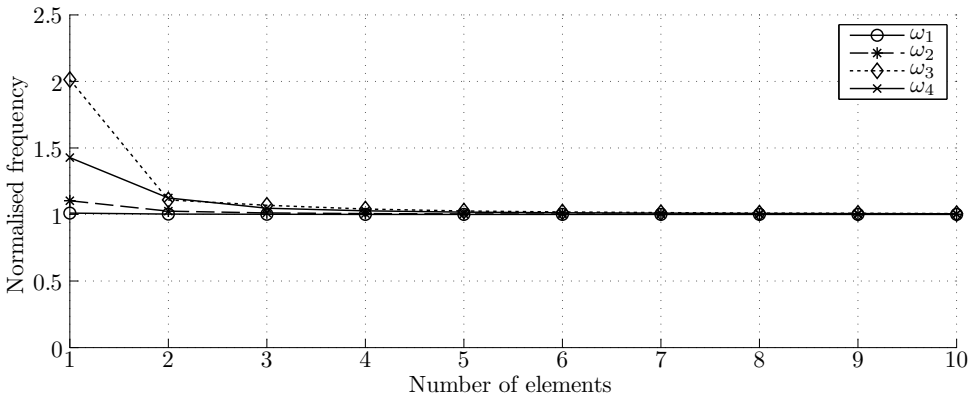

Fig. 7.2 Convergence of Goland wing natural frequencies

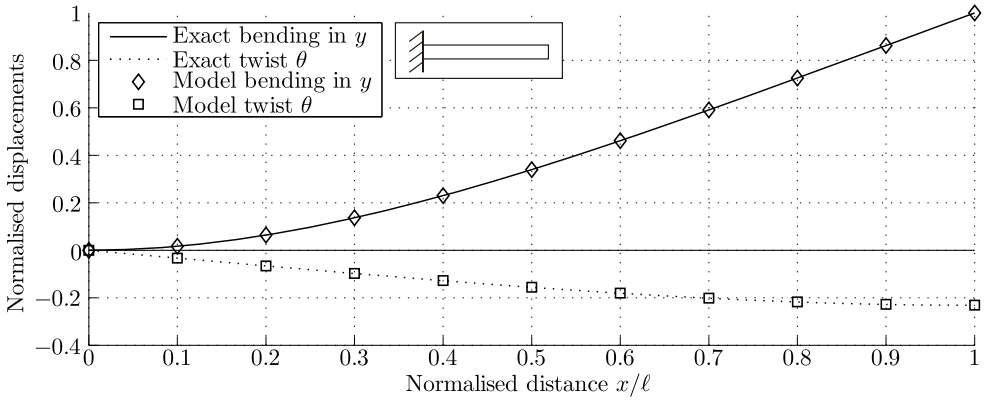

Fig. 7.3 Mode 1 of the Goland wing without fluid effects. Calculated from a 10 element discrete model and compared to the exact solution.

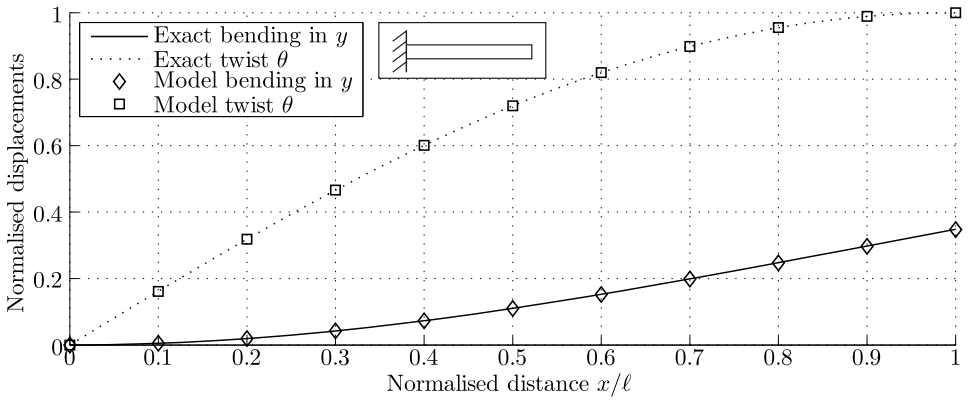

Fig. 7.4 Mode 2 of the Goland wing without fluid effects. Calculated from a 10 element discrete model and compared to the exact solution.

The discrete and two-degree-of-freedom models show similar variation of the eigenvalues with wind speed. The most immediate difference between the figures produced from the two models is the greater number of eigenvalues in the discrete case. However, the first two eigenvalues in both models, which are complex conjugate pairs, follow the same overall pattern for the steady, quasi-steady and unsteady cases. Table 7.4 gives the flutter speed and frequency calculated from the discrete model and percent difference from the exact result. Similar to the two-degree-of-freedom case, the steady and quasi-steady assumptions give poor estimates of the flutter boundary. However, the fully unsteady 10 element discrete model yields a flutter speed and frequency within 0.15% of the exact solution. In fact, Table 7.5 shows that the discrete model estimates the flutter speed to within 1% with as few as 2 elements.

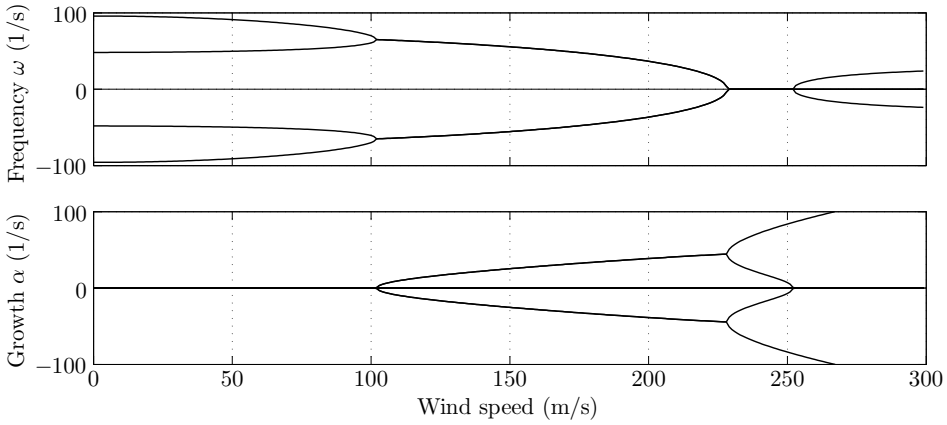

(a) Steady aerodynamic loading, flutter occurs at 102 m/s and 65.0 rad/s.

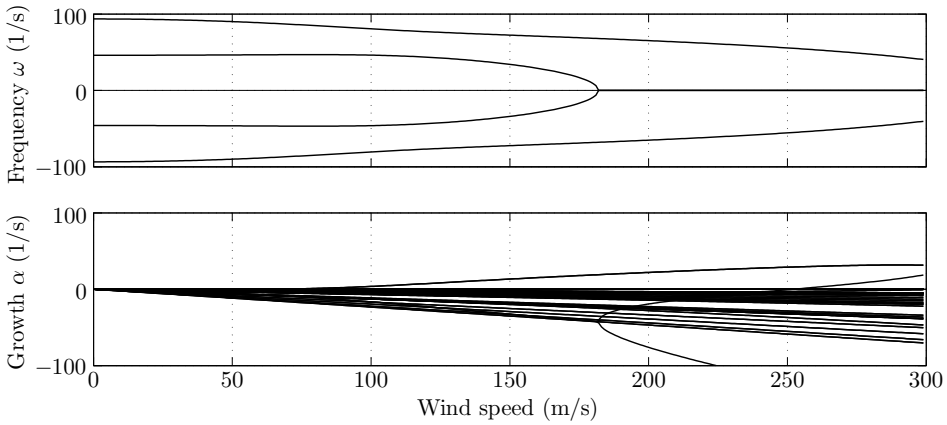

(b) Quasi-steady aerodynamic loading, flutter occurs at 64.6 m/s and 87.8 rad/s.

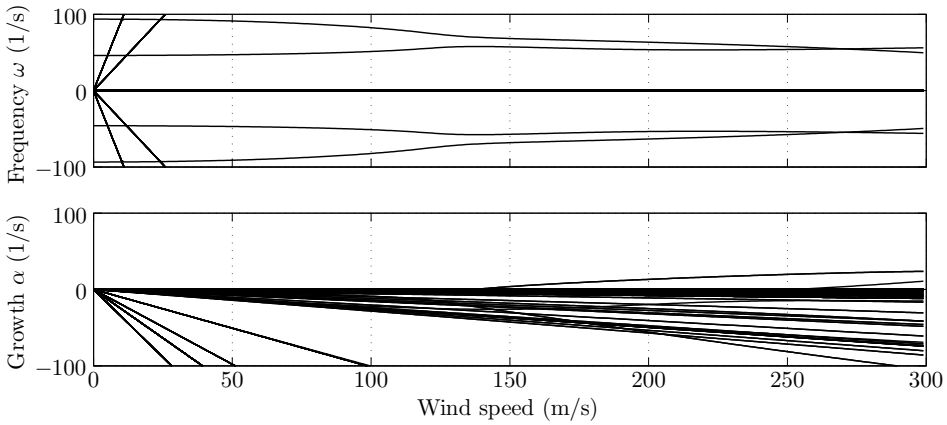

(c) Unsteady aerodynamic loading, flutter occurs at 137 m/s and 70.7 rad/s.

Fig. 7.5 Growth rate and frequency of eigenvalues of the 10 element discrete Goland model assuming steady, quasi-steady and unsteady aerodynamic loading.

In conclusion, the fully unsteady discrete model has proven to correctly model the structural and aeroelastic coupling of the Goland wing case. Although this validates the flexural, torsional and aeroelastic behaviour of the discrete model, it does not include the effect of tension, which is addressed in the following section.

Table 7.4 Flutter boundary of discrete Goland wing model.

Aerodynamic assumption	Flutter speed		Flutter frequency	
	(m/s)	(% error)	(rad/s)	(% error)
Steady	102	25	65.0	8.1
Quasi-steady	64.6	53	87.8	24
Unsteady	137	0.2	70.7	0.8

Table 7.5 Discrete model of Goland wing flutter speed convergence.

Number of elements	Flutter speed (m/s)	Percent difference
1	124.5	9.2 %
2	135.8	1.0 %
3	136.6	0.41 %
4	136.8	0.27 %
10	137.0	0.15 %

7.2 Benchmark Case: Tensioned Beam

As described in section 5.3.3, the discrete streamlined cable model includes the effect of tension through a geometric stiffening term. The closed-form solution of a uniform tensioned beam is used to verify that the tension is correctly incorporated into the model.

Bokaian [19] gives expressions for the natural frequencies and mode shapes for a uniform beam under tension subject to a number of end conditions. Bokaian defines the dimensionless tension parameter

$$\tau = \frac{P\ell^2}{2EI}, \tag{7.3}$$

which gives an indication of whether beam or string behaviour dominates. Beams with values of $\tau \geq 12$ behave like a string; for values of $\tau \leq 12$ the beam effects are significant. The discrete model results are compared to the analytical solution by modelling a fixed-fixed

beam with the cross-sectional properties of the manufactured red polyester sample (calculated by the BECAS model) described in section 6.2.3. However, in order to compare the behaviour to the closed form solution, all the structural centres are assumed to be concentric. As the discrete model includes both beam and string behaviour, the length and tension of the validation case are chosen to give a value of $\tau = 8.4$ so that the model exhibits mixed beam and string behaviour. Table 7.6 gives a summary of the tensioned beam parameters.

Table 7.6 Properties used in the tensioned beam validation case.

Symbol	Property	Value	Units
ℓ	Length	1	m
P	Tension	100	N
m	Mass per unit length	0.065	kg/m
I_g	Moment of inertia per unit length	1.1×10^{-5}	kgm^2
EI_y	Bending stiffness	6.0	Nm^2
τ	Dimensionless tension parameter	8.4	-

Figure 7.6 shows the calculated natural frequencies of the first four modes normalised with respect to the analytical solution. With 6 elements, the discrete model calculates the first four natural frequencies to within 1% of the closed-form solution. Figures 7.7 and 7.8 compare the theoretical and discrete model solutions for the first two mode shapes. The closed-form solution is shown as a continuous line and the discrete solution with markers at each node. The discrete results show good agreement to the closed-form solution. Comparing the discrete model to this simple analytical case builds confidence that the geometric stiffening matrix correctly accounts for the effect of tension.

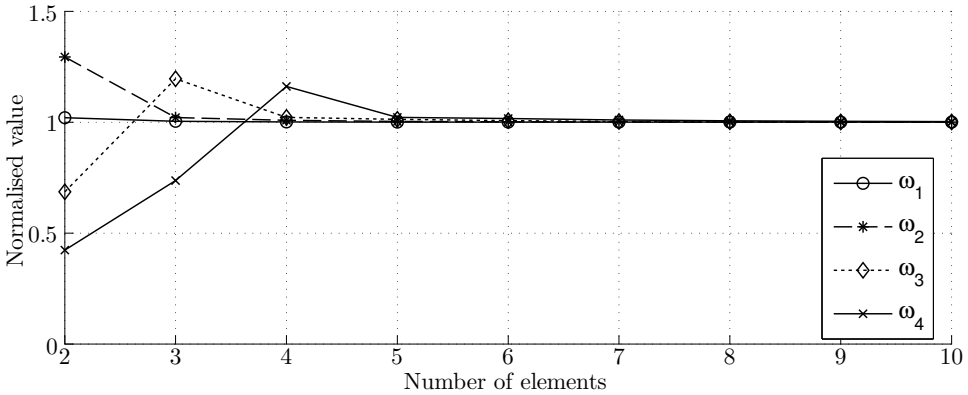

Fig. 7.6 Convergence of beam-string model.

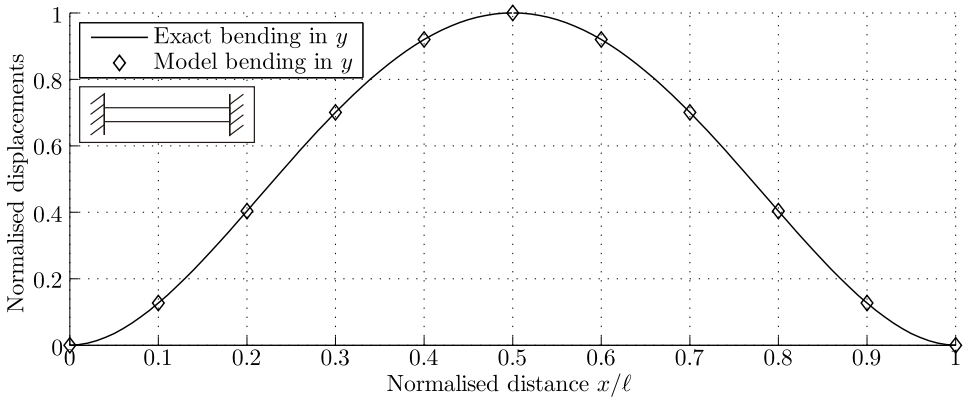

Fig. 7.7 Mode 1 of the tensioned beam. Calculated from a 10 element discrete model and compared to the exact solution.

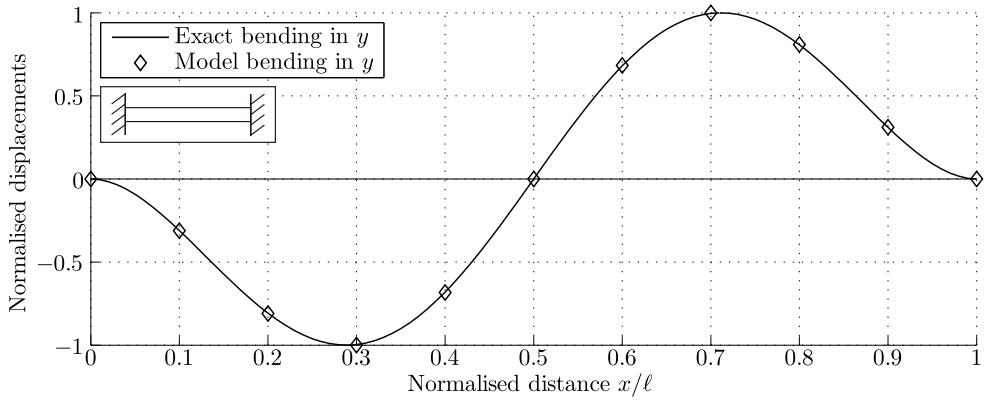

Fig. 7.8 Mode 2 of the tensioned beam. Calculated from a 10 element discrete model and compared to the exact solution.

The comparison of the discrete model to the Goland wing and tensioned beam cases has served to benchmark the discrete model. The two cases provided a means to verify that the model correctly accounts for inertial eccentricity, unsteady fluid effects and an applied tension. The comparison is very much between two theoretical models. The experimental results and observations acquired through the horizontal field experiment provide a real world comparison. In the next section the experimental results are analysed and compared to the discrete model.

7.3 Experimental Results

The horizontal experimental set-up described in Chapter 6 may not be representative of a specific streamlined cable application. However, the experiment provides an opportunity to

draw comparisons between a simplified model of the set-up, collected data and overall observations. The simplified model neglects the effect of gravity and assumes the streamlined cable is straight and subject to a constant external tension. Natural frequencies of the system are compared through impulse tests. A check on whether the streamlining reduces VIV is completed by analysing the measured frequencies on the bare and streamlined cable. The observed flutter behaviour is compared to the that predicted by the model.

7.3.1 Impulse Testing

As a simple test to determine the natural frequencies, the accelerometers were used to measure the impulse response of both the bare and streamlined cable. The acceleration was measured at a fixed location and an impulse was applied at various locations along the cable. The characteristics of the impulse were not measured. The natural frequencies are obtained from the measured acceleration response and compared to those obtained analytically or from the discrete model.

The bare cable provides a simple system with which to validate the measured values. The natural frequencies of the bare cable should approximately match the theoretical solutions for a taut string given by $\omega_n = \frac{n\pi}{L}\sqrt{\frac{P}{m}}$. Figure 7.9 shows the power spectral density (PSD) of the measured acceleration impulse response. The PSD is calculated from Welch's method using a Bartlett window and 50% overlap. The theoretical natural frequencies are calculated based on the measured mass per unit length of 0.03 kg/m, cable length of 50 m and applied tension of 785 N. The measured results show fairly good alignment for the first nine natural frequencies. Some discrepancy is expected between the analytical solution and the measured results due to effects such as cable sag (see Irvine and Caughey [71]) and wind loading. The measured wind speed varied throughout the measurement interval from 0 to 2 m/s. A wind speed of 2 m/s corresponds to a Reynolds number of approximately 700 and therefore a Strouhal number of approximately 0.2 (see Figure 2.16). Therefore, vortex shedding would likely have occurred at frequencies below 80 Hz and may have affected the measured results.

The same impulse test was repeated on the streamlined cable. For the streamlined cable, there is added complexity since the cross-section only has one axis of symmetry. Applying an impulse to the same point on the cross-section for a 50 m long cable, even without the addition of wind, is difficult. Figure 7.10 shows the measured PSD for the acceleration impulse response of the streamlined cable. The measured results are compared to a discrete streamlined cable model assuming no wind and pinned boundaries. The impulse is assumed

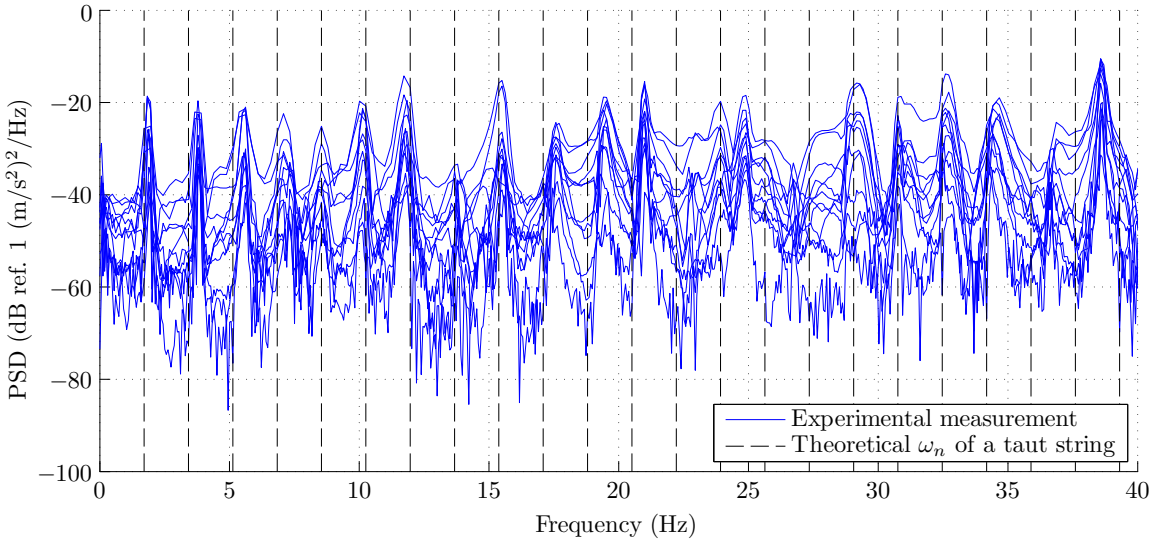

Fig. 7.9 Power spectral density of the measured acceleration impulse response of the bare red polyester cable under 785 N tension. The vertical lines show the natural frequencies calculated from the analytical solution for a taut string.

to be applied and measured along either the y or z axes, defined in the discrete model as axes perpendicular and parallel to the chord length respectively. The frequency response function $\mathbf{H}$ is given by

$$\mathbf{H} = \left(-\omega^2 \mathbf{M}_c + \mathbf{K}_c(1+i\eta)\right)^{-1} \tag{7.4}$$

where $\mathbf{M}_c$ is the streamlined cable mass matrix and $\mathbf{K}_c$ is the streamlined cable stiffness matrix. A complex stiffness is included to account for some structural damping with the loss factor η approximated as 0.01. Each element of the matrix $\mathbf{H}$ corresponds to the input and response at given nodes, i.e. the element on the n^{th} row and m^{th} column corresponds to the response for a unit impulse applied at the m^{th} node and measured at the n^{th} node. Figure 7.11 shows the discrete model acceleration PSD for input and response nodes corresponding to the experimental test. Comparing the experimental and discrete model PSD plots does not show an exact match, but does give natural frequencies which follow the same general pattern and spacing. This comparison provides at least a little confidence that the discrete model gives reasonable results.

7.3.2 Vortex-Induced Vibration

The main advantages of streamlining a cable are the reduction in drag and VIV. In order to verify whether the manufactured streamlined cable inhibits VIV, the recorded frequencies

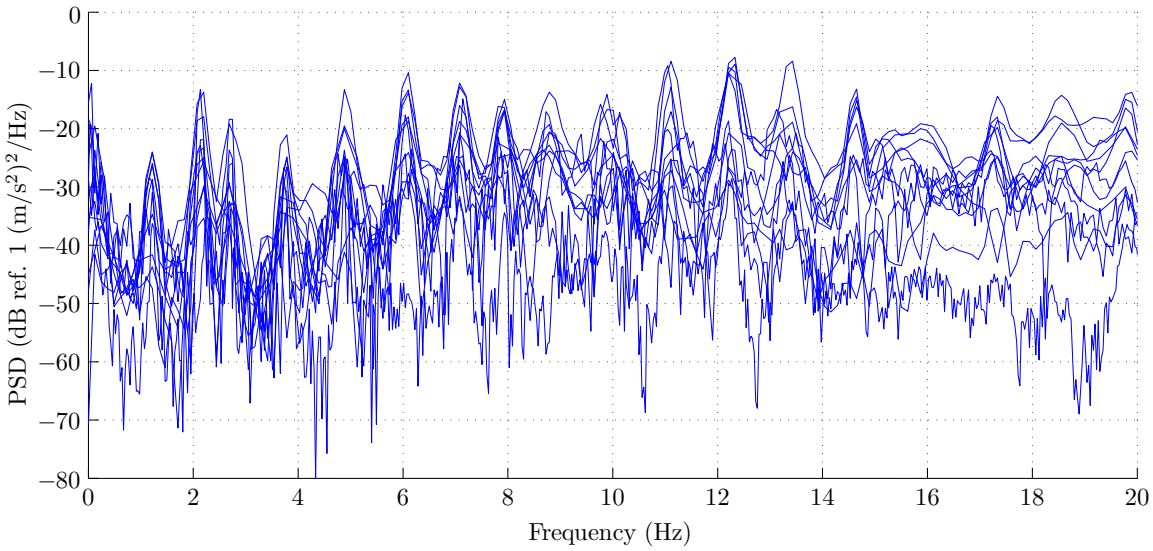

Fig. 7.10 Power spectral density of the measured acceleration impulse response of the streamlined PolyWire cable under 785 N tension.

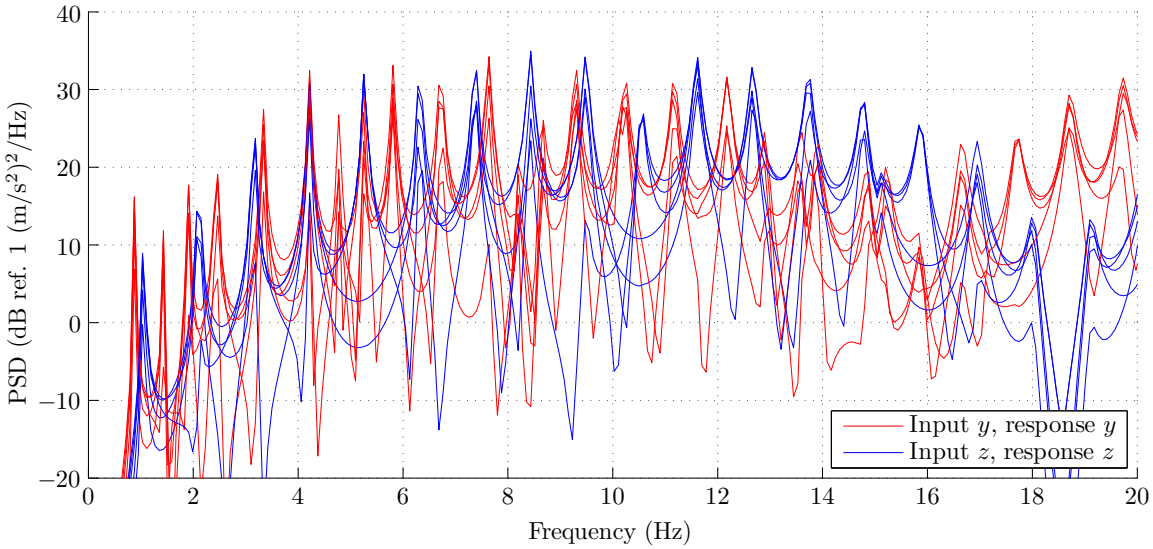

Fig. 7.11 Power spectral density determined from a 36 element discrete model of the streamlined PolyWire cable under 785 N tension.

of the bare and streamlined cable are compared to the theoretical vortex shedding frequency. The acceleration of the streamlined and bare cables, and the wind speed were recorded for a 15 minute (900 second) windy period. Figures 7.12 (a) and (b) plot the measured response as spectrograms for the bare and streamlined cable respectively. The x-axis of the spectrogram gives frequency, the y-axis time and the plotted colour indicates the relative amplitude of the response (warm colours indicate high amplitude and cool colours low amplitude).

The estimated vortex shedding frequency at a given time is calculated from the measured wind speed, the Strouhal number and the characteristic length. The Strouhal number for the bare, circular cross-section cable is taken as 0.2 (see Figure 2.16) and the characteristic length is the 6 mm cable diameter. The Strouhal number for the streamlined profile is taken from Yarusevych and Boutlier [137] who compare the vortex shedding properties of NACA 0012, NACA 0018 and NACA 0025 aerofoils which have boundary layer separation without reattachment at low Reynolds numbers (up to 40,000). They find that the Strouhal number – scaled with a characteristic dimension of the aerofoil height when projected onto a plane normal to the flow direction – is approximately constant at 0.2. The authors also note the Strouhal number for flat plates oriented perpendicular to the flow direction, which is comparable to an aerofoil oriented perpendicular to the flow, is approximately 0.14. Over the course of the experiment, the streamlined cable was observed to align itself with the wind as the wind speed increased. The estimated vortex shedding frequency for the streamlined profile can therefore be taken as a range bounded by the aligned and perpendicular cases. The Strouhal number, characteristic length and vortex shedding frequency estimates for the bare cable, aligned streamlined cable and perpendicular streamlined cable are summarised in Table 7.7.

The vortex shedding frequencies given in Table 7.7 are calculated from the measured wind speed and overlaid on the spectrogram as a solid black line. For the bare cable, the measured response shows a correlation to the vortex shedding frequency as the high am-

Table 7.7 Vortex shedding frequency from Strouhal number for circular and streamlined profiles, note that $\mathrm{St} = fl/U$.

Profile shape and orientation	Strouhal number St	Characteristic length l	Vortex shedding frequency f
	-	(m)	(Hz)
Circular cross-section	0.2	0.01	$f_\mathrm{c} = 20U$
Aerofoil aligned with flow	0.2	0.01	$f_\parallel = 20U$
Aerofoil perpendicular to flow	0.14	0.05	$f_\perp = 2.8U$

plitude response shown by warm colours generally follows the estimated vortex shedding frequency. Comparatively if aligned, the streamlined cable does not exhibit such a strong correlation between the measured frequencies and the expected vortex shedding frequency range. The figure does show excitation at the expected frequencies if the profile is perpendicular to the wind. The above comparison is not meant to be an exhaustive analysis of the vortex shedding characteristics. It provides an indication that the manufactured streamlined cable reduces VIV when aligned and highlights the potential for problems to arise if the section is not aligned with the wind.

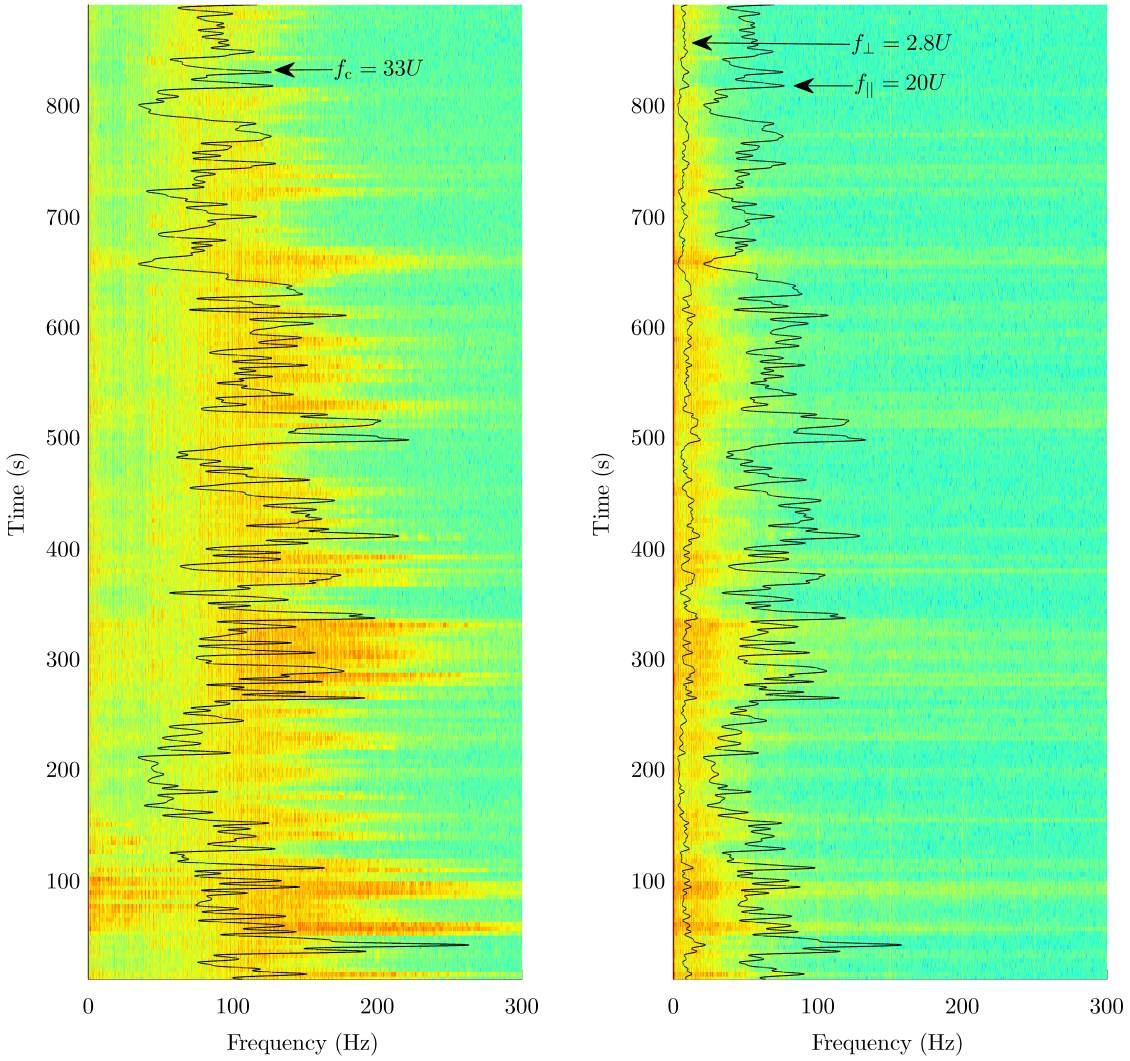

(a) Bare cable.

(b) Streamlined cable.

Fig. 7.12 Spectrogram of bare and streamlined cable under a 300 N tension. The black line indicates the theoretical vortex shedding frequency given the measured wind speed.

7.3.3 Experimental Observations

The horizontal set-up of the streamlined tethers yielded some interesting observational data. The manufactured streamlined RedPoly and PolyWire cables were tested over a number of days. The two cables have the same inner fibre cable and the PolyWire sample has a small 1.2 mm diameter steel wire at the leading edge. Section 6.2 gives a detailed description of the samples with Tables 6.6 and 6.7 listing their cross-sectional properties. The main difference between the two streamlined cables is the position of the centre of mass. The RedPoly sample has a centre of mass located at r=-0.44, which corresponds to a position that is 27% of the chord length, measured from the leading edge. The PolyWire sample has a centre of mass located at r=-0.52, or 24% of the chord from the leading edge.

The RedPoly and PolyWire cable tests were each run on different occasions. Each test was set-up in the field when the weather forecast predicted a period of windier days. The aim of the test was to compare the behaviour of the two cables in approximately similar wind conditions. The wind speed and direction data over the course of each test period is summarised by a wind rose. Figures 7.13 (a) and (b) give the wind roses for the RedPoly and PolyWire tests respectively. The wind rose shows the frequency of wind from a given direction, at a given speed. The wind roses show that for both testing periods the wind came most frequently from the north-east, meaning it blows from the north-east towards the south-west. The streamlined cable is oriented approximately 45 degrees counter-clockwise from the north, meaning it runs from north-west to south-east (see Figure 6.20). Thus, the cable is oriented perpendicular to the highest frequency wind direction. The maximum wind speed seen by the RedPoly cable, in a direction perpendicular to the cable orientation, was about 9 m/s. The maximum perpendicular wind speed seen by the PolyWire cable was about 6 m/s.

Over the course of the testing the PolyWire cable was observed to align itself with the wind and did not exhibit any unstable behaviour. Unfortunately, the data from the orientation sensors did not prove very useful in empirically quantifying the cable's orientation. At higher wind speeds, the central portion of the streamlined cable was observed to align itself with the wind but the ends of the streamlined cable did not appear able to overcome the friction in the swivels. Conversely, the RedPoly sample exhibited very unstable behaviour. At wind speeds between 4.5 to 6.5 m/s at a tension of 700 N the cable oscillated wildly and fluttered. The observed unstable behaviour was recorded with a HD Sony video camera at 50 frames per second (FPS) with 48,000 Hz audio. According to the Nyquist criteria, the maximum observable of the video and audio sampling rates are 25 Hz and 24,000 Hz respectively. The oscillation frequency was interpreted frame-by-frame from the video to be

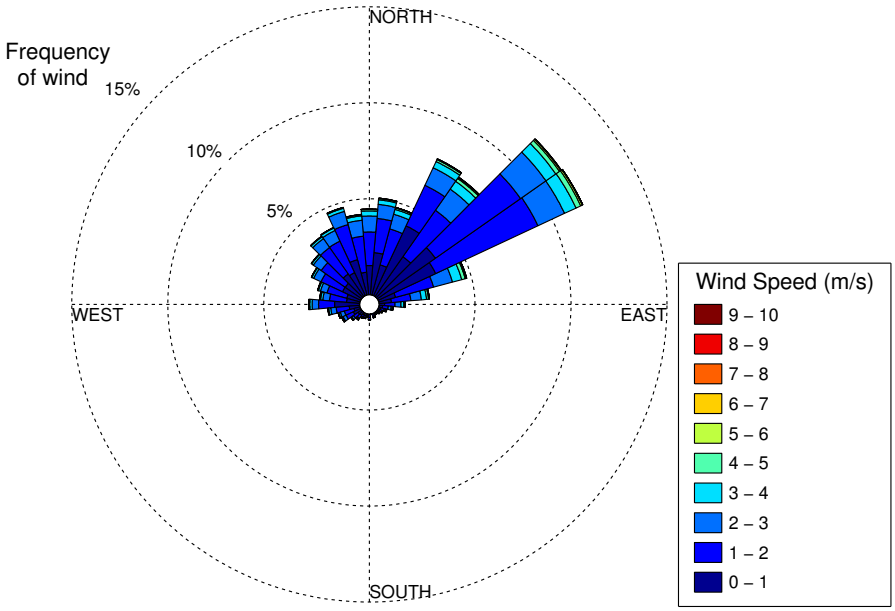

(a) RedPoly test.

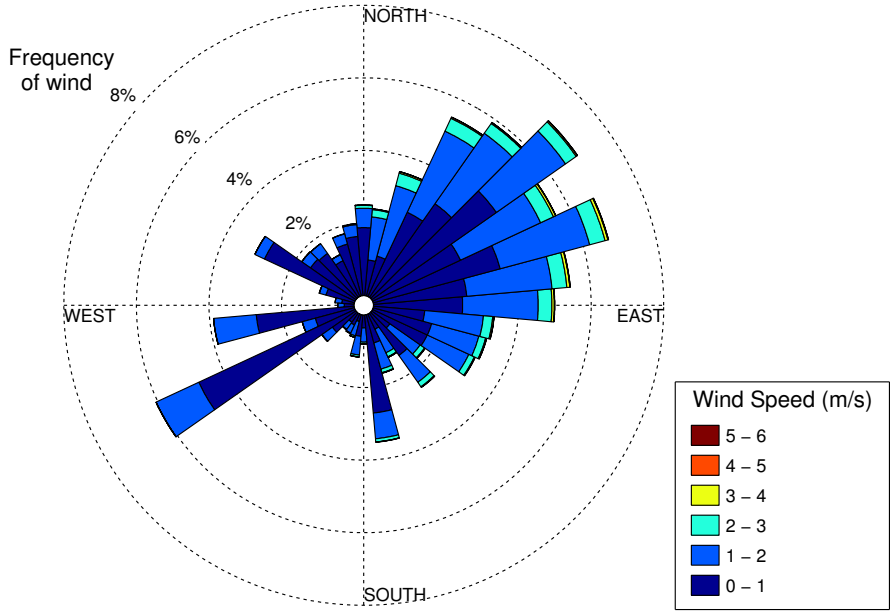

(b) PolyWire test.

Fig. 7.13 Wind rose diagrams summarising the wind speed and direction data for the RedPoly and PolyWire test periods.

8.3 Hz. As a verification of the visually measured frequency, the power spectral density of the audio frequency was also analysed. Figure 7.14 gives the PSD of the audio signal which shows a small peak at 8.3 Hz. The increase in the audio power spectrum at the visually observed flutter frequency gives better confidence that the 8.3 Hz frequency is not an aliased frequency.

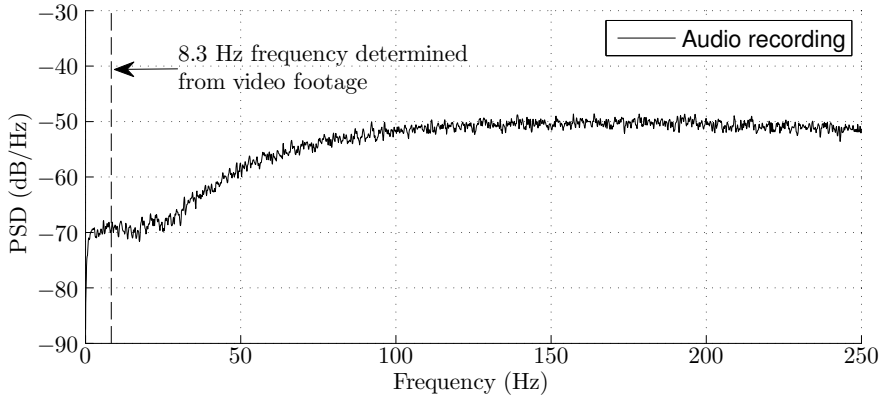

Fig. 7.14 Power spectrum of flutter audio with vertical line indicating the visually observed flutter frequency.

The stability of the RedPoly and PolyWire streamlined cables was calculated using the discrete model described in Chapter 5. The discrete model of the horizontal streamlined cable set-up assumes the cable is straight, under constant tension and has pinned, torsionally-fixed boundaries. The wind is assumed to act uniformly along the length of the cable. This general configuration will be taken as the base-case streamlined cable model and is depicted in Figure 7.15. The cross-sectional properties of the base-case discrete model are taken as either the BECAS calculated properties of the RedPoly and PolyWire samples, repeated here in Table 7.8.

The observed behaviour of the RedPoly and PolyWire experiments is compared to the results of the simplified base-case model. The eigenvalues for the discrete model are calculated at increasing wind velocities and checked for instability, in the same way the flutter speed was determined for the Goland wing case. The convergence of the flutter speed value

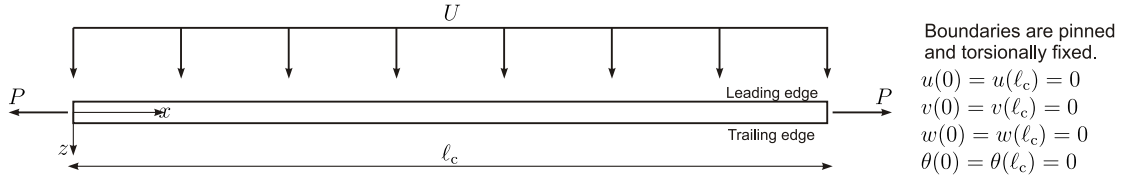

Fig. 7.15 Base-case pinned-pinned streamlined cable subject to constant tension and wind.

Table 7.8 Base-case streamlined cable properties as calculated by BECAS

Symbol	RedPoly	PolyWire	Units
m	0.065	0.070	kg/m
I_G	1.1E-05	1.1E-05	kgm^2
r	-0.44	-0.52	-
EA	0.16	0.16	MN
p	-0.80	-0.90	-
EI_y	6.0	8.1	Nm^2
EI_z	0.45	0.45	Nm^2
GJ	0.25	0.27	Nm^2
s	-0.48	-0.51	-

for the discrete model is verified and used to choose an appropriate number of elements with which to model the base-case. The flutter speed U_f and frequency ω_f of the base-case with the properties of the RedPoly and PolyWire properties, at tensions of 0 N, 400 N and 800 N were calculated with an increasing number of elements. Figures 7.16 and 7.17 show the convergence of the flutter speed and frequency, normalised with respect to the value calculated using 50 elements. Based on the flutter speed and frequency of the RedPoly and PolyWire base-cases, modelling with 28 elements or more gives less than 1% error.

Having checked the convergence of the discrete model, the flutter results are compared to the experimentally observed behaviour. As described above, at a tension of 700 N, the RedPoly sample was observed to flutter at 8.3 Hz in winds between 4.5 to 6.5 m/s. Conversely, no flutter behaviour was observed in the PolyWire sample, which was subject to wind speeds up to 6 m/s. The discrete model predicts the onset of instability at much lower wind velocities around 0.6 m/s to 0.7 m/s at a frequency of 1.3 Hz. Instability is also predicted in both the RedPoly and PolyWire samples. Table 7.9 summarises the experimentally observed and calculated flutter instabilities.

Table 7.9 Experimentally observed and model predicted flutter speed and frequency.

Cable	Method	Flutter speed (m/s)	Flutter frequency (Hz)
RedPoly	Observed	4.5-6.5	8.3
	Discrete model	0.6	1.3
PolyWire	Observed	None	None
	Discrete model	0.7	1.3

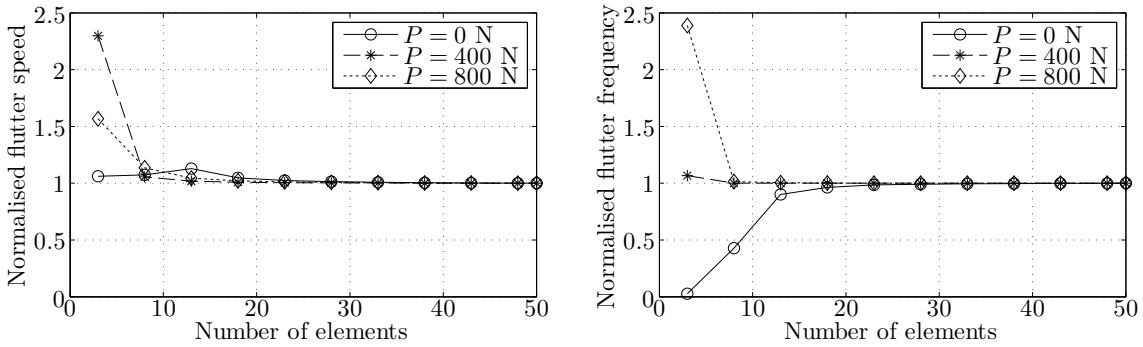

(a) Flutter speed, U_f. (b) Flutter frequency, ω_f

Fig. 7.16 Convergence of 50 m RedPoly streamlined cable model. Values are normalised with respect to the 50 element result.

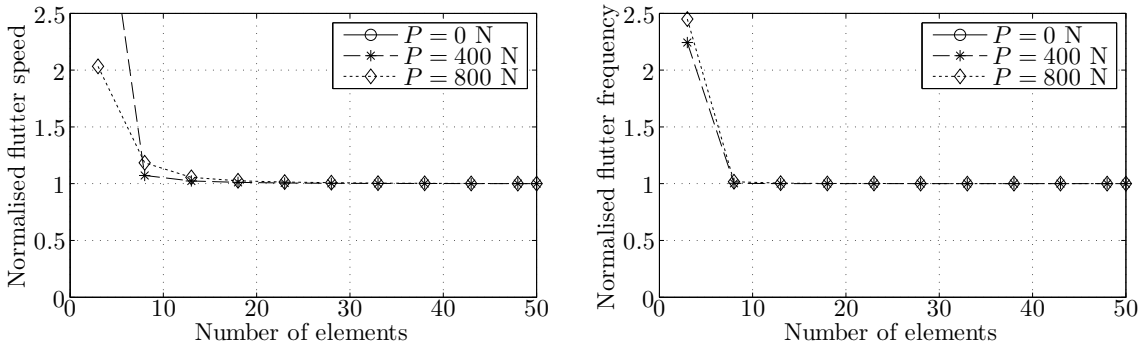

(a) Flutter speed U_f. (b) Flutter frequency, ω_f

Fig. 7.17 Convergence of 50 m PolyWire streamlined cable model. Values are normalised with respect to the 50 element result.

Other than the fact that instability was predicted and observed in the RedPoly case, the discrete model results do not agree with the experimental observations. The base-case discrete model is a simplification of the experimental set-up and does not account for a number of effects such as gravity or gustiness. As discussed in Chapter 6, the calculated cross-sectional properties may also differ from the experimental case as they are an estimate based on practical measurable properties and available material data. As well, the manufacturing process and testing itself imparted inconsistencies such as variable foam density and position of the steel wire over the length. As such, exact like-for-like comparisons are difficult to make. However, the discrete model can be used to explore how some of these various effects, such as the cross-sectional properties and gustiness, affect the system's stability.

7.4 Conclusions

This chapter has explored both analytical and experimental validation cases for the two-degree-of-freedom and discrete streamlined cable models. The discrete model gave excellent agreement with the analytical benchmark cases of the Goland wing and tensioned beam. The experimental results from the horizontal set-up were compared to a simplified discrete model of the experiment. The impulse response of the bare cable was compared to analytical solutions and the experimental data gave good agreement for the first nine natural frequencies. The experimentally measured impulse response for the streamlined cable was compared to the discrete model results. The experimental and model results showed general agreement for the first few natural frequencies and gave approximately the correct spacing between natural frequencies. As a verification of the VIV suppression characteristics of the streamlined cable, a spectrogram of the bare cable and streamlined cable response in a windy period spanning 15 minutes was compared to the published vortex shedding frequency values. The bare cable response did appear to follow the vortex shedding frequency whereas the streamlined cable did not, giving an indication that the streamlined cable does suppress VIV. Finally, the observed flutter behaviour between the RedPoly and PolyWire samples was compared to the behaviour predicted by the simplified discrete model of the horizontal set-up. Though the experimentally observed values do not compare well with the model's predicted values, they did show that the stability is affected by changes in the streamlined cable properties. Specifically, the movement of the centre of mass towards the leading edge of the PolyWire cable was observed to increase its stability. Though the experimental set-up and the discrete model are perhaps too dissimilar to compare like-for-like, the experiments have given insight into some of the practical issues associated with designing, manufacturing and implementing a streamlined cable. In the next chapter, the scope of the discrete model as a tool to investigate stability is demonstrated. The discrete model is used to investigate how properties such as the streamlined cable's cross-sectional characteristics, the wind loading profile and variations in tension affect stability.

Chapter 8

Model Results

The streamlined models developed in the current work are general in nature, therefore they could be used to model a number of streamlined cable applications. Furthermore, for a given application, the models can be used to investigate how variation of the models' input parameters affect stability. The modelled and measured properties of the manufactured streamlined cables provide a realistic starting point from which to investigate the stability of streamlined cables. The developed models are used to explore the effect of varying properties – such as changes in the location of the centres, magnitude of tension, length, stiffness, distribution of wind and variation of tension – on the stability of the streamlined cable.

8.1 Base-Case Definition

The 50 m samples of manufactured streamlined cable are taken as a realistic base-case from which to explore the stability of streamlined cables. The properties of the RedPoly and the PolyWire streamlined cables from Table 7.8 are used. The base-case is taken as the simple configuration described in section 7.3.3 and consists of a straight length of streamlined cable, subject to a constant external tension, uniform wind and pinned boundary conditions (see Figure 7.15).

To reduce the base-case to a form compatible with the two-degree-of-freedom model, the elasticity needs to be represented by equivalent spring stiffnesses. The bending spring stiffness is estimated from the analytical expression for the central deflection of a pinned-pinned beam subject to a distributed load [36] as

$$k_{\mathrm{b}} = \frac{384 E I_{zz}}{5\ell^4}. \tag{8.1}$$

The torsion stiffness is estimated from the analytical solution for a fixed-fixed shaft subject to a distributed torque as

$$k_{\mathrm{t}} = \frac{8GJ}{\ell^2}. \tag{8.2}$$

The stiffness due to tension is estimated from the analytical solution for the first natural frequency of a string under tension as

$$k_{\mathrm{p}} = \left(\frac{\pi}{\ell}\right)^2 P. \tag{8.3}$$

The discrete and two-degree-of-freedom models are used to explore how changes in the base-case properties affect the stability.

8.2 Centre of Mass Position

In classic flutter analysis of a wing, which is not subject to tension, the relative location of the centre of mass and the aerodynamic centre to the shear centre strongly influences the wing's stability. As described in the literature review, Blevins [17] helpfully summarises the stability results for the classic two-degree-of-freedom flutter case with quasi-steady fluid loading as Table 2.2. The classic results indicate that divergence is present when the aerodynamic centre is forward of the shear centre and flutter is present when the centre of mass is aft of the shear centre. The RedPoly sample has an aerodynamic centre forward, and a centre of mass aft, of the shear centre, indicating that it will flutter and diverge. The PolyWire sample has an aerodynamic centre aft, and a centre of mass forward, of the shear centre, indicating that it will not flutter nor diverge. The two-degree-of-freedom and discrete model, which include fully-unsteady fluid loading, are used to explore how stability of the base-case, with and without the inclusion of tension, compare to each other and this classic result.

8.2.1 Neglecting Tension

Neglecting the effect of tension, the only difference between the extended two-degree-of-freedom model detailed in Chapter 3 and Blevins classic flutter model is the inclusion of fully-unsteady fluid effects. Figures 8.1 (a) and (b) show how the flutter and divergence speeds vary with changes in the position of the centre of mass. The calculated results are for the base-case with the RedPoly and PolyWire cable properties. The dimensionless location of the centre of mass ranges from -1 to 1 and corresponds to the coordinate system depicted

in Figures 3.2 and 5.5. According to this coordinate system, -1 is the leading edge, 0 is the semi-chord and 1 as the trailing edge. The red, blue and green dotted vertical lines show the values of the dimensionless position of the mass, shear and aerodynamic centre locations r, s and q respectively.

The results of Figure 8.1 (a) compare well with Blevins criteria. The RedPoly sample has an aerodynamic centre forward of the shear centre which indicates that the section will always diverge. This corresponds to the result in Figure 8.1a (a) since, even though the divergence speed varies with the location of the centre of mass, it exists for a centre of mass located anywhere along the chord of the streamlined section. Figure 8.1a (a) also shows agreement to Blevins flutter speed condition since flutter exists for all values of the centre of mass aft of the shear centre. In fact, the flutter speed asymptotes towards infinity as it approaches the shear centre.

Figure 8.1 (b) shows the equivalent results for the base-case with PolyWire properties. Blevin's criteria holds for flutter but not strictly for divergence. For the PolyWire sample, the aerodynamic centre is aft of the shear centre yet, the results show that the streamlined cable diverges if the centre of mass is aft of a value slightly greater than the aerodynamic centre. Unlike conventional divergence, the divergence in this case is associated to the inertia of the system. In a physical sense, this instability is related to the fact that when the centre of mass is aft of the aerodynamic centre, the lift and d'Alembert inertia force form a couple acting to rotate the body in the same direction as the displacement. When the centre of mass is aft of the aerodynamic centre, the lift and inertia force couple act in a direction opposite the displacement. This is consistent with the inertia of the system being relatively high compared to the torsional stiffness. The flutter condition follows Blevins criterion, as the figure shows that flutter occurs only when the centre of mass is aft of the shear centre.

Overall the unsteady two-degree-of-freedom model compares well to Blevins general quasi-steady results for flutter but not always for divergence. The difference between the two results is likely due to the fact that wings have relatively high torsional stiffness compared to a streamlined cable. Thus, divergence due to the inertia is not usually within the realm of realistic solutions for a wing.

The same analysis is completed using a discrete 35 streamlined-beam-element model of the base-case. Figures 8.2 (a) and (b) show the flutter and divergence with varying position of the centre of mass for the RedPoly and PolyWire samples, respectively. For positions of the centre of mass aft of the shear centre, the two-degree-of-freedom model results in Figure 8.1 and the discrete model results in Figure 8.2 are nearly identical. However, for positions of the centre of mass forward of the shear centre, where the two-degree-of-freedom model

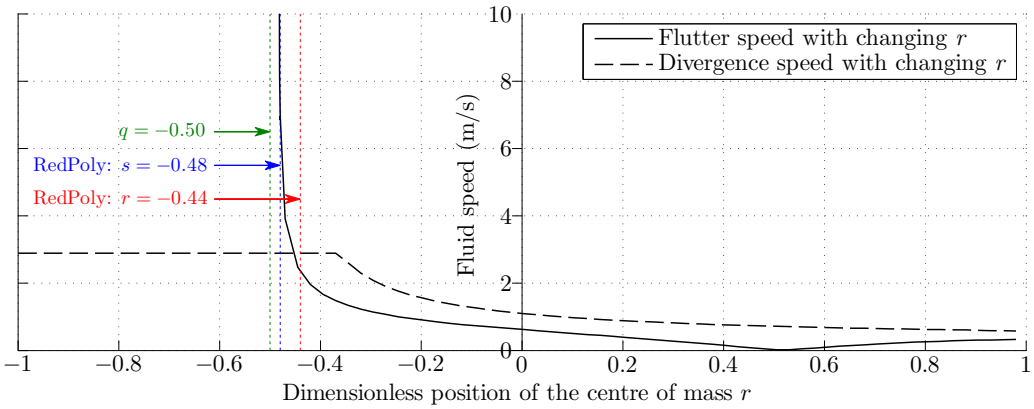

(a) RedPoly properties. The intersection of the flutter and divergence speeds with the r value for the RedPoly sample predicts flutter and divergence at 2.4 m/s and 2.9 m/s respectively.

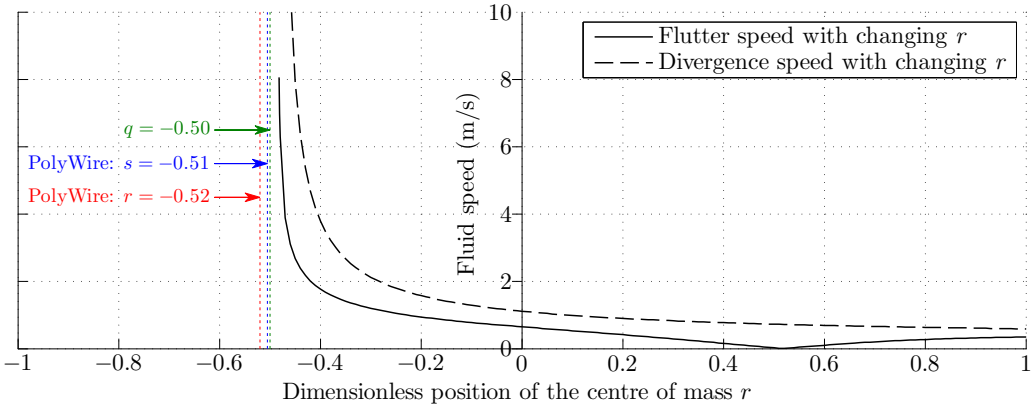

(b) PolyWire properties. No intersection of the flutter and divergence with the r value of the PolyWire sample predicts no flutter or divergence.

Fig. 8.1 Predicted flutter and divergence speed as a function of the position of the centre of mass using the two-degree-of-freedom base-case model with RedPoly or PolyWire properties and no applied tension.

predicts no flutter, the discrete model does. The additional flutter region found in the discrete model corresponds to higher frequency instabilities. For example, taking the RedPoly case, the flutter frequencies for positions of the centre of mass aft of the shear centre vary between 3.0 rad/s to 5.6 rad/s. Conversely, the flutter frequencies for positions of the centre of mass forward of the shear centre vary between 61 rad/s to 64 rad/s. This demonstrates one of the limitations of the two-degree-of-freedom model: the elasticity of the system is reduced to represent a specific mode of vibration and thus overlooks other modes of instability. For the region where the first mode is unstable, the two-degree-of-freedom model provides a simple, computationally efficient alternative for analysing instability.

The analysis of a case without tension is representative of existing work on streamlined

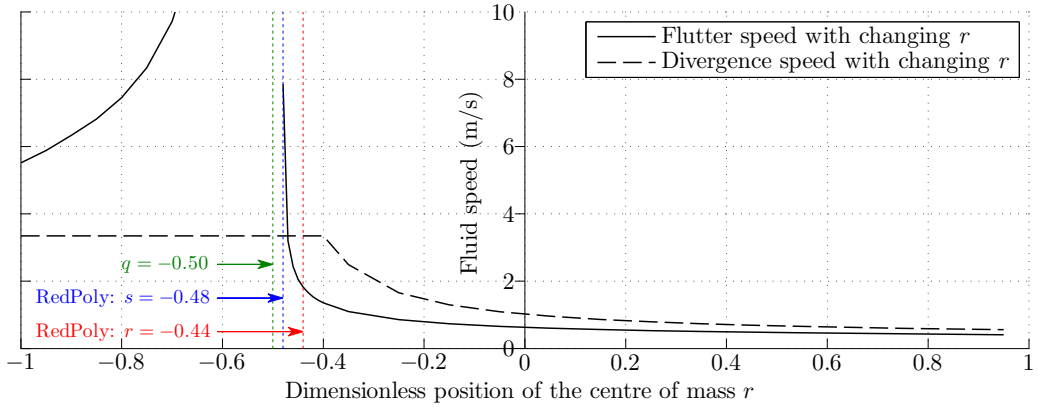

(a) RedPoly properties. The intersection of the flutter and divergence speeds with the r value for the RedPoly sample predicts flutter and divergence at 1.8 m/s and 3.5 m/s respectively.

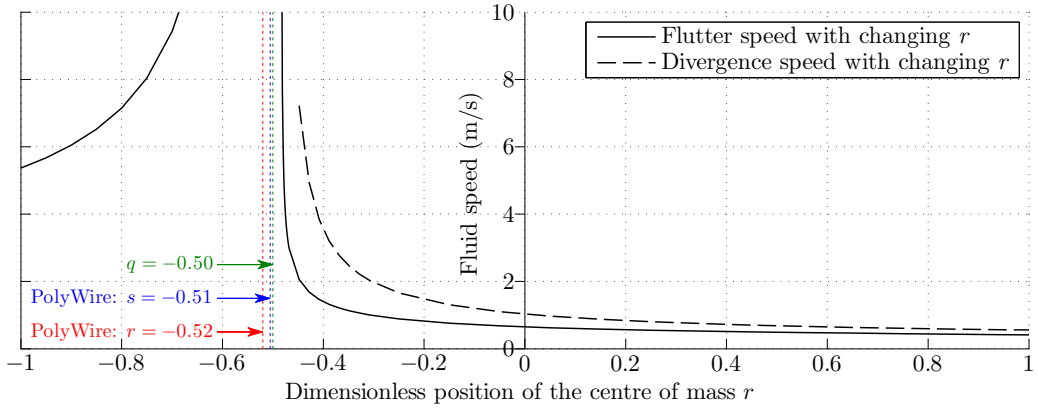

(b) PolyWire properties. No intersection of the flutter and divergence with the r value of the PolyWire sample predicts no flutter or divergence.

Fig. 8.2 Predicted flutter and divergence speed as a function of the position of the centre of mass using the discrete base-case model with RedPoly or PolyWire properties and no applied tension.

bodies such as aircraft wings. The differentiating factor for a streamlined cable is the additional applied tension.

8.2.2 Including Tension

The two-degree-of-freedom and discrete models are now used to investigate the impact of the addition of an applied tension. The models are used to calculate the flutter and divergence speed at varying tensions for the base-case with both RedPoly and PolyWire properties.

Figure 8.3 (a) and (b) show how the flutter and divergence speeds for the RedPoly and

PolyWire samples vary with increasing tension. At a tension of zero, the flutter and divergence speeds agree with the results obtained in Figures 8.1 and 8.2 from the previous section. Looking at the discrete model results, as the tension increases from zero, the flutter speed of the RedPoly case decreases exponentially from 1.8 m/s to about 0.6 m/s at 500 N. The PolyWire cable is stable to flutter at zero tension but as the tension increases there is a critical point – in the range shown here at approximately 75 N – where an onset of flutter occurs. At the critical tension, the flutter speed asymptotes to infinity and, as the tension is further increased, the flutter speed decays exponentially. At tensions above approximately 250 N, the flutter speed results from the RedPoly and PolyWire case converge to approximately the same value. The results from the two-degree-of-freedom do not give the same critical values, but do follow the same general relationship as the discrete model. For increasing tension, both models show a decrease in stability to flutter. Two-degree-of-freedom model is more computationally efficient, and for this case, appears to be a useful tool to gain a preliminary understanding of the a simple streamlined cable's stability behaviour.

Opposite to the flutter case, the divergence case in Figure 8.3 (b) shows an increase in stability with increased tension. At zero tension, the value of 3.5 m/s for the discrete RedPoly case matches the result found in the previous section. Then, as the tension increases, the divergence speed increases and appears to approach a limit of about 20 m/s. The addition of tension to the PolyWire case appears not to affect the divergence condition. Without tension there was no divergence and, with increasing tension, no divergence speed is found.

The reason for the decrease in flutter stability and increase in divergence stability with increased tension can likely be attributed to the fact that the centre of tension in both the RedPoly and PolyWire configurations is forward of the mass and aerodynamic centres. As described in the derivation of both the two-degree-of-freedom and discrete models, the addition of tension effectively increases the stiffness of the streamlined cable. The effect of increasing the tension appears to have the same general result found in classic flutter theory, where the shear centre is replaced by the tension centre. In the case of the RedPoly and PolyWire cross-sections, the centre of tension is forward of the aerodynamic centre causing an increase in divergence stability and the centre of tension is forward of the centre of mass causing a decrease in the flutter stability. The next section takes a more in depth look into how the behaviour of the RedPoly and PolyWire base-case varies with changes in the location of the centre of tension.

In the current section, the two-degree-of-freedom model was seen to give the correct overall flutter and divergence relations to increases in tension. However, it did not give correct magnitudes and a known limitation is that it neglects higher mode instabilities. Used

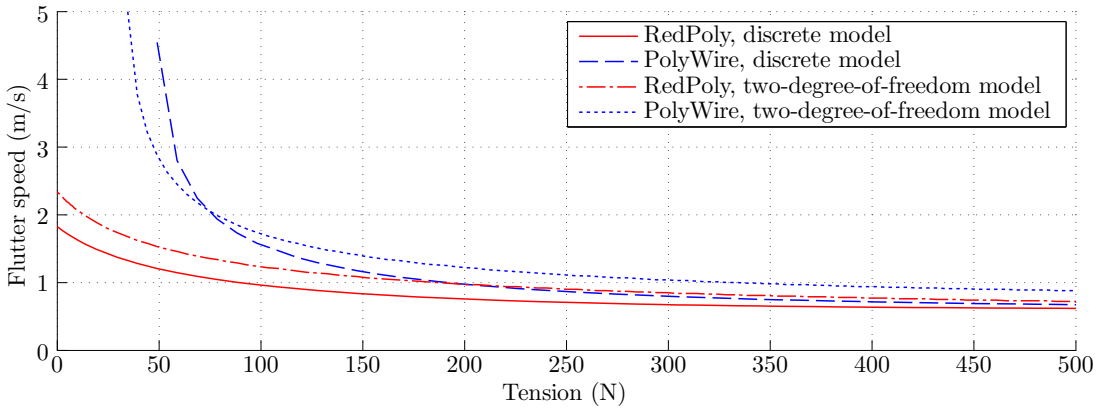

(a) Flutter relation given increasing tension.

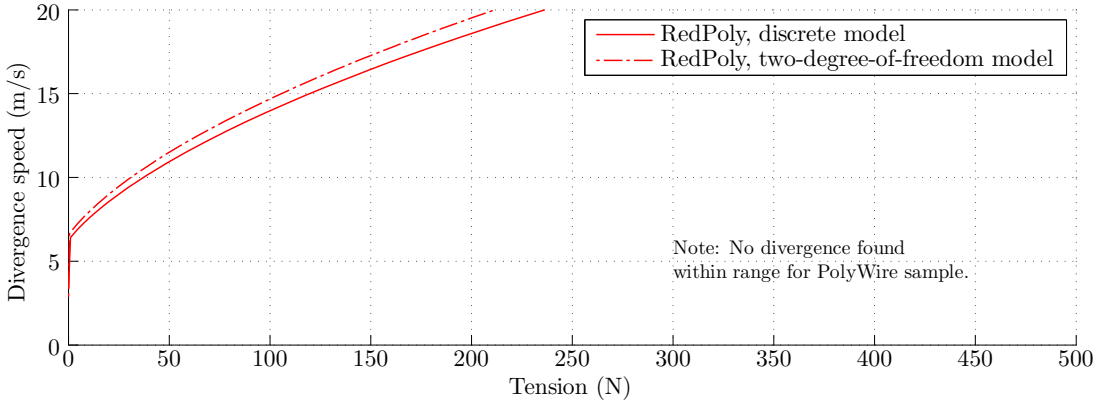

(b) Divergence relation given increasing tension.

Fig. 8.3 Predicted flutter and divergence speed with increasing tension using the discrete and two-degree-of-freedom base-case model with RedPoly or PolyWire properties.

within these known limitations, the two-degree-of-freedom model shows promise as a preliminary tool and is appealing due to its simplicity and computational efficiency. For a thorough analysis of a streamlined cable system, any two-degree-of-freedom model results would need to be verified using the discrete model. Therefore, in the interest of removing repetition by presenting results from both the two-degree-of-freedom and discrete model, for the remainder of this chapter, only the discrete model is used.

8.3 Position of Tension Centre

The influence of the location of the centre of tension, as the magnitude of the tension increases is explored. The analysis is completed with the same 35 streamlined-beam-element model used in the previous section.

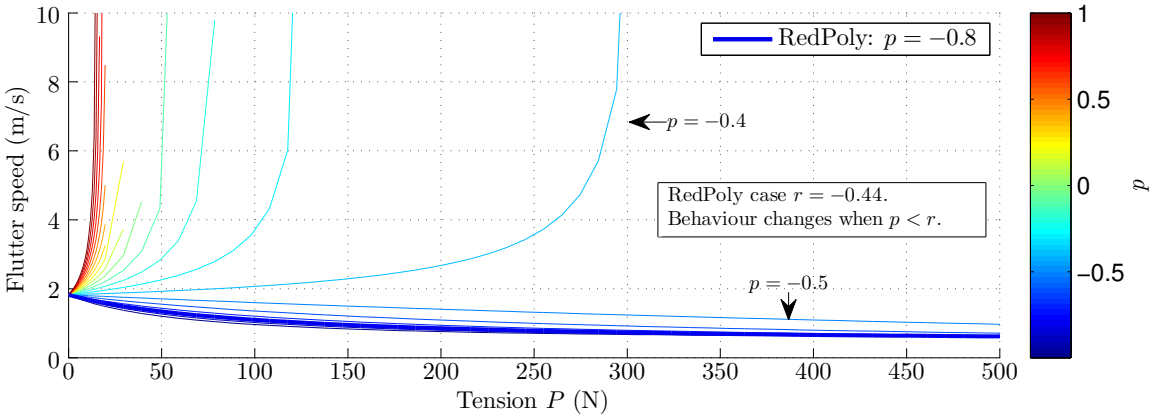

(a) Flutter speed given RedPoly properties.

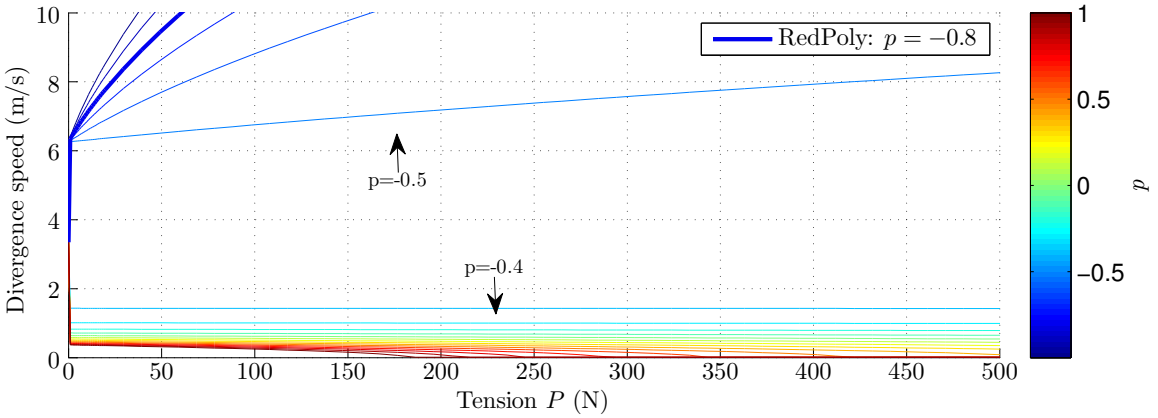

(b) Divergence speed given RedPoly properties.

Fig. 8.4 Predicted stability from the discrete model of the base-case at varying tension. Contours show the relation for values of the centre of tension p ranging from 1 (location at leading edge) to -1 (location at trailing edge) in increments of 0.1.

Figures 8.4 and 8.5 shows the variation of the flutter and divergence speed with tension. The thick line in each plot shows the result for the baseline RedPoly or PolyWire case and are equivalent to results shown in Figure 8.3 in the previous section. The contours give the relationship for various locations of the centre of tension over a range from p=-1 to p=1 in increments of 0.1. This corresponds to moving the centre of tension from the leading edge to the trailing edge. The cool colours indicate a location near the leading edge and warm colours a location near the trailing edge.

Sub-figures 8.4(a) and 8.4(b) show the flutter and divergence relations for the RedPoly sample; sub-figures 8.5(a) and 8.5(b) show the equivalent relations for the PolyWire sample. The RedPoly case has a centre of mass of r=-0.44. With increasing tension, the RedPoly case becomes more stable to flutter when p>-0.4 and less stable to flutter when p<-0.5. This

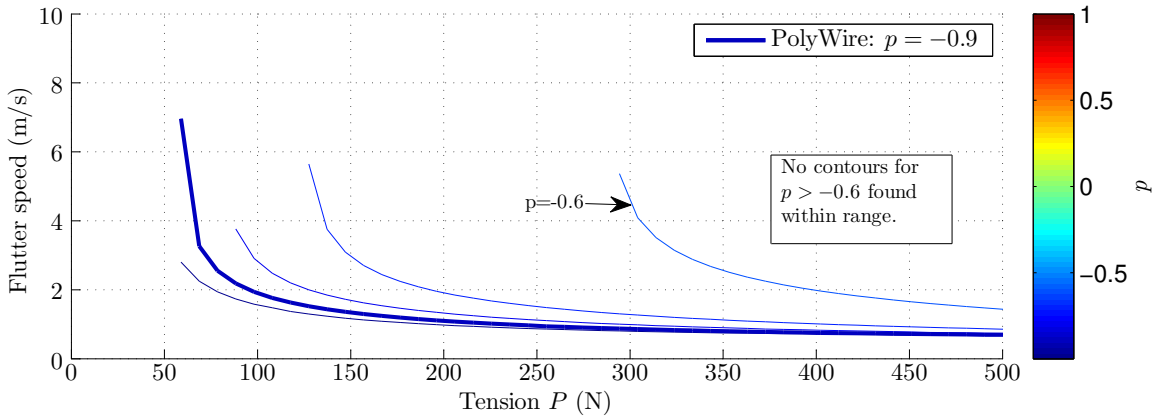

(a) Flutter speed given PolyWire properties.

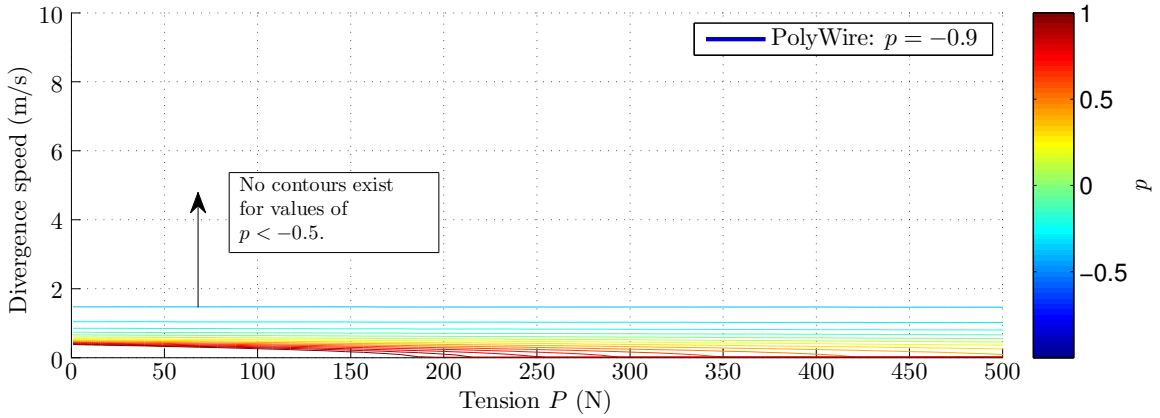

(b) Divergence speed given PolyWire properties.

Fig. 8.5 Predicted stability from the discrete model of the base-case at varying tension. Contours show the relation for values of the centre of tension p ranging from 1 (location at leading edge) to -1 (location at trailing edge) in increments of 0.1.

indicates that for values of $p>r$, there is an increase in flutter stability and for values of $p<r$, there is a decrease in flutter stability. This result is attributed to the fact that as the tension increases, the stiffness effects become dominated by those due to tension, instead of those related to bending and shear. Drawing an analogy to classic flutter, the same general stability condition of having the centre of mass forward of the centre associated with the stiffness (classically the shear centre) appears to hold, i.e. as tension increases the system is more stable with a centre of mass forward of the centre of tension. For the divergence results, the same analogy to the classic flutter model holds. For $p<q$, where $q = -0.5$ is the aerodynamic centre, the divergence speed increases and for $p>q$ the divergence speed decreases. Note that for the RedPoly case, increasing the flutter and divergence stability have opposing requirements. For a change in the position of the centre of tension only,

greater flutter stability requires the centre of tension to move towards the trailing edge and for greater divergence stability requires it to move towards the leading edge.

Figures 8.5(a) and 8.5(b) show the results for the PolyWire sample, which support the general conclusions from the RedPoly case. For the flutter case, moving the centre of tension towards the trailing edge causes an increase in stability. When the centre tension is aft of the centre of mass, located at r=-0.51, no flutter stability can be found. For the divergence case, values of $p<q$ are stable.

This analysis has shown how the respective locations of the cross-sectional centres play an important role in the streamlined cable's stability behaviour. The stability of the streamlined cable appears to follow the same general criteria as classic flutter, except, for a streamlined cable a trade-off exists between the influence of the stiffness acting at the shear and tension centres. In the preceding analysis, the effect of movement of the centre of mass and centre of tension have been analysed. To get a broader understanding on the influence of the location of the four centres, a more high level analysis is undertaken.

8.4 Position of Structural Centres

As seen in the previous analysis, the location of centres relative to one another plays an important role on the overall stability of the streamlined cable. To get a general understanding of which configurations of the positions of the centres offers greater stability, a preliminary analysis is completed.

In the current model, there are four centres which may or may not be coincident. Assuming no centres coincide, there are 24 permutations of the order. Based on the geometry of a streamlined body, the 3 structural centres are unlikely to be located between the semi-chord point and the trailing edge. The position of the aerodynamic centre will not vary significantly from the quarter chord point. Therefore, as an initial analysis of the affect of the location of the centres, the 24 cases were run assuming that the aerodynamic centre is always located at quarter chord and that the remaining 3 centres are evenly spaced around it. Here the spacing is taken as $1/8^{\text{th}}$ of the semi-chord b and it is assumed that no two centres are ever more than $1/8b$ apart. Given this assumption, Figure 8.6 depicts the possible locations of the centres along the cross-section.

For each permutation, the base-case discrete model with the PolyWire properties was used to determine the flutter and divergence speed over a range of tension. Figure 8.7 shows the permutation tree with the flutter and divergence speed, with increasing tension, indicated by the colours below. As shown in the colour bar, cool colours denote lower wind speed

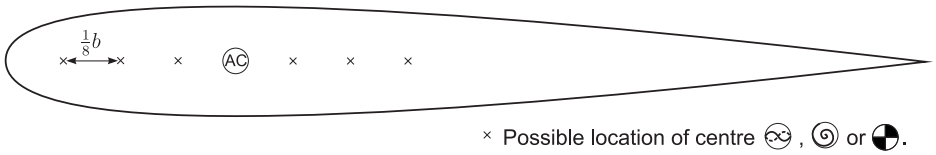

Fig. 8.6 Possible location of the centres, giving 24 permutations of the order.

(below approximately 10 m/s) and warm colours denote high wind speeds up to 30 m/s. Grey results indicates that no flutter or divergence speed was found within the specified wind speed range of 0 to 30 m/s. Consequently, more stable permutations are indicated by warm and/or grey colours whereas unstable configurations are indicated by cool colours. The flutter speed corresponds to the left column and the divergence speed the right column beneath a given permutation. The numbers along the bottom of the figure given a reference number for each of the 24 configurations.

As may be expected from the previous analysis, and indeed general flutter theory, the most stable configurations to flutter and divergence are when the centre of mass is forward of the other three centres and the shear and tension centre are forward of the aerodynamic centre. This behaviour is observed in the cases 13 through to 18, which all have the centre of mass forward of the remaining three centres. The left-hand columns give the flutter stability, which is similar behaviour for cases 13 to 17. For these cases the flutter stability increases with an increase in the tension. In terms of divergence, given by the right-hand columns, the only two cases which exhibit stability (since no values for divergence are found within the studied range) are cases 13 and 15. Both of these cases have the shear and tension centre forward of the aerodynamic centre, a result consistent with the classic flutter theory.

Of cases 13 to 18, the one inconsistent with the classic flutter theory is case 18. Case 18 has a centre of mass forward of the shear centre, but the model predicts a decrease in the flutter frequency with an increase in tension. It is interesting to compare case 18 to case 17, the only difference between the two being that the shear and tension centre have switched positions. Both models predict the same divergence behaviour but opposing flutter behaviour. The reason for this interesting difference is not immediately clear and it could be investigated in more detail. However, this case is just one example of the many interesting aspects of the plot which could be analysed. In addition to the 23 other permutation cases in this plot alone, the figure could be re-run for cases with, for example, different spacing between the centres, stiffness and inertial properties, boundary conditions or cable length. The goal of the present analysis is not to analyse each individual case, but to gain an overall understanding of how the positions of the cross-sectional centres may affect stabil-

ity and demonstrate how the streamlined cable model could be useful tool in the analysis, development and design of streamlined cables.

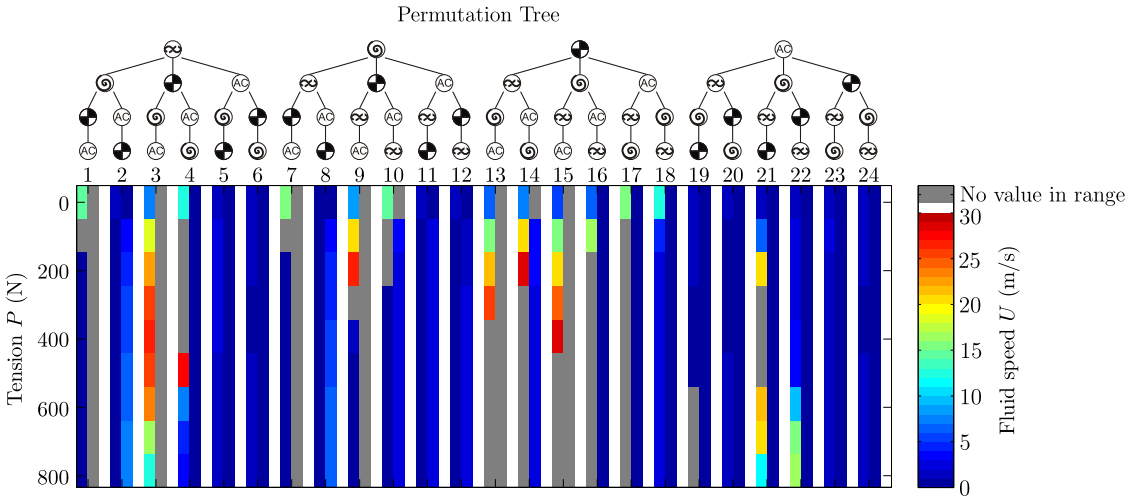

Fig. 8.7 Flutter and divergence speed, with increasing tension for the 24 location permutations. For each permutation case the left column corresponds to the flutter speed and the right column the divergence speed.

8.5 Sensitivity Analysis

Using the discrete model, the sensitivity of the flutter stability to changes in the boundary conditions, length, stiffness and fluid density are briefly examined. The examples given here are not for a specific application. However, throughout the analysis, the relevance of each parametric change to potential applications is discussed. Though the analysis does not present an exhaustive parametric study, it provides some insight on the stability of streamlined cables and demonstrates the model's potential as a design and analysis tool. The analysis thus far has taken compared the behaviour of the base-case with the RedPoly and PolyWire sample properties. Of the two cases, the PolyWire sample is the more stable of the two due the fact that the aerodynamic centre is aft of both the shear and tension centre and the centre of mass is forward of the shear centre. As such, for the following sections the base-line parameters are always taken as those from the PolyWire sample.

Depending on the streamlined cable application, various boundary conditions may be implemented. For example, the Goland wing model presented in Chapter 7 assumed fixed-free boundaries to represent an aircraft wing. A tethered balloon or kite could be considered

as pinned at the bottom with an applied external drag and lift force at the top. The base-case assumes pinned-pinned, torsionally-fixed boundaries, similar to the observed behaviour of the horizontal streamlined cable experiments. In the horizontal experiment set-up, swivels were included at the boundaries in an attempt to create torsionally free boundaries. As a simple sensitivity case, the affect of using torsionally-free versus torsionally-fixed boundaries is explored. An analogy for this case could be investigating the influence of friction in the swivels (i.e. a high friction swivel is comparable to being fixed).

Figure 8.8 shows how the flutter velocity varies with tension for both boundary conditions. It can be seen that, for this particular configuration, the addition of torsional freedom increases the stability at low tension (around 100 N). For tensions greater than 200 N, the stability for both cases are approximately equal. These results indicate that the friction in the swivels would only affect the overall the flutter stability at relatively low tensions.

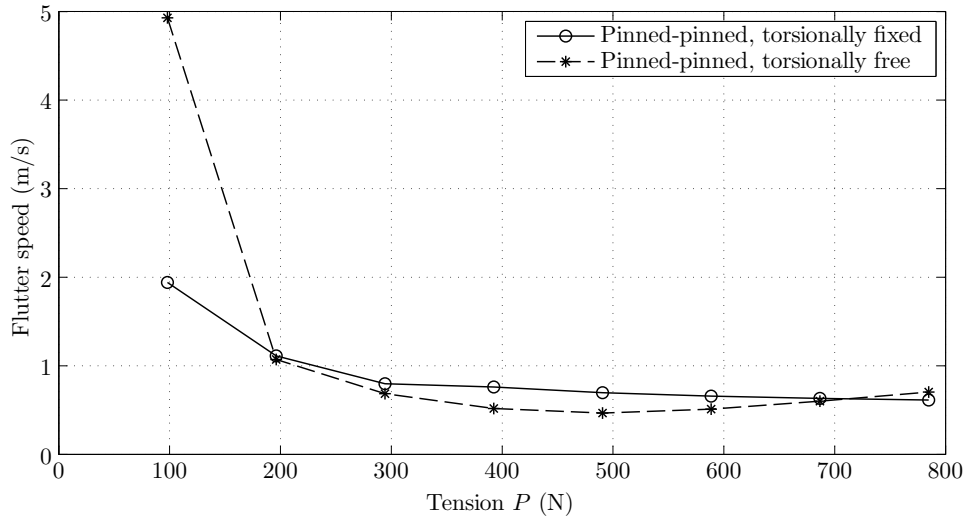

Fig. 8.8 Sensitivity of flutter speed of PolyWire sample to variations in the boundary conditions.

Using the pinned-pinned, torsionally-free case as a reference, the sensitivity of the streamlined cable model to variations in length, stiffness and fluid density is explored. Changes in length could be related to a number of potential streamlined cable applications. For example, relative to the 50 m base-case, short lengths of streamlined cable could be used to reduce drag on the bridle line of kites or the ropes of racing yachts. Longer lengths of streamlined cable could be used as the tether of a high-altitude balloon or the line of a kite-power generator. Figure 8.9 shows how the flutter speed as a function of tension is affected by changes in the base-case streamlined cable length. The overall results show that

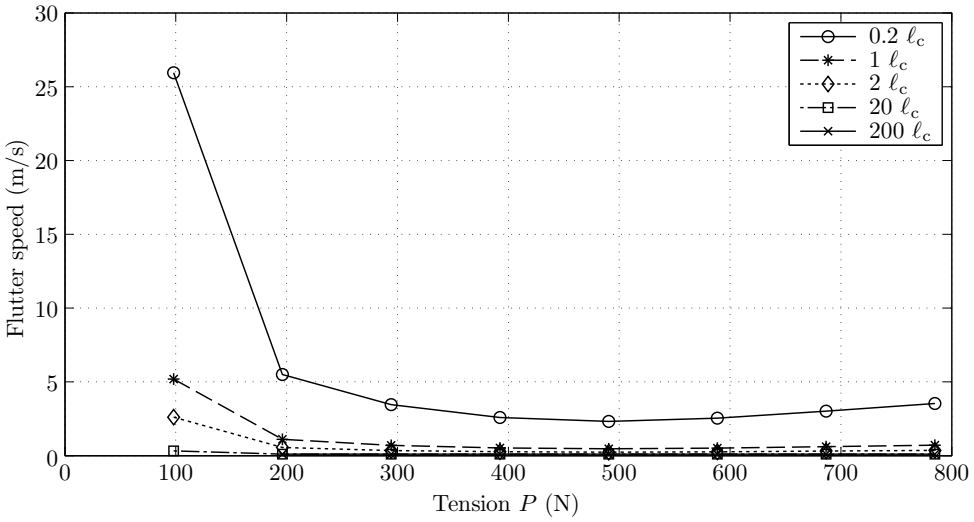

Fig. 8.9 Sensitivity of flutter speed of PolyWire sample to variations in length.

shorter lengths are more stable and longer lengths are less stable to flutter.

The sensitivity of the model to changes in stiffness is also explored. The streamlined cable model has axial, bending (in two directions) and torsional stiffness denoted by EA, EI_y, EI_z and GJ respectively. Figure 8.10 shows how the flutter boundary for the base-case varies with changes in the four stiffness properties. It is evident from the figure that the torsional stiffness plays the most significant role in terms of the flutter stability. In fact, the variations in the axial and bending stiffness do not visibly alter the overall stability. As a general conclusion, a lower torsional stiffness appears to give a more stable streamlined cable. An analogy could be drawn to a weather-vaning system, which can be thought of as having a torsional stiffness of zero.

A final case, explores how the fluid density affects stability. The potential applications of this scenario relate to both increases and decreases in fluid density. Decreases in fluid density are relevant to streamlined cables operating at very high altitudes, for example, as a high-altitude balloon tether. The natural extension of the model to applications with increased fluid density are for a streamlined cable operating in water, for example as a towed cable array or off-shore riser. Figure 8.11 shows how the flutter speed boundary changes with variations in fluid density. The relationship does not appear to be straightforward. The model predicts an increase in stability for both increasing and decreasing fluid density. The relationship is complex due to the interaction of the unsteady fluid effects from the apparent fluid velocity, apparent mass and the induced-flow from shed vortices. The densities of 0.1ρ, 0.5ρ and ρ correspond to air densities at an altitude of 18 km, 6.5 km and 0 km respectively.

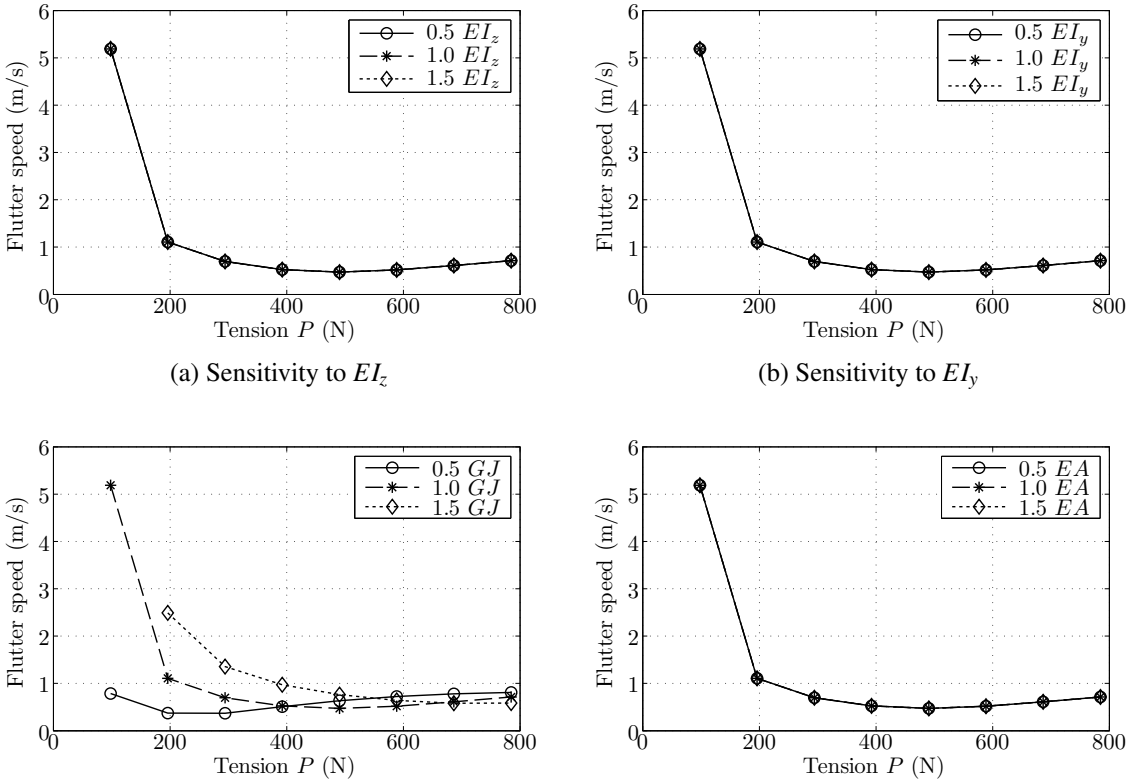

(a) Sensitivity to EI_z

(b) Sensitivity to EI_y

(c) Sensitivity to GJ

(d) Sensitivity to EA

Fig. 8.10 Sensitivity of the flutter velocity to changes of the stiffness.

The density of 5ρ is not directly related to any of the applications discussed in the current work, but shows that the flutter speed tends to increase as the density increases. For the given baseline case explored, densities equivalent to those of water (i.e. 1000ρ) gave no flutter speed within the studied fluid speed and tension range.

The sensitivity analysis presented here takes an initial look at how changes in certain parameters, which are related to specific streamlined cable applications, affect the overall stability. For the a streamlined cable with the PolyWire case properties and with pinned-torsionally free boundaries, the overall findings were that shorter and less torsionally rigid configurations are more stable. The conclusions drawn are of a very general nature and if anything, what the analysis perhaps demonstrates most clearly, is how the predicted stability is specific to a given situation. This emphasises the importance of having models to accurately predict the stability behaviour for a given set of input parameters.

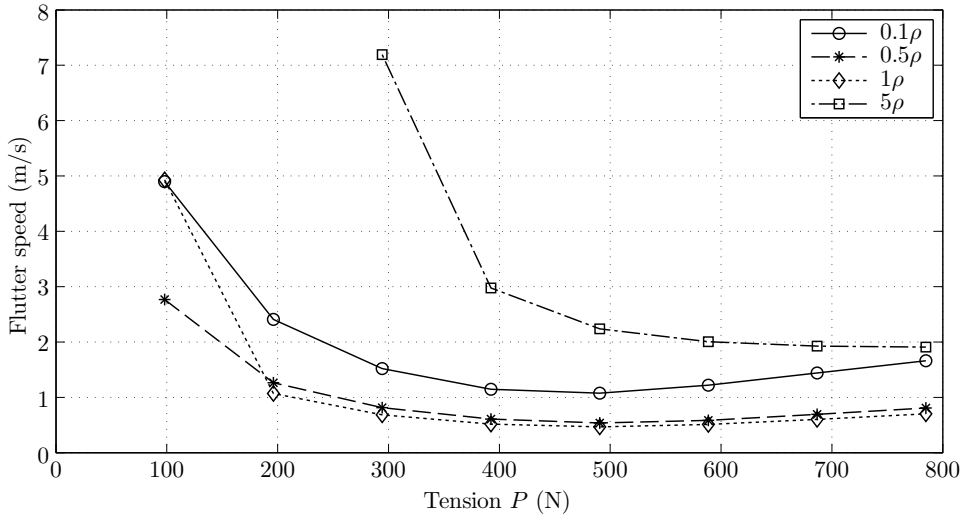

Fig. 8.11 Sensitivity of flutter speed of PolyWire sample to variations in fluid density.

8.6 Fluid Velocity Profile

Any environmental application of a streamlined cable, be it outside or underwater, will be subject to spatially and temporally varying fluid velocity profiles. Here, the effect of spatially varying fluid velocity profiles is explored using the discrete streamlined cable model. A simple fluid loading profile is considered: a central region x_ℓ of the streamlined cable is subject to a fluid speed U and the rest of the cable to a fluid speed U_o. The wind profile loading is depicted in Figure 8.12. The modelled streamlined cable has the PolyWire properties with pinned-pinned and torsionally-free boundaries. The velocity U_o is considered as constant and relatively small, taken here as 0.1 m/s, compared to the local velocity U. The flutter stability boundary is determined by calculating the eigenvalues for an increasing value of U, and checking the result for positive growth rate. The flutter velocity is taken as the minimum velocity of U to give a positive growth rate. This flutter velocity is calculated for a range of wind loading ratios (x_ℓ/ℓ_c), tensions and streamlined cable lengths.

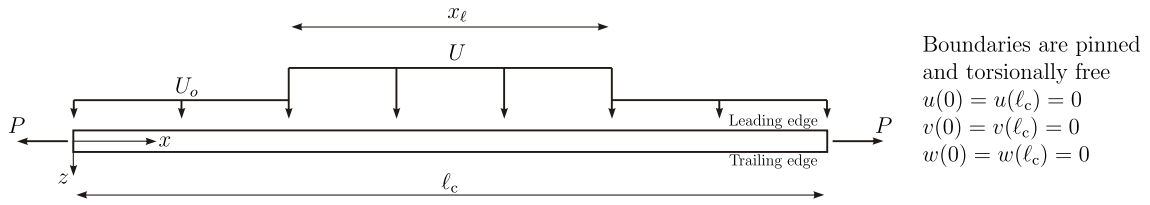

Fig. 8.12 Simple localised fluid excitation. Fluid flows with velocity U over the central region x_ℓ.

Figure 8.13 shows how the flutter velocity and frequency varies with changes in the extent of the wind zone x_ℓ/ℓ_c for constant tensions of 50 N, 100 N, 250 N and 500 N. Values of $x_\ell/\ell_c = 1$ indicate a uniform wind profile. This case is equivalent to the base-case and it can be seen that the values match those given in Figure 8.8. As the extent of the wind zone x_ℓ/ℓ_c approaches zero, the wind loading becomes equivalent to a point load and the flutter velocity tends to infinity. The figure shows how even this simple wind loading case can exhibit interesting behaviour. For this particular case, the flutter velocity in Figure 8.13(a) appears to asymptote when the extent of the wind zone is approximately 0.25. By examining the corresponding flutter frequency, shown in Figure 8.13(b), a step change in the frequency is seen at this $x_\ell/\ell_c = 0.25$ point.

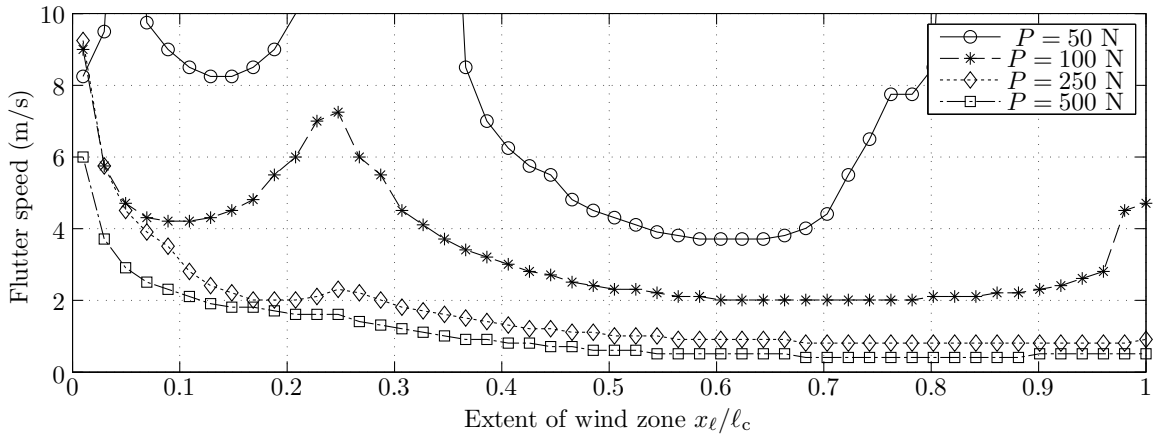

(a) Flutter speed.

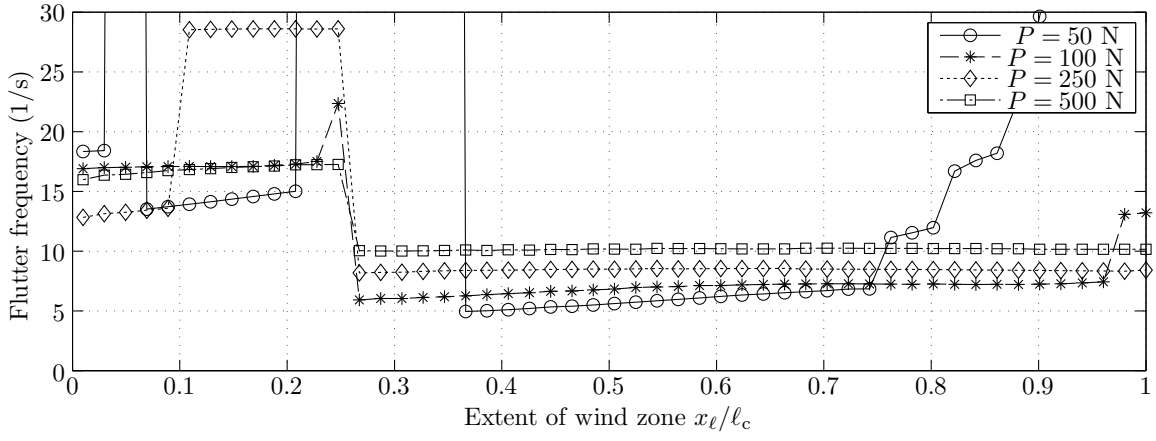

(b) Flutter frequency.

Fig. 8.13 Predicted stability of the base-case for a localised wind of changing length scale under constant tension *P*. The local wind acts at the center of the streamlined cable.

Looking a little more closely at how the stability varies with changes in the wind velocity profile, the deflected shape for the 100 N tensioned case at five loading profiles is examined. Figure 8.14 shows the same results as Figure 8.13, but only for the P=100 N case and shows the location of the five chosen cases A, B, C, D and E corresponding to loading fractions of approximately 0.01, 0.2, 0.3, 0.5 and 1 respectively. For all the investigated cases, no significant displacement was exhibited in the axial or fluid flow directions. The deflected shape is dominated by the y and θ displacements, which correspond to the plunge and pitch motion of the streamlined cross-section. Figures 8.15 to 8.19 show the normalised deflected shape in y and θ over the course of half a cycle of period T. The deflections are normalised by $\mathbf{Q}_{max}$, which is the eigenvector element with the largest absolute value. This normalisation converts the selected element $\mathbf{Q}_{max}$ to have unity for its real part and zero for its imaginary part.

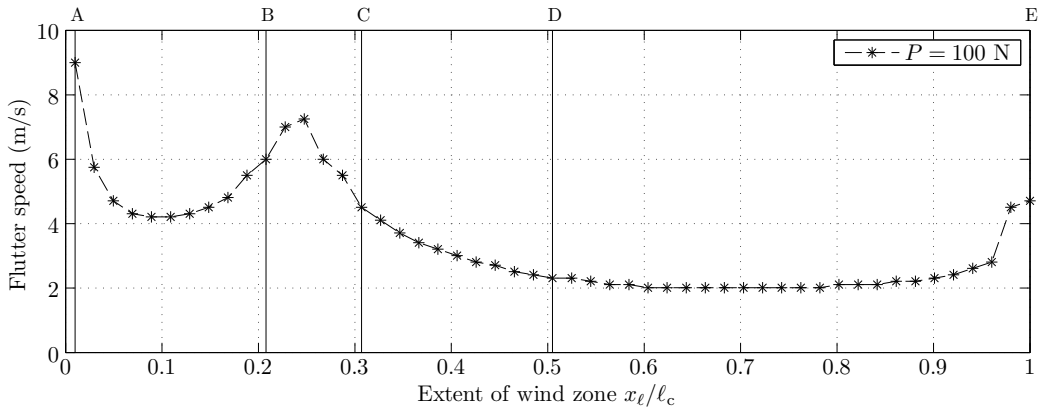

(a) Flutter speed.

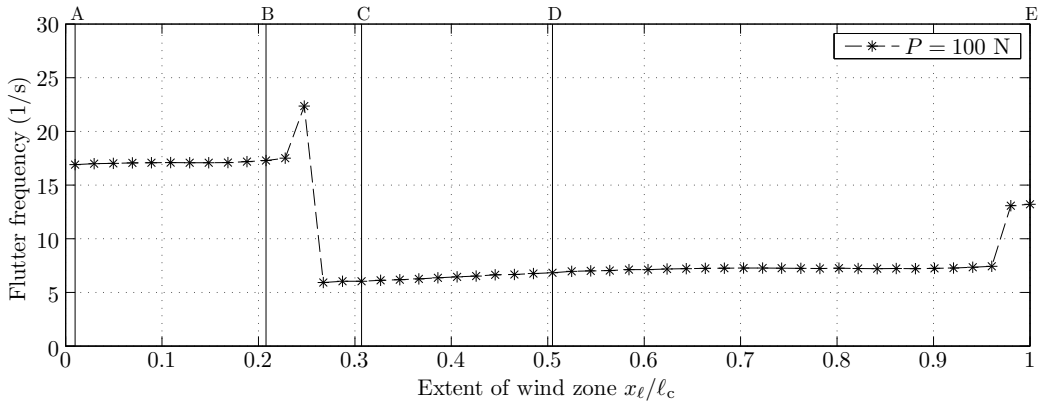

(b) Flutter frequency.

Fig. 8.14 Predicted stability of the base-case for a localised wind of changing length scale under constant tension P. The local wind acts at the center of the streamlined cable.

Figure 8.15 shows the deflected shape for Case A, for a wind zone of 0.01. The wind zone acts over a relatively small length scale and is comparable to applying a point load at the centre of the streamlined cable. This can be seen in the deflected shape, as there is a slightly pointed shape where the load is applied at $x/\ell_c = 0.5$. Case B, shown in Figure 8.16, is subject to a wind zone extent of 0.20, and has a very similar deflected shape to Case A. Indeed, the deflected shape for wind profiles of $x_\ell/\ell_c < 0.25$ (occuring before the jump in frequency) are all of the same general form. Interestingly, the deflection bowl (length scale between the two nodes on either side of the loaded region) for the cases between $x_\ell/\ell_c =$ 0.01 to 0.25 is approximately 25% of the overall length. It appears that once the length scale of the wind loading matches the length scale of the deflection bowl, the flutter instability changes to a different mode. As the length scale of the wind loading approaches this scale, the wind velocity to onset flutter tends to infinity. For cases with an extent of the wind zone greater than 0.25, the flutter frequency and deflected shape changes. Take for example, cases C and D with $x_\ell/\ell_c = 0.3$ and 0.5 with the deflected shapes shown in Figures 8.17 and 8.18 respectively. For these two cases the flutter instability occurs at a lower frequency and the deflected shape is asymmetric about the loading point. This behaviour can be compared to the mid-point being fixed and the wind exciting a flutter instability on a cable which is half the length. Beyond a wind zone of 0.25, the flutter frequency and deflected shape remains approximately constant until the cable is almost uniformly loaded and $x_\ell/\ell_c = 0.96$. For a wind zone greater than 0.96, as seen in Figure 8.13(b), there is another jump in the flutter frequency. The instability for Case E occurs at a frequency between the previous two cases and the deflected shape is shown in Figure 8.19. In summary, the analysis shows how the wind loading profile can significantly alter the flutter instability behaviour.

Another aspect which is explored, is how the overall length affects the flutter instability for this simple wind profile case. Figure 8.20 shows the flutter velocity and frequency, similar to Figure 8.13, but for a constant tension of 250 N and changing overall cable length from 25 m to 1,000 m. Note that the ℓ_c=50 m case here is equivalent to the P=250 N case in the previous figures. Interestingly, the relation to the extent of the wind zone does not seem to change with length, it keeps the same overall form but changes in magnitude. For shorter cable lengths, the streamlined cable is more stable and the flutter velocity increases; at greater cable lengths the streamlined cable is unstable in even slight wind. Figure 8.21 shows the deflected shape for streamlined cable lengths of 25 m, 50 m and 100 m when $x_\ell/\ell_c = 0.3$ (case A shown in Figure 8.20). At first glance the figure appears to plot the deflected shape for only one case. However, on closer inspection it can be seen that the deflected shapes are almost identical for the three streamlined cable lengths and all overlap.

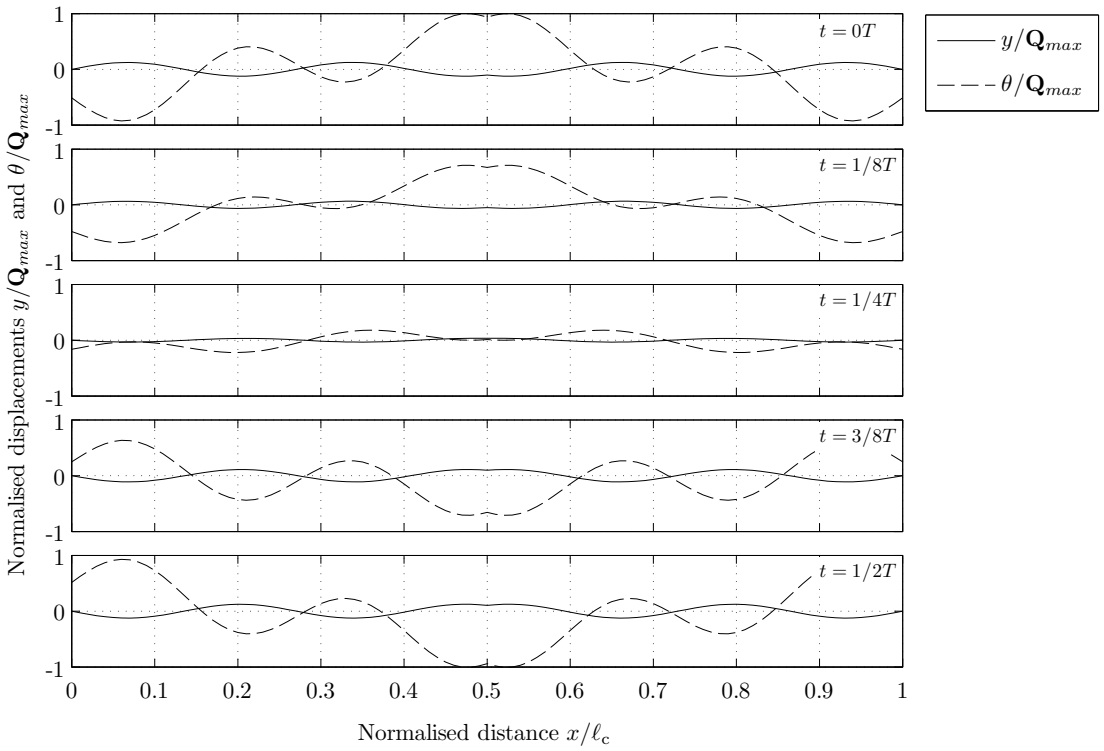

Fig. 8.15 Displacement in y and θ over half a cycle for Case A (depicted in Figure 8.14a).

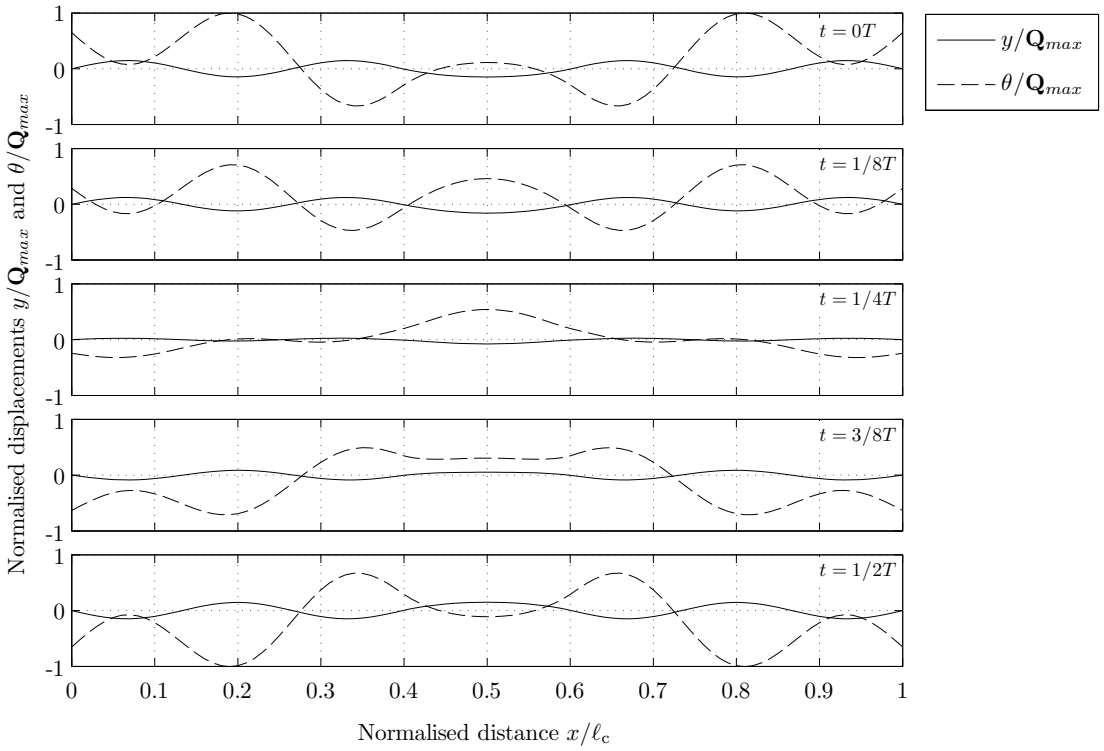

Fig. 8.16 Displacement in y and θ over half a cycle for Case B (depicted in Figure 8.14a).

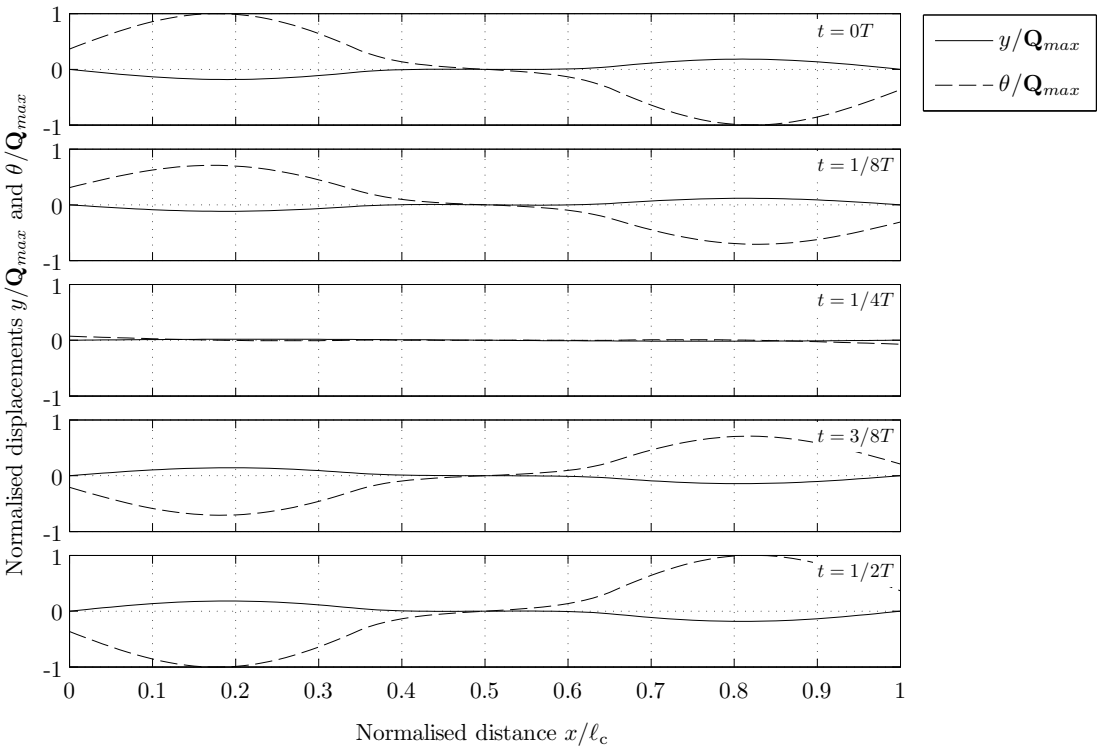

Fig. 8.17 Displacement in y and θ over half a cycle for Case C (depicted in Figure 8.14a).

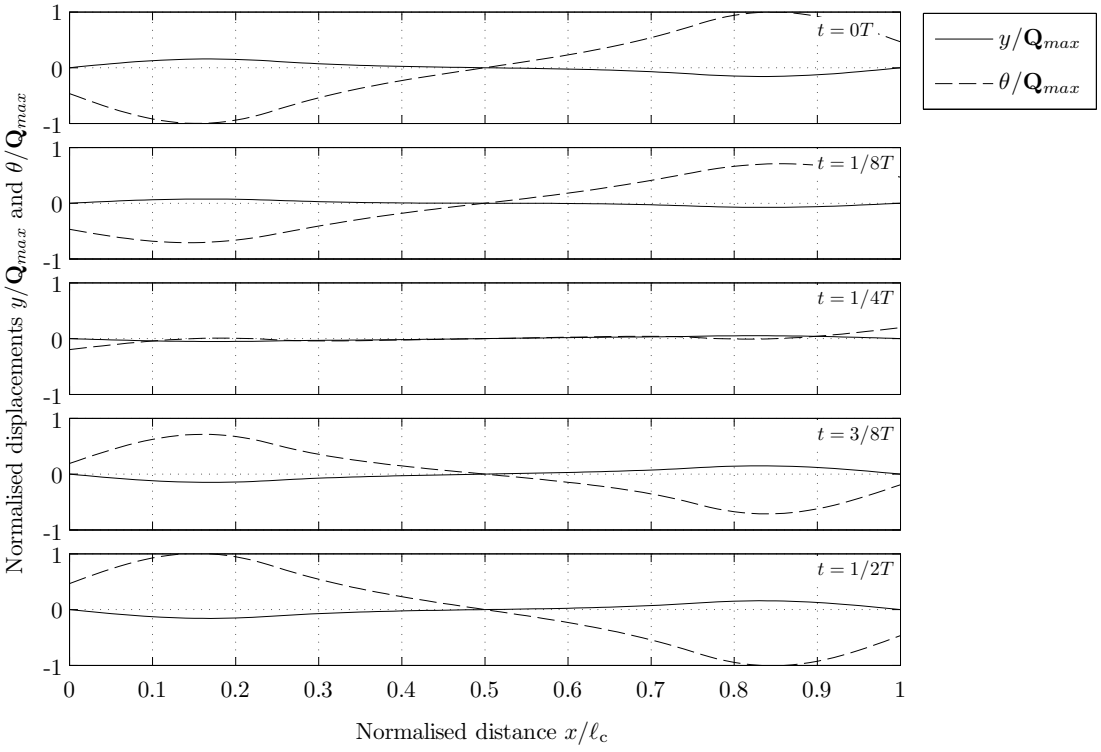

Fig. 8.18 Displacement in y and θ over half a cycle for Case D (depicted in Figure 8.14a).

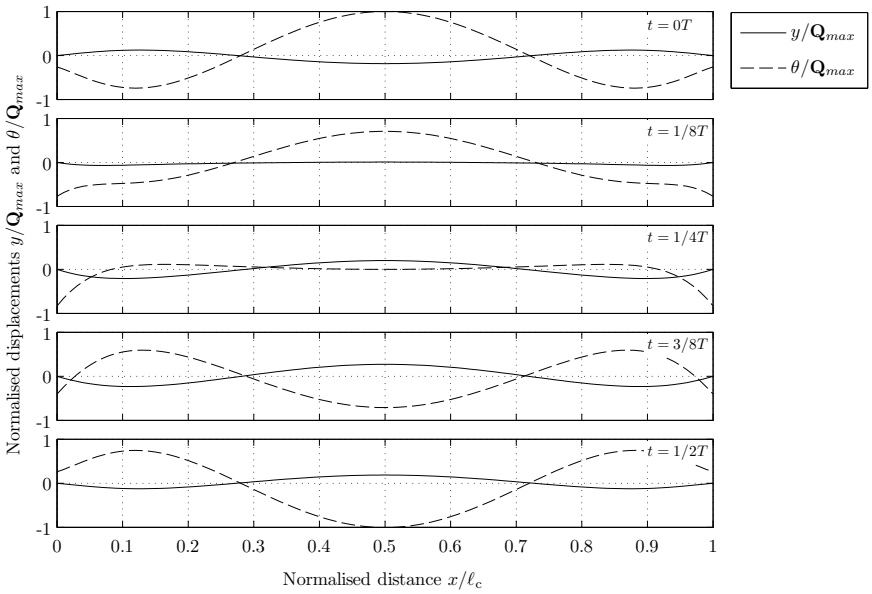

Fig. 8.19 Displacement in y and θ over half a cycle for Case E (depicted in Figure 8.14a).

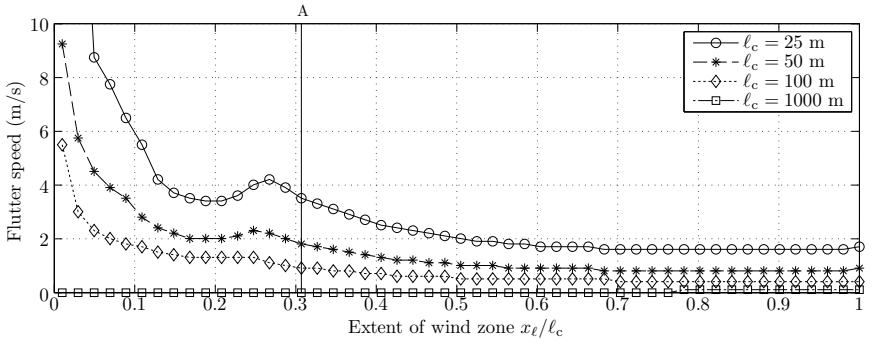

(a) Flutter speed.

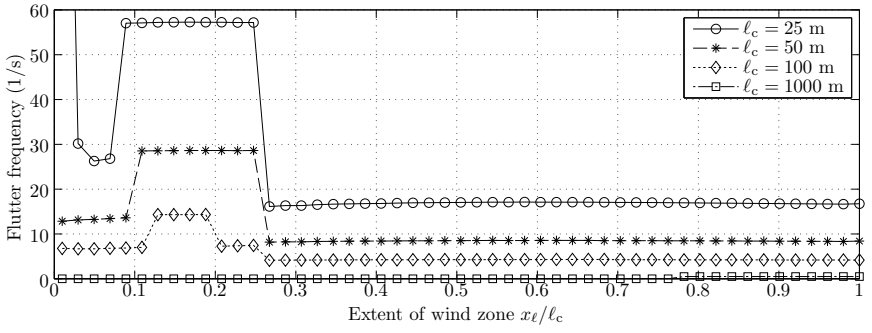

(b) Flutter frequency.

Fig. 8.20 Predicted stability of the base-case of length L under a tension of 250 N given a localised wind. The local wind acts at the center of the streamlined cable.

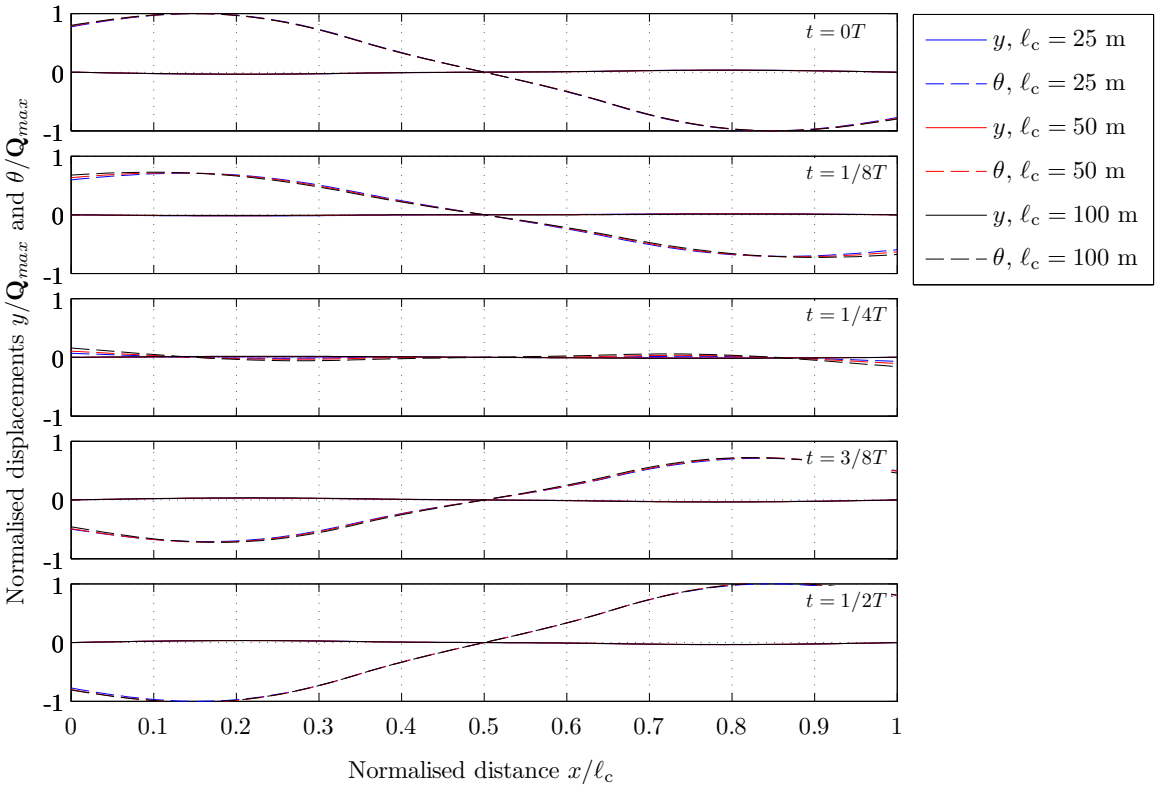

Fig. 8.21 Displacement in y and θ over half a cycle for 3 cable lengths for loading case Case A (depicted in Figure 8.20a).

This section has demonstrated the ability of the discrete streamlined cable model to investigate the effect of varying wind profile. An example of a streamlined cable subject to a centrally localised wind was given. The effects of varying tension and length were explored. Given changes in length and tension, the magnitude of the critical flutter speed and frequency changed but the overall relation to the extent of the wind zone kept the same general form. This relatively simple case displayed some interesting interactions between the mode of instability and the profile of the wind loading. For example, the mode of instability experienced a sudden change in behaviour when the extent of the wind zone became greater than the length of the deflection bowl. The example presented here was for a streamlined cable of particular properties and boundary conditions, chosen based on known values from the manufacturing and experimental work discussed in Chapters 6 and 7. The example serves to demonstrate the complex relationship between the details of the wind input and the system's stability. As the example has shown, the discrete model can be used as a tool to investigate how a specific wind profile affects the stability for a given streamlined cable configuration.

8.7 Varying Tension

Many of the mentioned applications such as tethered balloons, kite-power generators, towed cables and off-shore risers require a vertical configuration. The tension along the length of such a vertical set-up varies due to gravity. The effect of varying tension can be investigated using the discrete streamlined-cable model. A simple case is given to demonstrate the model's capabilities and provide an initial investigation of how varying tension may affect a streamlined cable's dynamic behaviour.

Figure 8.22 depicts the straight vertical configuration subject to a top tension P_{top}. The system roughly parallels that of a tethered balloon or kite, where the tension P_{top} would be the tension provided from the lift of the balloon or kite. The streamlined cable is divided into N elements each subject to a tension P_N dependent on the mass of the streamlined cable m, the length of an element ℓ and gravity g. A constant uniform fluid velocity U is assumed to act over the entire length of the streamlined cable. As in the previous section, the boundaries of the cable are considered as pinned and torsionally free.

The flutter velocity is calculated for a range of top tensions for streamlined cables 50 m, 100 m and 500 m in length. The streamlined cable is assumed to have the PolyWire cross-sectional properties. Figure 8.23 shows how the flutter speed varies with increased top tension. The results are shown as a function of the top tension normalised with respect to the weight of the streamlined cable $m\ell_{\text{c}}g$. A normalised tension of $P_{\text{top}}/m\ell_{\text{c}}g = 1$ provides only enough tension to support the weight of the streamlined cable and means the tension at the bottom of the cable is zero. The figure also compares the variable tension case to corresponding constant tension case. The constant tension case assumes gravity is zero so that the tension over the length of the cable is equal to the tension applied at the top. The equivalent tension case for each length is shown with a dashed line.

The results show that as the magnitude of P_{top} increases, the constant and variable tension cases converge. The two cases converge because for relatively high applied tensions, the change in tension due to gravity becomes negligible. At lower normalised tensions, the applied tension and weight of the cable are of similar magnitude. In this particular case, for the same top tension, the effect of the decrease in tension due to gravity causes an increase in the critical flutter speed. Comparing the deflected shape at the flutter point for the constant and variable tension cases shows how the inclusion of variable tension causes a dramatic change to the mode of instability.

Figures 8.24 and 8.25 show the unstable motion of the constant tension and variable tension cases at a normalised tension of 1.75 over half a cycle of period T (denoted by

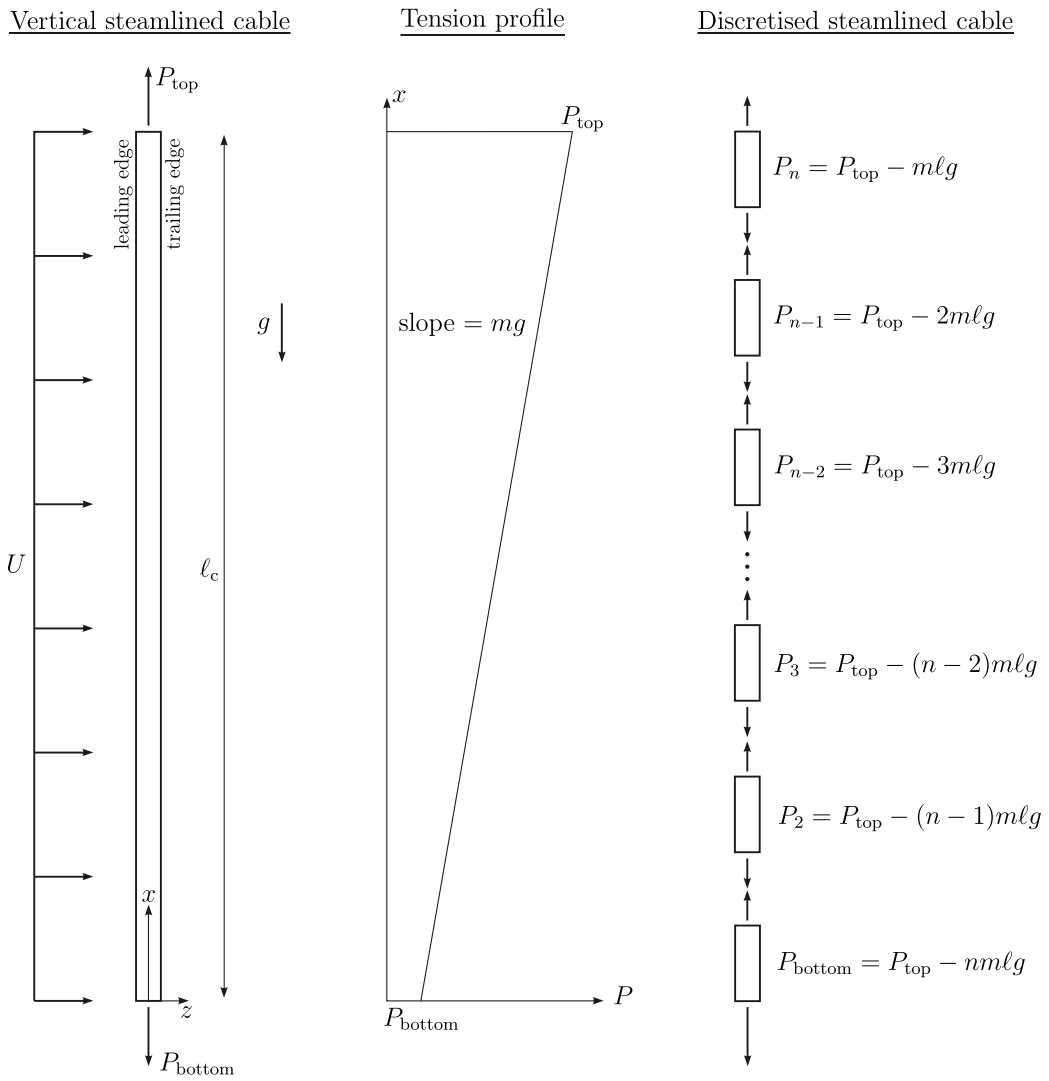

Fig. 8.22 Varying tension with gravity.

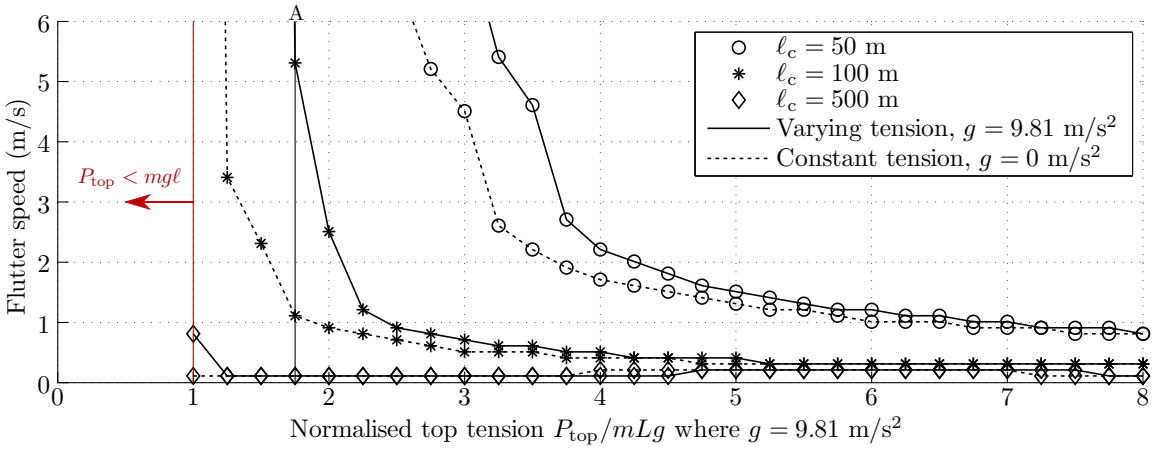

Fig. 8.23 Flutter speed with varying tension along the streamlined cable.

A in Figure 8.23). The constant tension case shows a mode shape which is asymmetric about the mid-point of the cable. Conversely, the variable tension case is not symmetric and the instability occurs at a higher frequency mode. The wavelength of the unstable mode is greater in the upper portion of the cable where the tension is higher. For example, at $t = 1/4T$ of the variable tension case (Figure 8.25), the wavelength of the y displacement in the upper and lower portion of the streamlined cable are approximately $0.4\ell_c$ and $0.6\ell_c$ respectively.

The example given here demonstrates the discrete model's ability to handle variable tension and highlights how the variation in tension may affect the overall stability. In cases where the applied tension is of the same order as the weight, the unstable mode loses its symmetry. When the applied external tension is high relative to the weight of the cable, the solution approaches the constant tension case. The case presented here is for a specific set of input conditions and illustrates the scope of the model as a tool to investigate the dynamic behaviour of variable tension streamlined cables.

8.8 Conclusions

This chapter demonstrates how the developed discrete model can be used to analyse the stability of a streamlined cable. The cross-sectional properties obtained through measurement and modelling of the manufactured cable were used as a baseline from which to investigate the behaviour of a streamlined cable. The model's capabilities to explore a number of problems were demonstrated by applying it to study how variations in the cross-sectional properties, wind profile and tension distribution influence the overall stability of the system.

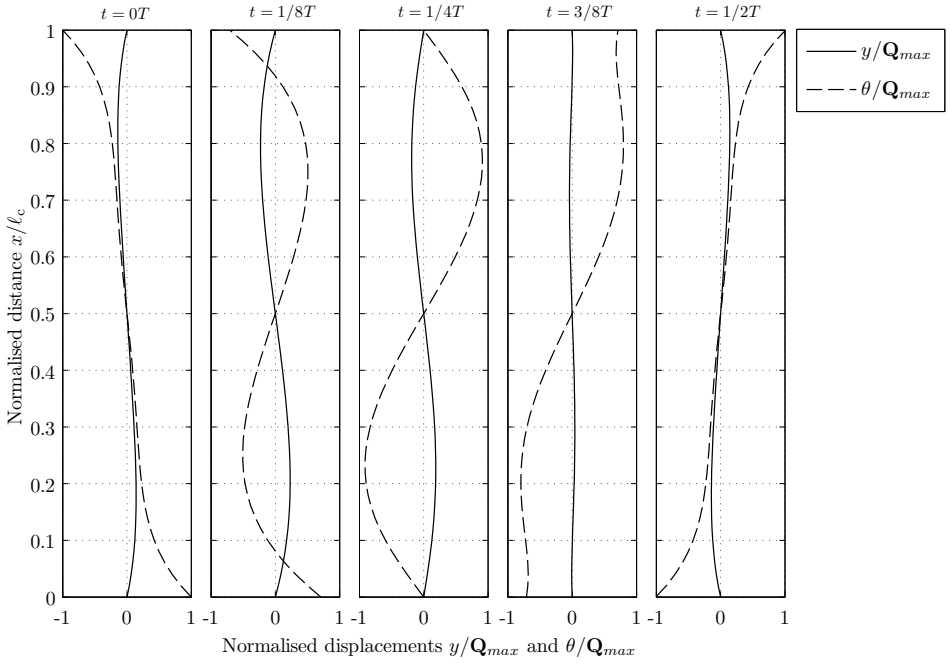

Fig. 8.24 Deflected shape of the 100 m length assuming constant tension at Case A (depicted in Figure 8.23).

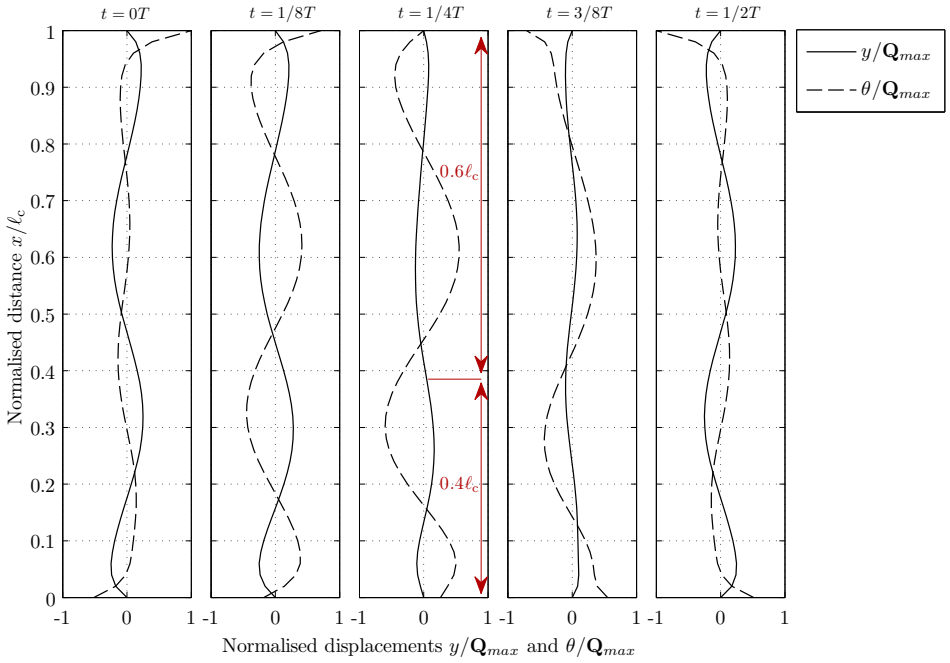

Fig. 8.25 Deflected shape of the 100 m length assuming varying tension at Case A (depicted in Figure 8.23).

Although the results given are for a streamlined cable case with no specific application in mind, the work underlines how the stability of a streamlined cable is sensitive to a number of parameters. The presented analysis emphasised the important role the relative positions of the structural centres play in determining stability. Results similar to those from classic aeroelastic theory were found, except they incorporated the additional influence of the centre of tension. The centre of tension appears to influence stability in the same way as the shear centre. This seems a logical finding as both centres are related to the stiffness of the structure. The affects of variable flow velocity and tension profiles were investigated. The results demonstrated that these inputs play an important role in determining the overall stability of the cable, as they alter the mode of instability.

The developed discrete model is a simple model which can explore the dynamics and stability of a streamlined cable. It includes a number of effects such as unsteady fluid flow, off-set structural and loading centres and geometric stiffening. The results from the examples given illustrate how the stability of a streamlined cable is highly case dependent. This underlines the importance of having validated and accurate models to help predict the dynamics and stability of streamlined cables. The current model is general in nature and provides a foundation for future work on streamlined cables.

Chapter 9

Conclusions and Recommendations for Further Work

This chapter summarises the work completed and reviews the objectives of the research. The conclusions drawn and limitations discussed naturally point to the areas of interest for future research, which are also presented and discussed.

9.1 Conclusions

The overall objective of the undertaken research was to help build a better understanding of the dynamics and stability of streamlined cables through theoretical modelling and experimental testing. As presented in the literature review, a stable streamlined cable is desirable for applications such as high-altitude tethered balloons and kite-power generators because of its potential to reduce drag and VIV. Though the streamlining offers benefits in terms of reduced drag and VIV suppression, it also introduces the potential for instabilities such as divergence and flutter. The general aim of the current work was to contribute to the understanding of the dynamics and stability of streamlined cables. To summarise how this aim was achieved, the contributions of the presented research are listed below. After which, a more thorough discussion of each contribution is given.

1. A review of existing and potential applications of streamlined cables – including faired towed cable arrays, faired risers, high-altitude tethered balloons and kite power generators – established the current need for the development of streamlined cables and appropriate models to characterise their dynamic behaviour.

2. Modelling tools were developed and verified against benchmark cases and compared to experimental results. The models provide a tool to assess and predict the dynamic behaviour and stability characteristics of a streamlined cable.

3. A streamlined cable manufacturing process was developed in conjunction with the SPICE project, ESE Ltd. and DT Ltd. Simple tools to analyse the properties of the manufactured cable were created and where possible compared to experimental measurements or results from existing cross-sectional analysis tools.

4. A number of experimental tests using the manufactured streamlined cable were conducted, including tests in the wind tunnel, with kites, with balloons and a horizontal set-up equipped with a number of sensors to monitor the behaviour. The streamlined cables tested exhibited both stable and unstable behaviour.

5. Model results for a baseline streamlined cable were given to demonstrate the capabilities of the model and gave preliminary results on how the position of the structural centres, a non-uniform fluid loading profile and variations in tension can affect the stability and dynamics of a streamlined cable.

Prior to presenting any new work, a review of the existing body of work demonstrated the wide range of relevant research areas spanning structural dynamics of beams and cables, aeroelasticity and composite structures. The review focused first on the existing applications of streamlined cables, which are limited to off-shore towed cable arrays and risers. Recent research in high-altitude tethered balloons and kite power generators has further fuelled interest in the use of streamlined cables. To provide appropriate streamlined cable models, the current research drew from theory developed for fixed wing aircraft, helicopters, wind turbines, composite structures and cable dynamics.

Three models were developed over the course of the presented work, each laying a bit of groundwork for the next. The first model was an extension of the classic two-degree-of-freedom flutter model to include the effect of tension acting offset from the conventional bending and torsional stiffness terms. The relatively simple structural model presented a convenient opportunity to include more comprehensive aerodynamic theory. In the two-degree-of-freedom model, a finite-state induced-flow theory was used to model fully unsteady-flow around the aerofoil. The second model presented was a continuous streamlined cable model with the scope to include wave-propagation effects in the spanwise direction of the streamlined cable. Here, wave-propagation techniques including spatial,

temporal and power flow analysis were introduced as a means to study the stability characteristics of the streamlined cable. The final most comprehensive model developed, was a discrete, finite-element model of the cable for small deformations. This model has the scope to deal with complex cross-sectional properties including offset structural centres and cross-coupling, stress-stiffening effects from the applied external tension and non-linear effects such as varying fluid loading profiles and variations in tension along the cable length.

A more practical approach to streamlined cable development was taken alongside the theoretical approach. A manufacturing process for streamlined cable was developed through the SPICE project by ESE Ltd. and DT Ltd. The manufacturing process was the first of its kind to produce streamlined cable of this type, which was of composite construction with the internal tension element being streamlined using PU foam and a polyethylene skin. The manufacturing process allowed for the centres of mass to be altered. Two streamlined cables with similar cross-sectional properties, but with different positions of the centre of mass, were manufactured and tested. The experimental tests demonstrated that moving the centre of mass towards the leading edge gave a more stable overall construction, which was generally consistent with the findings from the developed streamlined cable models.

In the final chapter, the capabilities of the streamlined cable model were demonstrated and some of the dynamic behaviour of the streamlined cable were explored. The initial findings found that the most stable cross-sectional configurations for flutter and divergence for a streamlined cable under tension had centres of mass forward of the tension and shear centre, and tension and shear centres forward of the aerodynamic centre. This finding was consistent with classic flutter theory generally used for fixed wing aircraft. The effect of varying fluid loading profile and varying tension were shown to have an important influence on the stability boundary. Depending on the fluid loading profile, the mode shape and frequency of the unstable mode can vary significantly. Similarly, for a system under varying tension, the change in the mode shape affects the frequency and magnitude of the critical flutter velocity.

The work presented provided a base-line model from which further work on streamlined cables can be completed. Recommendations for further work to continue the streamlined cable development process, both theoretically and empirically, are provided in the next section.

9.2 Recommendations for Further Work

The recommendations for further work can roughly be divided into the areas related to the theoretical modelling and areas related to the manufacturing and testing. Continuing work in both areas is important as different sets of problems are addressed, all of which contribute to the development and implementation of streamlined cables.

The models developed in the current work provide a foundation for future research. The discrete, finite element streamlined cable model is for small deformations from an initially straight configuration and has used eigenvalue analysis to assess the stability characteristics. Recommendations for future work include extending the model to include initial and large deformations. The discrete model presented has been developed in a way to facilitate a transition to time domain and control theory analysis. Specifically, the chosen unsteady aerodynamic model (finite-state flow induced model) is written in terms of the time domain. This could be useful in the analysis of certain streamlined cable applications. For example, control strategies using winching at the bottom have been suggested for high-altitude tethered balloons applications and form the basis of kite-power generators. As the presented model is general in nature, further work could focus on using the model to analyse more specific applications such as a high-altitude tethered balloon or kite-power generator.

In extending the model to large deformations, future work should include the effect of drag. In the current work, the focus was on building a simple, preliminary model to assess the fundamental stability and dynamics of a streamlined cable. As the model developed was for small deformation, the effect of drag was neglected since the streamlined cable is assumed to be initially straight and aligned with the wind. Given a small displacement from the aligned configuration, the force of lift generated is significantly larger than that of drag for small angles of attack, thus drag was neglected. For large deformations, this may not be the case. Thus, it is recommended that further work includes the effect of drag and quantifies its effect on the overall stability.

In terms of the manufacturing process and experimental testing, the current work has provided some of the necessary groundwork. There is scope to improve the streamlined manufacturing process. Nevertheless, the streamlined cable machine is functioning and can produce streamlined cable for future testing. Testing vertical configurations of streamlined cable is desirable as it would provide a better representation of potential streamlined cable applications. These future tests could include more experiments using balloons or kites or, similar to the horizontal test, the streamlined cable could be supported more permanently using a crane or by hanging the streamlined cable off a structure such as a bridge.

Overall, this works has shed light on a complicated and multi-disciplinary problem. The benefits of a streamlined cable are highly dependent on the context within which it is used. For cases where potential reduced drag and VIV benefits have been identified, the current work provides tools to help assess and characterise the dynamics and stability of the streamlined cable so these benefits may be exploited.

References

[1] Abbott, I. H. (1959). *Theory of Wing Sections : Including a Summary of Airfoil Data*. McGraw-Hill, New York.

[2] Aglietti, G. S. (2009). Dynamic response of a high-altitude tethered balloon system. *Journal of Aircraft*, 46(6):2032–2040.

[3] Aglietti, G. S., Redi, S., Tatnall, A. R., and Markvart, T. (2009). Harnessing high-altitude solar power. *IEEE Transactions on Energy Conversion*, 24(2):442–451.

[4] Albers, J. and DaSilva, M. L. (1977). Innovative risers speed drilling in the high-current areas off brazil. *Oil and Gas Journal*, 75(16):74–81.

[5] Argatov, I. and Silvennoinen, R. (2010). Energy conversion efficiency of the pumping kite wind generator. *Renewable Energy*, 35(5):1052–1060.

[6] Badesha, S., Euler, A., and Schroeder, L. D. (1996a). Very high altitude tethered balloon parametric sensitivity study. In *AIAA 34th Aerospace Sciences Meeting and Exhibit*, Reno, Nevada.

[7] Badesha, S. S. (2002). SPARCL: a high-altitude tethered balloon-based optical space-to-ground communication system. *Proceedings of SPIE*, 4821:181–193.

[8] Badesha, S. S. and Bunn, J. C. (2002). Dynamic simulation of high altitude tethered balloon system subject to thunderstorm windfield. In *AIAA Atmospheric Flight Mechanics Conference and Exhibit*, pages 512–522, Monterey, California. AIAA.

[9] Badesha, S. S., Euler, A. J., and Schroder, L. D. (1996b). Very high altitude tethered balloon trajectory simulation. *AIAA 21st Atmospheric Flight Mechanics Conference*, pages 651–656.

[10] Banerjee, J. R. (1999). Explicit frequency equation and mode shapes of a cantilever beam coupled in bending and torsion. *Journal of Sound and Vibration*, 224(2):267–281.

[11] Bauchau, O. A. and Hong, C.-H. (1987). Finite element approach to rotor blade modeling. *Journal of the American Helicopter Society*, 32(1):60–67.

[12] Bely, P. Y., Ashford, R., and Cox, C. D. (1995). High-altitude aerostats as astronomical platforms. *Proceedings of SPIE*, 2478:101–116.

[13] Belytschko, T. and Mindle, W. L. (1980). Flexural wave propagation behavior of lumped mass approximations. *Computers and Structures*, 12(6):805–812.

[14] Bhaskar, A. (2003). Waveguide modes in elastic rods. *Proceedings of the Royal Society A: Mathematical, Physical and Engineering Sciences*, 459(2029):175–194.

[15] Bisplinghoff, R. L. (1975). *Principles of Aeroelasticity*. Dover Publications, New York.

[16] Blasques, J. P. and Stolpe, M. (2012). Multi-material topology optimization of laminated composite beam cross sections. *Composite Structures*, 94(11):3278–3289.

[17] Blevins, R. D. (1977). *Flow-induced Vibration*. Van Nostrand Reinhold, New York.

[18] Blevins, R. D. (1984). *Applied Fluid Dynamics Handbook*. Van Nostrand Reinhold, New York.

[19] Bokaian, A. (1990). Natural frequencies of beams under tensile axial loads. *Journal of Sound and Vibration*, 142(3):481–498.

[20] Buckham, B. J. (2003). *Dynamics modelling of low-tension tethers for submerged remotely operated vehicles*. Ph.D., University of Victoria.

[21] Cesnik, C. E. S. and Hodges, D. H. (1997). VABS: A new concept for composite rotor blade cross-sectional modeling. *Journal of the American Helicopter Society*, 42(1):27–38.

[22] Cesnik, C. E. S., Hodges, D. H., and Sutyrin, V. G. (1996). Cross-sectional analysis of composite beams including large initial twist and curvature effects. *AIAA journal*, 34(9):1913–1920.

[23] Chai, Y. T., Varyani, K. S., and Barltrop, N. D. P. (2002). Three-dimensional lump-mass formulation of a catenary riser with bending, torsion and irregular seabed interaction effect. *Ocean Engineering*, 29(12):1503–1525.

[24] Chen, H., Yu, W., and Capellaro, M. (2010). A critical assessment of computer tools for calculating composite wind turbine blade properties. *Wind Energy*, 13(6):497–516.

[25] Collar, A. R. (1978). The first fifty years of aeroelasticity. *Aerospace*, 5(2):12–20.

[26] Cook, R. D., Malkus, D. S., and Plesha, M. E. (1989). *Concepts and Applications of Finite Element Analysis*. Wiley, New York, 3rd ed edition.

[27] Coulombe-Pontbriand, P. (2005). *Modeling and experimental characterization of a tethered spherical aerostat*. M.Sc., McGill University.

[28] Coulombe-Pontbriand, P. and Nahon, M. (2009). Experimental testing and modeling of a tethered spherical aerostat in an outdoor environment. *Journal of Wind Engineering and Industrial Aerodynamics*, 97(5-6):208–218.

[29] Cremer, L. and Heckl, M. (1973). *Structure-Borne Sound : Structural Vibrations and Sound Radiation at Audio Frequencies*. Springer, Berlin.

[30] Crítzos, C. C., Heyson, H. H., and Boswínlde, R. W. (1955). Aerodynamic characteristics of NACA 0012 airfoil section at angles of attack from 0 to 180. Technical report, National Advisory Committee for Aeronautics.

[31] Crutzen, P. J. (2006). Albedo enhancement by stratospheric sulfur injections: a contribution to resolve a policy dilemma? *Climatic Change*, 77(3-4):211–220.

[32] CWA Products Ltd. (2001). *Towing tank tests of CWA cable fairings*. CWA Products Ltd. www.cwaproducts.co.uk. Accessed: May 20 1011.

[33] Davidson, P., Burgoyne, C., Hunt, H. E. M., and Causier, M. (2012). Lifting options for stratospheric aerosol geoengineering: advantages of tethered balloon systems. *Philosophical Transactions of the Royal Society A: Mathematical, Physical and Engineering Sciences*, 370(1974):4263–300.

[34] DeAndrade, O. and Duggal, A. (2010). Analysis, design and installation of polyester rope mooring systems in deep water. *Proceedings of the Offshore Technology Conference*.

[35] Delft University of Technology (2012). Kite Power: Laddermill. www.kitepower.eu/technology.html. Accessed: April 9 2014.

[36] Department of Engineering (2009). *Structures Databook*. University of Cambridge.

[37] Driscoll, F. (2000). Development and validation of a lumped-mass dynamics model of a deep-sea ROV system. *Applied Ocean Research*, 22(3):169–182.

[38] Elliott, S. D., McKay, J. M., and McKee, R. B. (1965). Tethered aerological balloon system. Technical report, U.S. Naval Ordnance Test Station, China Lake.

[39] EnerKite GmbH (2014). EnerKite. www.enerkite.com/EN/. Accessed: April 10 2014.

[40] Euler, A. J., Badesha, S. S., and Schroeder, L. D. (1995). Very high altitude balloon feasibility study. In *11th Lighter-than-air Systems Technology Conference*, pages 46–51, Clearwater Beach, Florida.

[41] Every, M. J., King, R., and Weaver, D. S. (1982). Vortex-excited vibrations of cylinders and cables and their suppression. *Ocean Engineering*, 9(2):135–157.

[42] Fagiano, L., Milanese, M., Member, S., and Piga, D. (2010). High-altitude wind power generation. *IEEE Transactions on Energy Conversion*, 25(1):168–180.

[43] Fehlner, L. F. and Pode, L. (1952). The development of a fairing for tow cables. Technical Report C-433, David Taylor Model Basin.

[44] Folb, R. (1975). Experimental determination of the hydrodynamic loading for ten cable fairing models. Technical report, David W. Taylor Naval Ship Research and Development Center.

[45] Friedland, B. (1986). *Control System Design : An Introduction to State-Space Methods*. McGraw-Hill, New York ; London.

[46] Fung, Y. C. (1969). *Introduction to the Theory of Aeroelasticity*. Dover Publications, New York.

[47] Gaudern, N. (2009). *Wind turbine design*. M.Eng., University of Cambridge.

[48] Geuzaine, C. and Remacle, J.-F. (2009). Gmsh : A 3-D finite element mesh generator with built-in pre- and post-processing facilities. *International Journal for Numerical Methods in Engineering*, 79:1309–1331.

[49] Goland, M. (1945). Flutter of a uniform cantilever wing. *Journal of Applied Mechanics*, 12(4):A197–A208.

[50] Goland, M. and Luke, Y. L. (1948). The flutter of a uniform wing with tip weights. *Journal of Applied Mechanics*, 15(1):13–20.

[51] Goldstein, H. (2002). *Classical Mechanics*. Addison Wesley, London, United Kingdom, 3rd edition.

[52] Google (2013). Google Earth. www.google.co.uk/intl/en_uk/earth/. Accessed: September 24 2013.

[53] Graff, K. F. (1975). *Wave Motion in Elastic Solids*. Clarendon Press, Oxford.

[54] Grant, R. and Patterson, D. (1977). Riser fairing for reduced drag and vortex supression. In *Proceedings of the Offshore Technology Conference*, Houston, Texas.

[55] Griffith, S., Lynn, P., Montague, D., and Hardham, C. (2009). *Faired tether for wind power generation systems*. World Intellectual Property Organization: WO 2009/142762 A1.

[56] Hartsuijker, C., Welleman, J. W. (2007). *Engineering Mechanics. Volume 2: Stresses, Deformations, Displacements*. Springer, Dordrecht, Netherlands.

[57] Hegemier, G. A. and Nair, S. (1977). A nonlinear dynamical theory for heterogeneous, anisotropic, elastic rods. *AIAA Journal*, 15(1):8–15.

[58] Hembree, B. and Slegers, N. (2010). Efficient tether dynamic model formulation using recursive rigid-body dynamics. *Proceedings of the Institution of Mechanical Engineers. Part K: Journal of Multi-body Dynamics*, 224(4):353–363.

[59] Hesse, H. and Palacios, R. (2012). Consistent structural linearisation in flexible-body dynamics with large rigid-body motion. *Computers and Structures Structures*, 110-111:1–14.

[60] Hodges, D. H. (1990). A mixed variational formulation based on exact intrinsic equations for dynamics of moving beams. *International Journal of Solids and Structures*, 26(11):1253–1273.

[61] Hodges, D. H. (2003). Geometrically exact, intrinsic theory for dynamics of curved and twisted anisotropic beams. *AIAA Journal*, 41(6):1131–1137.

[62] Hodges, D. H. (2006). *Nonlinear Composite Beam Theory*. American Institute of Aeronautics and Astronautics, Reston, Va.

[63] Hodges, D. H., Atilgan, A. R., Cesnik, C. E. S., and Fulton, M. V. (1992). On a simplified strain energy function for geometrically nonlinear behaviour of anisotropic beams. *Composites Engineering*, 2(5-7):513–526.

[64] Hodges, D. H. and Pierce, A. G. (2011). *Introduction to Structural Dynamics and Aeroelasticity*. Cambridge University Press, Cambridge, 2nd edition.

[65] Hodges, D. H. and Yu, W. (2007). A rigorous, engineer-friendly approach for modelling realistic, composite rotor blades. *Wind Energy*, 10(2):179–193.

[66] Hoerner, S. F. (1965). *Fluid-Dynamic Drag : Practical Information on Aerodynamic Drag and Hydrodynamic Resistance*. S.F. Hoerner, New Jersey, 2nd edition.

[67] Hung, C. and Nair, S. (1984). Planar towing and hydroelastic stability of faired underwater cables. *AIAA Journal*, 22(12):1786–1790.

[68] Hunt, H. E. M. (2014). Matlab Solutions. www2.eng.cam.ac.uk/~hemh/matlab/matlab.htm. Accessed: April 19 2014.

[69] Huntsman Polyurethanes (2000). *Pipe insulation fact sheet*. Hunstman Holland BV, Everberg, Belgium.

[70] Irvine, H. M. (1981). *Cable Structures*. MIT Press, Cambridge, Massachusetts.

[71] Irvine, H. M. and Caughey, T. K. (1974). The linear theory of free vibrations of a suspended cable. *Proceedings of the Royal Society A: Mathematical, Physical and Engineering Sciences*, 341(1626):299–315.

[72] Jacobs, E. N., Ward, K. E., and Pinkerton, R. M. (1933). The characteristics of 78 related airfoil sections from tests in the variable-density wind tunnel. Technical Report No. 460, National Advisory Committee for Aeronautics (NACA).

[73] Jones, S. P. and Krausman, J. A. (1982). Nonlinear dynamic simulation of a tethered aerostat. *Journal of Aircraft*, 19(8):679–686.

[74] Jones, S. P. and Schroeder, L. D. (2001). Nonlinear dynamic simulation of a tethered aerostat: a fidelity study. *Journal of Aircraft*, 38(1):64–68.

[75] Khorasanchi, M. and Huang, S. (2009). Preliminary instability-analysis of deepwater riser with fairings. In *Proceedings of the ASME 2009 28th Conference on Ocean, Offshore and Artic Engineering*, Honolulu, Hawaii.

[76] Kite Power Solutions Ltd. (2014). KPS: Kite Power Solutions. www.kitepowersolutions.com. Accessed: April 10 2014.

[77] Kitenergy S.r.l. (2014). KITEnrg: Altitude wind generation. www.kitenergy.net. Accessed: April 10 2014.

[78] Lambert, C. (2006). *Dynamics and control of a multi-tethered aerostat positioning system*. Ph.D., McGill University.

[79] Lambert, C. and Nahon, M. (2003). Stability analysis of a tethered aerostat. *Journal of Aircraft*, 40(4):705–715.

[80] Lambert, C., Nahon, M., and Chalmers, D. (2006). Study of a multitethered aerostat system: experimental observations and model validation. *Journal of Aircraft*, 43(4):1182–1189.

[81] Lambert, C. M. (2002). *Dynamics modeling and conceptual design of a multi-tethered aerostat system*. M.Sc., University of Victoria.

[82] Leishman, J. G. (2000). *Principles of Helicopter Aerodynamics*. Cambridge University Press, Cambridge.

[83] Likins, P. W. (1973). *Elements of Engineering Mechanics*. McGraw-Hill, New York, McGraw-Hill [1973].

[84] Lockheed Martin Corporation (2014). Lighter-than-air systems. www.lockheedmartin.co.uk/content/dam/lockheed/data/ms2/documents/Lighter-Than-Air-brochure.pdf. Accessed: April 4 2014.

[85] Loyd, M. L. (1980). Crosswind kite power (for large-scale wind power production). *Journal of Energy*, 4(3):106–111.

[86] Makani Power Inc. (2014). Advanced wind energy: airborne wind turbines. www.google.com/makani/. Accessed: April 10 2014.

[87] Malcolm, D. J. and Laird, D. L. (2007). Extraction of equivalent beam properties from blade models. *Wind Energy*, 10:135–157.

[88] Martienssen, W. and Warlimont, H. (2005). *Springer Handbook of Condensed Matter and Materials Data*. Springer.

[89] Munson, B. R., Young, D. F., and Okiishi, T. H. (2006). *Fundamentals of Fluid Mechanics*. Wiley, Hoboken, New Jersey, 5th edition.

[90] Murua, J. (2012). *Flexible aircraft dynamics with a geometrically-nonlinear description of the unsteady aerodynamics*. Ph.D., Imperial College London.

[91] Murua, J., Palacios, R., and Graham, J. M. R. (2010). Modeling of nonlinear flexible aircraft dynamics including free-wake effects. In *AIAA Guidance, Navigation and Control Conference*, pages 1–25, Toronto, Ontario.

[92] Murua, J., Palacios, R., and R. Graham, J. M. (2012). Assessment of wake-tail interference effects on the dynamics of flexible aircraft. *AIAA Journal*, 50(7):1575–1585.

[93] Nair, S. and Hegemier, G. (1979). Stability of faired underwater towing cables. *Journal of Hydronautics*, 13(1):20–27.

[94] NASA Dryden Flight Research Center Photo Collection (2001). NASA Photo: ED01-0209-3. www.dfrc.nasa.gov/gallery/photo/index.html. Accessed: April 8 2014.

[95] Newland, D. E. (1989). *Mechanical Vibration Analysis and Computation*. Dover Publications Inc., Mineola, New York.

[96] Nitta, K., Yamana, M., and Vicente (Ed.), J. D. (2012). *Poisson's ratio and mechanical nonlinearity under tensile deformation in crystalline polymers*. InTech, Available from: http://www.intechopen.com/books/rheology/poisson-s-ratio-and-mechanical-nonlinearity-under- tensile-deformation.

[97] Nordson EFD (2014). Static Mixers. www.nordson.com/en-us/divisions/efd/products/tah/static-mixers/pages/static-mixers.aspx. Accessed: April 14 2014.

[98] Ockels, W. J. (1997). *Wind-driven driving apparatus employing kites*. United States Patent: US6072245.

[99] Ockels, W. J. (2001). Laddermill, a novel concept to exploit the energy in the airspace. *Aircraft Design*, 4(2-3):81–97.

[100] Païdoussis, M. P., Price, S. J., and Langre, E. D. (2010). *Fluid-Structure Interactions: Cross-Flow-Induced Instabilities*. Cambridge University Press, Cambridge, United Kingdom.

[101] Patil, M. J. and Hodges, D. H. (2006). Flight dynamics of highly flexible flying wings. *Journal of Aircraft*, 43(6):1790–1799.

[102] Patil, M. J., Hodges, D. H., and Cesnik, C. E. S. (1999). Characterizing the effects of geometrical nonlinearities on aeroelastic behavior of high-aspect-ratio wings. In *International Forum on Aeroelasticity and Structural Dynamics*, Williamsburg, Virginia.

[103] Peters, D. A., Karunamoorthy, S., and Cao, W. (1995). Finite state induced flow models. Part I: two-dimensional thin airfoil. *Journal of Aircraft*, 32(2):313–322.

[104] Przemieniecki, J. S. (1968). *Theory of Matrix Structural Analysis*. McGraw-Hill, New York, London.

[105] Redi, S., Aglietti, G. S., Tatnall, A. R., and Markvart, T. (2010). An evaluation of a high altitude solar radiation platform. *Journal of Solar Energy Engineering*, 132(1):011004.

[106] Redi, S., Aglietti, G. S., Tatnall, A. R., and Markvart, T. (2011). Dynamic response to turbulence of tethered lighter-than-air platforms. *Journal of Aircraft*, 48(2):540–552.

[107] Roberts, B. W., Shepard, D. H., Caldeira, K., Cannon, M. E., Eccles, D. G., Grenier, A. J., and Freidin, J. F. (2007). Harnessing high-altitude wind power. *IEEE Transactions on Energy Conversion*, 22(1):136–144.

[108] Rolls-Royce Canada Ltd. - Naval Marine (2012). *TufNose and TufLine fairing system: a unique drag-reducing faired towcable system*. ODIM Brooke Ocean. www.brooke-ocean.com/downloads.html. Accessed: April 4 2014.

[109] RosAeroSystems (2011). Augur RosAeroSystems: Aerostats. http://rosaerosystems.com/aero/. Accessed: April 4 2014.

[110] Royal Institution Channel (2012a). Components: Image Processing. www.richannel.org/collections/2012/components#/components--tether-dynamics. Accessed: April 17 2014.

[111] Royal Institution Channel (2012b). Components: Tether Dynamics. www.richannel.org/collections/2012/components#/components--image-processing. Accessed: April 17 2014.

[112] Shabana, A. A. (1998). *Dynamics of Multibody Systems*. Cambridge University Press, Cambridge, 2nd edition.

[113] Shaw, R. (2012). *Video Capture for a Tethered Balloon*. M.Eng., University of Cambridge.

[114] Shaw, R. (2013). *3D Motion Capture for High-altitude Tethered Balloons*. M. Phil., University of Cambridge.

[115] Sheldahl, R. E. and Klimes, P. C. (1981). Aerodynamics characteristics of seven symmetrical airfoil sections through 180-degree angle of attack for use in aerodynamics analysis of vertical axis wind turbines. Technical report, Sandia National Laboratories: Energy Report.

[116] Simiu, E. and Scanlan, R. H. (1996). *Wind Effects on Structures : Fundamentals and Applications to Design*. John Wiley and Sons, New York, Chichester, 3rd edition.

[117] Slocum, S. T., Ding, Z. J., and Frank, W. R. (2004). Flutter instability in riser fairings. In *Proceedings of the Offshore Technology Conference*, Houston, Texas.

[118] SPICE Project (2014). *SPICE: Stratospheric particle injection for climate engineering*. www.spice.ac.uk. Accessed: April 9 2014.

[119] Stanney, K. and Rahn, C. (2006). Response of a tethered aerostat to simulated turbulence. *Communications in Nonlinear Science and Numerical Simulation*, 11(6):759–776.

[120] Steger, C. (1996). On the calculation of moments of polygons. Technical Report FGBV-96-04, Forschungsgruppe Bildverstehen (FG BV), Informatik IX Technische Universität München.

[121] Svendsen, M. N. (2011). *Wind turbine rotors with active vibration control*. Ph.D., Technical University of Denmark.

[122] Taggart, S. and Tognarelli, M. A. (2008). Offshore drilling riser VIV suppression devices – what's available to operators? In *Proceedings of the 27th Internaional Conference on Offshore Mechanics and Artic Engineering*, Estoril, Portugal.

[123] Talbot, J. P. (2002). *On the performance of base-isolated buildings: a generic model*. Ph.D., University of Cambridge.

[124] TCOM L.P. (2011). TCOM Aerostat Systems. www.tcomlp.com/aerostat-platforms/. Accessed: April 4 2013.

[125] The Royal Society (2009). Geoengineering the climate: science, governance and uncertainty. Technical Report September, The Royal Society, London, United Kingdom.

[126] Theodorsen, T. (1934). General theory of aerodynamic instability and the mechanism of flutter. Technical Report No. 496, NACA, Langley Field.

[127] Timoshenko, S. P. (1987). *Theory of Elasticity*. McGraw Hill, New York, 3rd edition.

[128] Tjavaras, A. A., Zhu, Q., Liu, Y., Triantafyllou, M. S., and Yue, D. K. P. (1998). The mechanics of highly-extensible cables. *Journal of Sound and Vibration*, 213(4):709–737.

[129] Tong, W. (2010). *Wind Power Generation and Wind Turbine Design*. WIT Press, Southampton.

[130] Wagner, H. (1925). Uber die entstehung des dynamischen auftriebs von tragflugeln. *ZAMM - Journal of Applied Mathematics and Mechanics*, 5(1):17–35.

[131] Washizu, K. (1982). *Variational Methods in Elasticity and Plasticity*. Pergamon, Oxford, 3rd edition.

[132] Wayne, J. (1980). *Helicopter Theory*. Princeton University Press, Princeton, Guildford.

[133] White, F. M. (1999). *Fluid Mechanics*. McGraw-Hill, Boston, 4th edition.

[134] Williams, P., Lansdorp, B., and Ockesl, W. (2008). Optimal crosswind towing and power generation with tethered kites. *Journal of Guidance, Control, and Dynamics*, 31(1):81–93.

[135] Witkiewicz, W. and Zielinski, A. (2006). Properties of the polyurethane (PU) light foams. *Advances in Materials Science*, 6(2):35–51.

[136] Wright, J. R. and Cooper, J. E. (2007). *Introduction to Aircraft Aeroelasticity and Loads*. John Wiley and Sons, Chichester.

[137] Yarusevych, S. and Boutilier, M. S. H. (2011). Vortex shedding of an airfoil at low reynolds numbers. *AIAA Journal*, 49(10):2221–2227.

[138] Young, W. C. (1989). *Roark's Formulas for Stress and Strain*. McGraw-Hill, New York, London, 6th edition.

[139] Yu, W. (2002). On Timoshenko-like modeling of initially curved and twisted composite beams. *International Journal of Solids and Structures*, 39(19):5101–5121.

[140] Yu, W., Hodges, D. H., Hong, X., and Volovoi, V. V. (2002). Validation of the variational asymptotic beam sectional analysis. *AIAA Journal*, 40(10):2105–2112.

[141] Zandbergen, T. (2008). Low drag line: the design and modeling of a cable. Technical report, TU Delft, Delft, Netherlands.

[142] Zanon, M., Gros, S., Andersson, J., and Diehl, M. (2013). Airborne wind energy based on dual airfoils. *IEEE Transactions on Control Systems Technology*, 21(4):1215–1222.

Appendix A

Prototype Streamlined Section Manufacturing

In the initial stages of manufacturing, short streamlined sections were prototyped at the Cambridge University Engineering Department (CUED). The prototyped sections were manufactured by injecting foam in a rapid prototyped NACA 0020 mould. To alter the position of the centre of mass, a brass rod was included within the section or part of the foam material was removed. Figures A.1 and A.2 show the mould disassembled and two die halves from an end-on view.

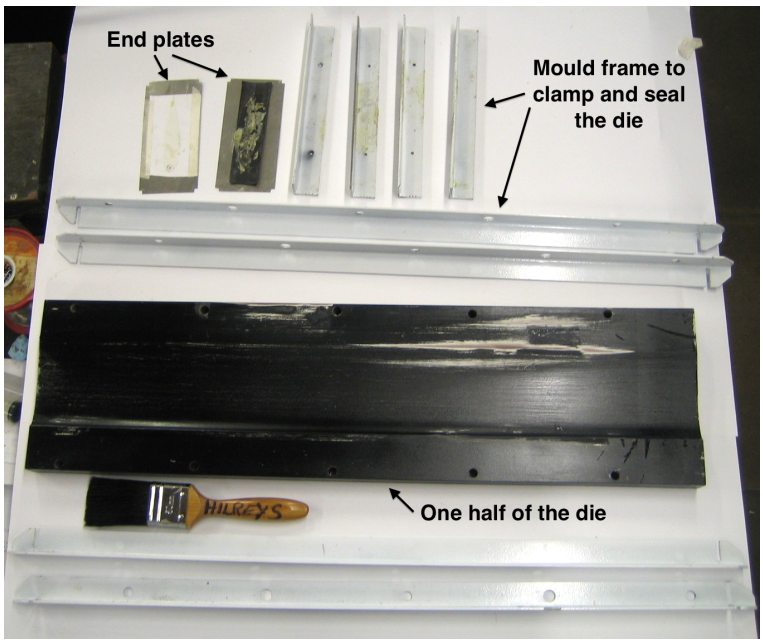

Fig. A.1 Disassembled mould showing the frame and one half of the die.

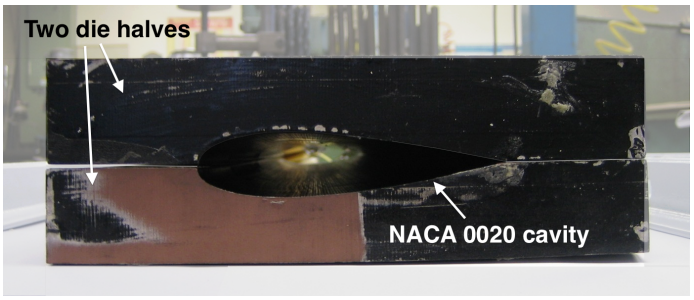

Fig. A.2 End-on view of the two die pieces which form the NACA 0020 mould cavity.

To manufacture a section, the mould was lined with thin plastic sheeting, the internal elements (cable, wire, brass rods, etc.) were secured to one of the end plates and the mould was assembled except for the opposite end-plate. Then, a two-part foam, from Huntmans Polyurethane [69], was mixed and injected into the mould. The final end-plate was then quickly fastened, sealing the expanding foam inside the mould. Manufacturing these short sections highlighted two issues: sufficiently mixing the foam and quickly injecting it into the mould. The mixing and injecting stage is very time sensitive since the foam begins to expand as soon as the two precursors are combined. Two mixing and injection methods were tested.

The first was using a specially designed static mixing and injection system from Nordsend EFD [97]. The system consists of an injection gun and a specially designed mixing nozzle. The injection gun has two barrels which are filled with the two foam precursors. When injected, the two foam precursors are forced through the nozzle, which has an internal ladder-like system to mix the two parts as they travel through it. Figure A.3 shows the injection gun and three types of static mixing nozzle. The design was appealing due to its relative simplicity (no moving parts) and the fact that the nozzle could easily be incorporated into a larger scale manufacturing process. Unfortunately, through testing, none of the nozzles sufficiently mixed the two parts to produce a good quality foam.

The second mixing method used a electrically driven mixer to combine the two foam precursors inside a large syringe-like injector manufactured at CUED. Figure A.4 shows the mixing paddle and the foam injector. This method produced much higher quality foam than the commercial nozzles.

Having produced foam of sufficient quality, another challenge was ensuring that the correct amount of foam was injected into the mould. Too little foam and the desired shape would not be achieve; too much foam and the density would be greater than desired. Figure A.5 shows some of the short streamlined samples produced at CUED using the second mixing method.

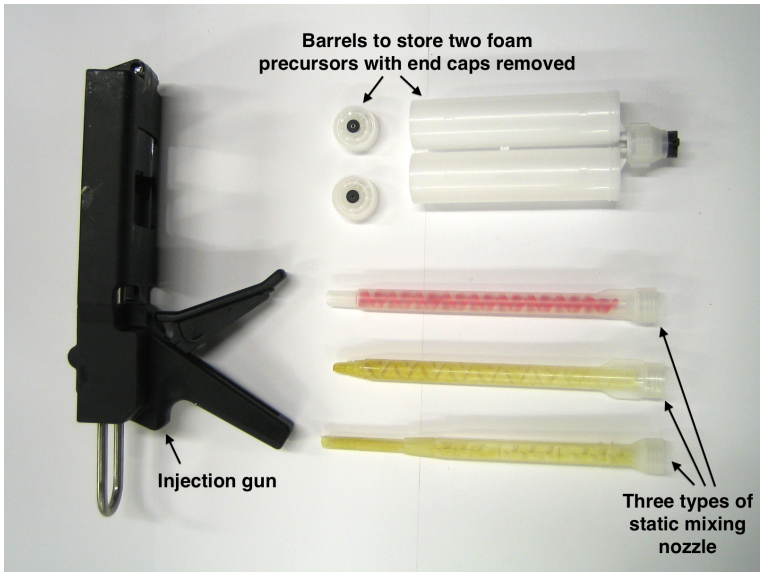

Fig. A.3 Nordson EFD two part mixing system.

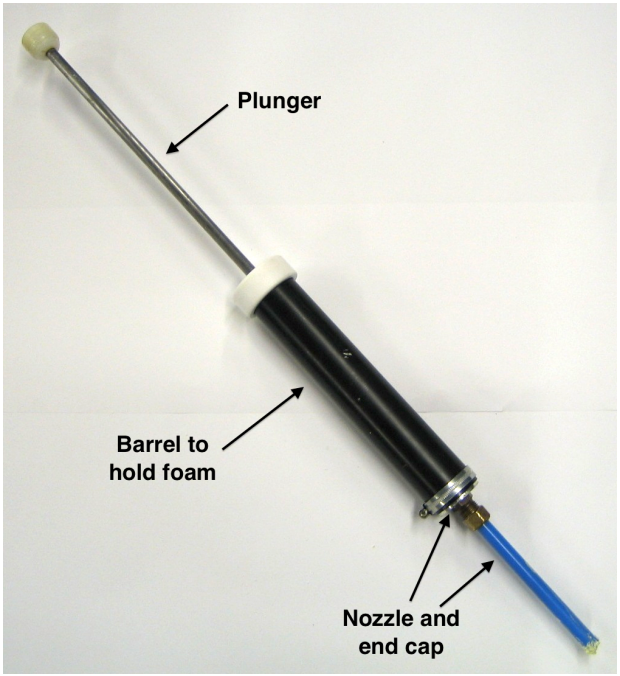

(a) Assemble foam injector.

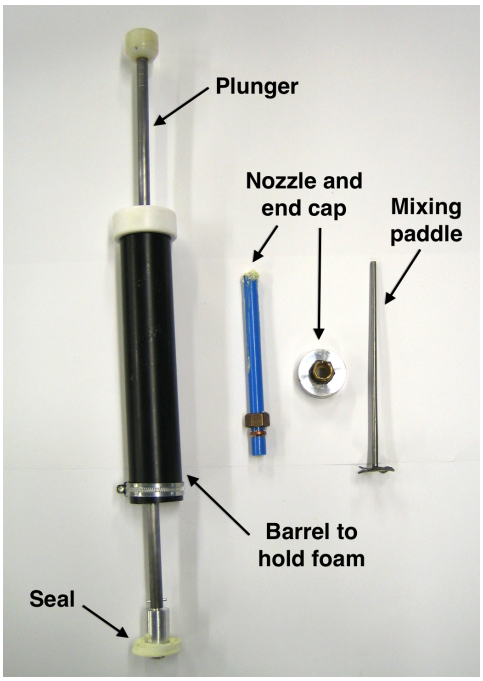

(b) Disassemble injector and mixing paddle.

Fig. A.4 Mixing paddle and the injector which consists of a plunger, nozzle and barrel.

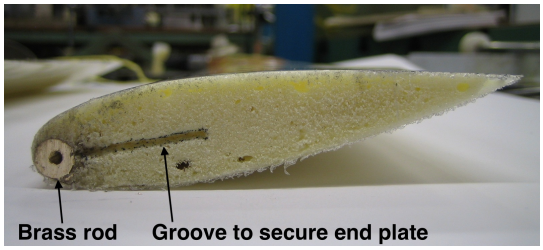

(a) 8 mm brass rod at leading edge.

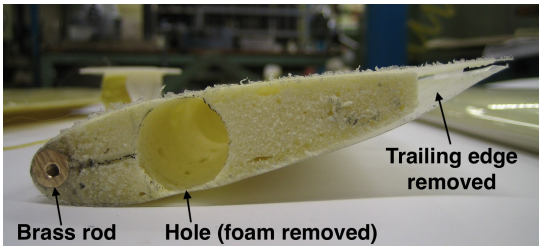

(b) 8 mm brass rod at leading edge. 18 mm hole and trailing edge foam removed.

Fig. A.5 NACA 0020 streamlined samples with 100 mm chord.

Prototyping these sections highlighted some of the design challenges for the full-scale continuous streamlined cable production. Specifically, identifying the required level of mixing to produce high quality foam, the sensitivity of the process to timing, the challenge of incorporating additional internal elements to change the location of the centre of mass and, finally, the trade-off between producing low density foam and achieving a good fill of the mould.

Appendix B

Measurement of Streamlined Cable Properties

The current section describes and reports the experimentally measured cross-sectional properties of the manufactured streamlined cable. The measured properties include: the centre of mass, the shear centre, the bending stiffness and the torsional stiffness. For each measured property the experimental methodology is described and the measured results are presented.

Centre of Mass

To measure the centre of mass, a small test section of the streamlined cable was used. Pins were placed on either side of the section at a measured location along the chord. Figure B.1 shows how the section is supported by the pins and with the trailing edge placed on the mass balance. The position of the centre of mass can be determined knowing the total mass of the section, the location of the pins and the weight indicated on the balance. Using the same cross-sectional conventions described in Chapters 3 to 5 gives the equation

$$m(r-\mathcal{F}) = N(1-\mathcal{F}) \tag{B.1}$$

where m is the total mass of the sample, r is the dimensionless position of the centre of mass, N is the mass measured on the balance and $\mathcal{F}$ is the dimensionless position of the pin. Equation (B.1) gives the unknown distance to the centre of mass in terms of the measured values. To improve the accuracy of the results, measurements were taken for a position of the pin ranging along the chord. By plotting the moment relationship as $(1-\mathcal{F})/m + \mathcal{F}/N$ versus $1/N$ the slope of the best fit line is equal to the position of the centre of mass. Figure

B.2 gives an example plot for the blue polyester sample, with the line of best fit shown. Table B.1 summarises the measured results for the four samples. The coefficient of determination R^2 for all the measurements was greater than 0.98, indicating a high quality of the best fit line.

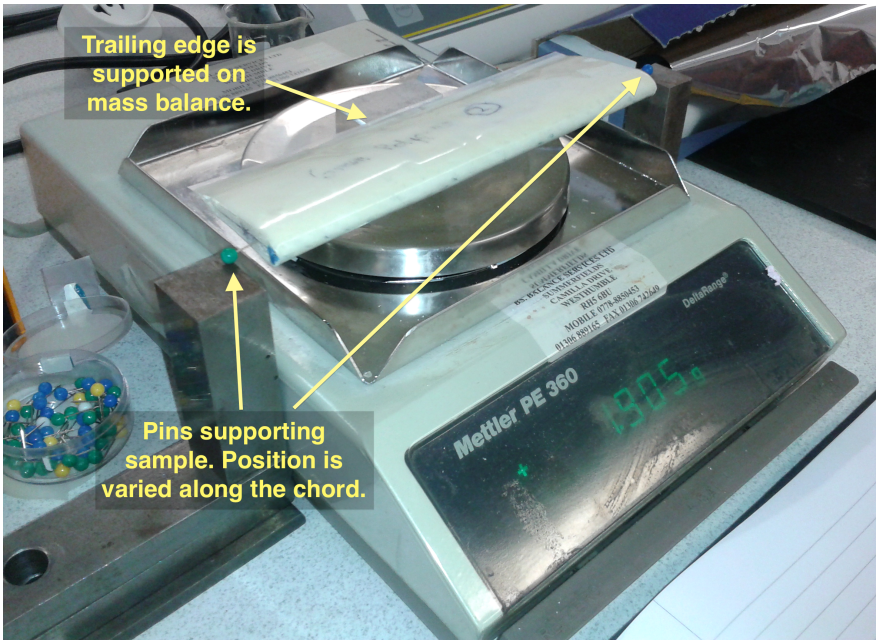

Fig. B.1 Test set-up to measure the centre of mass of manufactured streamlined cable section.

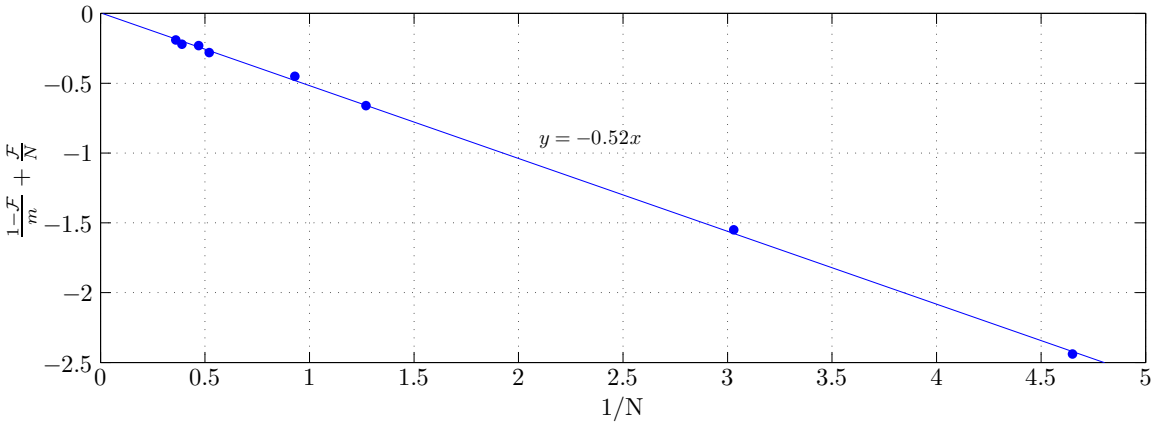

Fig. B.2 Measured results for the PolyWire sample. The slope of the best fit line gives the dimensionless position of the centre of mass r.

Table B.1 Dimensionless position of the centre of mass r from best fit line of measured results and the corresponding coefficient of determination R^2.

Sample	Centre of mass r	R^2
Blue polyester	-0.33	1.0
Wound steel	-0.55	0.98
Red polyester (RedPoly)	-0.44	1.0
Polyester and steel (PolyWire)	-0.52	1.0

Shear Centre

The shear centre is defined as the location where torsion and shear decouple. If a transverse force is applied at the shear centre, the beam will deform in pure translation; if the force is applied offset from the shear centre, the beam will both translate and twist. To determined the location of the shear centre a piece of the streamlined cable was mounted in a simply-supported configuration. A small mass was placed at varying positions along the chord and the movement of the streamlined cable was recorded. To record the movement, a small piece of mirror was fastened to the cable and a laser pointer was set-up vertically (a hanging string was used to align the laser to vertical). The laser hits the piece of mirror and is reflected onto a piece of graph paper. The general set-up is shown in Figure B.3.

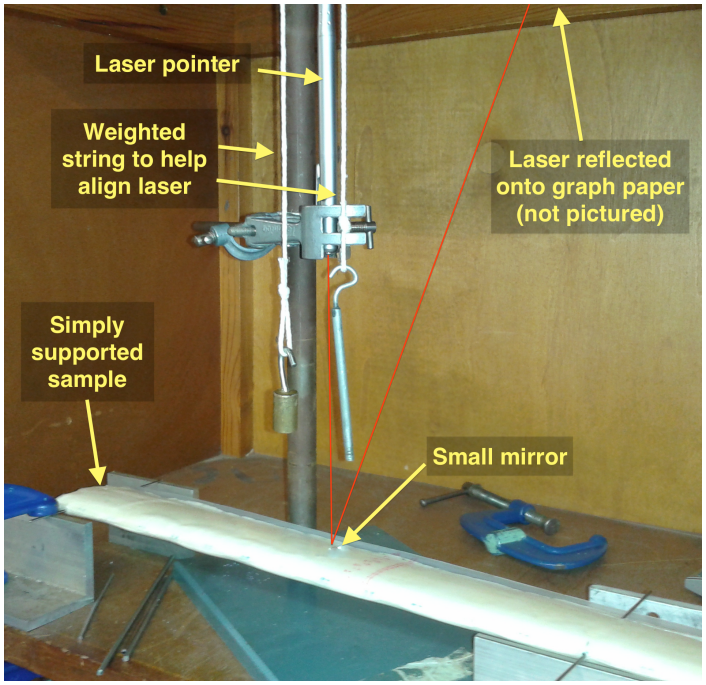

Fig. B.3 Test set-up to determine the shear centre of a streamlined cable section.

If the force from the mass causes pure translation, the point on the graph paper from the reflected laser will not move. If the mass causes the beam to twist, the point from the laser reflection will move. The results of the experiment are plotted below in Figure B.4 for the blue polyester and wound steel samples. The intercept of the best fit line with the location where the movement of the laser is zero (i.e. intercept with the x-axis of the graph) gives the location of the shear centres. The shear centre for the blue polyester and wound steel sample are measured at 11.1 mm and 10.3 mm from the leading edge respectively.

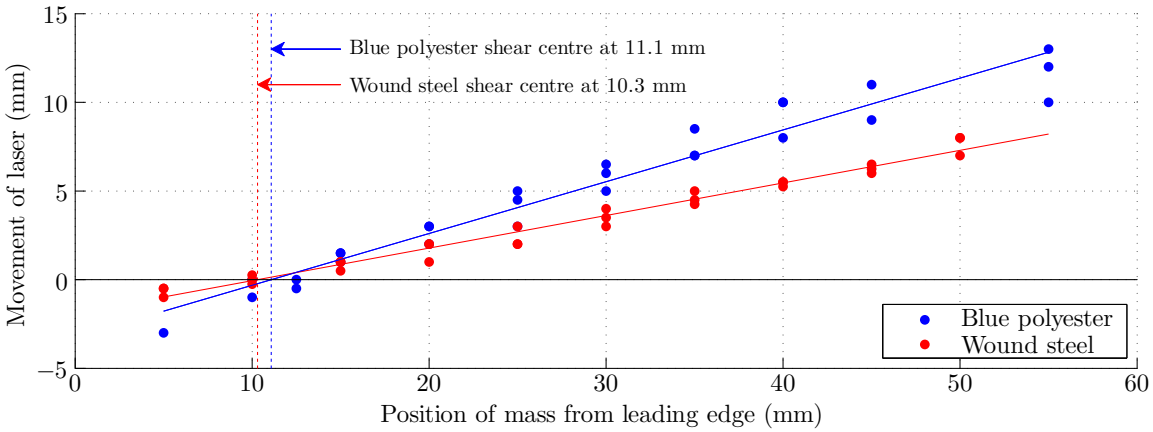

Fig. B.4 Movement of reflected laser given an applied load at varying position along the cross-section. The shear centre corresponds to the location where the load causes no movement of the reflected laser.

Bending Stiffness

The bending stiffness was measured by simply supporting a section of streamlined cable, adding a mass to the centre of the section and measuring the deflection. The stiffness EI_z can be calculated from classic beam theory knowing the magnitude of the applied force and the resulting deflection. The deflection at the centre point of the beam is

$$v\left(\frac{\ell}{2}\right) = \frac{F\ell^3}{48EI_z} \tag{B.2}$$

where F is the applied load, ℓ is the length of the beam, v is the translational displacement and EI_z is the bending stiffness [36]. Plotting the deflection v versus $\frac{F\ell^3}{48}$ gives Figure B.5, where the slope of the best fit line corresponds to EI_z. Measurements were taken for the blue polyester and wound steel samples and yielded a bending stiffness of 0.25 Nm^2 and 0.3 Nm^2 respectively. The coefficient of determination R^2 for both linear fits is equal to 0.96.

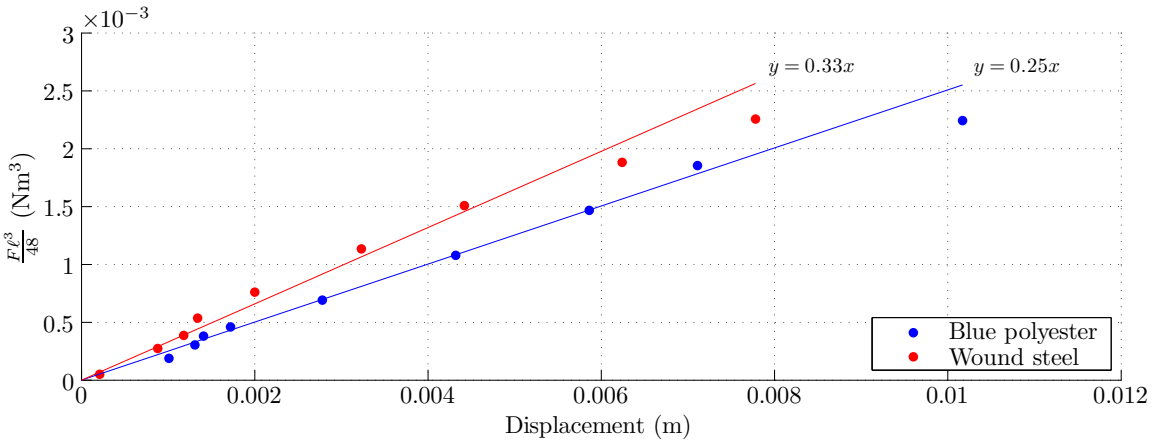

Fig. B.5 Measured displacement and loading to determine EI_z.

Torsional Stiffness

The torsional stiffness was measured by hanging the streamlined cable section vertically with the top end clamped and the bottom end free. A known moment was applied using a mass and pulley system and the rotation of the section was recorded. A photograph of the set-up is shown in Figure B.6.

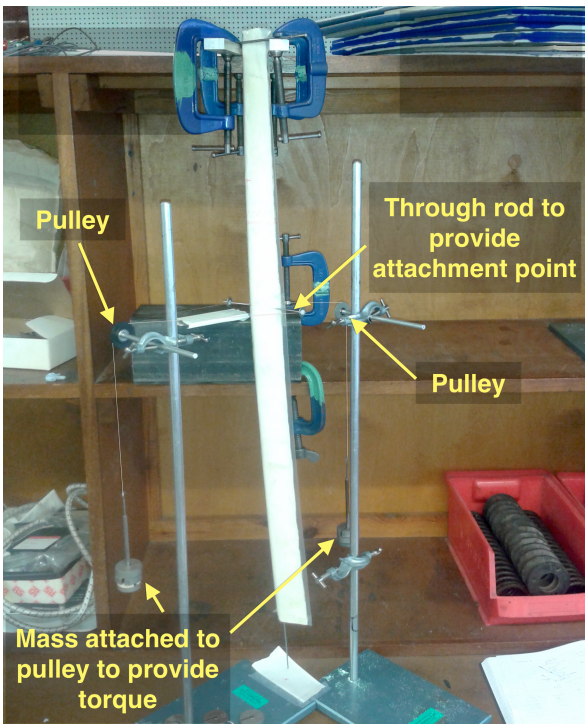

Fig. B.6 Test set-up to determine the torsional stiffness of the streamlined cable.

Knowing the relation $T = GJ\frac{\theta}{\ell}$ from classic beam theory, the torsional stiffness GJ can be calculated from the applied torque and the measured rotation. Figure B.7 plots the torque relation so that the slope of the best fit line gives GJ. The measured results give a torsional stiffness for the blue polyester and wound steel cable of 0.17 Nm^2 and 0.14 Nm^2 with R^2 of 0.95 and 0.92 respectively. During the experiment, after the loading was removed it was observed that the streamlined cable did not return to its original position. This hysteretic behaviour is seen from the difference in the two measured rotation values at the initial torque and final torque measurements. These measurements correspond to 0.05 Nm and 0.03 Nm for the blue polyester and wound steel samples respectively.

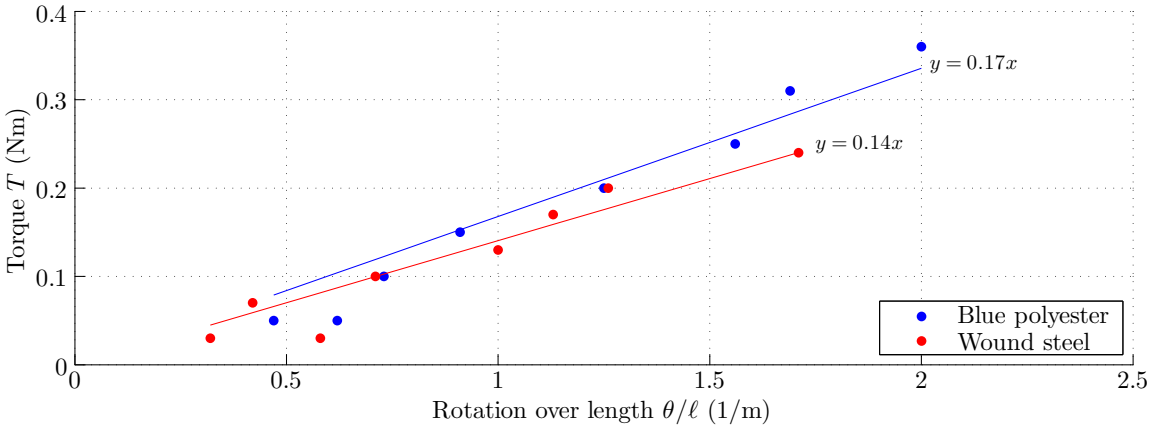

Fig. B.7 Measured torque and deflection to give torsional stiffness.